An investigation of the Reynolds-number Dependence of the Axisymmetric Jet Mixing Layer using a 138 Hot-wire Probe and the POD

by

Daehan Jung

A dissertation submitted to the
Faculty of the Graduate School of the
State University of New York at Buffalo
in partial fulfillment of the requirements for the degree of

Doctor of Philosophy

September 2001

Department of Mechanical and Aerospace Engineering

To Heetae, Yoontae, and Hyejung

Abstract

The Proper Orthogonal Decomposition (POD) technique is applied to find the effects of Reynolds number and the characteristics of the organized motions or coherent structures as a function of downstream position in a turbulent axisymmetric shear layer. In this experiment measurements were made at positions of $x/D = 2$ to 6 spaced $0.5x/D$ apart along downstream direction for the three different jet Reynolds number of 78 400, 117 600, and 156 800. Data were taken simultaneously at all measuring positions using 138 hot-wire probes.

One of the goals of this investigation was to quantify how the energy distribution among the various modes varied as a function of Reynolds number and to determine when or if ever the asymptotic trends become Reynolds number independent. Also, since the earlier experiments were performed at only a single downstream position, another goal was to investigate whether the modal character of the flow changed with downstream position.

In brief, the distributions of POD mode energy have strong dependence on x/D. Even more surprising, mode-0 behaves in a manner entirely different than the higher modes. Also, the results are very nearly independent of Reynolds number. The lowest azimuthal mode (mode-0) for all POD Modes, which dominate the dynamics at $x/D = 2$ dies off rapidly downstream. On the other hand, for the higher azimuthal modes, the peaks shift to lower mode numbers and actually increase with downstream distance. The eigenvalues from the first POD mode vary as a function of mode azimuthal number for ($m \geq 1$), downstream distance and Reynolds number. With

scaling by x/D, they collapse for all Reynolds numbers onto a single curve.

The full-field streamwise instantaneous fluctuating velocity was reconstructed from the POD modes. Modes constructed from these show clearly that the "volcano"-like events around $x/D = 2$ to 3 evolve into a more"propeller"-like pattern where the number of "blades" diminishes downstream. It will be argued that this behavior is similar to that predicted from inviscid instability theory.

Acknowledgements

I would like to thank, first of all, my mentor Professor William K. George for his unrelenting guidance and support throughout the research and beyond. My stay in TRL (Turbulence Research Laboratory) was a wonderful time to be with him and to discuss turbulence with him. He showed me what the scientist is and how the scientist works as an advisor and a frontier in turbulence.

I also want to thank Professor Dale B. Taulbee and Professor Hui Meng for being on my dissertation committee. I would like to thank Professor Lawrence Ukeiley of the University of Mississippi for being the outside reader. I also would like to thank Dr. Mark Glauser (Syracuse University), and Dr. Daniel Ewing (Mcmaster University, Canada) for the constructive comments for my research.

I would like to give special thanks to Scott Woodward for his help for my experiments. He was a great helper to finish my research including the operation of the experiment and computer networking as a staff and a good friend with Lu. Also, I would like to appreciate all my colleagues, Dr. Martin Wosnik (CTH, Sweden), Dr. Asad Sadar (Air International), Dr. Honglu Wang, Dr. Luciano Castillo (RPI), PhD. Candidate Stephan Gamard, and PhD candidate Peter Johansson (CTH, Sweden). They are very kind and helped me a lot to settle down this TRL, to enjoy American (Swedish) life, and to improve academic research as well. Also, I could not forger the help from Kenny at machine shop, Daniel Kook at TRL.

I would like to thank Heetae, Yoontae, and Hyejung for all their endless love and support in spite of a poor dad and husband. Without their help, I am sure that it

would not have been possible to achieve my research goals. I really appreciate what they have done for me. Also, I would like to thank to my mom and brothers, my parent-in-law and brother-in-law, and sisters-in-law. I would like to express special thanks priest Dominic Jung (St. Andrew Kim at Buffalo) who taught me how to trust God and support me as spiritual guidance.

I would like to express my appreciation to the Korea Air Force Head Quarters and Korea Air Force Academy for their financial support and allowing me to have the opportunity for my PhD. program as well.

I would like to have a chance to contribute what I learned here to my student as what Bill have done for me.

Contents

List of Figures

List of Tables

Chapter 1

Introduction

The existence of large-scale structures in turbulent flows has been known for a number of years. It is also known that these large-scale structures play important roles in applications, like chemical mixing, noise control, momentum transfer, drag reduction, combustion enhancement, etc. Since the large-scale structures are embedded inside the turbulent motion, it is very difficult to identify and extract them from the chaotic turbulent flows. Therefore much effort has been devoted to various flows, including wall-bounded flow (boundary layer), planar shear layer, circular shear layer, flows in complex geometries, etc.

The axisymmetric turbulent jet has been investigated for many years and by many researchers. These include Crow & Champagne (1971); Yule (1978); Lau & Fisher (1975); Armstrong *et al.* (1977); Hussain & Clark (1981); Glauser *et al.* (1987); Glauser (1987); Liepmann (1991); Ukeiley *et al.* (1991); Martin & Meiburg (1991); Liepmann & Gharib (1992); Grinstein *et al.* (1995); and most recently Citriniti & George (2000); Taylor *et al.* (2001). These efforts have been well summarized by Gad-el-Hak *et al.* (1998), and Holmes *et al.* (1996).

To identify the large-scale structure, various kind of experimental techniques have been used. Crow & Champagne (1971) suggested the evolution of orderly flow from an instability of the jet. Using flow visualization and forcing, they observed an evolution

from a sinusoid to a helix, and finally to a train of axisymmetric waves. Hussain & Clark (1981) also used flow visualization to demonstrate the presence of coherent structures. Later Hussain and his coworkers used conditional sampling technique to show how the vortical structures interact and coalesce. Liepmann (1991), and Liepmann & Gharib (1992) used a combination of flow visualization and velocity measurement techniques (LDV and DPIV) for Reynolds numbers from 3 000 to 25 000. They observed strong streamwise vorticity, and suggested it was important in the entrainment process and the dynamics of the near-field.

Apart from the experimental method, Michalke (1984), and Michalke & Hermann (1982) suggested, using inviscid linearized stability theory, that the large scale structure in an axisymmetric jet is dominated by the axisymmetric (mode-0) and azimuthal mode-1 in the near jet exit.

Although there have been many experiments performed to identify the large-scale structures and to extract the structure from the turbulent flow, there are some significant limitations of the techniques used to define the large-scale structure. Flow visualization techniques can show lots of valuable information, but only at low Reynolds number. As suggested by Delville *et al.* (1998), instantaneous and real time information about the large-scale structures is necessary for active control. The conditional sampling approach also has important limitations. Since the phase of the structure must be locked by the conditional sampling technique, the temporal evolution of the structure is limited.

The proper orthogonal decomposition (POD) was introduced to the turbulence by Lumley (1967) as a method to define the large-scale structure as an identifiable manner. Various kind of applications have been performed to extract the coherent structures by decomposing the velocity field into characteristic eddies with random coefficients. Moin & Moser (1989) applied the POD to a channel flow using a numerical simulation and found that the dominant eddy contributes as much as 76% to the turbulent kinetic energy. Glauser (1987) and Glauser & George (1987*b*) first applied

the POD to the axisymmetric mixing layer without any controlled excitation of the layer, and showed that a low-dimensional description of the time dependent velocity field was possible. Ukeiley *et al.* (1991, 1992, and 1993) used POD in a lobed mixer, and showed the influence of the large-scale structure on the flow. Arndt *et al.* (1997) used the POD for the unsteady pressure field surrounding an axisymmetric jet and showed that the general characteristics of the structure could be represented by the POD streamwise eigenfunctions. Taylor *et al.* (2001) applied the POD to the subsonic shear layer ($Ma = 0.3$ to 0.85), and suggested that the POD modes are insensitive to variations of Reynolds numbers.

In an earlier version of this experiment, Citriniti & George (2000) obtained the dynamics of the large structures from instantaneous realizations of the streamwise velocity field using 138 simultaneously-sampled hot-wire anemometer probes. They showed that only a few azimuthal Fourier modes are necessary to represent the evolution of the large scale structure from the turbulent field. Furthermore, the velocity reconstructions using the POD provided evidence for both azimuthally coherent structures that exist near the potential core, and for counter-rotating, streamwise vortex pairs (or ribs) in the region between successive azimuthally coherent structures, as well as coexisting for short periods with them. They also observed that the most spatially correlated structure in the flow ejects fluid in the streamwise direction in a volcano-like eruption, and attributed this to the attempted leap-frogging of vortex rings in the flow as suggested by Grinstein *et al.* (1995).

The Glauser and Citriniti experiments were purposely performed at Reynolds numbers that were presumed sufficiently high to insure near Reynolds number independence of the large scale structures. Recently Holmes *et al.* (1996) suggested that perhaps more complicated representations might be necessary at higher Reynolds number. Therefore, one of the goals of the present investigation was to quantify how the energy distribution among the various modes varied as a function of Reynolds

number and to determine when, or if ever, the asymptotic trends become Reynolds number independent. Also, since both the Glauser and Citriniti experiments were performed at only a single downstream position, another goal was to investigate whether the modal character of the flow changed with downstream position.

In this experiment, data are presented at Reynolds numbers of 78 400, 117 600, and 156 800 for the jet mixing layer at downstream positions ranging from $x/D = 2.0$ to 6.0. The eigenvalues resulting from the POD are examined for various azimuthal modes and POD (radial) modes in the range of $x/D = 2.0$ to 6.0 of the axisymmetric shear layer, and various Reynolds numbers.

To extract the large scale coherent features from the axisymmetric mixing layer, and make clear the inter-relations between the azimuthal modes or/and the POD (radial) modes, the original velocity field is reconstructed using the eigenvalues and the eigenfunctions obtained from the POD. For the reconstruction of the original velocity field, the measurements were made simultaneously at all 138 points. The evolution of the coherent structures was observed, and which modes were dominant along downstream positions.

The presentation of this dissertation is as follows: The fundamental theory of the POD will be presented in Chapter 2. The experimental facility and set up is described in detail in Chapter 3. Statistical results including the mean velocity, turbulence intensity, and spectral distribution are presented in Chapter 4. Chapter 5 is devoted to the results of the POD. Of special interest is the energy distribution of eigenvalues for the POD, and their dependence on frequency and the azimuthal mode numbers. Also, the dependence of the eigenvalues and eigenfunctions on the downstream positions and Reynolds numbers will be described in detail. Chapter 6 presents the original velocity reconstructions. These show the inter-relation of the various modes, and their evolution along the downstream directions. Finally in Chapter 7, the important results from this dissertation are briefly summarized.

Chapter 2

The Proper Orthogonal Decomposition

2.1 Introduction

The Proper Orthogonal Decomposition (hereafter POD) was introduced to the turbulence group by Lumley (1967). The POD is a linear procedure, and produces a basis for the modal decomposition of an ensemble of functions, such as data obtained from experiments. It also provides the most efficient way of capturing the dominant components of an infinite dimensional process with only a finite number of modes (Holmes *et al.* 1996; George 1988).

This chapter introduces the fundamental idea of the POD. It shows how the eigenfunctions it produces can be used to decompose the flow field, and how they can be used to reconstruct it in whole or in part. The application of the POD to the axisymmetric jet will be presented in detail.

2.2 The proper orthogonal decomposition

2.2.1 The POD theorem

We define the instantaneous velocity vector, $u_i(\vec{x},t)$, as a function of space, $\vec{x}$, and time, t, in a space-time random field. Further, we define the ensemble average, $< u_i(\vec{x},t) >$, over a series of separate experiments. The experiments described herein are assumed stationary in time, so the time average obtained from successive measurements during a single run is equivalent to the ensemble average.

We seek candidate deterministic basis functions, $\phi_i^{(n)}(\vec{x},t)$, which are optimal for finite dimensional representations of $u_i(\vec{x},t)$, say $u_i^N(\vec{x},t)$ defined by:

$$u_i^N(\vec{x},t) = \sum_{n=1}^{N} a_n \, \phi_i^{(n)}(\vec{x},t) \tag{2.1}$$

For the POD used here, the deterministic functions, $\phi_i(\vec{x},t)$, are defined by choosing ϕ to maximize the averaged projection of u onto ϕ in a Hilbert space (Lumley 1970; Holmes *et al.* 1996); i.e.,

$$max \; \frac{\int_D \phi_i^*(\cdot) u_i(\cdot) \, d(\cdot)}{[\int_D \phi_l(\cdot)\phi_l^*(\cdot) \, d(\cdot)]^{1/2}} = \alpha \tag{2.2}$$

where the asterisk denotes the complex conjugate, the subscripts i, j indicate coordinate direction, and the independent variable, $(\cdot)$, is a representation of the appropriate spatial and temporal location. At this point, there are no restrictions in the domain D. The projection is normalized to eliminate amplitude dependence and emphasize instead the degree of projection.

To maximize α, we define:

$$max \; \frac{\left\langle \int_D \phi_i^*(\cdot) u_i(\cdot) \, d(\cdot) \int_D \phi_i(\cdot') u_i^*(\cdot') \, d(\cdot') \right\rangle}{\int_D \phi_l(\cdot)\phi_l^*(\cdot) \, d(\cdot)} = \overline{\alpha^2} = \lambda \tag{2.3}$$

where $<>$ or the overbar denotes the ensemble average. For the statistics of $\overline{\alpha^2}$, the

best ϕ is the one which gives the largest magnitude of $\overline{\alpha^2}$ in some average sense. Thus ϕ is selected to maximize $\overline{\alpha^2}$.

To find extrema in Equation 2.3 with the constraint $\| \phi \|^2 = \int_D \phi_l(\cdot)\phi_l^*(\cdot)d(\cdot) = 1$, the functional for this constrained variational problem in the *calculus of variations* is:

$$J[\phi] = \left\langle \int_D \phi_i^*(\cdot)u_i(\cdot)d(\cdot) \int_D \phi_j(\cdot')u_j^*(\cdot')d(\cdot') \right\rangle - \lambda \left(\int_D \phi_l(\cdot)\phi_l^*(\cdot)d(\cdot) - 1 \right) \tag{2.4}$$

and a necessary condition for an extremum is that the functional derivative vanish for all variations $\phi + \epsilon\phi'$ in the deformation path of the maximizing function ϕ; i.e.,

$$\frac{d}{d\epsilon} J[\phi(\cdot) + \epsilon\phi'(\cdot)]_{\epsilon=0} = 0 \tag{2.5}$$

where ϵ denotes a scale factor. This becomes using Equation 2.4:

$$\begin{aligned}
&\frac{d}{d\epsilon} J[\ \phi + \epsilon\phi'\ ]_{\epsilon=0} \\
&\quad = \frac{d}{d\epsilon}[\left\langle \int_D u_i(\cdot)\{\phi_i(\cdot) + \epsilon\phi_i'(\cdot)\}^* d(\cdot) \int_D \{\phi_j(\cdot') + \epsilon\phi_j'(\cdot')\}u_j^*(\cdot')d(\cdot') \right\rangle \\
&\qquad -\lambda \int_D \{\phi_l(\cdot) + \epsilon\phi_l'(\cdot)\}\{\phi_l(\cdot) + \epsilon\phi_l'(\cdot)\}^* d(\cdot) + \lambda] \mid_{\epsilon=0} \\
&\quad = \iint_D \left\langle u_i(\cdot)u_j^*(\cdot') \right\rangle \{[\phi_i(\cdot)\phi_j'^*(\cdot')]^* + \phi_j(\cdot')\phi_i'^*(\cdot)\} d(\cdot)d(\cdot') \\
&\qquad -\lambda \int_D \{[\phi_l'^*(\cdot)\phi_l(\cdot)]^* + \phi_l'^*(\cdot)\phi_l(\cdot)\}\, d(\cdot) \\
&\quad = \left\{ \int_D \left[\int_D \langle u_i^*(\cdot)\, u_j(\cdot') \rangle\, \phi_i(\cdot)\, d(\cdot) - \lambda\phi_j(\cdot') \right] \phi_j'^*(\cdot')\, d(\cdot') \right\}^* \\
&\qquad + \int_D \left[\int_D \left\langle u_i(\cdot)u_j^*(\cdot') \right\rangle \phi_j(\cdot')\, d(\cdot') - \lambda\phi_i(\cdot) \right] \phi_i'^*(\cdot)\, d(\cdot) \\
&\quad = 0
\end{aligned} \tag{2.6}$$

where the kernel is the averaged cross-correlation function defined by:

$$\begin{aligned} < u_i(\cdot)\, u_j^*(\cdot') > &= R_{ij}(\cdot,\cdot') \\ &= R_{ji}^*(\cdot',\cdot) \end{aligned} \tag{2.7}$$

Therefore, Equation 2.6 reduces to:

$$2\int_D \left[\int_D R_{ij}(\cdot,\cdot')\,\phi_i(\cdot')\,d(\cdot') - \lambda\phi_j(\cdot)\right]\phi_j^{'*}(\cdot)\,d(\cdot) = 0 \tag{2.8}$$

Since $\phi_j^{'*}(\cdot)$ is an arbitrary variation, Equation 2.8 may be written as a function of space, $\vec{x}$, and time, t; i.e.,

$$\int_D R_{ij}(\vec{x},t,\vec{x}',t')\,\phi_i(\vec{x}',t')\,d(\vec{x}',t') = \lambda\phi_j(\vec{x},t) \tag{2.9}$$

Thus the problem of optimally determining the deterministic function, ϕ_i, leads to an integral eigenvalue problem with the kernel defined by the cross-correlation of the random vector field in the domain, D (George 1988). This is a homogeneous linear integral equation of the second kind. For fixed integration limits, the equation is referred to as Fredholm's equation in the linear integral equation theory (Lovitt 1950).

2.2.2 Fields of finite total energy

For fields of finite total energy and a symmetric kernel, the properties of the eigenvalues and eigenfunctions of the integral eigenvalue Equation 2.9 can be discussed by the Hilbert-Schmidt theory. The main properties of interest in the Hilbert-Schmidt theory are summarized as (Lumley 1967; George 1988):

- There is not one, but a discrete set of solutions to Equation 2.9, which can be

written as:

$$\int_D R_{ij}(\vec{x},t,\vec{x}',t')\phi_i^{(n)}(\vec{x}',t')\,d(\vec{x}',t') = \lambda^{(n)}\phi_j^{(n)}(\vec{x},t), \quad n = 1,\,2,\cdots \tag{2.10}$$

where each eigenfunction, $\phi_i^{(n)}$, is associated with a real positive eigenvalue, $\lambda^{(n)}$.

- This set can be chosen in such a way that the eigenfunctions, $\phi_i^{(n)}$, are orthonormal; i.e.,

$$\int_D \phi_i^{(n)}(\vec{x},t)\,\phi_i^{(m)*}(\vec{x},t)\,d(\vec{x},t) = \delta_{nm} \tag{2.11}$$

  where δ_{nm} is the Kronecker delta function. The orthogonality implies that eigenfunctions of different order do not interact with each other in their contribution to second-order statistics.

- Since the eigenfunctions form a complete set, the random vector field, $u_i(\vec{x},t)$, can be reconstructed from them; i.e.,

$$u_i(\vec{x},t) = \sum_{n=1}^{\infty} a_n \phi_i^{(n)}(\vec{x},t). \tag{2.12}$$

  where the random coefficients are given by:

$$a_n = \int u_i(\vec{x},t)\,\phi_i^{(n)*}(\vec{x},t)\,d(\vec{x},t) \tag{2.13}$$

  since coefficients of different order are uncorrelated; *i.e.*,

$$< a_n a_m^* >= \lambda^{(n)}\,\delta_{nm} \tag{2.14}$$

  Note that unlike Equation 2.10 which only requires information on the two-point correlation, the entire velocity field at a single instant is required by Equation 2.13.

- The kernel $R_{ij}(\vec{x},t,\vec{x}',t')$ can be expressed as a bilinear combination of the eigen-

functions $\phi^{(n)}$ with a diagonal decomposition of the averaged cross correlation function; i.e.,

$$R_{ij}(\vec{x},t,\vec{x}',t') = \sum_{n=1}^{\infty} \lambda^{(n)} \phi_i^{(n)}(\vec{x},t)\, \phi_j^{(n)*}(\vec{x}',t') \tag{2.15}$$

- The eigenvalues, $\lambda^{(n)}$, are all positive ($\lambda^{(n)} \geq 0$), and their sum is finite.
- The expression is optimal in the sense that the eigenfunctions are arranged in descending order ($\lambda^{(1)} > \lambda^{(2)} > \lambda^{(3)} > \cdots$), and each is as large as possible.
- The contribution of each eigenfunction to the total turbulent kinetic energy in the domain can be determined with the properties of Equations 2.12 and 2.14. The kinetic energy at a point is given by:

$$\langle u_i(\vec{x},t)\; u_i^*(\vec{x},t)\rangle = \left\langle \left(\sum_{n=1}^{\infty} a_n \phi_i^{(n)}(\vec{x},t)\right)\left(\sum_{m=1}^{\infty} a_m \phi_i^{(m)}(\vec{x},t)\right)^* \right\rangle \tag{2.16}$$

From Equation 2.14, it follows that:

$$\begin{aligned} < u_i(\vec{x},t)\, u_i^*(\vec{x},t) > &= \sum_{n=1}^{\infty}\sum_{m=1}^{\infty} < a_n a_m^* > \phi_i^{(n)}(\vec{x},t)\, \phi_i^{(m)*}(\vec{x},t) \\ &= \sum_{n=1}^{\infty} \lambda^{(n)} \phi_i^{(n)}(\vec{x},t)\, \phi_i^{(n)*}(\vec{x},t) \end{aligned} \tag{2.17}$$

Thus each eigenvector makes an independent contribution to the kinetic energy at a point.

The kinetic energy at a point can be integrated over the entire domain to yield

the total energy as:

$$\begin{aligned} E &= \int_D < u_i(x)\, u_i^*(x) > dx \\ &= \sum_{n=1}^{\infty} < a_n^2 > \\ &= \sum_{n=1}^{\infty} \lambda^{(n)} \end{aligned} \tag{2.18}$$

Thus the energy is recovered as the sum of eigenvalues.

In summary, the POD provides a modal decomposition of the random vector field, and an optimal basis for representation of the flow. Since each eigenvalue contains the greatest possible kinetic energy of the field on average, the POD is the most efficient way to reconstruct the large scale dynamics of the flow. Thus it should be no surprise that the POD has proven to be a very useful tool to investigate the dynamics of the large scale structure of the turbulent motion (George 1988; Moin & Moser 1989; Citriniti & George 2000).

2.2.3 The POD and the stationary, homogeneous, and periodic flows

If the vector field is stationary in time, homogeneous in space in one or more coordinates or periodic, the eigenfunctions of the POD (Equation 2.9) become harmonic functions (Lumley 1967; George 1988; Holmes *et al.* 1996). In the former cases it is convenient to first perform the Fourier decomposition, then apply the POD theorem to the Fourier transformed random field. If the field is periodic, the eigenfunctions are discrete Fourier modes. Thus it is more convenient to work with a Fourier series decomposition.

Consider, for example, the case of a statistically axisymmetric flow which is stationary in time, and periodic and homogeneous in θ. The temporal Fourier transform

of the flow field is given by:

$$\hat{u}_i(r,\theta,f) = \int_{-\infty}^{\infty} u_i(r,\theta,t)\; e^{-i\,2\pi f t}\, dt \tag{2.19}$$

where, $\hat{u}_i$ stands for the Fourier-transformed u_i. This can in turn be represented as a Fourier series in the azimuthal coordinate, θ; i.e.,

$$\hat{\hat{u}}_i(r,m,f) = \frac{1}{2\pi}\int_0^{2\pi} \hat{u}_i(r,\theta,f) e^{-im\theta}\; d\theta \tag{2.20}$$

Now the POD can be applied in the remaining inhomogeneous direction, r, exactly as before; i.e.,

$$\begin{aligned}\iint_D B_{ij}(r,r',m,f)\; \phi_j(r',m,f)\, r' dr' \\ = \lambda(m,f)\; \phi_i(r,m,f)\end{aligned} \tag{2.21}$$

where the eigenvalue, λ, is a function of the azimuthal mode number, m, and frequency, f. B_{ij} is the averaged cross-spectral function defined as the Fourier series decomposition of the cross-spectrum over the appropriate variables; i.e.,

$$\begin{aligned}&B_{ij}(r,r',m,f) \\ &\quad = \frac{1}{2\pi}\iint_{-\infty}^{\infty} R_{ij}(r,r',\theta,\theta',t',t)\; e^{-i[m(\theta'-\theta)+2\pi f t]}\, d(\theta'-\theta)\, d(t'-t)\end{aligned} \tag{2.22}$$

Now this POD integral equation is similar to Equation 2.9, and all of the previous results can be applied. The only difference is that eigenvalues and random coefficients are functions of mode number and/or frequency, while the eigenfunctions are functions of the inhomogeneous coordinates as well.

2.3 POD application to the axisymmetric mixing layer

The first application of the POD to the axisymmetric turbulent jet mixing layer was reported by George *et al.* (1983), and Glauser (1987). The same facility was used by Citriniti & George (2000) and subsequently in the experiments reported here. The eigenfunctions and eigenvalues were estimated by assuming inhomogeneous conditions in the radial direction and 2π periodicity in the azimuthal direction. Only a single streamwise location was considered by Glauser (1987), so the inhomogeneity in the downstream direction did not enter the problem. Later, Citriniti (1996) assumed the same conditions, and applied the POD to get eigenfunctions and eigenvalues, then used them to reconstruct for the first time the entire original velocity field at a cross-section of the jet.

The coordinate system for the axisymmetric mixing layer is defined by $(x_1, x_2, x_3) = (x, r, \theta)$ in a cylindrical coordinate system, where x is the downstream position, r the radial position at fixed downstream position, and θ the azimuthal position (Figure 2.1). The velocity field is given by $u_i(x, r, \theta, t)$. Here, the downstream position, x, is fixed for this experiment, so the dependence on x will be removed in the equations.

In the flow field of the axisymmetric jet mixing layer, the velocity field is stationary in time, periodic in azimuthal direction, and inhomogeneous in radial direction (Glauser & George 1987*a*; Citriniti 1996). As discussed in the previous section, the instantaneous velocity must be Fourier decomposed in θ and t before the POD integral equation is applied directly to the radial direction.

2.3.1 Stationary direction

The velocity field, $u_i(r, \theta, t)$, in the mixing layer is statistically stationary in time. Then the Fourier transform of the velocity field in time direction is a function of

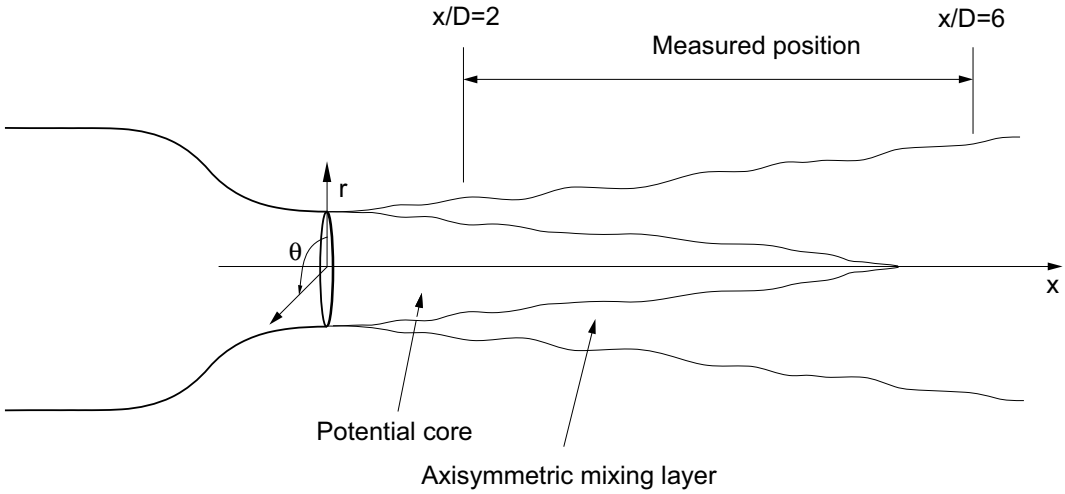

Figure 2.1: Schematic of the jet mixing layer

frequency, f, and given by:

$$\hat{u}_i(r,\theta,f) = \int_{-\infty}^{\infty} u_i(r,\theta,t)\, e^{-i2\pi ft}\, dt \tag{2.23}$$

2.3.2 Periodic direction

In the axisymmetric mixing layer, the single-point statistical properties are independent of the azimuthal coordinate, θ, and the two-point statistics can depend only on the difference in θ, say $\theta' - \theta$. So the periodic flow in θ is harmonic in $\theta' - \theta$ but is decomposed by discrete functions of the independent variable, $\theta' - \theta$ in a Fourier series; i.e.,

$$\begin{aligned}
\hat{\hat{u}}_i(r,m,f) &= \frac{1}{2\pi}\int_0^{2\pi} \hat{u}_i(r,\theta,f)\, e^{-im(\theta'-\theta)}\, d(\theta'-\theta) \\
&= \frac{1}{2\pi}\int_0^{2\pi} \left[\int_{-\infty}^{\infty} u_i(r,\theta,t)\, e^{-i2\pi ft}\, dt\right] e^{-im(\theta'-\theta)}\, d(\theta'-\theta)
\end{aligned} \tag{2.24}$$

where a double hat, $\hat{\hat{(\cdot)}}$, denotes that the function is double Fourier transform in time and azimuthal direction. The double Fourier transformed velocity field is a function

of frequency, f, and azimuthal Fourier mode, m, in addition to the radial coordinate, r. The streamwise coordinate, x, is treated as a passive parameter, so the resulting decomposition is really a "slice"-decomposition.

2.3.3 The full proper orthogonal decomposition

Using the transformed velocity in time and periodic coordinate, Equation 2.24, the POD integral equation can be obtained for the inhomogeneous coordinate, r, of the axisymmetric mixing layer as :

$$\int B_{ij}(r, r', m, f)\, \hat{\hat{\Phi}}_j(r', m, f)\; r'\, dr' = \hat{\hat{\lambda}}(m, f)\, \hat{\hat{\Phi}}_i(r, m, f) \tag{2.25}$$

where r is introduced as a Jacobian of the transformation from Cartesian to polar coordinates, and the two-point cross-spectra tensor, B_{ij}, is defined by

$$B_{ij}(r, r', m, f) = < \hat{\hat{u}}_i(r, m, f)\; \hat{\hat{u}}_j^*(r', m, f) > \tag{2.26}$$

Since the velocity is a function of the transform variables, m and f, so are the eigenfunctions and the eigenvalues.

The eigenfunctions and eigenvalues are obtained by applying the Hilbert Schmidt theory to the POD Equation 2.25. To utilize the Hilbert-Schmidt theory, however, the kernel must be Hermitian symmetric. But the kernel in Equation 2.25 is not due to the transformation Jacobian r'.

The kernel can be made Hermitian symmetric by dividing r' into two parts, multiplying the entire equation by $r^{1/2}$, and redefining the two-point cross-correlation tensor and orthogonal function. The integral eigenvalue Equation 2.25 is rearranged to form:

$$\int r^{\frac{1}{2}} B_{ij}(r, r', m, f)\, r'^{\frac{1}{2}} \hat{\hat{\Phi}}_j(r', m, f)\; r'^{\frac{1}{2}}\, dr' = \hat{\hat{\lambda}}(m, f)\, \hat{\hat{\Phi}}_i(r, m, f)\, r^{\frac{1}{2}} \tag{2.27}$$

The kernel and the orthogonal eigenfunctions can be redefined to be:

$$W_{ij}(r, r', m, f) = r^{\frac{1}{2}} B_{ij}(r, r', m, f)\, r'^{\frac{1}{2}} \tag{2.28}$$

and

$$\hat{\hat{\phi}}_i(r, m, f) = \hat{\hat{\Phi}}_i(r, m, f)\, r^{\frac{1}{2}} \tag{2.29}$$

Finally, the POD integral equation for an axisymmetric mixing layer, stationary in time, periodic in the azimuthal direction, and inhomogeneous in the radial direction, becomes:

$$\int W_{ij}(r, r', m, f)\, \hat{\hat{\phi}}_j(r', m, f)\, dr' = \hat{\hat{\lambda}}(m, f)\, \hat{\hat{\phi}}_i(r, m, f) \tag{2.30}$$

Since the kernel of Equation 2.30 is now Hermitian symmetric, the random vector field is of finite extent, and the Hilbert-Schmidt theory is applicable. The results of this theory are summarized below (Glauser 1987):

- A denumerable set of discrete solutions to Equation 2.30 exists for each frequency, f, and mode number, m, and Equation 2.30 may be written as:

$$\begin{aligned} \int W_{ij}(r, r', m, f)\, \hat{\hat{\phi}}_j^{(n)}(r', m, f)\, dr' &= \hat{\hat{\lambda}}^{(n)}(m, f)\, \hat{\hat{\phi}}_i^{(n)}(r, m, f), \\ n &= 1, 2, 3, \cdots \end{aligned} \tag{2.31}$$

  where n represents the discrete nature of the set.

- The eigenvalues are nonnegative real and ordered,

$$\hat{\hat{\lambda}}^{(1)}(m, f) > \hat{\hat{\lambda}}^{(2)}(m, f) > \hat{\hat{\lambda}}^{(3)}(m, f) \quad \cdots \quad > 0 \tag{2.32}$$

  and the sum is finite, i.e.,

$$\sum_n \hat{\hat{\lambda}}^{(n)} < \infty \tag{2.33}$$

- The eigenfunctions are orthogonal and can be normalized so that:

$$\int_D \hat{\hat{\phi}}_i^{(p)}(r,m,f)\,\hat{\hat{\phi}}_i^{(q)*}(r,m,f)\,dr = \delta_{pq} \tag{2.34}$$

- The velocity field can be expanded in the eigenfunctions, $\hat{\hat{\phi}}_i^{(n)}(r,m,f)$; i.e.,

$$r^{\frac{1}{2}}\hat{\hat{u}}_i^N(r,m,f) = \sum_n \hat{\hat{a}}_n(m,f)\;\hat{\hat{\phi}}_i^{(n)}(r,m,f) \tag{2.35}$$

  The random coefficients must be determined for each realization of the velocity field with the orthogonality of the eigenfunctions (Equation 2.34),

$$\hat{\hat{a}}_n(m,f) = \int r^{\frac{1}{2}}\hat{\hat{u}}_i(r,m,f)\,\hat{\hat{\phi}}_i^{(n)*}(r,m,f)\,dr \tag{2.36}$$

  where the coefficients are uncorrelated; i.e.,

$$< a_n\, a_m^* >= \hat{\hat{\lambda}}^{(n)}\,\delta_{mn} \tag{2.37}$$

- The two-point cross spectral tensor can be represented by:

$$\begin{aligned} B_{ij}(r,r',m,f) &= < \hat{\hat{u}}_i^N(r,m,f)\;\hat{\hat{u}}_j^{N*}(r',m,f) > \\ &= \sum_n \hat{\hat{\lambda}}^{(n)}\;\hat{\hat{\phi}}_i^{(n)}(r,m,f) r^{-\frac{1}{2}}\;\hat{\hat{\phi}}_j^{(n)*}(r',m,f) r'^{-\frac{1}{2}} \end{aligned} \tag{2.38}$$

- The turbulence kinetic energy is the double sum of the eigenvalues integrated

over all frequencies; i.e.,

$$\begin{aligned} E &= \int_f \int_r \sum_m < \hat{\hat{u}}_i^N(r,m,f)\ \hat{\hat{u}}_i^{N*}(r,m,f) > r\,dr\,df \\ &= \int_f \sum_n \sum_m < a_n^2(m,f) > \ df \\ &= \sum_n \sum_m \int_f \hat{\hat{\lambda}}^{(n)}(m,f)\,df \end{aligned} \tag{2.39}$$

Thus the eigenvalues measure the energy in each POD and azimuthal mode per unit frequency. And the sum is the total turbulent kinetic energy being considered. The energy is recovered in an optimal manner by the eigenfunctions and eigenvalues.

The POD provides a set of eigenfunctions, which make it possible to recreate the original instantaneous field. By choosing selected POD modes, azimuthal modes, and frequencies which contain most of the kinetic energy of the field, the dominant features can be extracted from the experimental data with very little information.

2.3.4 Application to experiments

Since only the streamwise velocity was measured at various radial, azimuthal, and downstream positions in these experiments, the POD integral eigenvalue of Equation 2.31 reduces to:

$$\int W_{11}(r,r',m,f)\,\hat{\hat{\phi}}_1^{(n)}(r',m,f)\,dr' = \hat{\hat{\lambda}}^{(n)}(m,f)\,\hat{\hat{\phi}}_1^{(n)}(r,m,f) \tag{2.40}$$

where the two-point cross-spectrum, $W_{11}(r,r',m,f)$, is an ensemble averaged statistical value obtained from experiments at discrete points. The velocity can then be represented as a linear combination of eigenfunctions as:

$$r^{\frac{1}{2}}\hat{\hat{u}}_1^N(r,m,f) = \sum_n \hat{\hat{a}}_n(m,f)\ \hat{\hat{\phi}}_1^{(n)}(r,m,f) \tag{2.41}$$

where

$$\hat{\hat{a}}_n(m,f) = \int r^{\frac{1}{2}} \hat{\hat{u}}_1(r,m,f)\, \hat{\hat{\phi}}_1^{(n)*}(r,m,f)\, dr \tag{2.42}$$

The kernel of Equation 2.40 is an ensemble averaged statistical value, but the coefficient, $\hat{\hat{a}}_n(m,f)$, is based on an instantaneous realization of the velocity field which has been decomposed into azimuthal modes and frequency; hence it is random, like $\hat{\hat{u}}_1$ itself.

In order to recover the POD coefficients, $\hat{\hat{a}}_n(m,f)$, it is very important that the velocity field must be measured *simultaneously* at all positions of interest to retain the phase information in the coefficient. Therefore a simultaneous measurement system was devised and utilized for the turbulent velocity field in the mixing layer so that the projection defined by Equation 2.42 can be accomplished without any phase delay (Citriniti 1996). This experiment is described in Chapter 3.

2.4 Numerical implementation

A numerical approximation was applied to solve the POD integral eigenvalue Equation 2.40. Since the two-point cross-spectra in Equation 2.40 is known only at discrete positions, the integral must be replaced by an appropriate quadrature rule.

Using the trapezoidal rule for the numerical integral, the discretized POD equation for each azimuthal mode and frequency combination becomes:

$$\sum_{j=1}^{N_r} W_{11}(r_i,r_j)\, \hat{\hat{\phi}}_1^{(n)}(r_j)\, H_j = \hat{\hat{\lambda}}^{(n)} \hat{\hat{\phi}}_1^{(n)}(r_i) \tag{2.43}$$

where N_r is the number of the radial measuring positions, and H_i is the quadrature weighting factor. Rewriting Equation 2.43 as a matrix eigenvalue equation (Baker 1977),

$$WHf = \Lambda f \tag{2.44}$$

where,

$$W = \begin{bmatrix} W_{11}(r_1, r_1) & W_{11}(r_1, r_2) & \cdots & W_{11}(r_1, r_{N_r}) \\ W_{11}(r_2, r_1) & W_{11}(r_2, r_2) & \cdots & W_{11}(r_2, r_{N_r}) \\ \cdots & \cdots & \cdots & \cdots \\ W_{11}(r_{N_r}, r_1) & W_{11}(r_{N_r}, r_2) & \cdots & W_{11}(r_{N_r}, r_{N_r}) \end{bmatrix}, \tag{2.45}$$

$$f = \begin{bmatrix} \hat{\hat{\phi}}_1(r_1) \\ \hat{\hat{\phi}}_1(r_2) \\ \vdots \\ \hat{\hat{\phi}}_1(r_{N_r}) \end{bmatrix}, \tag{2.46}$$

and the weighting factor is a diagonal matrix given by:

$$H = diag\,[\,H_1, H_2, \cdots, H_{N_r}\,] \tag{2.47}$$

The coefficient matrix, WH, is not Hermitian, but the numerical accuracy of the matrix eigenvalue solution can be improved by changing it into a Hermitian matrix ($X_{ij} = X^*_{ji}$) (Baker 1977). To make it Hermitian, we multiply Equation 2.44 by $H^{1/2}$, then the resulting coefficient matrix becomes a Hermitian matrix, $\hat{W}$, i.e.,

$$\hat{W}\,\hat{f} = \Lambda\,\hat{f} \tag{2.48}$$

where

$$\hat{W} = H^{\frac{1}{2}}\,W\,H^{\frac{1}{2}} \tag{2.49}$$

and

$$\hat{f} = H^{\frac{1}{2}}\,f \tag{2.50}$$

Now the transformed coefficient matrix, $\hat{W}$, is a Hermitian matrix.

The trapezoidal rule was used for integration, and the corresponding weighting factor matrix, H, is:

$$H_i = k_i \, \Delta r \tag{2.51}$$

where the unit distance of measurement in r is $\Delta r = 0.0127$, and $k_i = [1.65, 1, 1, 1, 1, 1]$ is the weighting factor. For the first weighting factor, an interpolation scheme is applied by assuming that the velocity field inside the innermost measuring position has the same velocity. This approximation is appropriate when the most inside measuring position is in the potential core, but beyond the potential region, this weighting factor is underestimated. And for the sixth weighting factor, this one was weighted by assuming that an extra measuring position is present after sixth position, but it has a zero velocity field value.

By applying a similar analysis, Equation 2.42 for the coefficients of the POD eigenfunctions becomes

$$\hat{\hat{a}}_n(m, f) = \sum_{i=1}^{N_r} r_i^{\frac{1}{2}} \hat{\hat{u}}_1(r_i, m, f) \, \hat{\hat{\phi}}_1^{(n)*}(r_i, m, f) \, H_i \tag{2.52}$$

where the equation is solved by first projecting on the instantaneous velocity field, and then integrating numerically with the trapezoidal weighting factor defined by Equation 2.51.

Chapter 3

The Experiment and Experimental Facility

3.1 Introduction

The goal of this experiment was to investigate the large scale or coherent structures of the fully developed turbulent shear layer in the axisymmetric jet and their contribution to the dynamics of turbulent motion. Measurements were made from $x/D = 2$ to $x/D = 6$ (spaced $0.5\,x/D$ apart) along the downstream direction at Reynolds numbers of $78,400$, $117,600$, and $156,800$. In order to preserve the phase information at the different positions, data were collected simultaneously at all 138 positions using a 138 hot wire probe array designed by Citriniti (1996), see also Citriniti & George (2000).

The experimental facility for simultaneous measurements at 138 positions consists of a jet facility with its control system, a 138 hot wire probe array with corresponding anemometers, and a high performance data acquisition system. These are described in detail in this chapter.

3.2 Experimental facility

3.2.1 Jet facility

The experiments were carried out in the turbulent mixing layer generated by an isothermal, non-reacting, incompressible, and axisymmetric jet. This jet facility (shown in Figure 3.1) was used previously by Glauser (1987), and Citriniti (1996).

The facility consists of 4 major parts: the blower, the diffuser, the settling chamber, and the jet nozzle. The blower (Dayton model No. 4C108) contains 6 impellers on a $10\frac{5}{8}\,in.$ wheel and operates at $3,450/2,850$ RPM for $60/50\,Hz$. The blower driven by a 1 HP 3 Phase AC motor and uses a motor controller (TOSHIBA industrial inverter, TOSVERT VF-S7) with frequency mode in the range of 0 to 60 Hz. An air filter box of dimensions $0.50 \times 0.35 \times 0.40\,m$ is installed at the blower inlet to remove unnecessary pressure fluctuations and noise.

The 0.6 m long diffuser has a flexible coupling made of artificial leather between the blower and the diffuser to avoid vibration by the blower. The $0.9\,m$ long settling chamber contains several layers of solid mesh screen, and honeycomb to remove large scale disturbance generated by the impellers.

The jet nozzle, 0.098 m exit diameter, has a smooth area contraction ratio of $10:1$ between the outlet of the settling chamber and the nozzle exit plane, the contour of which follows a fifth order polynomial curve.

Jet exit velocities could be controlled from $0.5\,m/s$ to $38\,m/s$ with the motor controller. This was monitored with a micromanometer (MERIAM Instrument Model 34FB2, range: $20\,in.$) and a pressure tranducer (SETRA Model 264, range: 0 to $10\,in$) connected via a silicon tube starting at the settling chamber. In this experiment, jet exit velocities, U_j, were 12, 18, and 24 m/s, which correspond to Reynolds numbers of $78,400$, $117,600$, and $156,800$ based on the nozzle diameter, D, and the jet exit velocity. The turbulence intensity at the jet exit varied between 0.23% and $0.35\,\%$, depending on the jet velocity. The shear layer at $1\,cm$ from the jet exit was

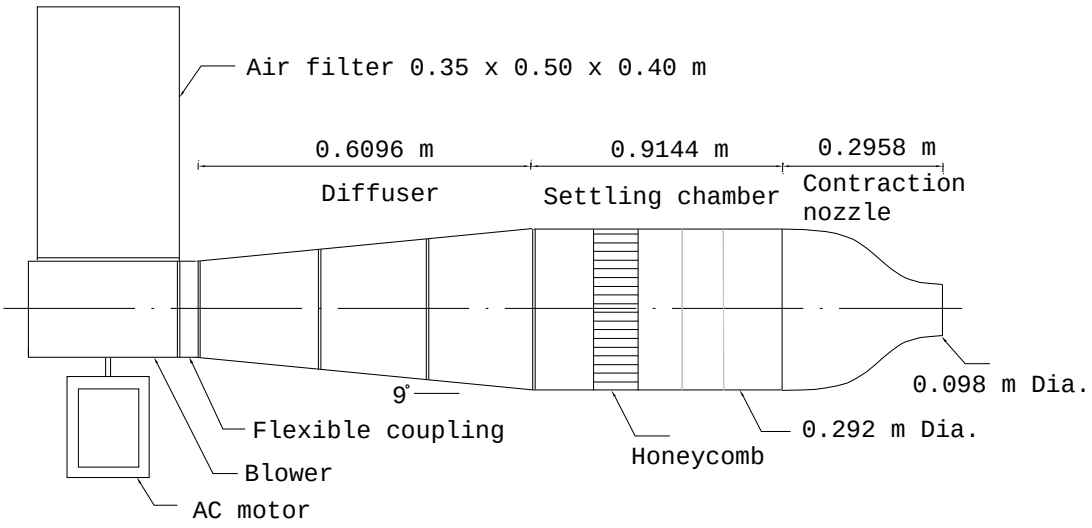

Figure 3.1: Schematic of jet apparatus

turbulent and $0.0012\,m$ thick based on $U/U_j = 0.99$.

A 3-component traversing unit was used to measure the velocity field of the mixing layer from $x/D = 2.0$ to $x/D = 6$ at spacings of $0.5\,x/D$. A step motor controller connected to the main computer was used to align the center and to position the 138 hot wire probe array. This traversing unit is also used for the setup of the calibration of the 138 hot wire probe array.

The whole jet facility is installed at the center of a $4.3\,m$ width, $4.6\,m$ high, and $11.4\,m$ long laboratory shielded with plastic vinyl to minimize the effects of boundary conditions to the experiments and to simulate a jet in an infinite boundary.

3.2.2 Flow characteristics of the jet

To decide the sampling criteria of the velocity field, it is important to investigate the range of the statistical characteristics of the field of interest. To avoid aliasing of the signal while sampling, it is necessary to know the maximum possible frequency of the flow.

The maximum frequency, f_k, is found using Taylor's hypothesis with the Kolmogorov microscale, η; i.e.,

$$f_k = \frac{U_c}{2\pi\,\eta}, \tag{3.1}$$

where the convection velocity is $U_c = 0.6\,U_j$ (*cf.* Davies *et al.* 1963). Using the Kolmogorov microscale for the mixing layer as suggested by George *et al.* (1984):

$$\eta = \left[\frac{1}{0.044}\right]^{\frac{1}{4}} \left[\frac{\nu}{U_j\,D}\right]^{\frac{3}{4}} \left(\frac{D}{x}\right)^{\frac{3}{4}} x. \tag{3.2}$$

The Kolmogorov microscale for the mixing layer in this experiment is in the range of 0.03 to $0.07mm$ for $x/D = 2$ to 6 and $U_j = 12$, 18 and $24m/s$. The resolution of these scales would require wires that were less than 2η in length (Wyngaard 1968), which is clearly impossible. But even if this were possible, it would also be required to space the wires at no greater than η to avoid spatial aliasing when the data are spatially

Fourier-transformed. Obviously it is not possible to measure all of the turbulence scales, and an alternative strategy must be devised. This is described in the next section.

3.3 Characteristics of the hot wire probe

3.3.1 Spatial resolution

The goal of this experiment is to investigate the large-scale dynamics of the jet mixing layer, since we are interested only in the range of the turbulent production and not the dissipation. Therefore we must device a technique which not only resolves these large scales, but also removes the smaller ones to avoid the spatial aliasing problems. This is exactly analogous to the problem of sampling in time at a rate below the Nyquist frequency (Glauser & George 1992).

Using the fact that the highest wave numbers in the turbulent flow do not contribute significantly to the total kinetic energy, Citriniti designed long hot wires to filter the high wave number scales in the turbulent field without losing information in the smallest wave numbers. Since the signals from the turbulent flows were filtered out by the long sensing hot wire before they were sampled, the small amount of energy, contained in the small physical scales, is not folded into the lower modes. Therefore the long sensing element hot wire is used as a spatial filter. This procedure and analysis is described in detail in (Citriniti *et al.* 1994*a*).

Since a hot wire averages the velocity field along its length, it can respond to fluctuating disturbances only if the spatial scale of the fluctuations is larger than twice the hot wire length scale. Therefore a maximum frequency resolvable by the hot wire is estimated (George & Taulbee 1992) as:

$$f_c = \frac{U_j}{2\,l_w}, \tag{3.3}$$

where l_w, the length of sensing element of the hot wire, equals 1 cm. Depending on Reynolds number, the limits of maximum frequency due to hot wire length are $600 Hz$, 900 Hz, and $1,200$ Hz. Therefore Nyquist frequency of the mixing layer should be larger than at least twice these maximum frequencies to avoid temporal aliasing. The actual sampling frequency in each anemometer has been set at $4,001.6$ Hz for all Reynolds numbers combined with trigger signal of the data acquisition process.

The frequencies: 600 $Hz, 900$ Hz and $1,200$ Hz from Equation 3.3 are very much lower than the maximum frequency, f_k, from Equation 3.1. Therefore spectra were measured at $x/D = 2$ and 6 for $Re_D = 78,400$ and $156,800$ to make sure that these frequencies cover the dominant portion of the kinetic energy of the flow in order to apply the POD. Considering all turbulent characteristics, as discussed in the previous section, sampling was made at a frequency of 142 kHz without a low pass filter, and 100 blocks are sampled to get the spectra with a single hot wire of $l/d = 200$, and using a Dantec 55M10 constant temperature anemometer at about $r/D = 0.5$. As shown in Figure 3.2, the measured spectra show at least a decade of a $k^{-5/3}$ range indicating that both flows are high Reynolds flows. The rolloff due to the probe filtering is beyond $10,000$ Hz. Since the sampling frequencies for three different Reynolds, 600 Hz, 900 Hz, and $1,200$ Hz, are well into the $k^{-5/3}$ range of the spectrum, the portion of the kinetic energy after these sampling frequencies contributes little to the mean kinetic energy of the flow. Thus it is clear that the main portion of the kinetic energy of the flow is covered by the long hot wire as expected. Nevertheless, in this experiment, sampling frequency was set at $4,001.6$ Hz to avoid aliasing. The frequency, $4,001.6$ Hz, will be discussed in detail in the section 3.4.2.

3.3.2 The 138 hot wire probe array

The 138 hot wire probe array as shown in Figure 3.3 is used to measure the velocity field of the jet mixing layer at 138 positions simultaneously. This array, designed and used in Citriniti (1996), consists of 138 single hot wire probes. Each single long

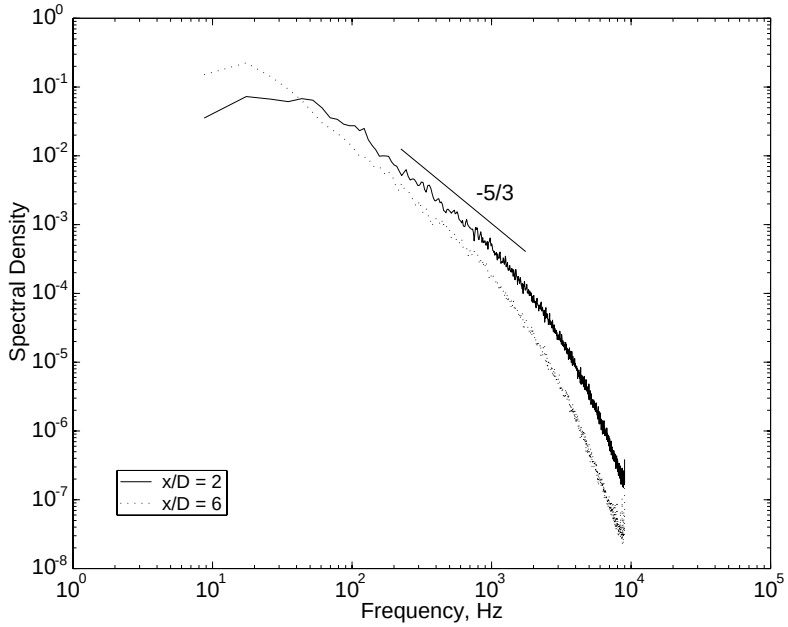

(a)

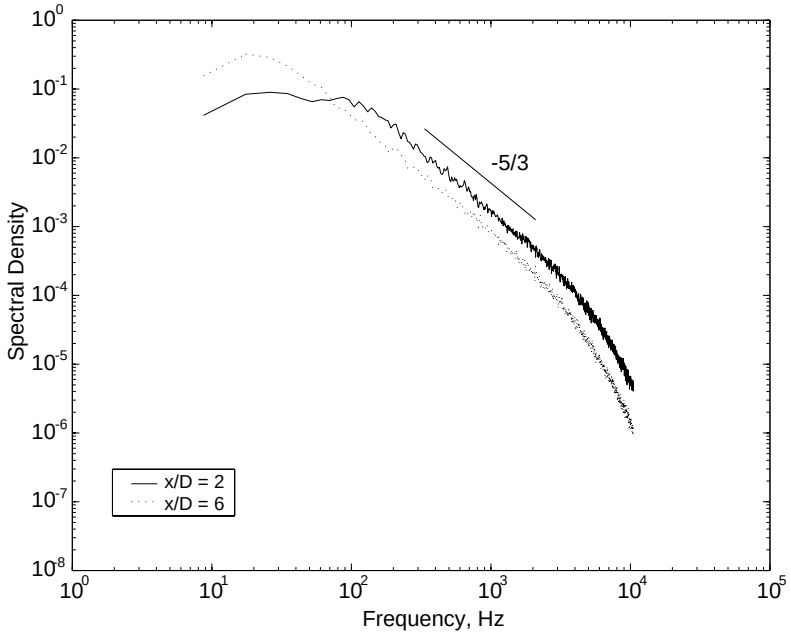

(b)

Figure 3.2: Spectral density from the mixing layer of the axisymmetric jet at about $r/D = 0.5$ (a) $Re_D = 78,400$, (b) $Re_D = 156,800$

wire probe ($l/d \approx 800$) is made of 1 cm long and unplated 12.7μm tungsten wire (Sigmund-Cohn, Mt. Vernon, NY). All these hot wires are made in the laboratory using the manufacturing process described in detail in Citriniti (1996) and which will be summarized below.

To determine the number of measurement positions needed to properly resolve the velocity field in the azimuthal direction for the application of the POD, Citriniti used the data presented by Glauser (1987). He designed 6 rings in radial direction to account for the spatial sampling criteria of Glauser & George (1992), who argued that 6 measurement positions were necessary in the radial direction to recover the turbulent kinetic energy. They further argued these are sufficient to represent the dynamics of the large scale turbulent structures in the mixing layer.

The probe array was designed to have 6 radial positions. The azimuthal distribution of probes at these radial positions was 6, 12, 24, 32, 32, 32, thus providing the 138 measurement positions described by Citriniti as shown in Figure 3.3. All the hot wire probes were oriented in the azimuthal direction in the probe array so as to attenuate energy in the higher azimuthal Fourier mode numbers as discussed earlier. All the characteristics of the long sensing element hot wire and the design schemes of the 138 hot wire probe array are described in detail in Citriniti (1996).

3.3.3 Hot wire anemometer

138 hot wire anemometers (hereafter TRL anemometer) were used to measure the velocity field simultaneously using the hot wires probe array. The anemometers were originally designed, manufactured, and tested carefully at the laboratory (Citriniti *et al.* 1994*b*). Since the maximum frequency of interest in the flow and the sampling rate necessary for each anemometer were relatively low, the extra circuitry found in most commercial anemometer systems which boosts frequency response onto the $50 - 60\,kHz$ range is unnecessary for this application. Therefore, over the range of parameters of interest, the TRL anemometer was a compact and effective anemometer

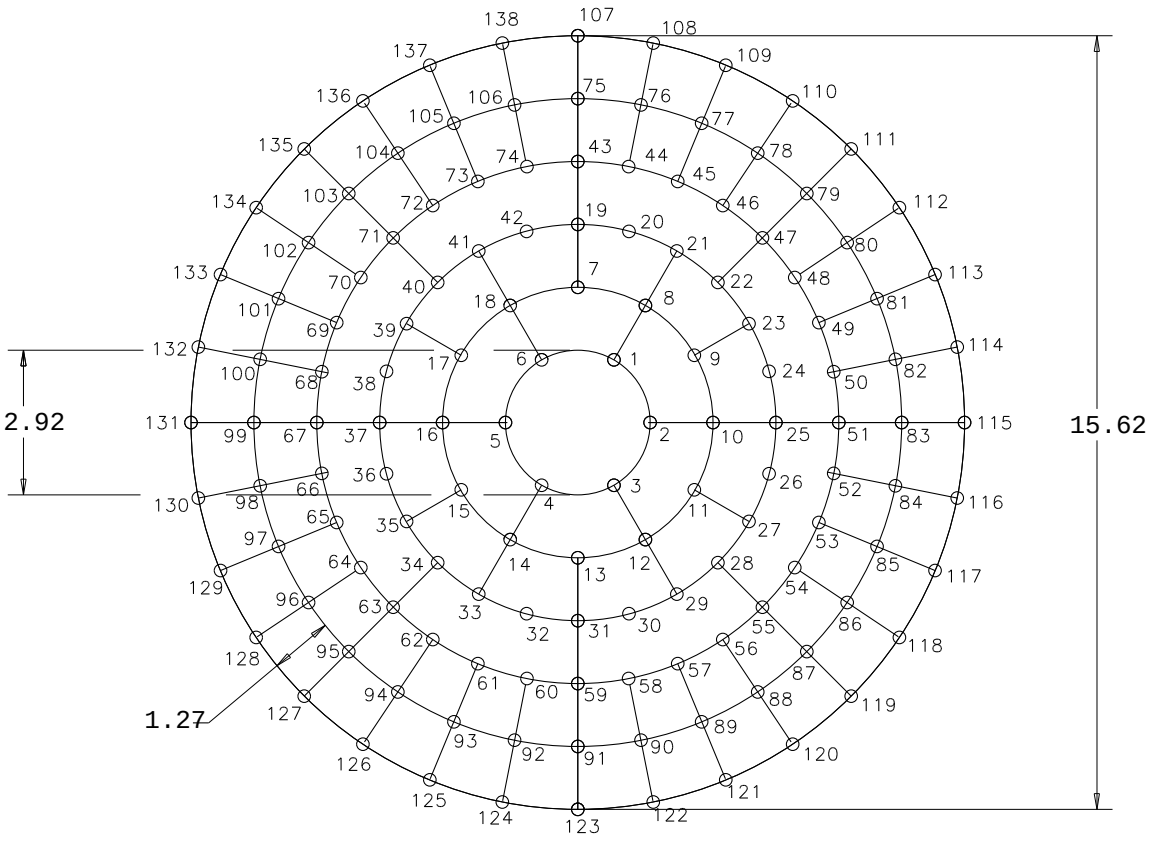

Figure 3.3: Schematic of the 138 hot wire probe array with measuring positions in *cm*. Each small circle represents the position of a single hot wire probe.

system which had a typical performance equal to that of the Dantec M systems (Woodward *et al.* 2001).

Each anemometer is mainly composed of a feedback loop including a Wheatstone bridge, output control, and sample/hold control. The main circuit of the anemometer was built around the feedback loop as suggested by Perry (1982). Each of the 9 boards has 16 anemometers, attached to the aluminum front plates, and mounted on a vertical rack as described in detail by Citriniti (1996).

The circuit performance and noise properties of the TRL anemometer compared to an industry standard anemometer. Woodward *et al.* (2001) showed that the true statistics of the turbulent velocity field were captured, the noise level was lower in the TRL anemometer than in the commercial one, and there was no cross-talk between anemometers on a board.

The anemometers were modified in the present experiments without changing the fundamental circuit of the hot wire anemometer shown in Figure 3.4. First, all the power supplies were replaced to reduce the high current draw, which produced unwanted noise as reported by Citriniti (1996) in the anemometers for the inner radii hot wire probes. In this experiment four set of power supplies were used, with each one operating 2 or 3 boards (each board consisting of 16 anemometers). The frequency response control and output voltage control at the op-amps was specially designed to keep the same voltage all the time while operating, without any voltage fluctuation which may introduce a DC offset in signal or instabilities in the board ground. The output signal was monitored to see the fluctuation level of the power supply under the same exit velocity for 130 minutes after at least 2 hours warming up. Maximum deviation of the output voltage is less than 1 % on all 9 boards, or all 6 rings of the 138 hot wire array, which proves that the TRL anemometer works without significant fluctuations in the voltage of the op-amps.

In Citriniti (1996), a low-pass Bessel filter was used to prevent aliasing of temporal signals due to the low overall sampling rate of each anemometer. But in this

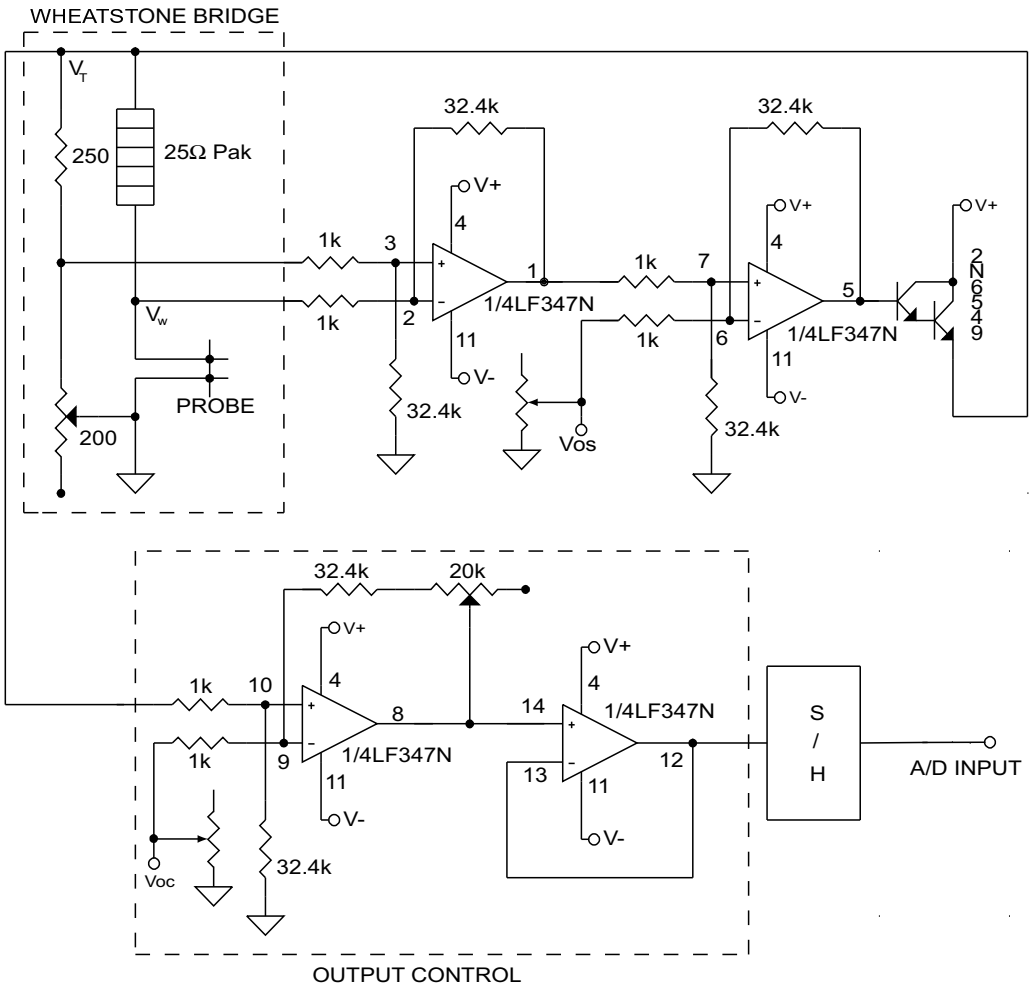

Figure 3.4: Hot wire anemometer circuit diagram

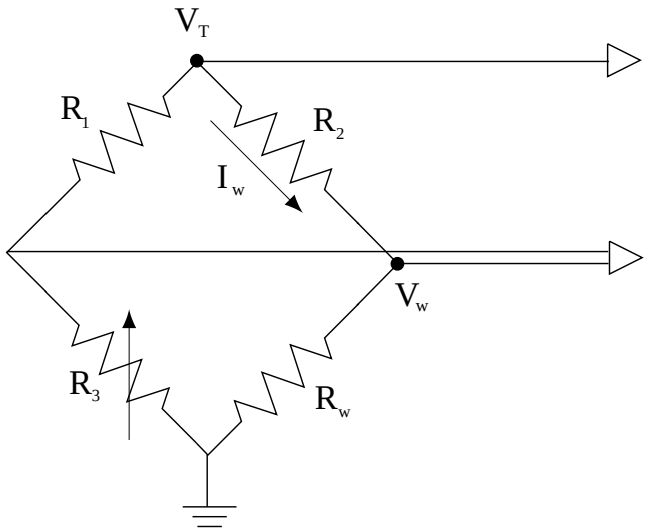

Figure 3.5: Schematic of the Wheatstone bridge, from Citriniti (1996)

experiment measurements are made at 4 001.6 Hz using Microstar DAP 5200a data acquisition processor. Therefore the low pass Bessel filters were removed from the anemometer. Also, the frequency response of the anemometer is comparatively low, and the spectra do not contain any significant information near or above the Nyquist frequency.

The control board of Citriniti, generating the control signal for S/H amplifier and controlling the analog multiplexer, was not used here since the Microstar DAP 5200a data acquisition processor samples signals fast enough to sample all 138 anemometers without delays, while also generating the control signal for the sample/hold amplifier.

Unlike a commercial hot wire anemometer, the overheat ratio of the TRL anemometer was adjusted after connecting the probe on the anemometer. Before connecting the probe, the resistance of the hot wire (cold resistance), R_{wc}, and the resistance of the cable, R_c, between the probe and the anemometer are measured. The overheat ratio, OR, is defined as:

$$OR = \frac{R_{wh}}{R_{wc}}, \tag{3.4}$$

where R_{wh} is the resistance of wire under operation (hot resistance). Using Ohm's law, the total resistance of a wire, R_w, under operation (Figure 3.5) is:

$$R_w = \frac{V_w}{I_w},$$

where $R_w = R_c + R_{wh}$ and I_w is the current in the probe arm of the bridge. The current through the hot wire, I_w is in terms of the bridge top voltage, V_T:

$$I_w = \frac{V_T - V_w}{R_2}.$$

Therefore, the total wire resistance is:

$$R_w = \frac{V_w}{V_T - V_w} R_2. \tag{3.5}$$

And R_w is obtained from Equation 3.4:

$$\begin{aligned} R_w &= R_c + R_{wh} \\ &= R_c + OR \cdot R_{wc} \end{aligned} \tag{3.6}$$

Finally from Equations 3.5 and 3.6, the relation between the bridge top voltage, V_T and the wire voltage, V_w, is:

$$\begin{aligned} \frac{V_T}{V_w} &= 1 + \frac{R_2}{OR \cdot R_{wc} + R_c} \\ &= constant. \end{aligned} \tag{3.7}$$

Since all the variables in the right hand side of Equation 3.7 are constant or previously measured values, the voltage ratio between the bridge top voltage and the wire voltage at a specific anemometer is obtained once the overheat ratio, OR, is given. In this experiment, the voltage ratio, V_T/V_w, is measured using the tip holes on the board and adjusted by a variable resistance, R_3, until this ratio reaches the calculated

constant in Equation 3.7 with $OR = 1.8$ in the region of potential core of the highest velocity of all three Reynolds numbers at the jet exit.

Since a very large number of power supplies, anemometers and sampling channels are used for collecting the data, all the ground connections are carefully examined to eliminate possible external noise, cross-talk, DC offset, or voltage difference on the ground board due to the high current draw in multiple channels. Mainly there are two grounds, AC ground for the main power, and DC ground for the anemometer and data sampling.

AC ground and DC ground were designed to be separated completely for all systems used including personal computer, power supplies, 5V auxiliary power supply for A/D converter, boards of hot wire anemometers, and pressure tranducer etc. 16 anemometers have a common ground on the circuit board which is shared with the DC power supply. Each power supply ground is separated from the other, and considered as a point ground without producing any ground loop including the PC. Also the ground of the data acquisition board or the PC with the analog to digital converter has a separate ground from the AC power supply, and is shared with the anemometer ground to avoid any ground loop with other circuits.

3.3.4 Calibration of hot wire probes

The single hot wires are calibrated with a digital linearizing scheme (George *et al.* 1989*a*). The voltage data from the single hot wire is converted to velocity by fitting a polynomial function to the voltage data. The effective velocity, U_{eff}, measured by the probe over a range of known velocities, is expressed as the sum of the output voltage of the single wire in its simplest form; i.e.,

$$U_{eff}^{p} = \sum_{n=0}^{N} a_n E^n, \tag{3.8}$$

where p is the power of U_{eff} and N the order of the polynomial fit.

There are two principal advantages in this scheme over the other schemes (King's law, etc). First, since the coefficients arise in a linear way, the principal uncertainty of the measured values lies with U; therefore a linear least square error scheme can be directly applied. Second, the desired quantity U can be easily calculated from Equation 3.8 by simple recursive multiplications without any inversion techniques. From other previous experiments at the Turbulence Research Laboratory at the University at Buffalo, it has been found that $p = 0.5$ and $N = 4$ has the best fit including in the range of low velocity; moreover using higher values of N adds very little accuracy in the given range. Therefore Equation 3.8 becomes:

$$U_{eff}^{0.5} = a_0 + a_1 E + a_2 E^2 + a_3 E^3 + a_4 E^4. \tag{3.9}$$

The calibrations of single hot wires were performed in the same jet facility used for the experiment. The velocity at the jet exit was calculated using Bernoulli's equation with the settling chamber pressure, which is connected with a silicon tube to a micromanometer (Meriam Instrument Co. Model 34FB2) and a pressure tranducer (Setra Systems Co. Model 264, Range: $0 - 10.0$"). Before calibrating the single hot wire, a calibration of the pressure tranducer was carried out against the micromanometer with an accuracy of 0.001 in of water.

A series of voltage outputs for each single hot wire and the pressure tranducer are collected by a Microstar DAP 5200a data acquisition processor, stored with a PC and the coefficients of Equation 3.8 or 3.9 are calculated in the velocity range from about 1 m/s to 28 m/s. The jet exit velocity controlled by a motor controller (TOSVERT VF-S7, Toshiba Industrial Co.) in frequency mode. 20 to 30 single hot wires were calibrated at the same time at $x/D = 0.5$ from the jet exit. This was possible since the velocity of the fluid at the jet exit was flat to within 0.1 % and the boundary layer was small enough so that the jet exit velocity could be assumed to provide a constant, laminar flow for calibration. All the positions of single wires are carefully monitored

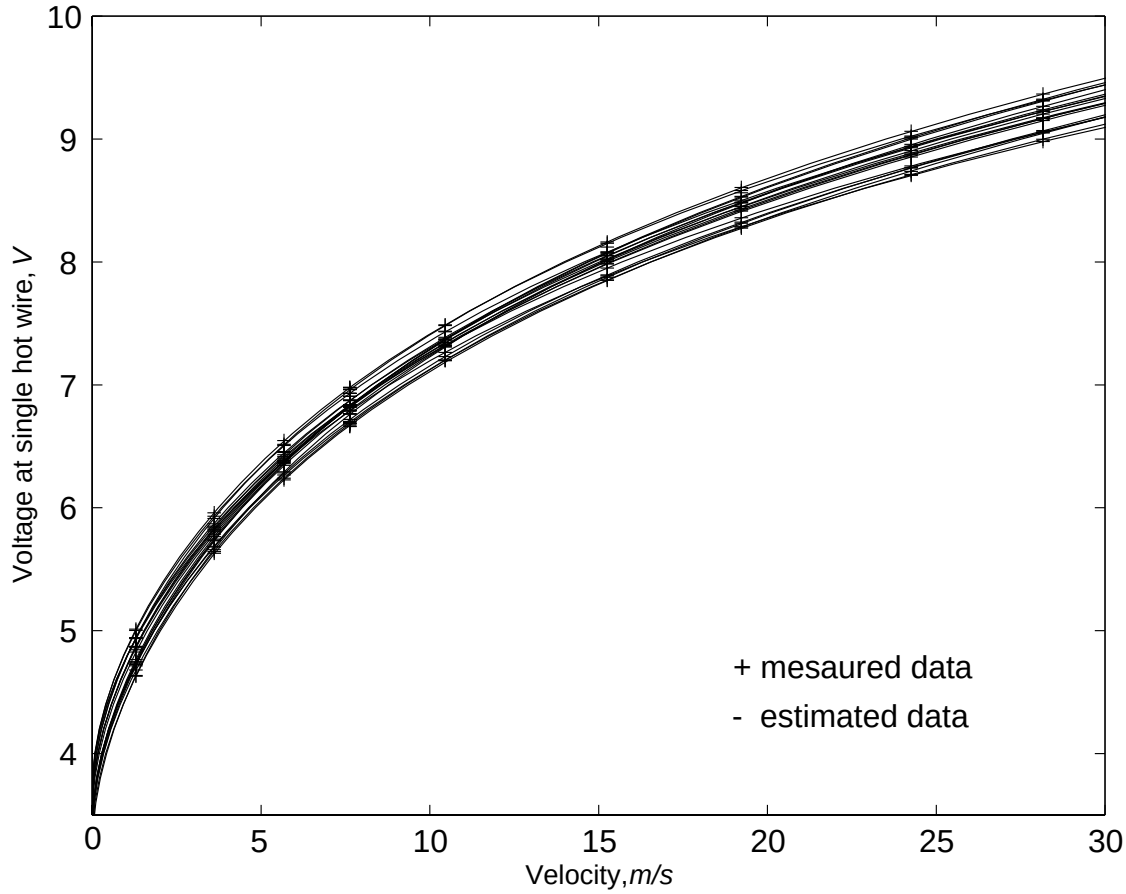

Figure 3.6: Sample of calibration data and corresponding polynomial fit

to ensure that they are in the potential core region before calibration. The sampling rate of this calibration is $4,000\,Hz$, and the sampling time $100\,sec$. Figure 3.6 shows some samples of the calibration data and the corresponding polynomial fit.

3.3.5 The effects of high turbulence intensity

In general, the local turbulence intensity of the axisymmetric jet is about 30 % max at the centerline and more than 100 % at the outer region. Due to this high turbulence intensity, principal limitations exist in using a single wire. It has a strong effect on errors of cross-flow, rectification, and drop-out. These effects increase with turbulence intensity (George *et al.* 1989*a*; Hussein *et al.* 1994), and leading terms in mean velocity error are (no cross flow; V,W = 0 by assumption):

$$U_m = U\left\{1 + \frac{1}{2}\frac{\overline{w^2}}{U^2} - \frac{1}{2}\frac{\overline{uw^2}}{U^3} + \frac{1}{2}\frac{\overline{u^2w^2}}{U^4} - \cdots\right\} \tag{3.10}$$

George *et al.* (1989*a*) suggested that the effects can be assumed to be unimportant only as long as the leading terms are negligible.

There is no question the turbulence measurements of this experiment are adversely affected by these cross-flow errors outside approximately the point at which the mean velocity is half its centerline value. The point of this experiment, however, is not the quantitative measurement of the turbulence (as in Hussein *et al.* 1994), but instead to examine how the turbulence is correlated over large distances, and how different large scales interact. Therefore, we expect that the effects of high turbulence intensity will not significantly affect the results of this experiment. This conclusion is substantiated by the recent application of these same techniques to the far jet by Gamard (preparing dissertation), and the axisymmetric far wake by Johannson (preparing dissertation). These flow show very similar modal decompositions, even though the turbulence intensity in the far jet are similar to these observed here, but in the wake the intensity is very low.

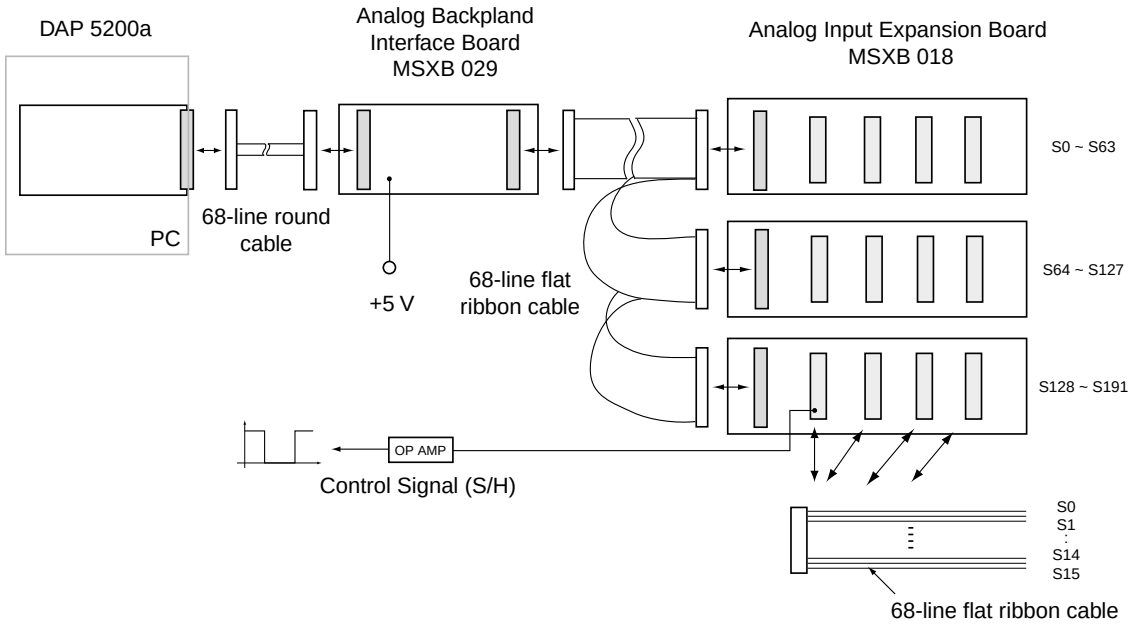

Figure 3.7: The diagram for data acquisition processor, DAP 5200a

3.4 Data sampling

3.4.1 Data acquisition procedure

We used a high-performance data acquisition processor since we were interested in the simultaneous measurements at all 138 positions at the required frequency. The data acquisition processor, DAP 5200a, from Microstar Laboratories, is an on-board operating system optimized for 32 bit operation in a PC expansion slot. It has the following features: an AMD K6-2 CPU, PCI bus interface, 14-bit A/D converter, $50\,ns$ TIME resolution, $800\,K$ samples per second, and selective input/output voltage ranges.

The data acquisition system mainly consists of the DAP 5200a processor, an analog backplane interface board, and an analog input expansion board as shown on Figure 3.7. The DAP 5200a is connected to the Microstar Laboratories Analog Backplane Interface Board, MSXB 029, through a 68-line round shielded cable on the back

panel of the PC, and its MSXB 029 interface board is connected to three Microstar Laboratories Analog Input Expansion Boards, MSXB 018, using a 68-line flat ribbon cable. These MSXB 018 boards are connected in serial with each other via 68-line flat ribbon cables. Each MSXB 018 input expansion board consists of four 16 single ended connectors ($S0$ to $S15$) and therefore multiplexes 64 analog inputs($S0$ to $S63$) into a data acquisition processor. A maximum of 192 analog channels ($S0$ to $S191$) can be connected to this data acquisition system. An auxiliary $+5\,V$ power supply is used for the operation of the analog backplane interface board.

A positive-edge trigger signal is made by using one of the analog output channel in the DAP 5200a as shown in Figure 3.8. The input and output clocks of the DAP 5200a has two modes, a channel list clocking[1] and a single channel clocking[2]. With channel list clocking selected, each positive edge of the external clock causes conversion of the entire channel list (channel 0 to 141). The channels are converted in sequence with channel 0 synchronized to the positive edge of the external clock, and each of the subsequent channels converted according to the TIME[3] command in DAP 5200a. To collect the data at all channels, the period of the external clock had to be equal to or greater than the TIME command times the number of channels. The exact period of positive edge signal is made at one of the analog output channel when channels greater than 256 are added in the channel list. The length of the positive edge signal is controlled by adding the proper number of channels, which is used for making the control signal for sample/hold amplifier through an amplifier in the section 3.4.2.

When connecting the 138 anemometers, all the ground connections were carefully

[1]The DAP 5200a starts conversion of an entire channel list on the positive edge of the clock.
[2]The DAP 5200a converts a single channel on the positive edge of the clock.
[3]TIME is the sample time used in the input procedure of the DAP 5200a, and the minimum sample time in the channel list of DAP 5200a is 1.25 μs for analog inputs.

checked to avoid making any ground loop in the data acquisition system including the PC and AC power line. The DC ground of the DAP 5200a, with the anemometer ground, and the DC power supply for the anemometer are connected at a single point grounding to avoid forming a loop.

Measurements are made simultaneously at all 138 positions with the 138 hot wire probe array. The duration of each block of $4,096$ samples was $1.02\,sec$ of all $400\,sec$ in total 388 blocks of data for each channel. The variability in a random system goes as (George *et al.* (1978)):

$$\epsilon \sim \frac{1}{\sqrt{N}} \frac{var\{x\}}{\overline{x^2}} \tag{3.11}$$

where N is the number of data blocks measured and $var\{x\}/\overline{x^2}$ is the variability of the signal itself. For these experiments $var\{x\}/\overline{x^2} < 1$, so the maximum variability of these measurements was approximately $5\,\%$.

3.4.2 Simultaneous sampling

To obtain data simultaneously at all 138 positions, a sample/hold amplifier, SHC298, was used in each anemometer board separately. It had a 12 bit throughput accuracy, less than $10\,\mu s$ acquisition time[4], wide-band noise less than $20\,\mu s\,V_{rms}$, reliable monolithic construction and TTL-CMOS-compatible logic input features.

The positive-edge triggered control signal for the sample/hold amplifier is generated by the Microstar 5200a Data Acquisition Processor as part of the sampling process. The sampling time here is $10.2\,\mu s$ and holding time $239.7\,\mu s$, so the resulting sampling frequency is $4\,001.6\,Hz$ $(= 1/(10.2{+}239.7\mu s))$ as shown in Figure 3.8. When the mode control is switched from hold-mode to sample-mode with the positive-edge triggered signal, the sample/hold amplifier samples data at all 138 anemometers simultaneously and holds the signals until it switched to the next sample-mode. During

[4]It is the required time for the sample/hold output to settle within a given error range of its final value,when switched from Hold to Sample.

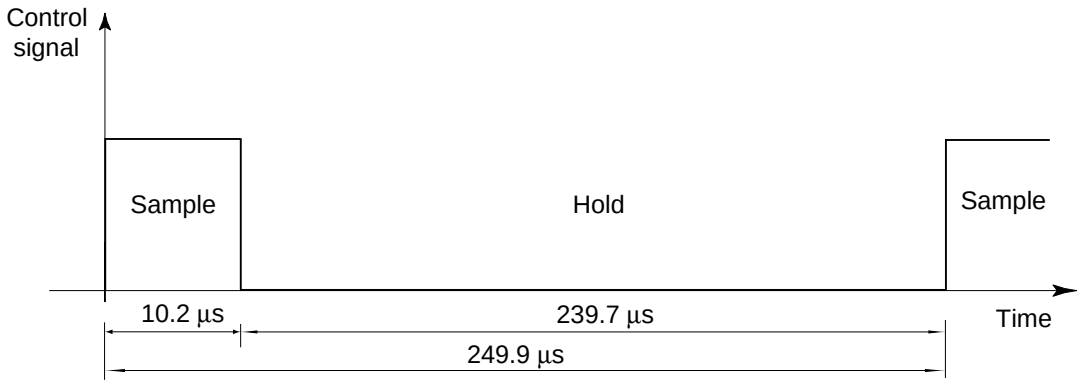

Figure 3.8: Control signal for sample/hold amplifier

the hold-mode, the Microstar DAP 5200a collects data from all the 138 anemometers and 3 auxiliary channels, and then saves them on the hard disk.

147 channels are used to acquire data from the hot wire probe array. They consist of the 138 channels for the hot wire probes, a channel for the pressure tranducer, two for room and jet temperature, and 6 channels for generating the control signal. The holding time of $239.7\mu s$ was calculated using $141\,ch \times 1.7\,\mu s$, and the sampling time of $10.2\,\mu s$ from $6\,ch \times 1.7\,\mu s$. The sampling time $1.7\,\mu s$ for each channel is selected to match the optimal sampling frequency, $4\,000\,Hz$, calculated by Equation 3.3 in the previous section. The resulting control signal is generated automatically by the Microstar DAP 5200a while operating, and is applied to all sample/hold amplifiers at each anemometer separately as the positive-edge trigger signal within the standard TTL logic ranges from 0 to +5 volts.

To check if the sample/hold samples data simultaneously within a given error band of its final value, a white noise (Figure 3.9) made by a Gaussian noise generator (Elgenco Inc.) is applied at the point between V_T and the op-amp on the output control (Figure 3.4), and is measured at $4\,000\,Hz$ for $400\,sec$ at two randomly selected channels (75 and 127). Sampling conditions are set to be the same as for the main experiments. Since there is an amplifier between the sample/hold amplifier and

the filter at each anemometer, it causes a difference in magnitude but phase in the sampled signal. The difference in magnitude due to the amplifier, however, can be recovered during calibration. Therefore only the phase difference between the channels was carefully investigated to verify the simultaneous data sampling at 138 different positions.

The simultaneously sampled data at two channels as shown in Figure 3.9 can be considered respectively as the input, $x(n)$, and output, $y(n)$, of a linear time invariant system, H. The identification of the nonparametric system can be proven by the relations between the power spectral density of $x(n)$ and the cross-spectral density of $x(n)$ and $y(n)$ by:

$$P_{xy}(f) = H(f)\, P_{xx}(f). \tag{3.12}$$

An estimate of the transfer function between $x(n)$ and $y(n)$ is:

$$H(f) = \frac{P_{xy}(f)}{P_{xx}(f)}. \tag{3.13}$$

Figure 3.10 shows the magnitude and the phase difference of the transfer function estimated by Equation 3.13 along frequency. The phase difference in degrees tells that the data sampling in this system is simultaneous within less than 0.2% error in degree of phase difference.

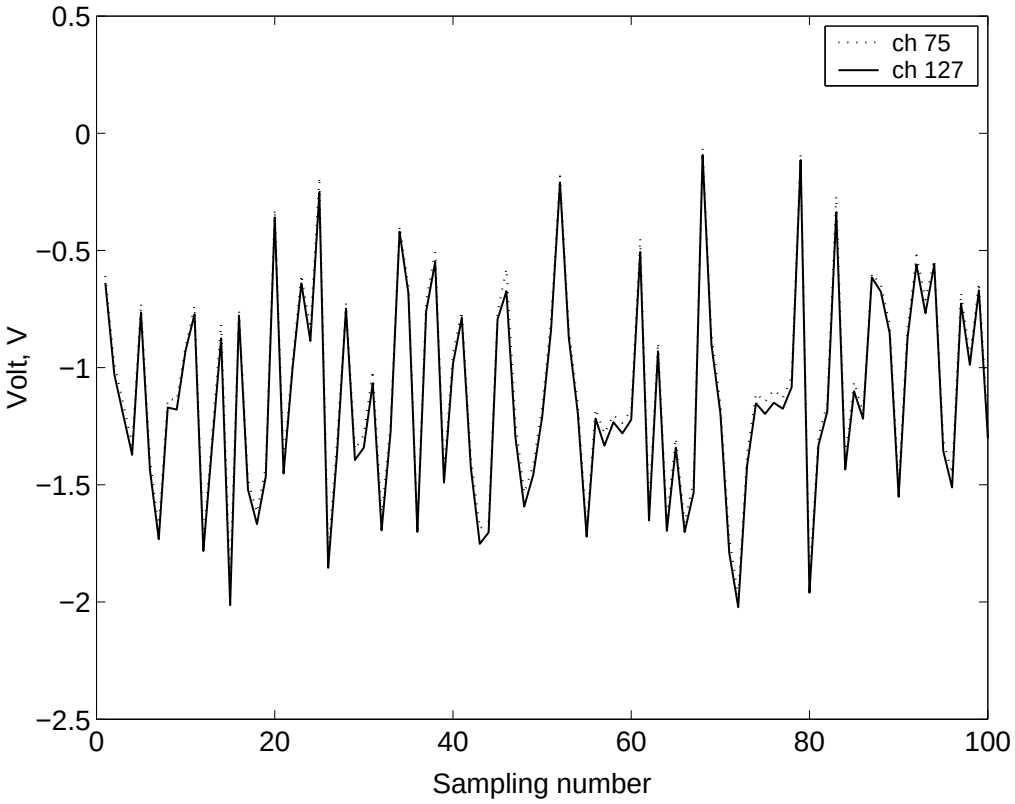

Figure 3.9: White noise collected simultaneously at two channels

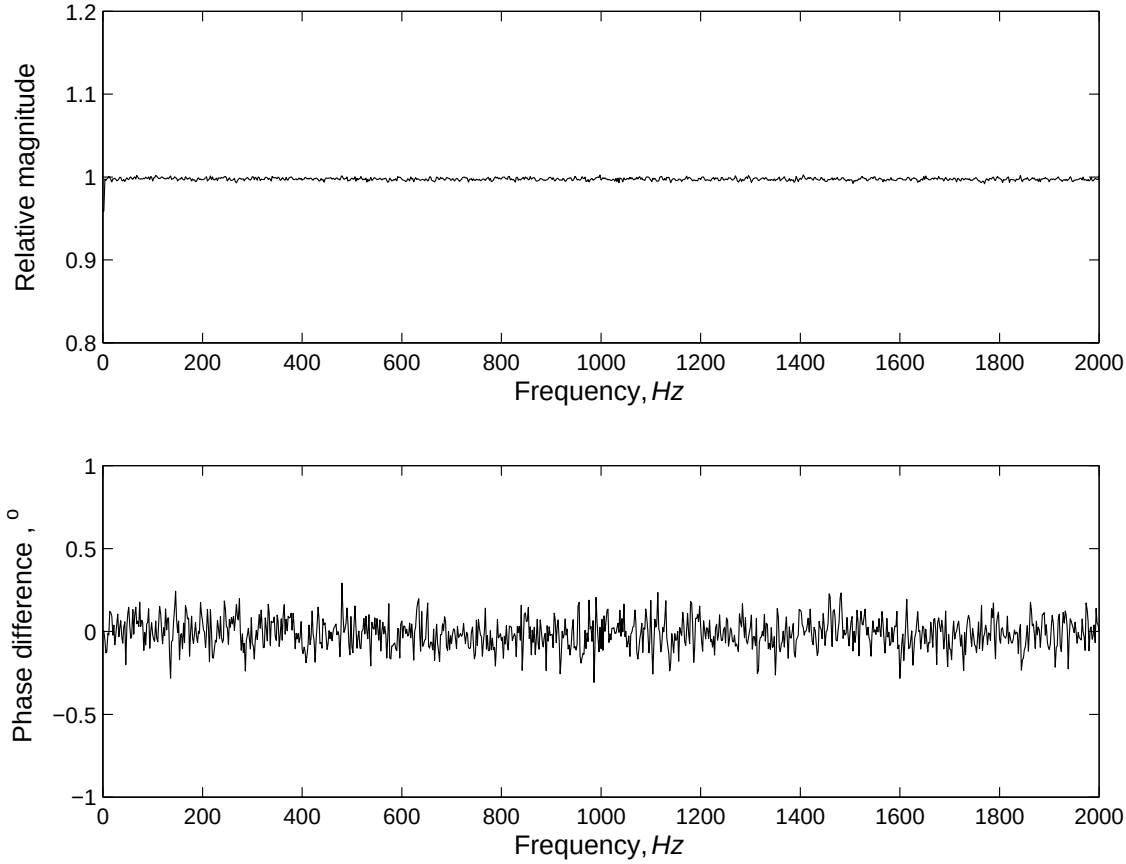

Figure 3.10: Magnitude and phase difference as a function of frequency

Chapter 4

Statistical Properties of the Jet Mixing Layer

4.1 Introduction

In this chapter, the flow field of the jet mixing layer is examined in detail, in order to ensure that it is behaving properly before carrying out the extensive POD analysis. Measurements were made of mean velocity, turbulence intensity, and spectral density at 9 positions and 3 Reynolds numbers. The measurements themselves are expected to be different from earlier results with smaller wires because of the very long wire probe used. Nevertheless, the differences are well understood (Citriniti & George 1997), so the measurements are useful for confirming both the nature of the flow and that the equipment is working.

4.2 The mean velocity

The 138-wire probe was used to measure the velocity field in the range of $x/D = 2$ to 6 with spacings of $0.5x/D$ along the downstream direction. The measurements were made at Reynolds numbers of 78 400, 117 600, and 156 800 corresponding to jet exit

velocities of $12\,m/s$, $18\,m/s$, and $24\,m/s$ respectively.

Statistics were computed from 388 blocks of 4096 samples at each position, corresponding to $400\,sec$ record length each. The variability of mean velocity is approximately 5% according to Equation 3.10.

Contour maps of mean values normalized by the nozzle exit velocity, U_{exit}, are presented in Figures 4.1 to 4.9. They show that the mean velocity field is axisymmetric to within the statistical error, thus confirming that an axisymmetric shear layer has been formed. The plots also show that much of the velocity field is within the bounds of the probe array in the near jet, even for the $x/D = 6$ position where the normalized mean velocity of the outermost ring is 0.36.

Normalized mean streamwise velocity profiles are shown in Figures 4.10 to 4.12 for the 9 measured positions with the three different Reynolds numbers plotted together. The radial coordinate is normalized by the downstream distance, x, from the exit plane of the jet. These profiles were computed using probes 2, 5, 10, 16, 25, 37, 51, 67, 83, 99, 115, and 131 of the 138 hot wire probe array (see Figure 3.3). The normalized mean velocity profile of Khwaja (1981) is also shown in Figures 4.10 to 4.12. The normalized mean values near the high speed side are from about 0.9 to 1.0, and from 0.1 to 0.35 near the low speed side.

The alignment of the 138 hot wire probe on the axis of the jet flow field can be checked using the uppermost figures in Figures 4.10 to 4.12. If the array had been perfectly aligned, the profile would have been symmetrical. It is clear that a slight position adjustment is necessary, and this was made.

These figures show clearly that less of the shear layer is covered by the measurements as the fixed probe array is moved downstream. The normalized mean values collapse reasonably well with each other and with profiles of Khwaja. This was as expected, since the long wire of the array should not affect the mean velocity measurements.

4.3 The turbulence intensity

The turbulence intensity, or the axial component of the Reynolds stress, is presented in Figures 4.13 to 4.15. The rms velocity has been normalized by the exit velocity, and the radial coordinate by streamwise distance from the jet exit plane. Also shown for comparison are the profiles of Khwaja (1981) and Glauser (1987).

Turbulence intensity profiles collapse very well, independent of downstream positions. The turbulence intensity based on the jet exit velocity is about 3 to 5 % near the centerline of the jet, and the maximum turbulence intensity is about 13 to 14 % at the peak near the $(r - R)/x = 0.0$.

The measurements are compared to Khwaja's and Glauser's. They are little higher than Khwaja's in the centerline of the jet and a little lower in the upper middle of the shear layer. This is perhaps in part attributable to the response of the long wire probes, but probably in larger part to the fact that Khwaja's measurements were made at much higher Reynolds number ($2.2 \times 10^5 \sim 5.4 \times 10^5$), and in a much larger facility with different upstream conditions.

The measurements here, however, are in better agreement with these of Glauser ($Re_D = 110\,000$) which were made in the same facility with small hot-wires. In fact, the long wire measurements are always below these of the smaller wires, exactly as would be expected from their reduced temporal and spatial resolution.

4.4 Power spectral density

Power spectral densities of the streamwise velocity are presented as a function of radius for three Reynolds numbers for different downstream distances in Figures 4.16 to 4.24. Each spectrum presented was taken from the same probe used for the mean velocity and the turbulence intensity profiles shown earlier.

The power spectra clearly vary greatly as a function of radial position. On the higher speed side of the mixing layer, corresponding to $r/D = 0.15$, and 0.28, there

are local peaks. These peaks disappear outside of $r/D \geq 0.41$. On the lower speed side of the mixing layer, the spectra show at least one full decade of $f^{-5/3}$ range denoting high Reynolds number turbulent flow.

The spectra are consistent with Petersen & Samet (1988), Glauser (1987), and Citriniti & George (2000). The Strouhal number, St_D, based on the jet diameter, D, exit velocity, and the local peak, or the preferred mode, will be discussed in the later chapter in detail combined with the POD results. As the downstream distance increases, as reported by Petersen & Samet (1988), the local peak moves toward lower frequencies at the two lower Reynolds numbers. But at the highest Reynolds number the local peak stays at almost the same frequency along the entire distance.

For the spectra for $r/D = 0.15$ and 0.28, there are two high spikes instead of the local peak about $50\,Hz \sim 120\,Hz$ until $x/D = 3.5$. To investigate the spikes in detail, the spectra shown in Figure 4.25 were measured at the center of $x/D = 0.0$ using a $1\,mm$ length of hot wire. There are three dominant peaks in these centerline spectra. Frequencies of $19.1\,Hz$, $29.1\,Hz$, and $38.7\,Hz$ of the motor controller correspond to the three different Reynolds numbers. The frequency of the peak 'a' corresponds to the frequency supplied by the motor controller. The peak 'b' is exactly the second harmonic of the frequency of the motor controller. The peak 'c' is also an harmonic with the motor controller but much stronger than the other peaks. This is perhaps why it also appears in all of the spectra in Figure 4.16 $\sim$ 4.24.

Although the first spike of Figure 4.16 $\sim$ 4.24 or the peak 'b' of Figure 4.25 is a harmonic of the motor controller frequency, it also corresponds to the blade-passing frequency, f_{bf}, of the centrifugal blower defined as:

$$f_{bf} = (Blower\ RPM) \cdot \frac{min}{60\,sec} \cdot \frac{Number\ of\ blades}{revolutions} \tag{4.1}$$

For the three flow speeds, the blower RPM were 3 450/2 850 at 60/50 Hz respectively, and the number of blades of the blower was 6. Therefore the blade-passing frequencies are about $119\,Hz$, $173\,Hz$, and $226\,Hz$ respectively. These blade-passing frequencies

also are harmonic with the frequency applied by the motor controller.

The second peak occurring only at $r/D = 0.28$ is considered to be a mechanical vibration of the probe. The peak is present only at the position corresponding to the second radial position of the probe array and in the potential core region until $x/D = 3.0$, and it has no harmonic relation with other frequencies. The higher frequency region of the $r/D = 0.15$ spectrum is dominated by the unavoidable electrical noise, but the noise level is very low compared to the remaining spectral values.

4.5 Summary of the single point statistical measurements

Measurements have been presented of the mean velocity profiles, turbulence intensity profiles, and velocity spectra for positions $2 \leq x/D \leq 6$, and for three different Reynolds numbers (78 400, 117 600, and 156 800). All of these are consistent with what has been measured before in the same facility, and in others as well.

The measurements are certainly not of the accuracy which could be achieved with smaller wires or alternative techniques (like an LDA), because of the removal of information by the long-wires. But they were intended only to be accurate representation of the spatially and temporally low-pass filtered velocity. Clearly their agreement with previous results provides confidence that no information essential to the energetic turbulence was removed.

(a)

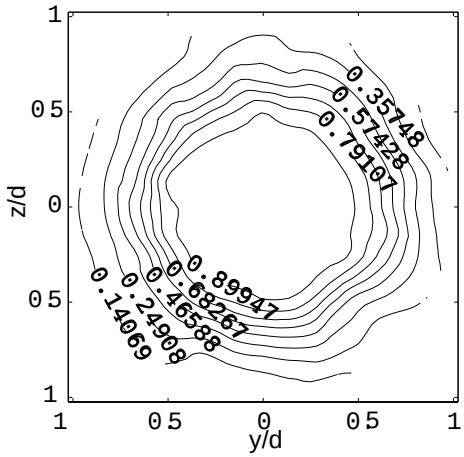

(b)

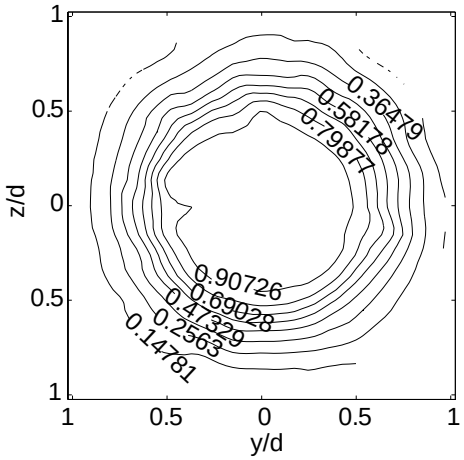

(c)

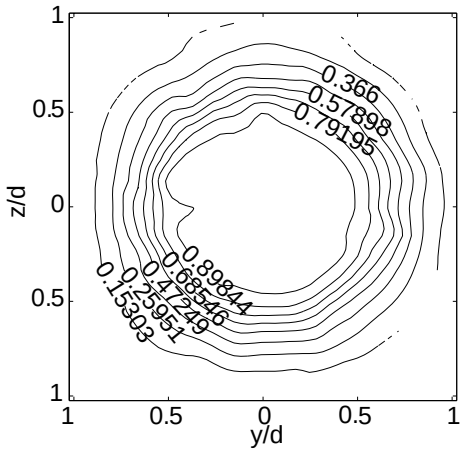

Figure 4.1: Contour map of the normalized mean velocity, U/U_{exit}, at $x/D = 2.0$: (a) $Re = 78,400$, (b) $Re = 117,600$, (c) $Re = 156,800$.

(a)

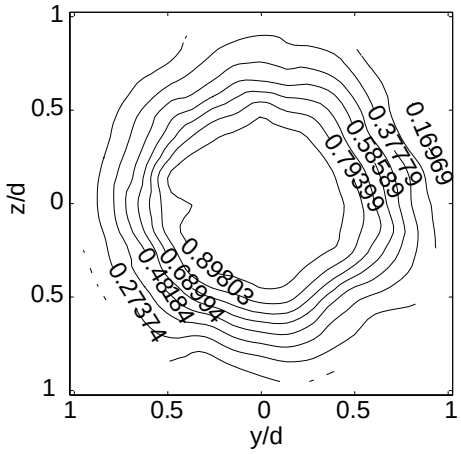

(b)

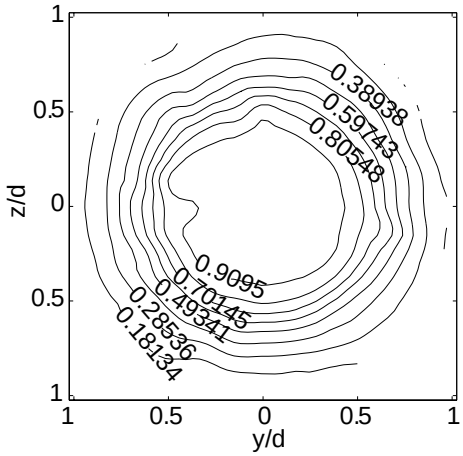

(c)

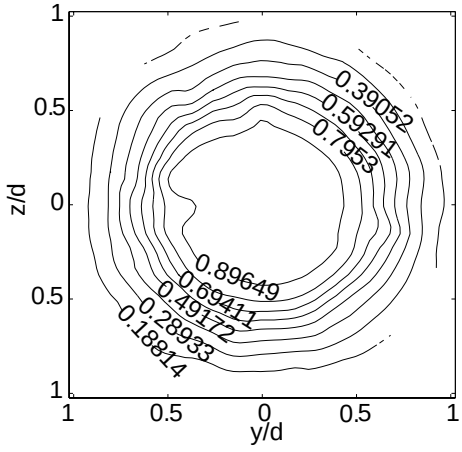

Figure 4.2: Contour map of the normalized mean velocity, U/U_{exit}, at $x/D = 2.5$: (a) $Re = 78,400$, (b) $Re = 117,600$, (c) $Re = 156,800$.

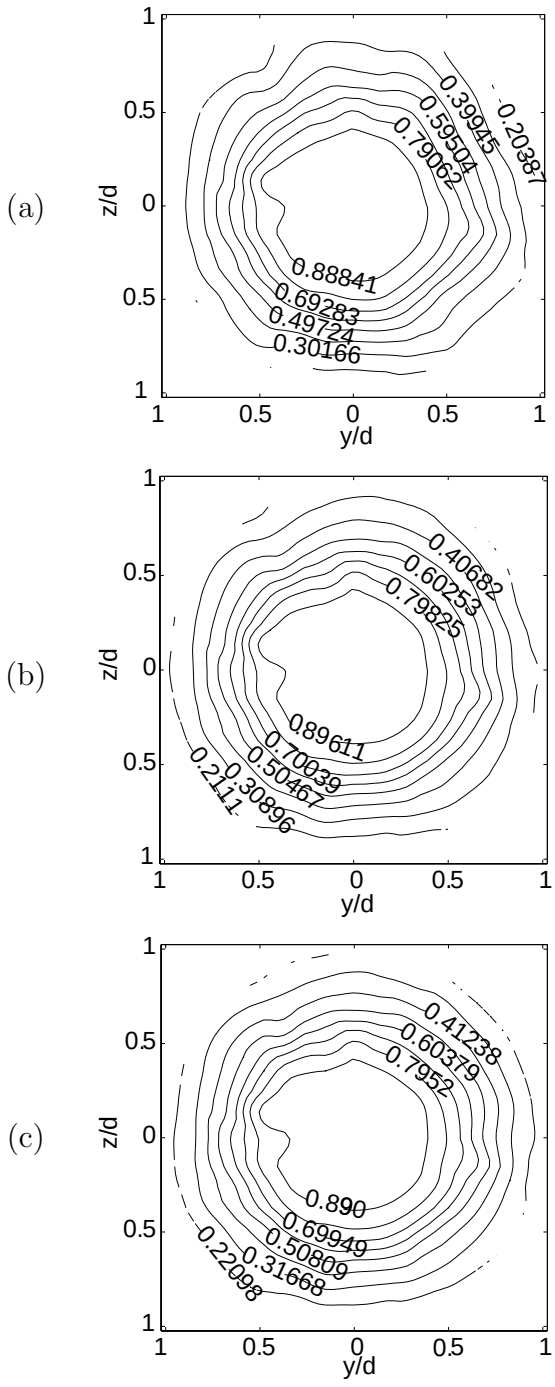

Figure 4.3: Contour map of the normalized mean velocity, U/U_{exit}, at $x/D = 3.0$: (a) $Re = 78,400$, (b) $Re = 117,600$, (c) $Re = 156,800$.

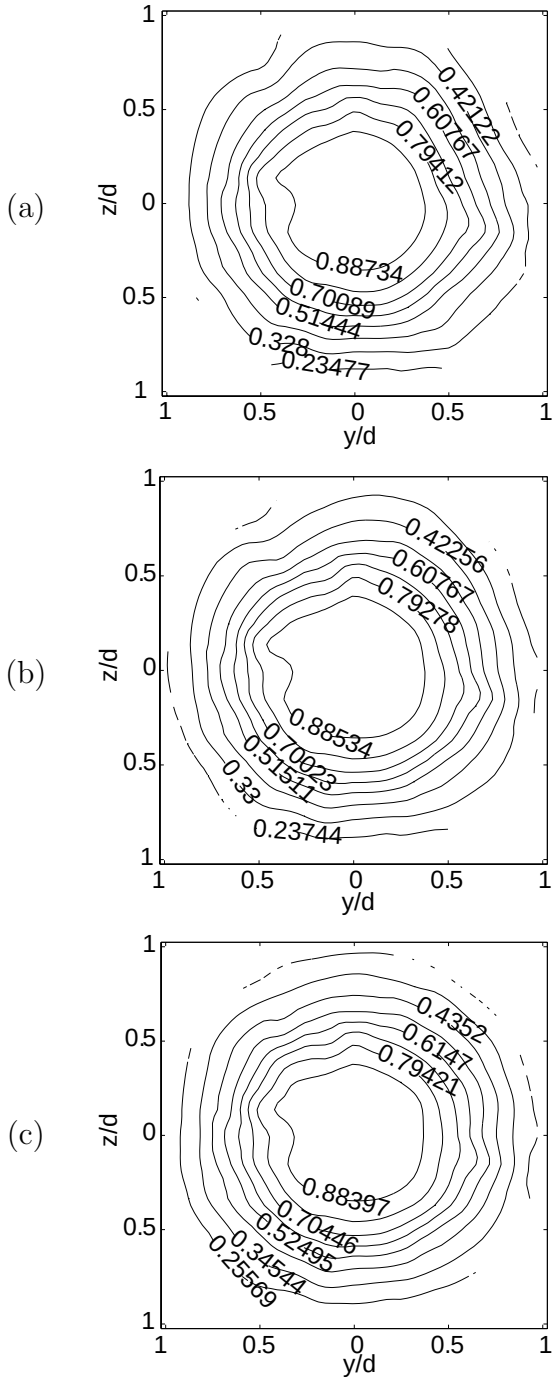

Figure 4.4: Contour map of the normalized mean velocity, U/U_{exit}, at $x/D = 3.5$: (a) $Re = 78,400$, (b) $Re = 117,600$, (c) $Re = 156,800$.

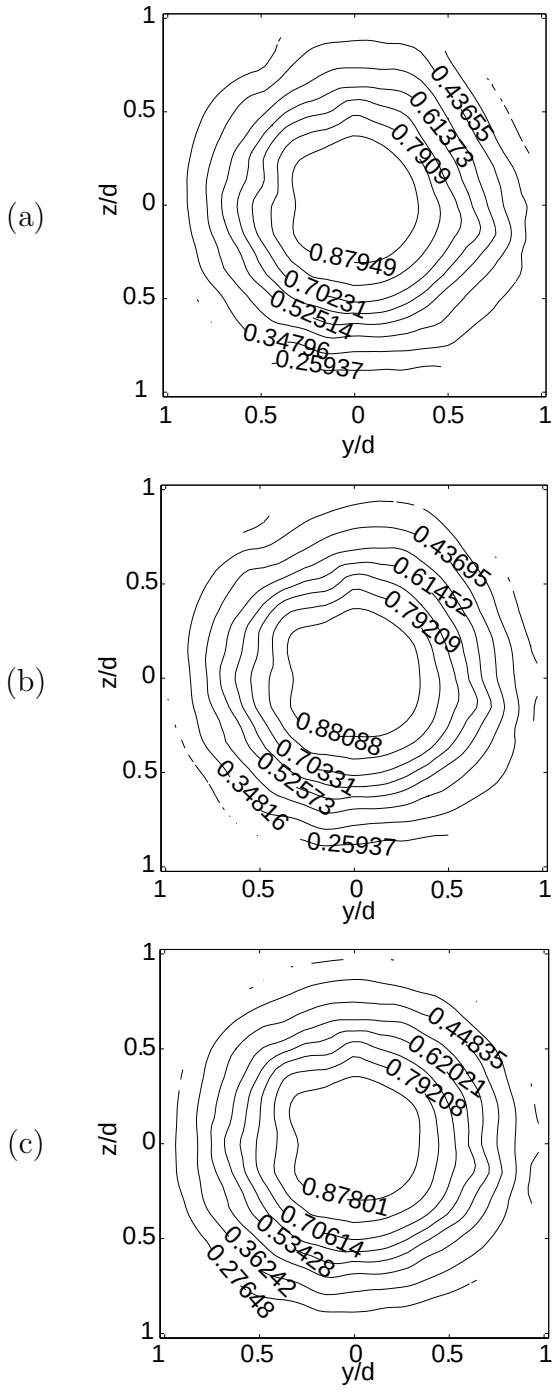

Figure 4.5: Contour map of the normalized mean velocity, U/U_{exit}, at $x/D = 4.0$: (a) $Re = 78,400$, (b) $Re = 117,600$, (c) $Re = 156,800$.

(a)

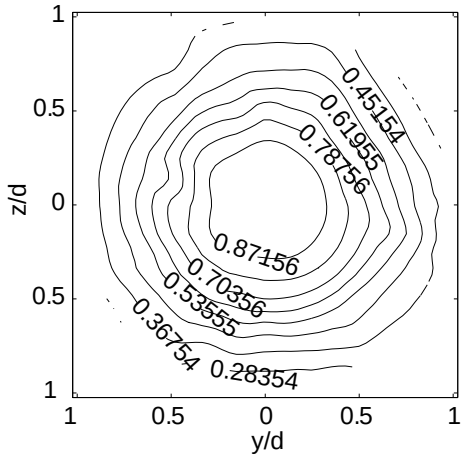

(b)

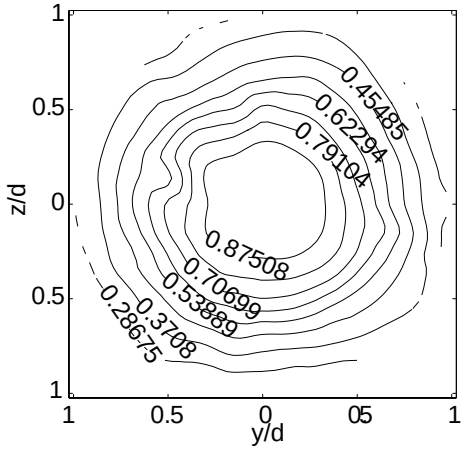

(c)

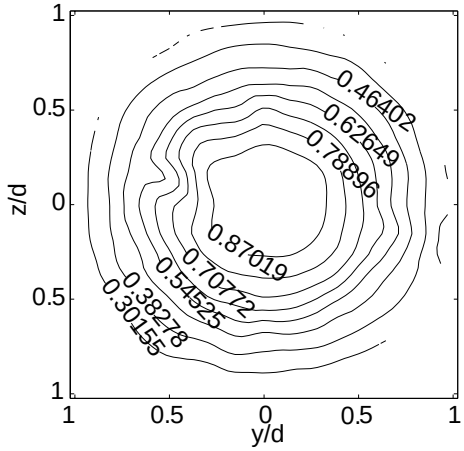

Figure 4.6: Contour map of the normalized mean velocity, U/U_{exit}, at $x/D = 4.5$: (a) $Re = 78,400$, (b) $Re = 117,600$, (c) $Re = 156,800$.

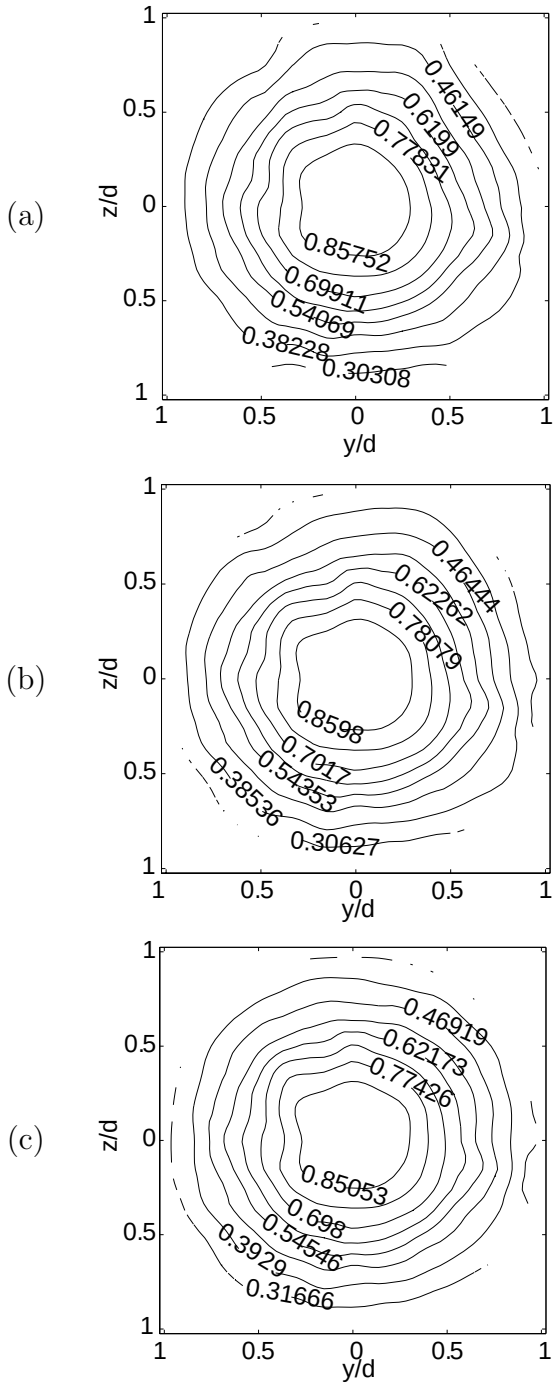

Figure 4.7: Contour map of the normalized mean velocity, U/U_{exit}, at $x/D = 5.0$: (a) $Re = 78,400$, (b) $Re = 117,600$, (c) $Re = 156,800$.

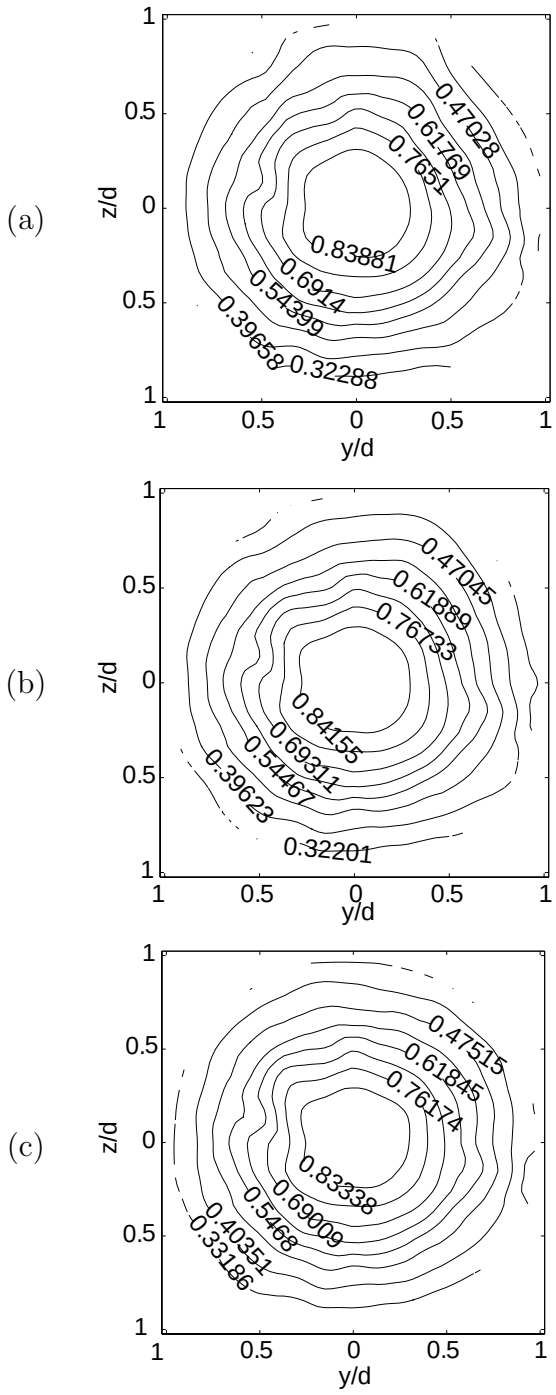

Figure 4.8: Contour map of the normalized mean velocity, U/U_{exit}, at $x/D = 5.5$: (a) $Re = 78,400$, (b) $Re = 117,600$, (c) $Re = 156,800$.

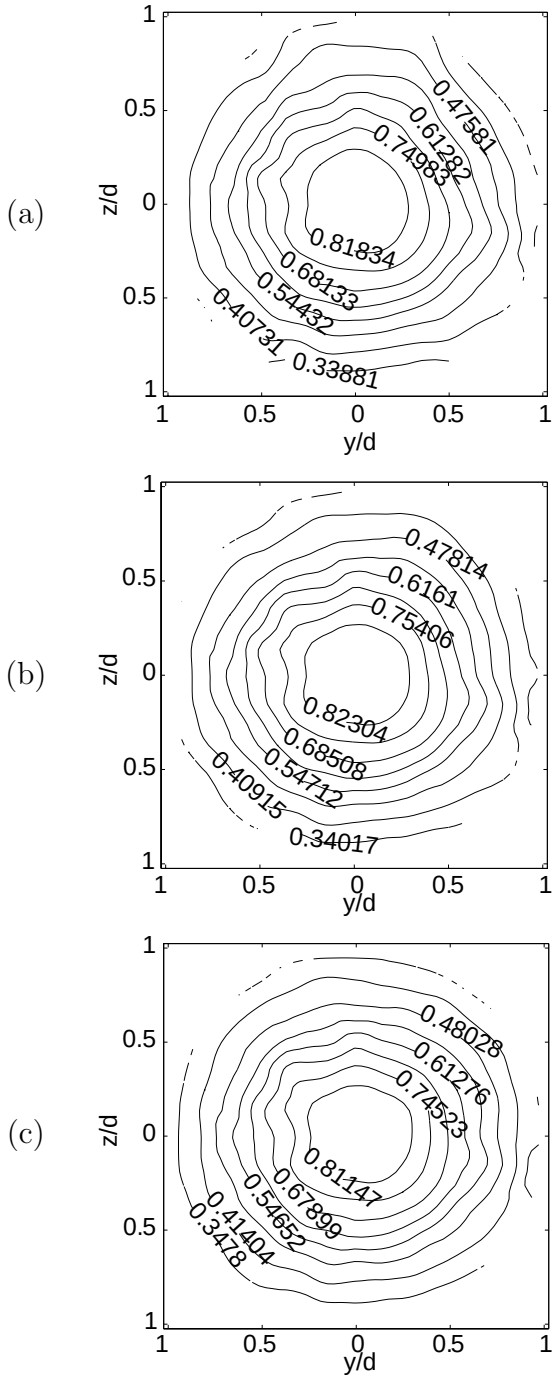

Figure 4.9: Contour map of the normalized mean velocity, U/U_{exit}, at $x/D = 6.0$: (a) $Re = 78,400$, (b) $Re = 117,600$, (c) $Re = 156,800$.

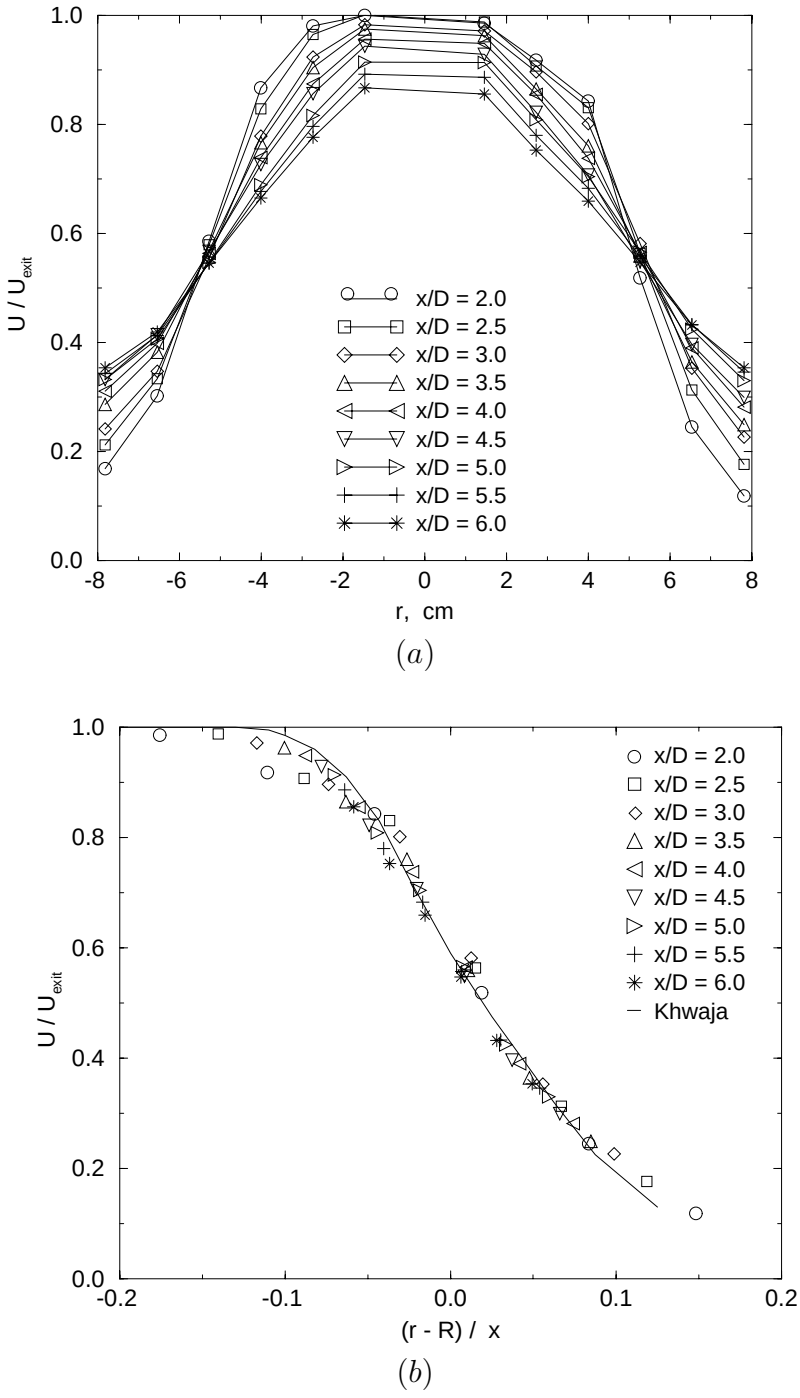

Figure 4.10: Normalized mean values of the streamwise velocity along a line in the 138-wire probe array at $Re = 78\,400$, (a) non-normalized r (cm), (b) normalized r.

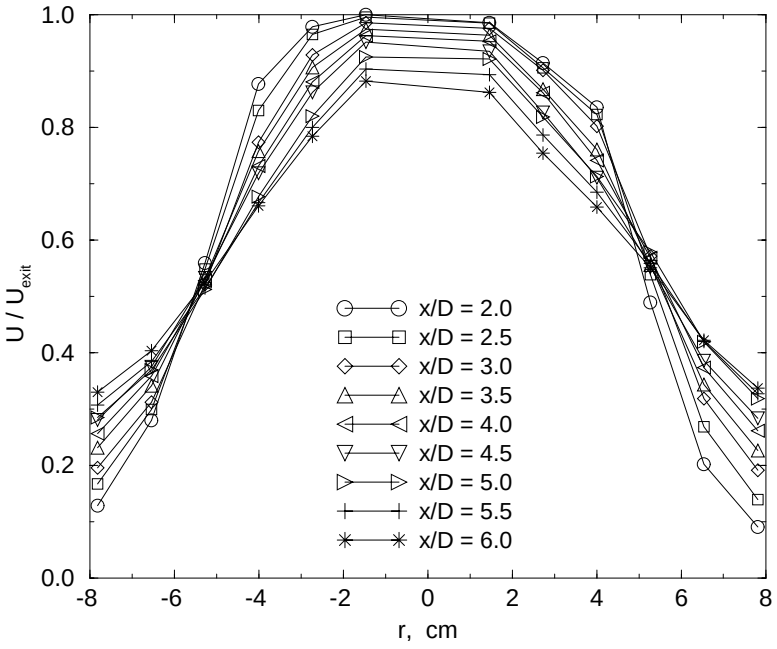

(a)

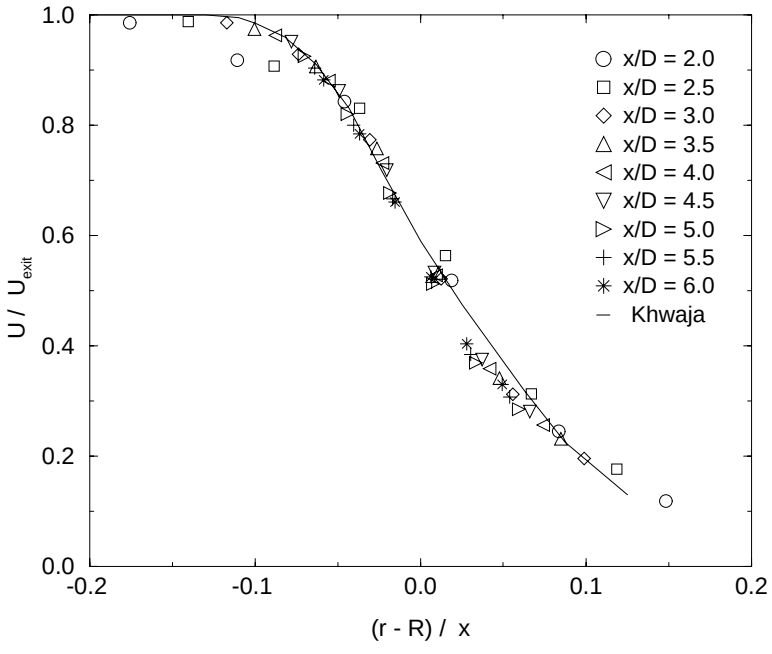

(b)

Figure 4.11: Normalized mean values of the streamwise velocity along a line in the 138-wire probe array at $Re = 117\,600$, (a) non-normalized r (cm), (b) normalized r.

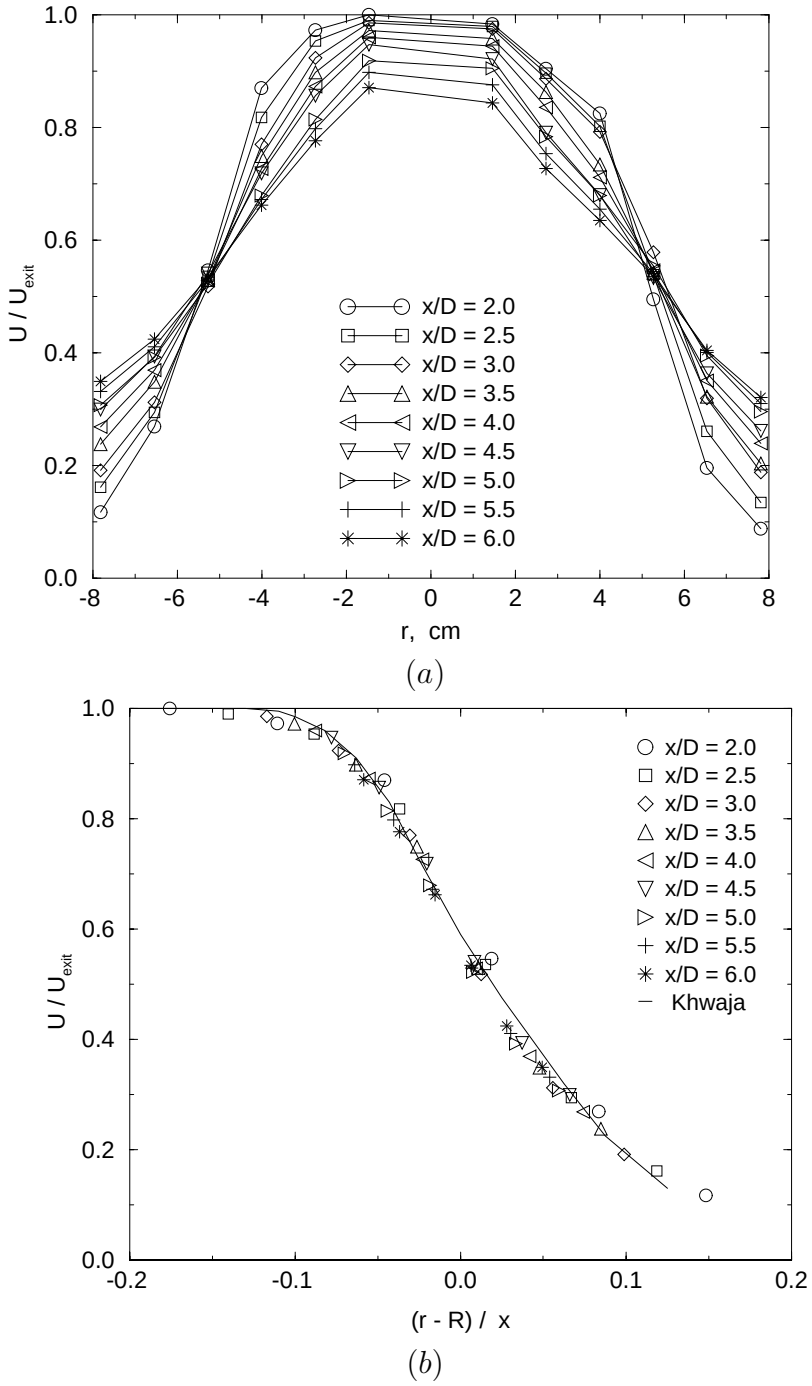

Figure 4.12: Normalized mean values of the streamwise velocity along a line in the 138-wire probe array at $Re = 156\,800$, (a) non-normalized r (cm), (b) normalized r.

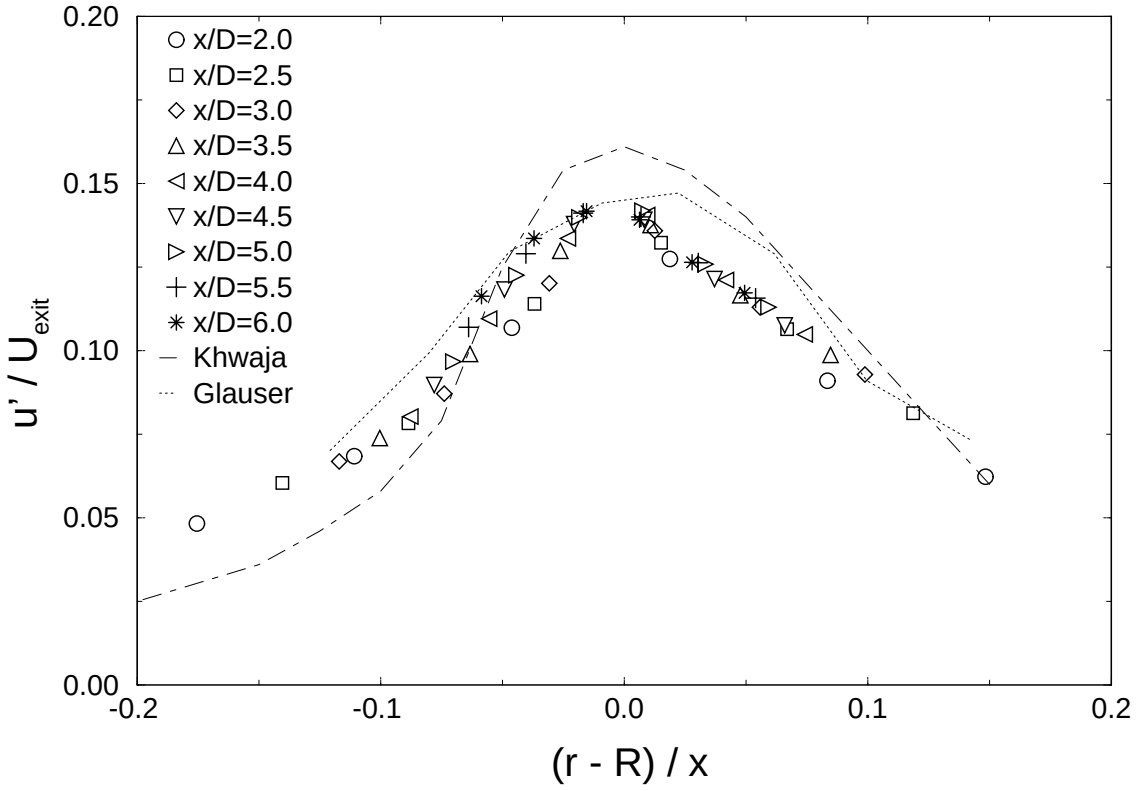

Figure 4.13: Turbulence intensity profiles based on the nozzle exit velocity, U_{exit}, along a radial line in the 138 hot wire probe array for $Re = 78\,400$.

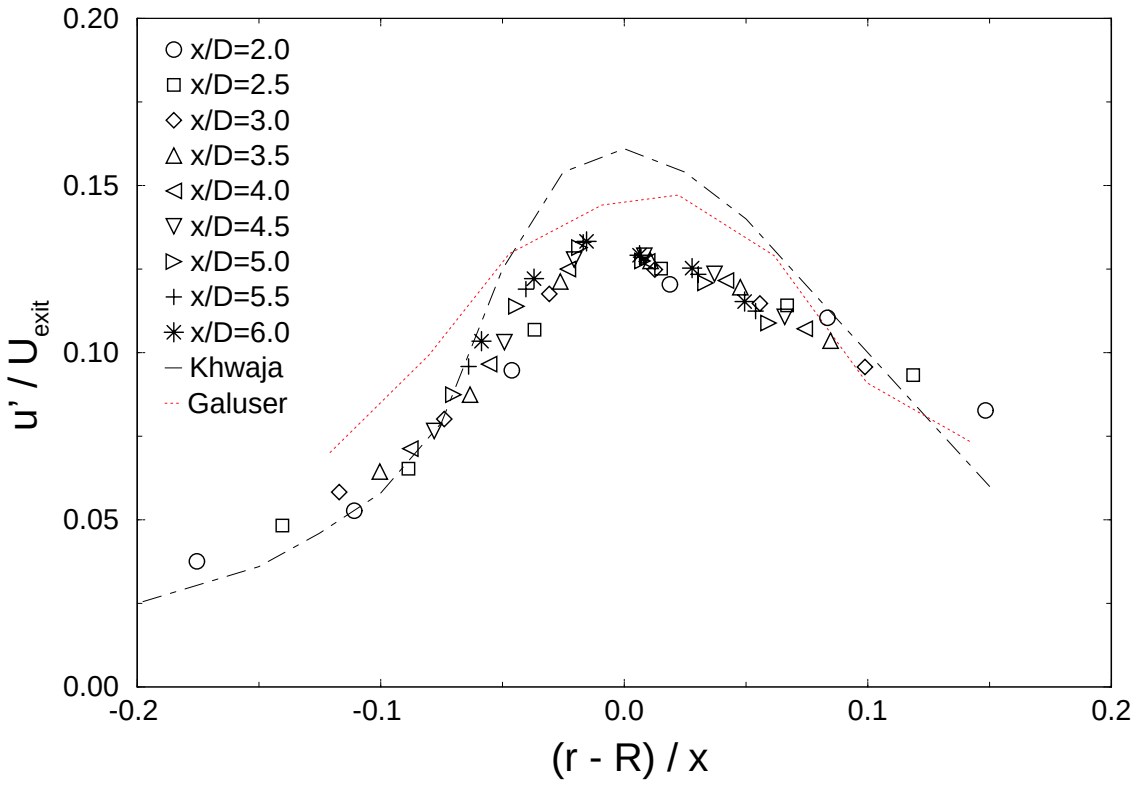

Figure 4.14: Turbulence intensity profiles based on the nozzle exit velocity, U_{exit}, along a line in the 138 hot wire probe array for $Re = 117\,600$.

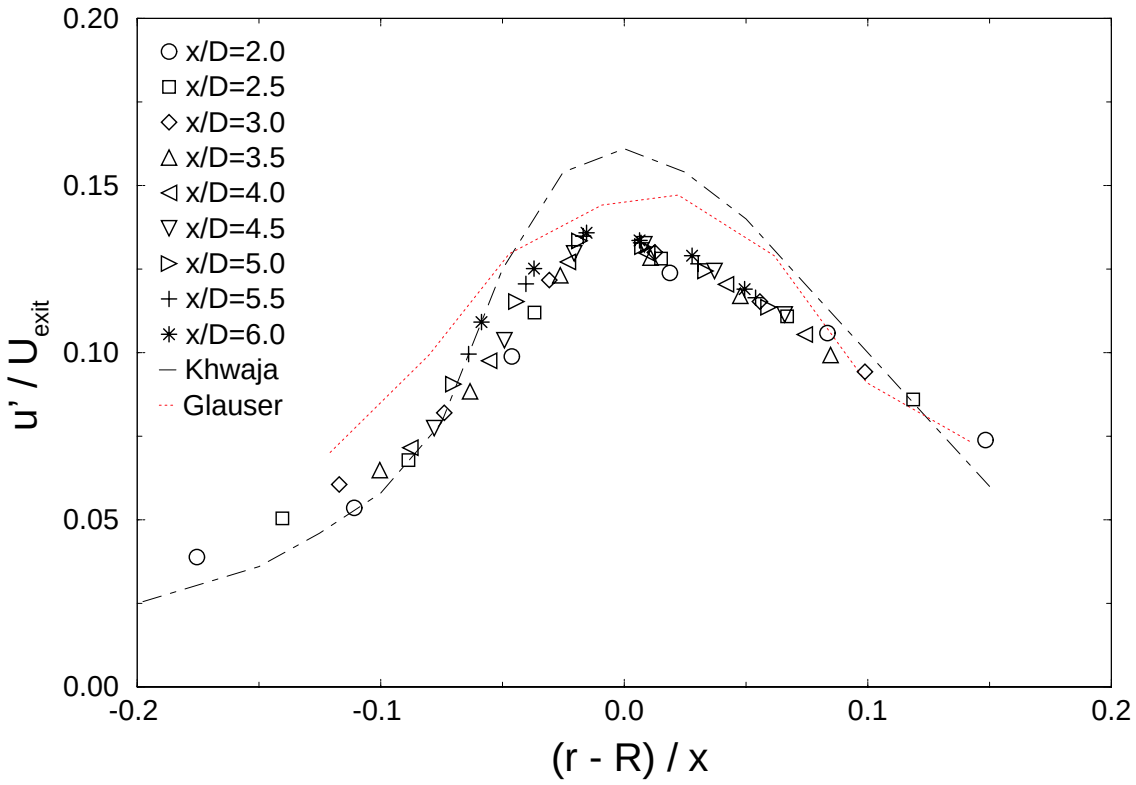

Figure 4.15: Turbulence intensity profiles based on the nozzle exit velocity, U_{exit}, along a line in the 138 hot wire probe array for $Re = 156\,800$.

(a)

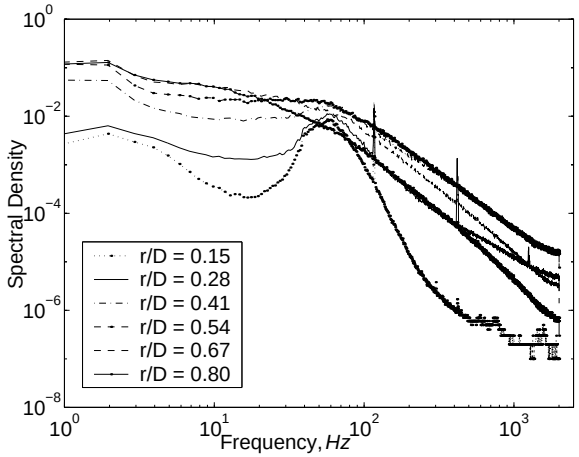

(b)

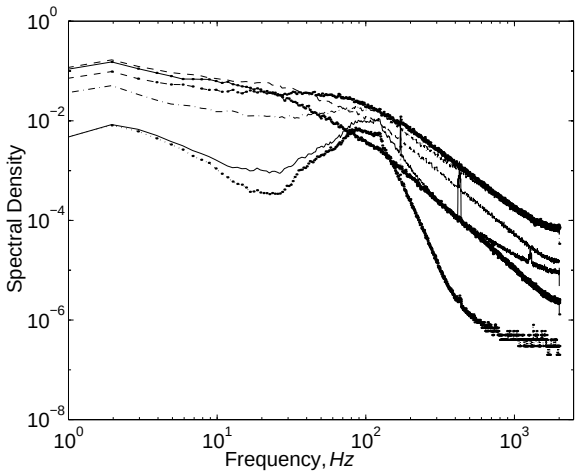

(c)

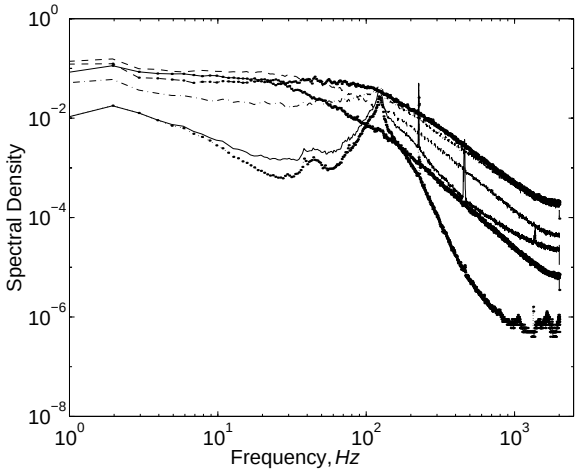

Figure 4.16: Power spectral density distributions along a line in the 138 hot wire probe array at $x/D = 2.0$, (a) $Re = 78\,400$, (b) $Re = 117\,600$, (c) $Re = 156\,800$.

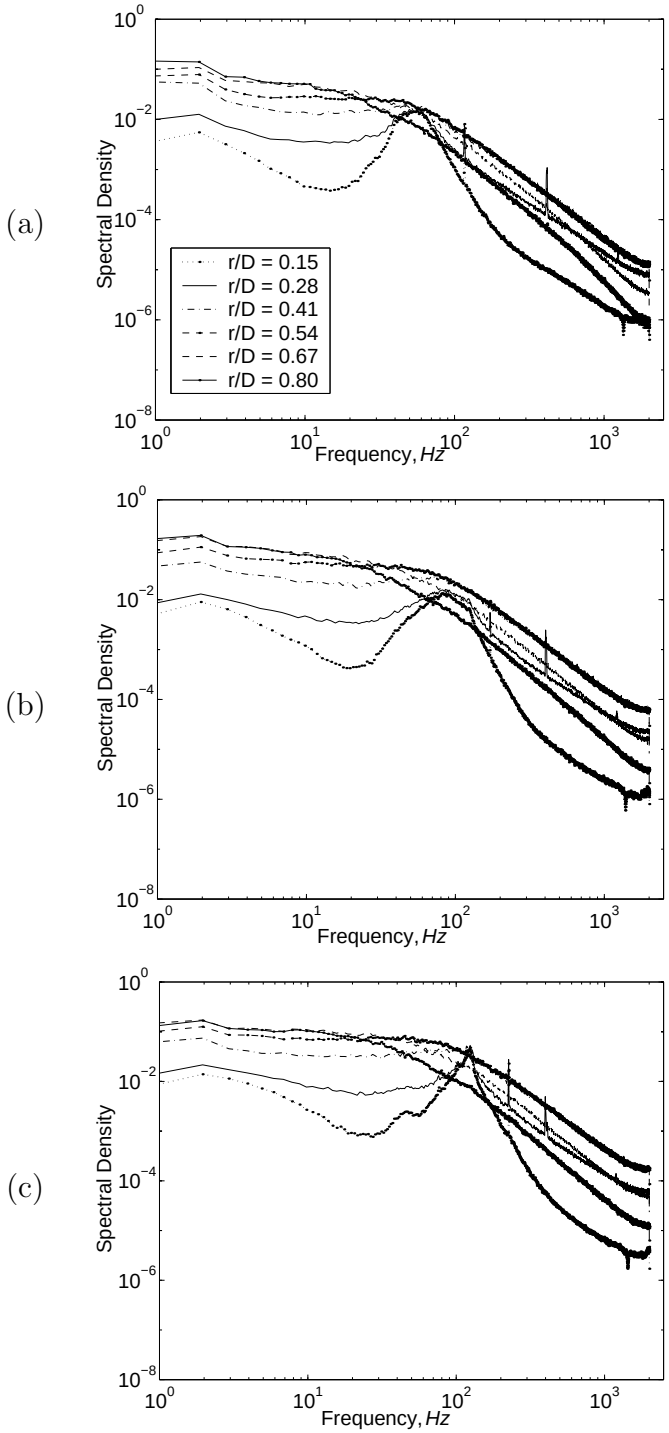

Figure 4.17: Power spectral density distributions along a line in the 138 hot wire probe array at $x/D = 2.5$, (a) $Re = 78\,400$, (b) $Re = 117\,600$, (c) $Re = 156\,800$.

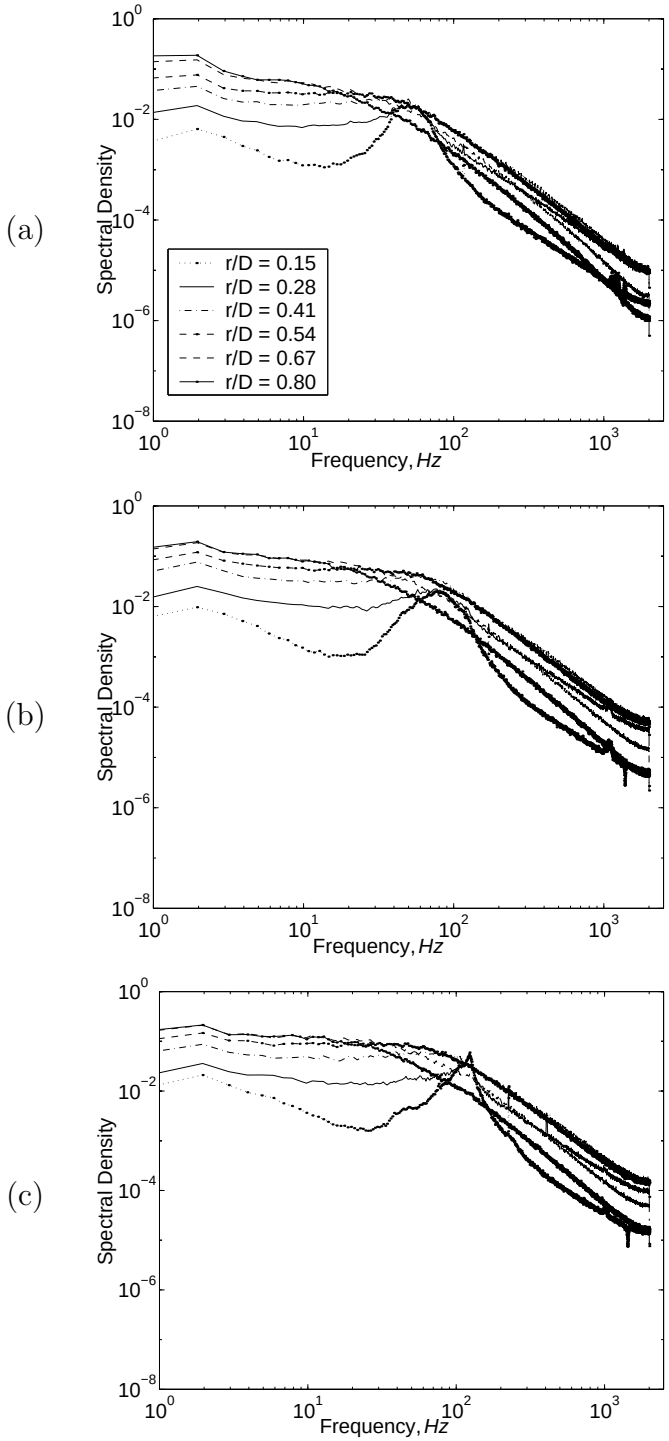

Figure 4.18: Power spectral density distributions along a line in the 138 hot wire probe array at $x/D = 3.0$, (a) $Re = 78\,400$, (b) $Re = 117\,600$, (c) $Re = 156\,800$.

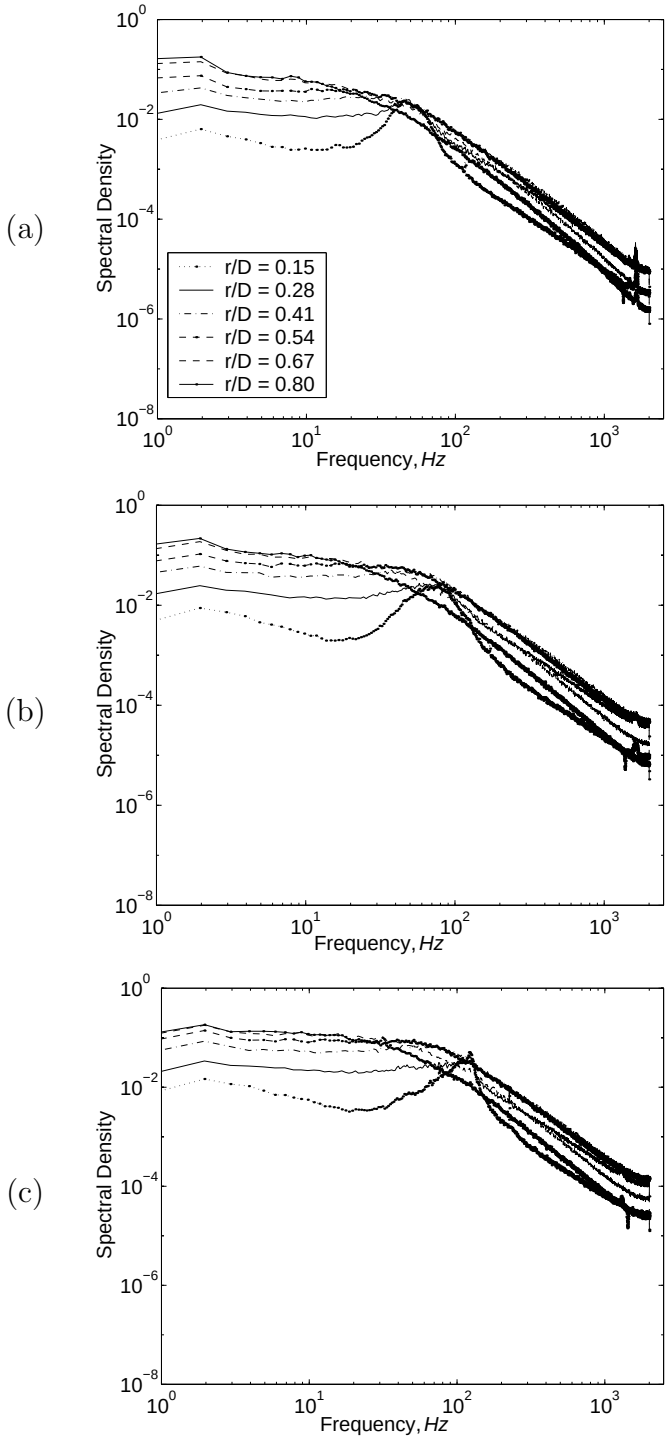

Figure 4.19: Power spectral density distributions along a line in the 138 hot wire probe array at $x/D = 3.5$, (a) $Re = 78\,400$, (b) $Re = 117\,600$, (c) $Re = 156\,800$.

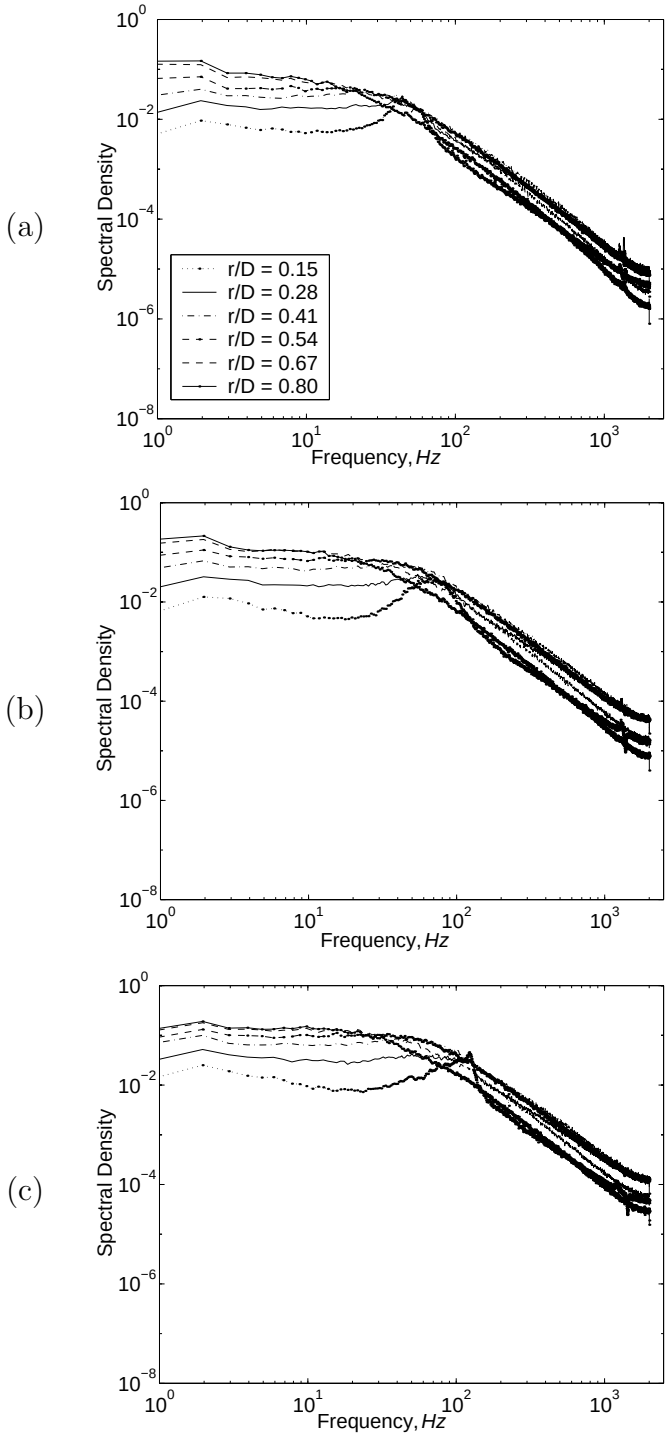

Figure 4.20: Power spectral density distributions along a line in the 138 hot wire probe array at $x/D = 4.0$, (a) $Re = 78\,400$, (b) $Re = 117\,600$, (c) $Re = 156\,800$.

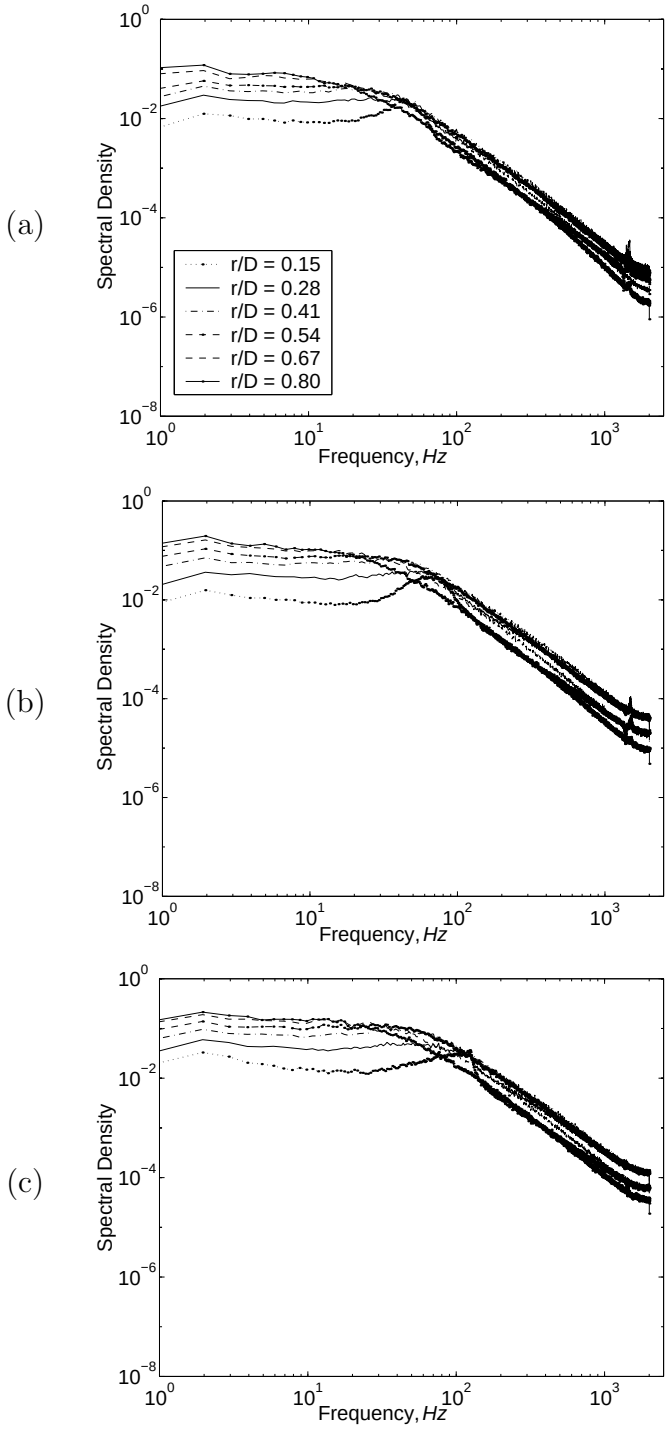

Figure 4.21: Power spectral density distributions along a line in the 138 hot wire probe array at $x/D = 4.5$, (a) $Re = 78\,400$, (b) $Re = 117\,600$, (c) $Re = 156\,800$.

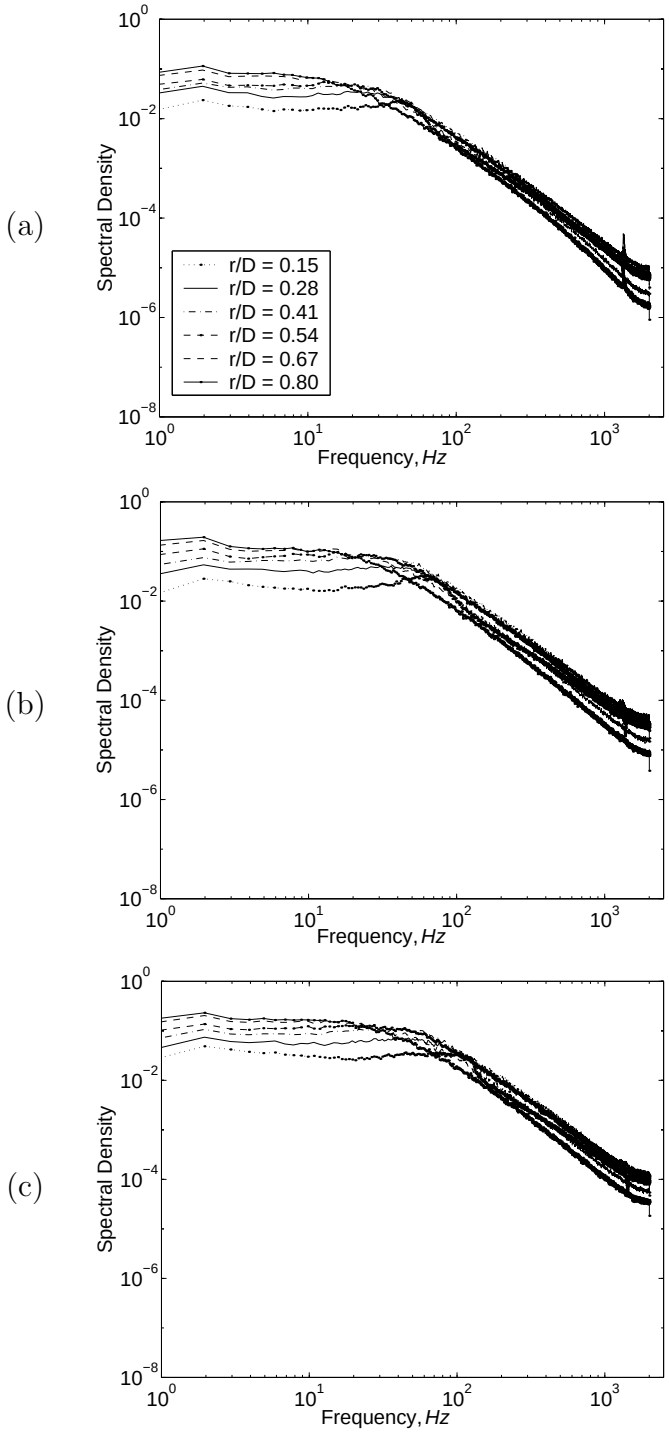

Figure 4.22: Power spectral density distributions along a line in the 138 hot wire probe array at $x/D = 5.0$, (a) $Re = 78\,400$, (b) $Re = 117\,600$, (c) $Re = 156\,800$.

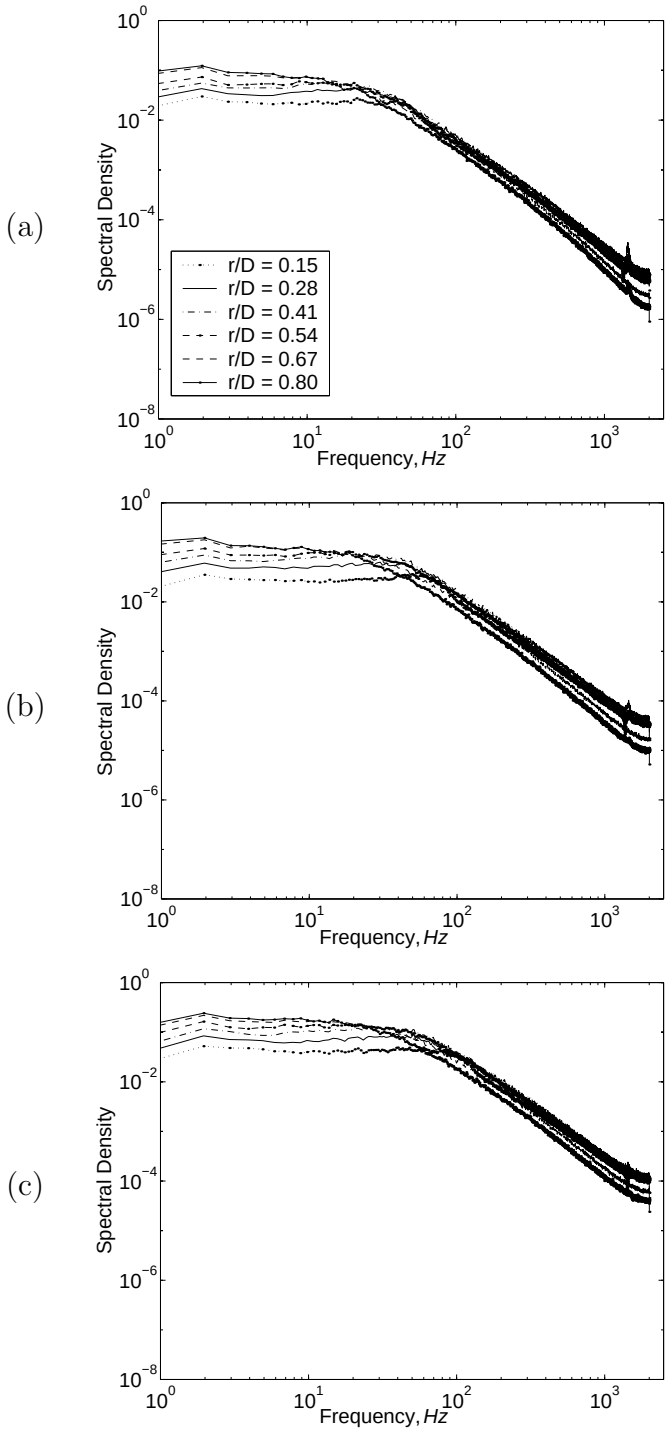

Figure 4.23: Power spectral density distributions along a line in the 138 hot wire probe array at $x/D = 5.5$, (a) $Re = 78\,400$, (b) $Re = 117\,600$, (c) $Re = 156\,800$.

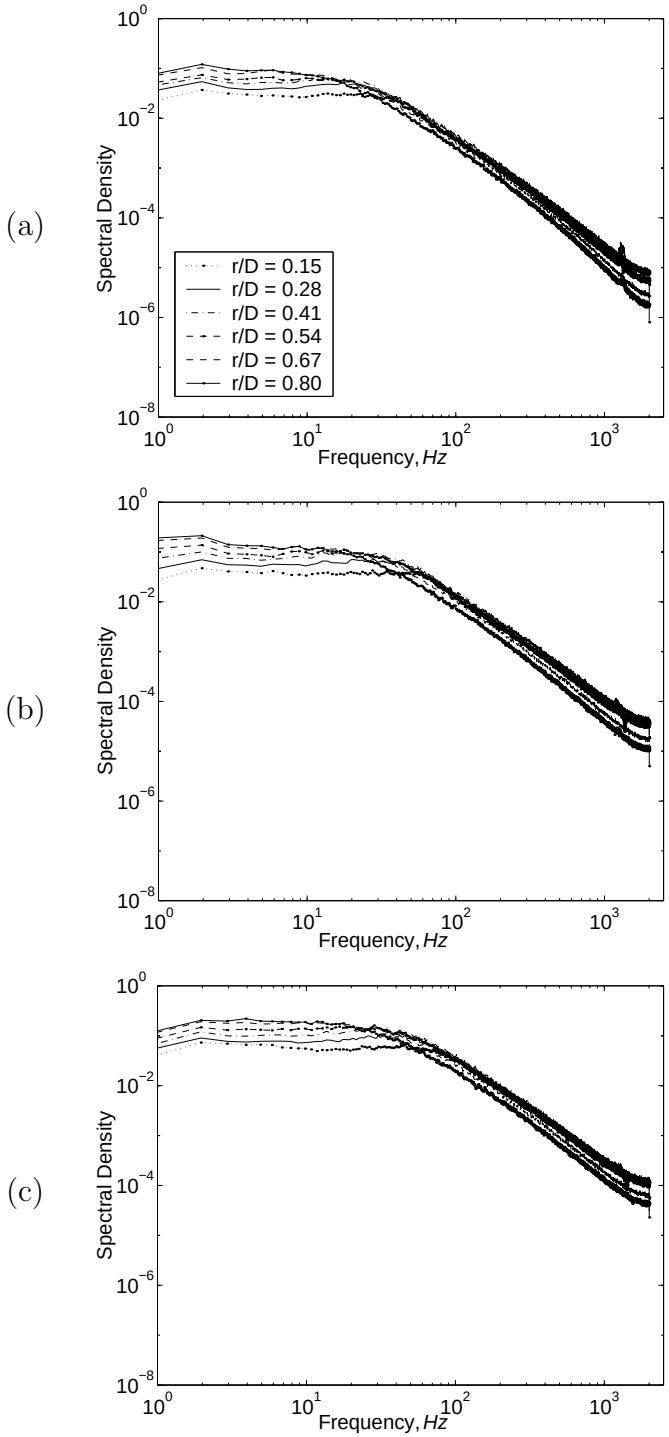

Figure 4.24: Power spectral density distributions along a line in the 138 hot wire probe array at $x/D = 6.0$, (a) $Re = 78\,400$, (b) $Re = 117\,600$, (c) $Re = 156\,800$.

(i)

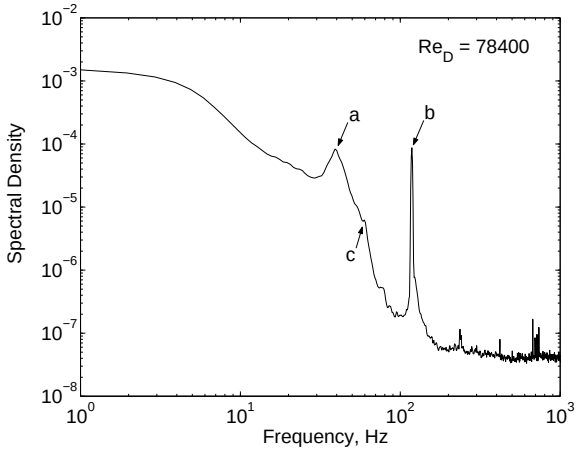

(ii)

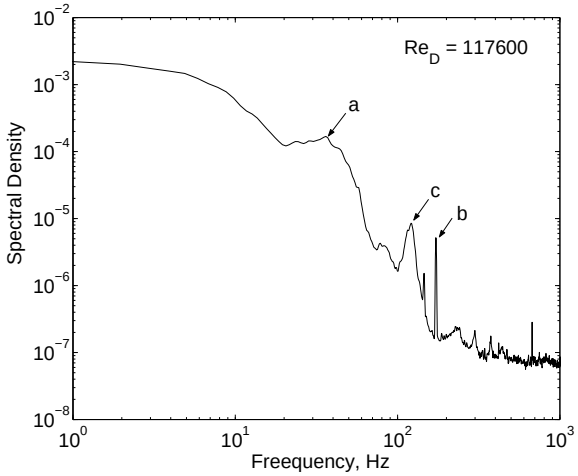

(iii)

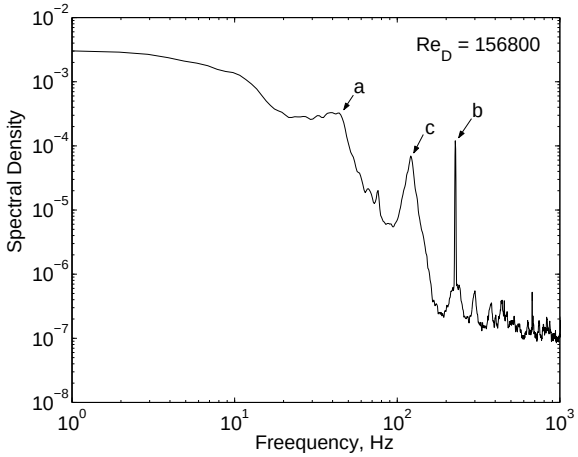

Figure 4.25: Power spectral density at $x/D = 0.0$, (i) $Re_D = 78\,400$, (ii) $Re_D = 117\,600$, and (iii) $Re_D = 156\,800$.

Chapter 5

The POD results

5.1 Introduction

The purpose of this chapter is to present and discuss the eigenvalues and eigenfunctions produced from the application of the POD to the jet data. Of particular interest is to see how the turbulent energy in the various POD modes is distributed among the various frequencies and azimuthal modes, and what these imply about the structure of the mixing layer. A discussion of what we believe these results mean will be presented in Chapter 7.

5.2 Eigenvalue distribution of the POD mode

The total turbulent kinetic energy at a cross-section of the flow (see Chapter 2) is equal to the sum of the POD eigenspectra, $\lambda^{(n)}(m, f)$, integrated over all the frequencies, f, and summed over azimuthal mode, m; i.e.,

$$E = \sum_n \sum_m \int_{-\infty}^{\infty} \hat{\hat{\lambda}}^{(n)}(m, f)\, df \tag{5.1}$$

Therefore the eigenspectra, $\lambda^{(n)}(m, f)$, show directly how the energy is distributed.

By assuming that the temporal variations occur over times long compared with the time for disturbances to pass the probe (George *et al.* 1989*b*)[1], the temporally varying signal can be interpreted as spatially varying using Taylor's hypothesis (George *et al.* 1984):

$$\frac{\partial}{\partial x} \approx \frac{1}{U_c}\frac{\partial}{\partial t} \tag{5.2}$$

or in a Fourier transformed form:

$$k \approx \frac{2\pi f}{U_c} \tag{5.3}$$

Thus, frequency measured here can be interpreted as wavelength ($\lambda = 2\pi/k$), and low frequency means long streamwise scales.

Figure 5.1 shows the distribution of the radial POD modes at the different downstream positions and three Reynolds numbers. These have been integrated over frequency, f, and summed over azimuthal mode number, m. The dominance of the first POD mode is very clear at all downstream positions and Reynolds numbers.

The percentages of each POD mode are presented in Table 5.1. For all the data the first POD mode is dominant and contains about 64.2 % to 68.7 % of the recovered POD turbulent kinetic energy, depending on downstream positions. The second POD mode contains about 17.3 % to 19.0 % of it. And the third POD mode has less than 10 % at all positions, while the rest of the first 3 POD modes are less than 10 % and negligible. Thus the first 3 POD modes represent more than 90 % of the turbulent kinetic energy of the flow. This agrees well with Citriniti & George (2000) and the earlier observation of Glauser & George (1987*b*). Clearly the POD is quite efficient. Therefore only the turbulent kinetic energy contained by the first POD mode will be considered in this chapter.

[1]Strictly speaking the turbulence intensity is not low enough to apply Taylor's hypothesis on the largest scales, so neither a temporal or spatial interpretation is exactly correct. But the spatial interpretation is the most correct at the turbulence intensities of the jet.

Re_D	x/D	percentage of the kinetic energy		
		$\lambda^{(1)}$	$\lambda^{(1)} + \lambda^{(2)}$	$\lambda^{(1)} + \lambda^{(2)} + \lambda^{(3)}$
78 400	2	66.79	84.91	94.78
	3	65.55	82.99	92.80
	4	68.73	86.04	93.86
	5	67.98	85.62	93.64
	6	65.72	83.38	92.25
117 600	2	66.13	85.21	95.15
	3	64.80	82.78	92.97
	4	64.30	82.09	91.90
	5	64.26	82.10	91.60
	6	65.32	83.03	92.07
156 800	2	66.18	85.18	95.25
	3	64.43	82.41	92.74
	4	63.79	81.68	91.60
	5	64.03	81.90	91.45
	6	65.08	82.90	91.95

Table 5.1: Percentage of the kinetic energy in the POD modes

5.3 Eigenvalue distribution

Figures 5.2 to 5.16 present the eigenspectra for the first POD mode (radial) as a function of frequency, f, and azimuthal mode number, m. Figures 5.2 to 5.6 show the lowest Reynolds number, 78 400; Figures 5.7 to 5.11, Reynolds number 117 600; and Figures 5.12 to 5.16, Reynolds number 156 800. It will be clear in later sections that the effect of Reynolds number is slight.

It is difficult to tell much from these three-dimensional projections; therefore simpler plots summed over mode number and/or frequency will be considered in the following sections. However, several observations can be made:

1. At $x/D = 2.0$, mode-0 (which contains more than 60 % of total energy at $x/D = 2.0$) is spread over a band of frequencies which ranges from about 0 to 150 Hz.

2. This energy in mode-0 moves to lower frequencies as x/D increases, and the

total energy in mode-0 decreases.

3. At $x/D = 2$, the energy in the higher azimuthal modes peaks at about $m = 6$, and this energy is concentrated at low frequencies (large streamwise spectral wave length).

4. The energy in higher modes ($m > 0$) moves to lower modes as x/D increases.

5. Corresponding to the diminution of mode-0 is the emergence of mode-1. This energy in mode-1 is also concentrated at low frequencies (large streamwise spectral wavelengths).

5.4 Behavior of the eigenvalue as a function of m

In this section only the azimuthal mode number, m, dependence of the eigenvalues is examined. A convenient measure is the normalized eigenvalue, $\xi^{(n)}(m)$, defined as:

$$\xi^{(n)}(m) = \frac{\int_f \hat{\hat{\lambda}}^{(n)}(m, f)\, df}{\sum_n \sum_m \int_f \hat{\hat{\lambda}}^{(n)}(m, f)\, df} \tag{5.4}$$

Note that the denominator is summed over all POD modes, n, all azimuthal modes, m, and is integrated over all frequencies, f. Thus the denominator is the total turbulent kinetic energy in the flow. The numerator, on the other hand, is only integrated over frequency.

The azimuthal dependences of the normalized energy distribution of the first 3 POD modes are presented in Figures 5.17 to 5.25 for the various Reynolds numbers and downstream positions. Figures 5.17 to 5.19 are for Reynolds number 78 400; Figures 5.20 to 5.22 for Reynolds number 117 600; and Figures 5.23 to 5.25 for Reynolds number 156 800.

As shown in Figures 5.17 to 5.25, the distributions of the first 3 POD mode energy have a strong dependence on the downstream position, x/D. The 0th azimuthal-

mode, $\xi^{(1)}(0)$, behaves in a manner entirely different than the higher azimuthal modes, $\xi^{(1)}(m)$, $m > 0$. The 0-azimuthal mode for first POD mode, $\xi^{(1)}(0)$, in Figure 5.26, which dominated the dynamics at $x/D = 3.0$ in the Glauser (1987) and Citriniti (1996), dies off rapidly downstream for all Reynolds numbers. This is consistent with an approach toward homogeneity in the downstream evolution, and suggests that perhaps some residual value may control the growth rate of the far jet. If so, this could provide an important clue as to why and how equilibrium similarity governs the far jet, and also why the jet growth rate may reflect the upstream conditions. The second and third POD modes (for 0-azimuthal mode, Figure 5.26) contain a very small portion of the kinetic energy, but behave in a similar manner.

For the higher azimuthal modes ($m > 0$), the peaks shift to lower mode numbers, and their amplitudes actually increase with downstream distance. These also show Reynolds number independence. And this trend happens for the second POD mode, $\xi^{(2)}(m)$, and the third POD mode, $\xi^{(3)}(m)$, as well.

This behavior of the azimuthal modes for $m \geq 1$ ($m > 0$) is consistent with the observations of George *et al.* (1984), and Khwaja (1981). They noted that the statistical properties of the axisymmetric jet shear layer appeared to scale in shear layer similar variables x and U_E, even though the equations did not admit to such solutions. Figures 5.27 to 5.29 show the eigenvalues for the first three POD modes for $m > 0$ and Reynolds numbers for all positions, but normalized in shear layer variables $\xi^{(n)}/(x/D)$ and $m \cdot x/D$. Clearly the first POD mode ($n = 1$) collapses well for all downstream positions with this normalization. The second POD mode also shows reasonable collapse. But the third POD mode, which has much lower level of the kinetic energy than the other mode, shows more deviation than the lower POD modes. This may be due to the increased numerical errors in the higher POD modes due to the limited spatial resolution. The collapse for the first and second POD mode occurs at the higher Reynolds numbers as well.

Figures 5.30 and 5.31 show the same data for the first two POD modes and

$m > 0$ with all Reynolds numbers plotted together. Clearly the first POD mode collapses for all three Reynolds numbers. This is in contrast to the suggestion by Holmes *et al.* (1996) who expected that more complicated modal structures might evolve with increasing Reynolds number. This collapse confirms the Reynolds number independence of the large scale structures as presumed by Glauser (1987) and Citriniti & George (2000). Similar independence of Reynolds numbers can also be seen in the second POD mode.

5.5 Dependence of the eigenspectra on frequency

Eigenspectra of the first POD mode, $\lambda^{(1)}(m, f)$, are summed over the azimuthal mode number, and displayed with the downstream position and Reynolds number in Figures 5.32 to 5.34. Since only the first POD mode is used, the level of energy is lower than these of Figures 4.16 to 4.24.

For all three Reynolds numbers, the largest portion of the turbulent kinetic energy is concentrated in the lower frequency range, $f < 200$. This again confirms that the long hot wire probe works well to catch the energy from the large size structures.

In Figures 5.35 to 5.49, the eigenspectra are displayed again to analyze the energy distribution of the azimuthal mode as a function of frequency. It is clearly seen that the 0th azimuthal mode is dominant over all frequency ranges until $x/D = 4.0$. The overwhelming of the 0th azimuthal mode by the higher modes with increasing downstream position is also clearly shown. As the 0-azimuthal mode dies off, the higher azimuthal mode ($m > 0$) starts to grow. By $x/D = 6$, only the lowest azimuthal modes dominate. This energy shift occurs mainly in the lower frequency range of $0 < f < 200$. Concurrent with this energy shift is the increase in azimuthal mode-1. Also the frequency of the peak also moves to lower frequencies than that of the 0th azimuthal mode.

The local peak from the eigenspectra can be compared to the local peak of the

velocity spectra taken from Figures 4.14 to 4.22. The Strouhal numbers, $St_D = fD/U_{exit}$, based on the frequency of the local peak, f, the jet exit diameter, D, and the exit velocity, are plotted as a function of downstream position in Figure 5.50. All are within the range of 0.24 to 0.64 as reported by Gutmark & Ho (1983).

Generally the Strouhal numbers decrease with increasing downstream positions for the lower Reynolds numbers. But Ho & Hsaio (1982) reported that it is almost constant and independent of downstream position at the highest Reynolds number. This does not appear to be the case here, however since both the Strouhal numbers from the azimuthal mode-0 and from the velocity spectra collapse well over whole range of downstream positions, independent of Reynolds number.

5.6 The eigenfunctions

The eigenfunctions, $\hat{\hat{\Phi}}_i(r, m, f)$, can be recovered using Equation 2.28 as:

$$\hat{\hat{\Phi}}_i(r, m, f) = \hat{\hat{\phi}}_i(r, m, f)\, r^{-\frac{1}{2}} \tag{5.5}$$

Those reported below are non-dimensionalized with the jet exit diameter,D, and then normalized by its magnitude (computed from the real and imaginary parts).

The eigenfunctions chosen for plotting were the 0th azimuthal mode, and the azimuthal mode which is the most dominant mode for $m > 0$. The frequency is chosen to be the peak of spectrum corresponding to its downstream positions. This is the same frequency used for the Strouhal number in the previous section. As shown in Figure 5.1, the first eigenvalue contains the largest portion of the kinetic energy, therefore only the first eigenfunction is considered here.

In Figures 5.51 and 5.52, the real and imaginary parts of the non-dimensional, normalized eigenfunctions, $D\,\hat{\hat{\Phi}}_i(r, m, f)$, are shown for the different downstream positions and Reynolds numbers. As noted above, the eigenfunctions are plotted only at the azimuthal mode-0 and at the frequency of the peak.

Figures 5.53 and 5.54 show similar eigenfunctions taken from the most dominant modes in Figures 5.17, 5.20, and 5.23; mode-6 at $x/D = 2.0$, mode-5 at $x/D = 3.0$, mode-4 at $x/D = 4.0$, mode-3 at $x/D = 5.0$, and mode-2 at $x/D = 6.0$. The frequencies are the same values as in Figures 5.51 and 5.52. There is a clear trend with the downstream distance. The peak of the eigenfunction decreases as x/D increases, and moves toward into the axis, consistent with the evolution of the mean profile and the filling in of the turbulence intensity at the centerline. They also reasonably collapse for Reynolds numbers at all x/D. The same trends are observed for the imaginary part as well, except $x/D = 6.0$. It should be noted, however, that the imaginary part appears to get smaller (relative to the real part) with increasing downstream distance, suggesting it may ultimately disappear altogether.

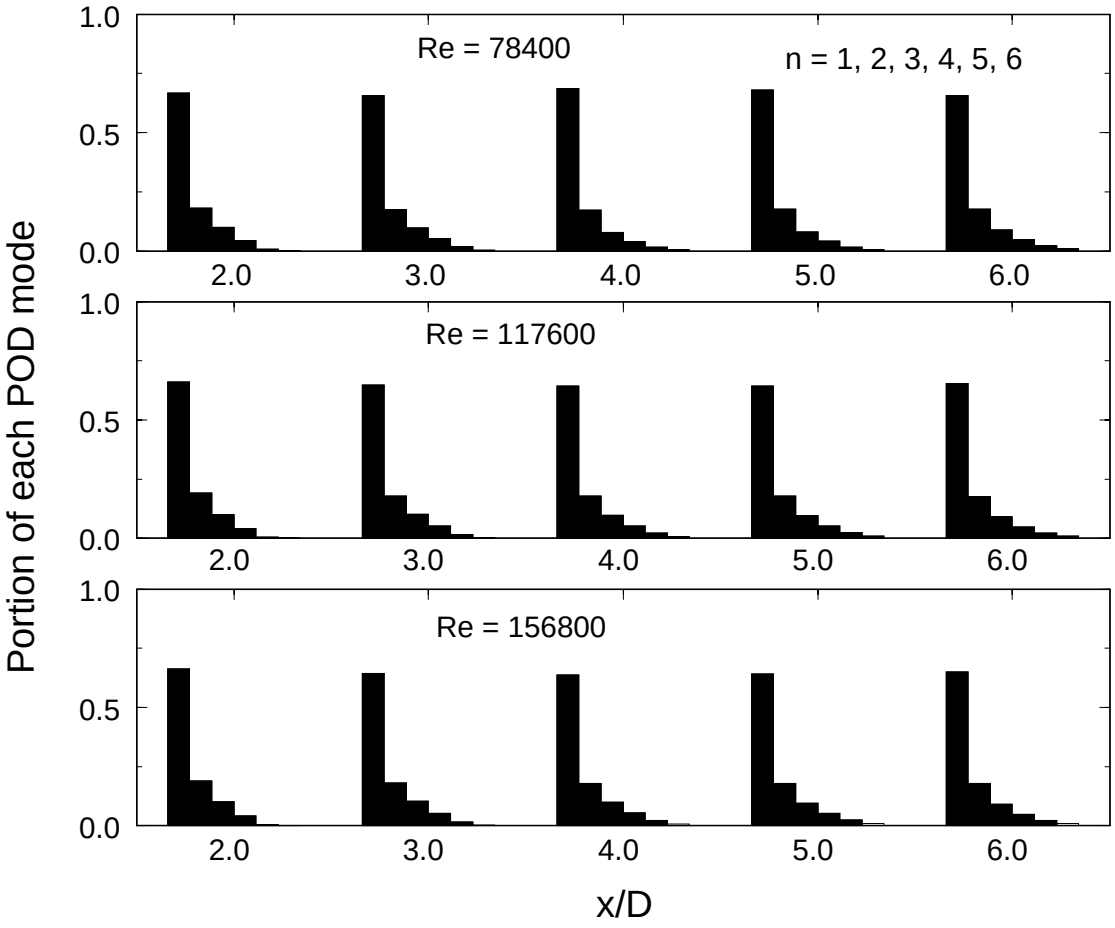

Figure 5.1: Eigenvalue distribution of the POD modes integrated over frequency, f, and summed over azimuthal mode number, m. The Reynolds numbers are: 78400 (top most), 117600 (middle), and 156800 (bottom most).

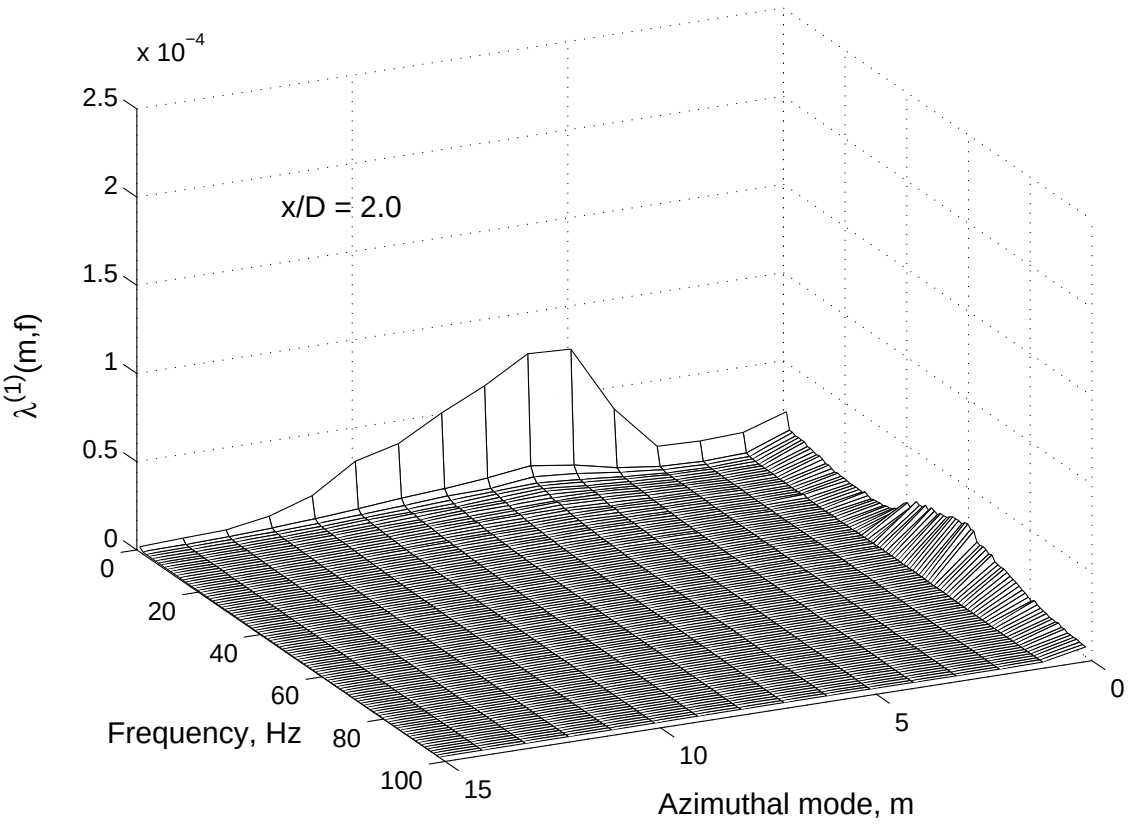

Figure 5.2: The first POD-mode energy, $\lambda^{(1)}(m, f)$, distribution with azimuthal mode number, m, and frequency, f, at $x/D = 2.0$ for $Re_D = 78\,400$.

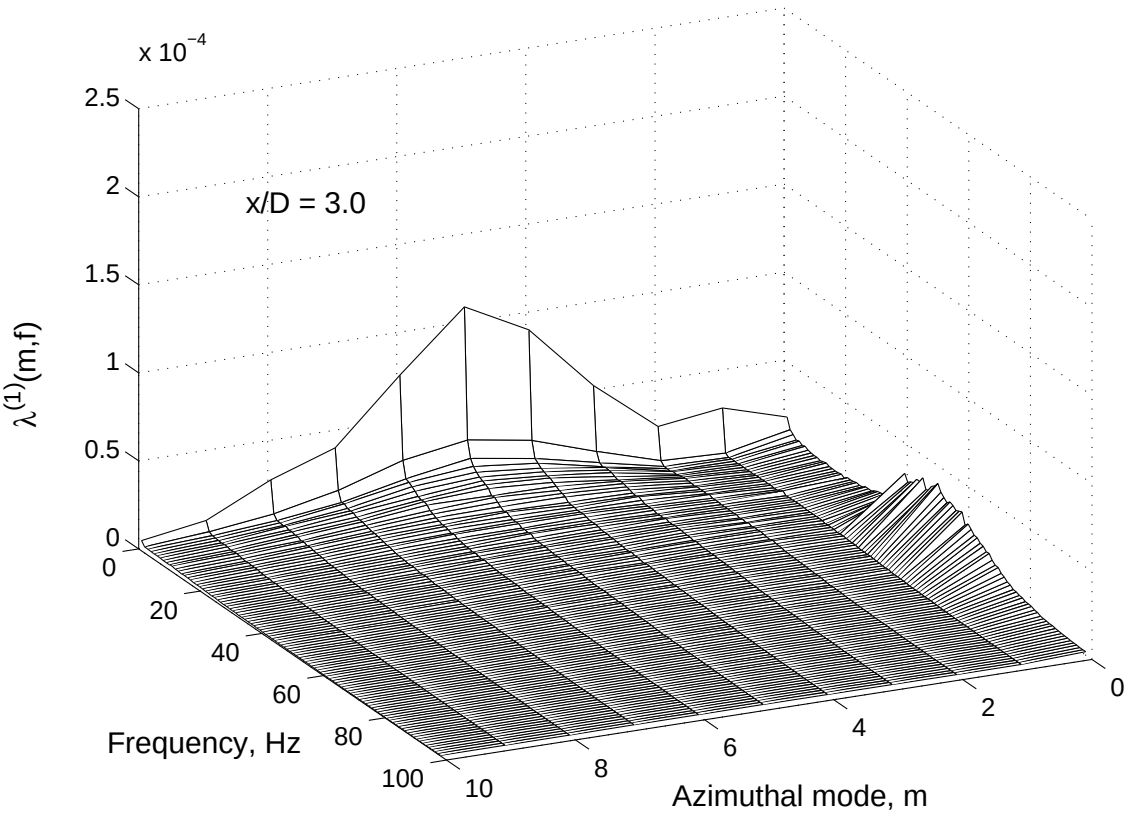

Figure 5.3: The first POD-mode energy, $\lambda^{(1)}(m, f)$, distribution with azimuthal mode number, m, and frequency, f, at $x/D = 3.0$ for $Re_D = 78\,400$.

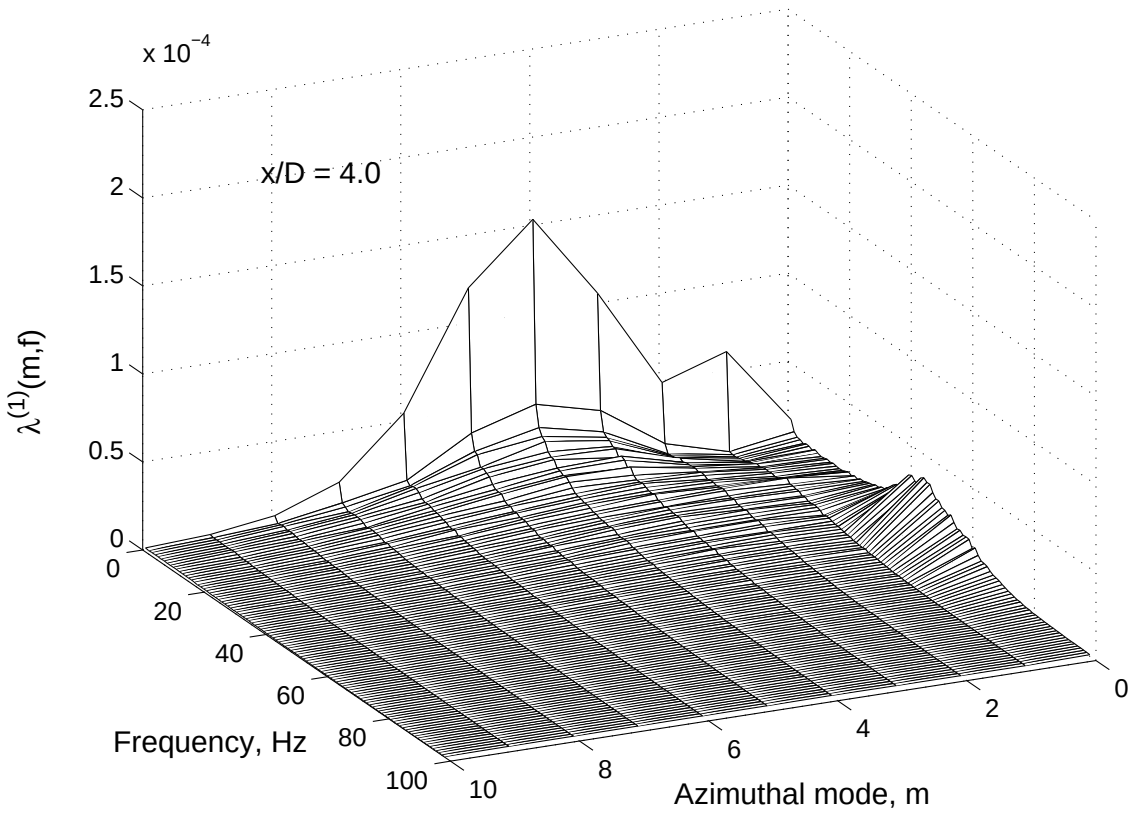

Figure 5.4: The first POD-mode energy, $\lambda^{(1)}(m, f)$, distribution with azimuthal mode number, m, and frequency, f, at $x/D = 4.0$ for $Re_D = 78\,400$.

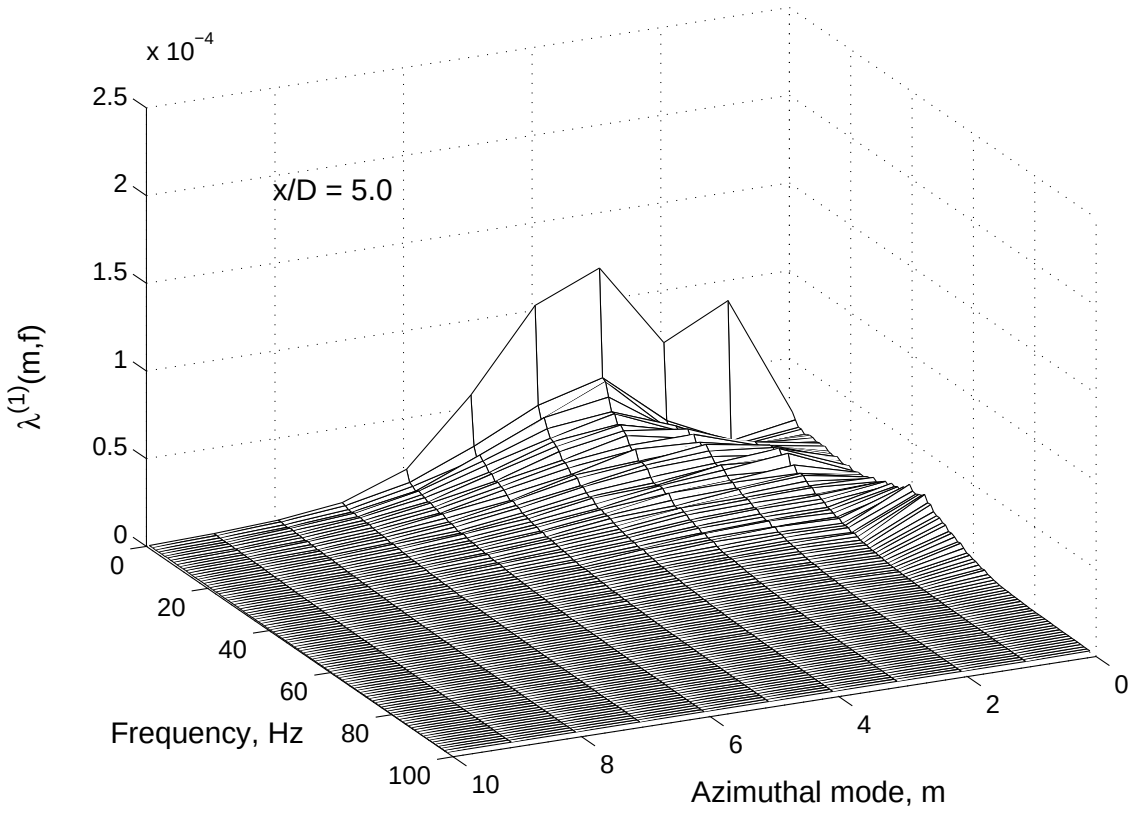

Figure 5.5: The first POD-mode energy, $\lambda^{(1)}(m, f)$, distribution with azimuthal mode number, m, and frequency, f, at $x/D = 5.0$ for $Re_D = 78\,400$.

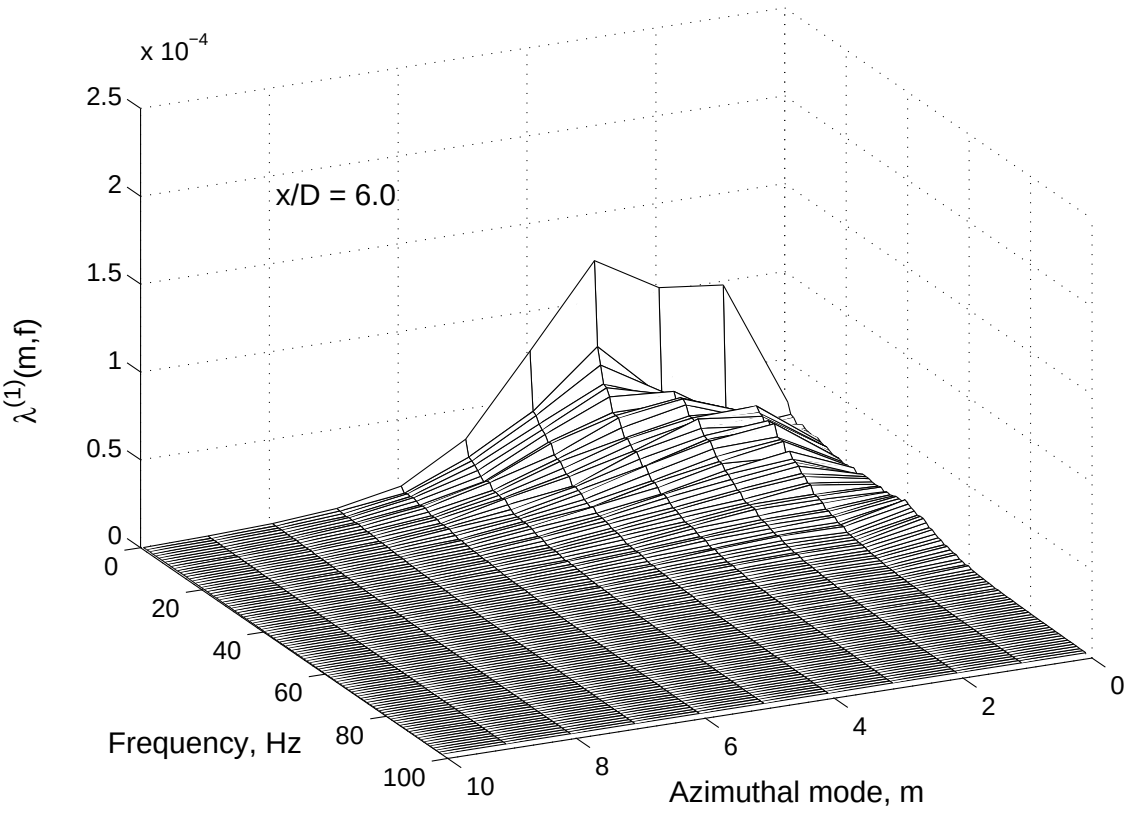

Figure 5.6: The first POD-mode energy, $\lambda^{(1)}(m, f)$, distribution with azimuthal mode number, m, and frequency, f, at $x/D = 6.0$ for $Re_D = 78\,400$.

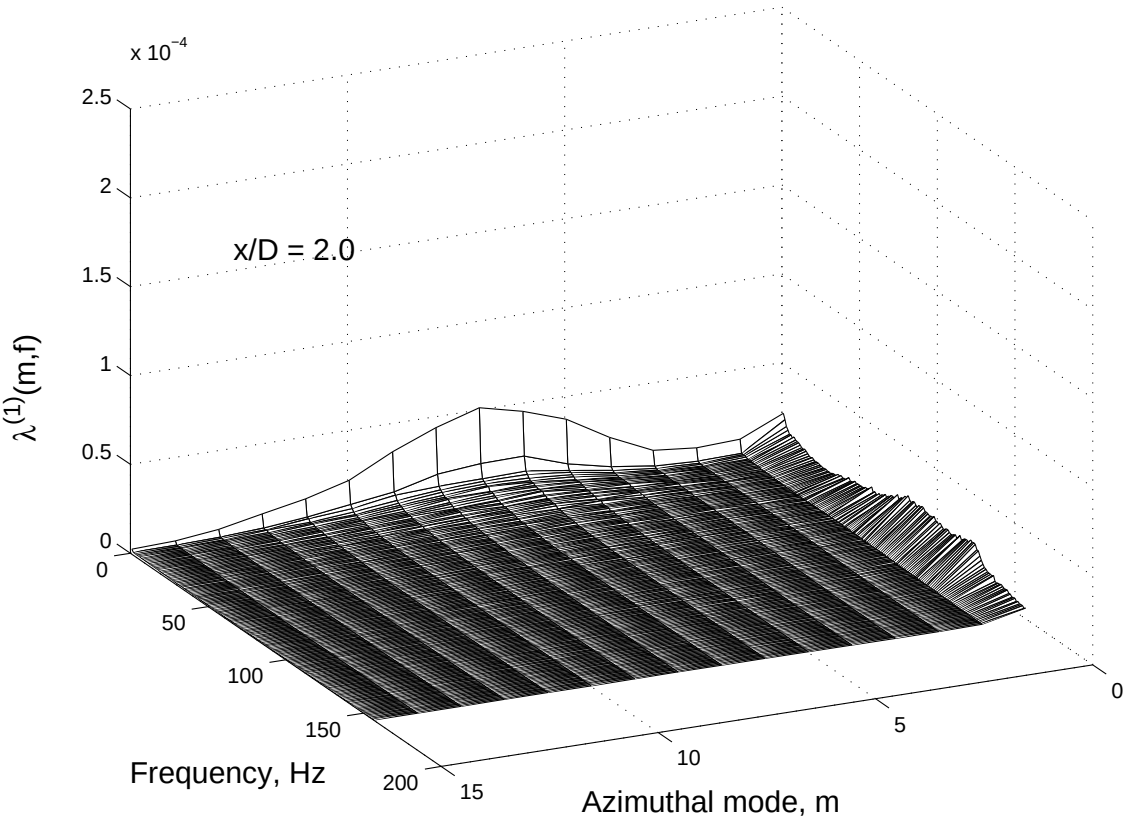

Figure 5.7: The first POD-mode energy, $\lambda^{(1)}(m, f)$, distribution with azimuthal mode number, m, and frequency, f, at $x/D = 2.0$ for $Re_D = 117\,600$.

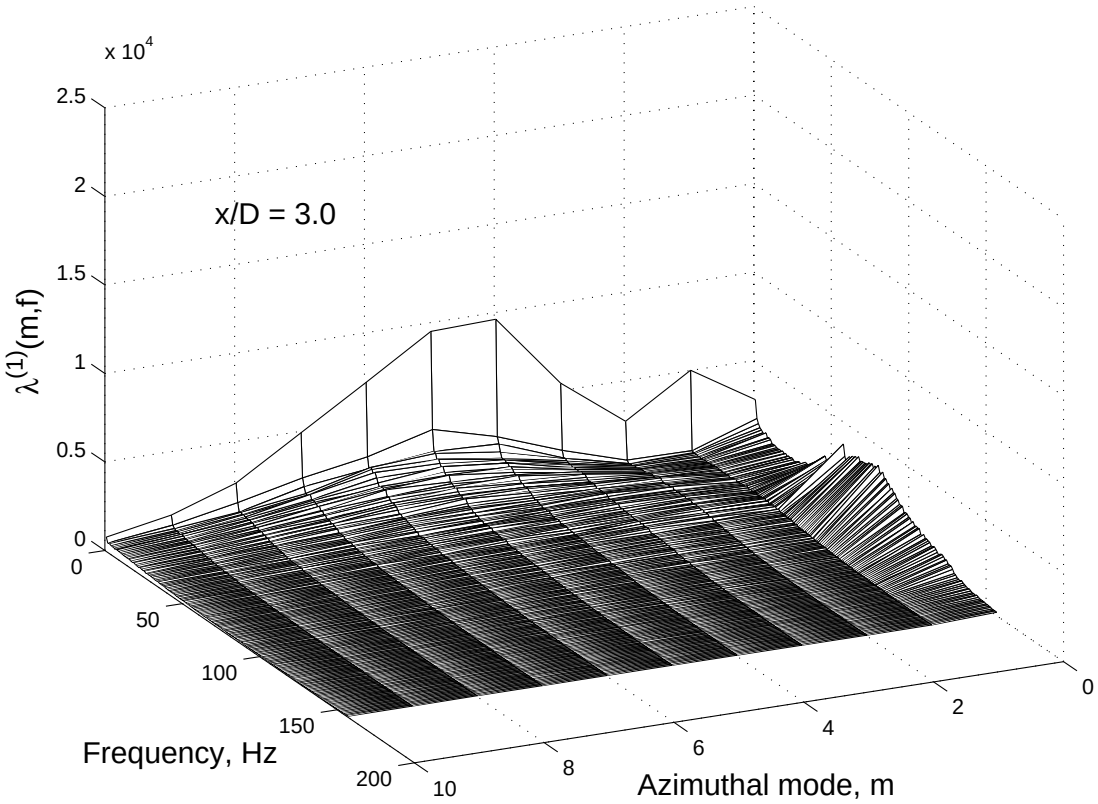

Figure 5.8: The first POD-mode energy, $\lambda^{(1)}(m, f)$, distribution with azimuthal mode number, m, and frequency, f, at $x/D = 3.0$ for $Re_D = 117\,600$.

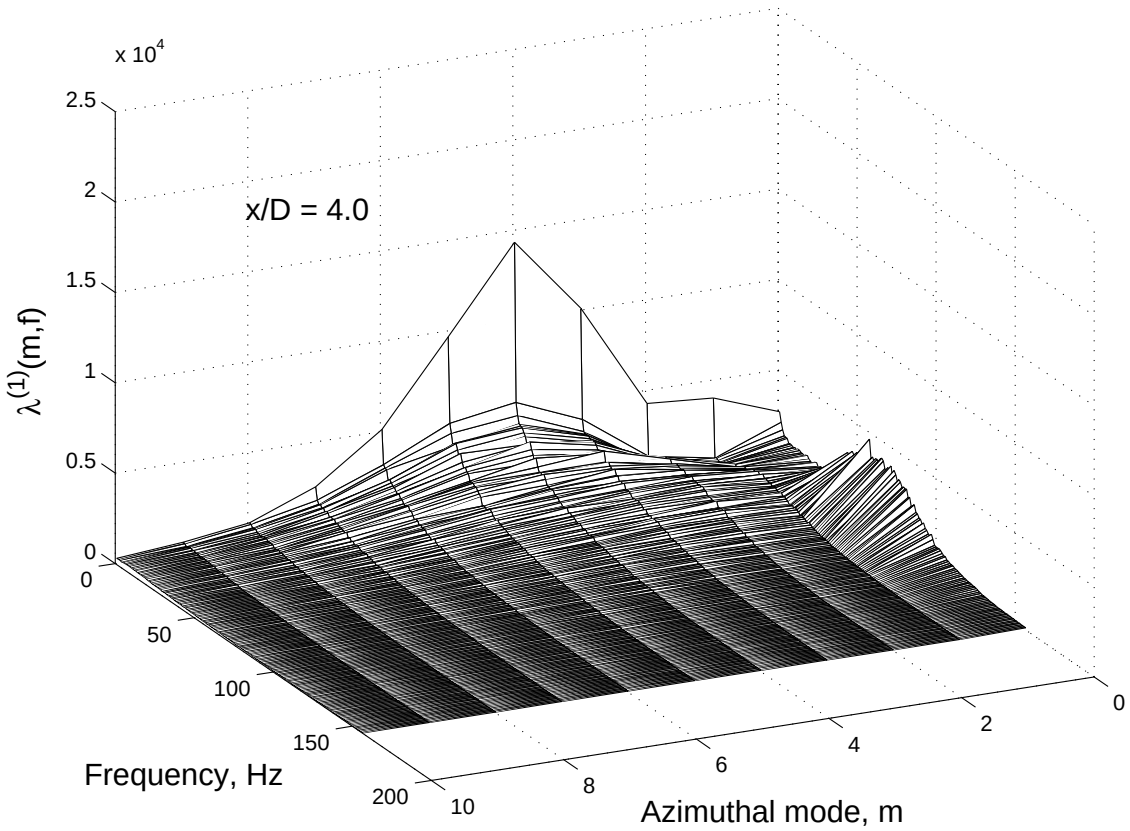

Figure 5.9: The first POD-mode energy, $\lambda^{(1)}(m, f)$, distribution with azimuthal mode number, m, and frequency, f, at $x/D = 4.0$ for $Re_D = 117\,600$.

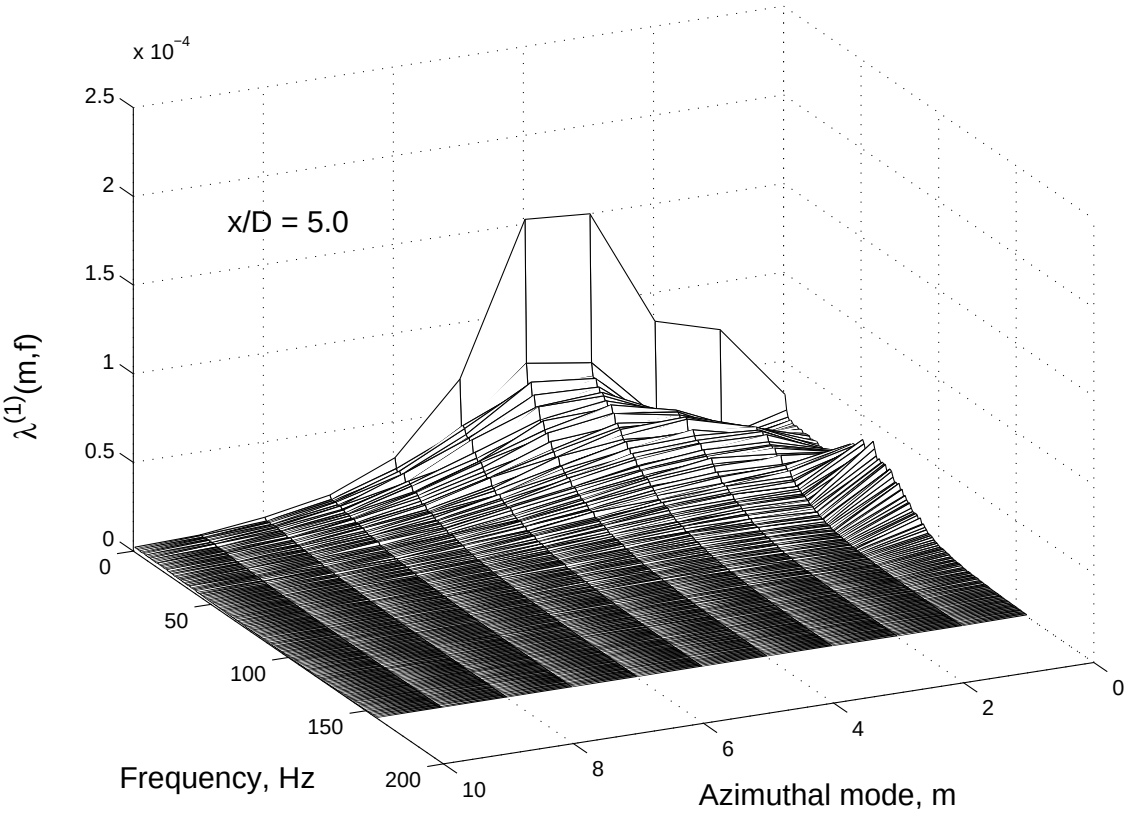

Figure 5.10: The first POD-mode energy, $\lambda^{(1)}(m, f)$, distribution with azimuthal mode number, m, and frequency, f, at $x/D = 5.0$ for $Re_D = 117\,600$.

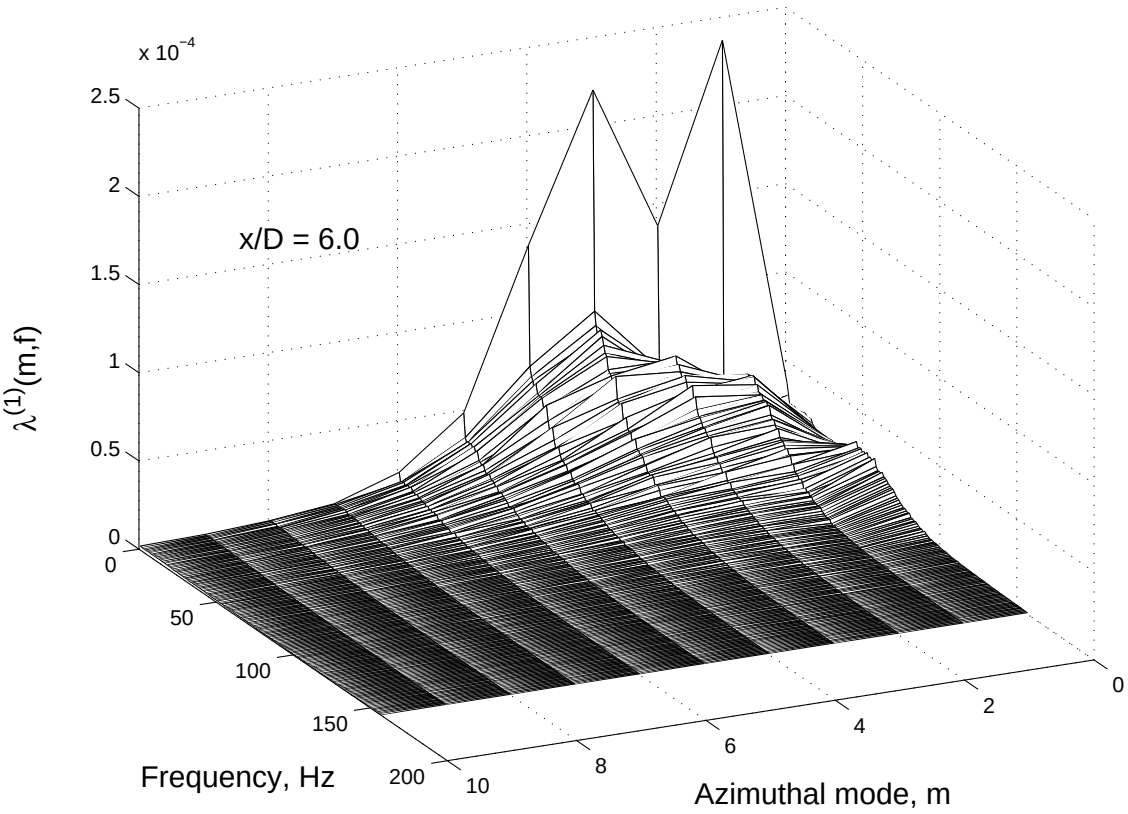

Figure 5.11: The first POD-mode energy, $\lambda^{(1)}(m, f)$, distribution with azimuthal mode number, m, and frequency, f, at $x/D = 6.0$ for $Re_D = 117\,600$.

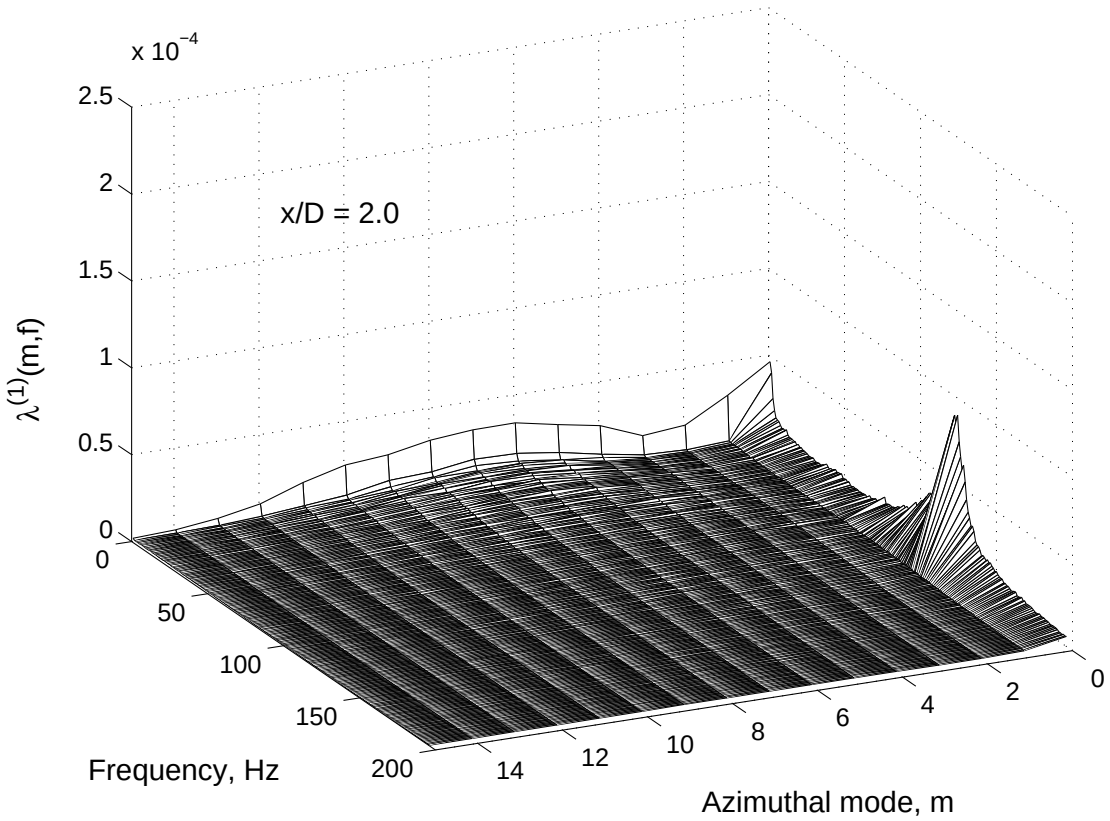

Figure 5.12: The first POD-mode energy, $\lambda^{(1)}(m, f)$, distribution with azimuthal mode number, m, and frequency, f, at $x/D = 2.0$ for $Re_D = 156\,800$.

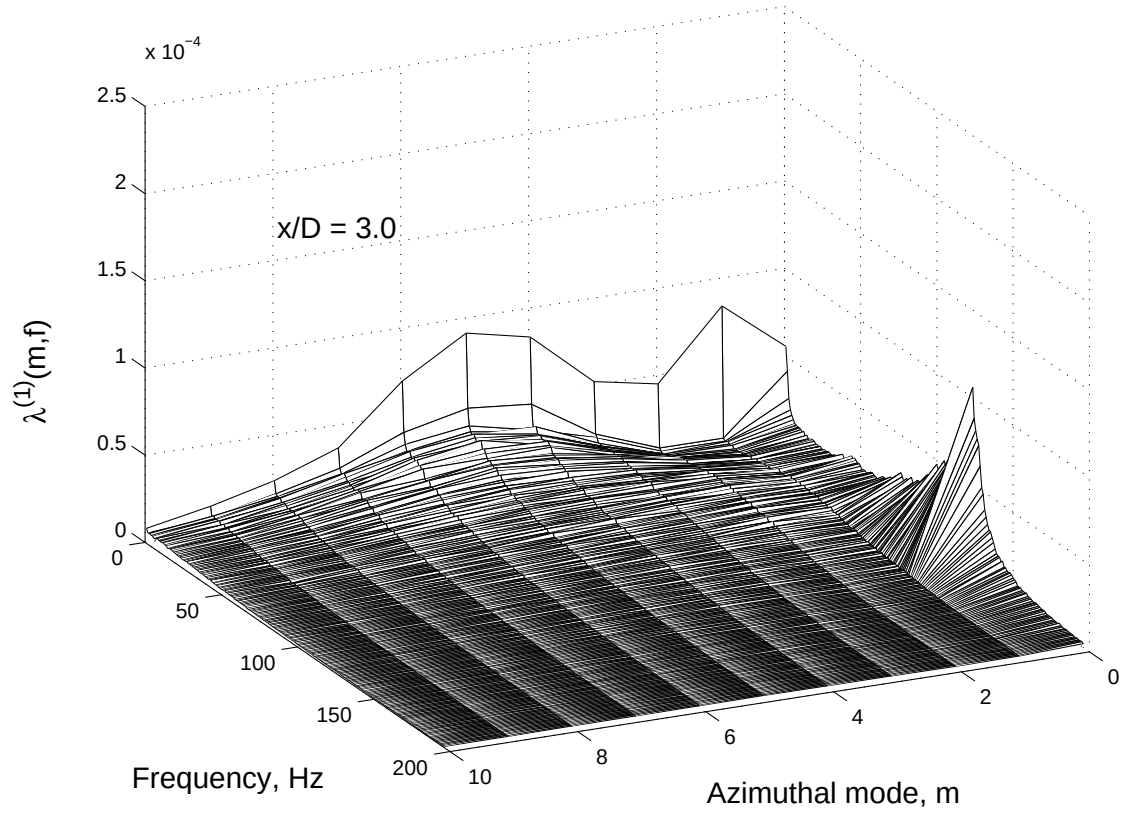

Figure 5.13: The first POD-mode energy, $\lambda^{(1)}(m, f)$, distribution with azimuthal mode number, m, and frequency, f, at $x/D = 3.0$ for $Re_D = 156\,800$.

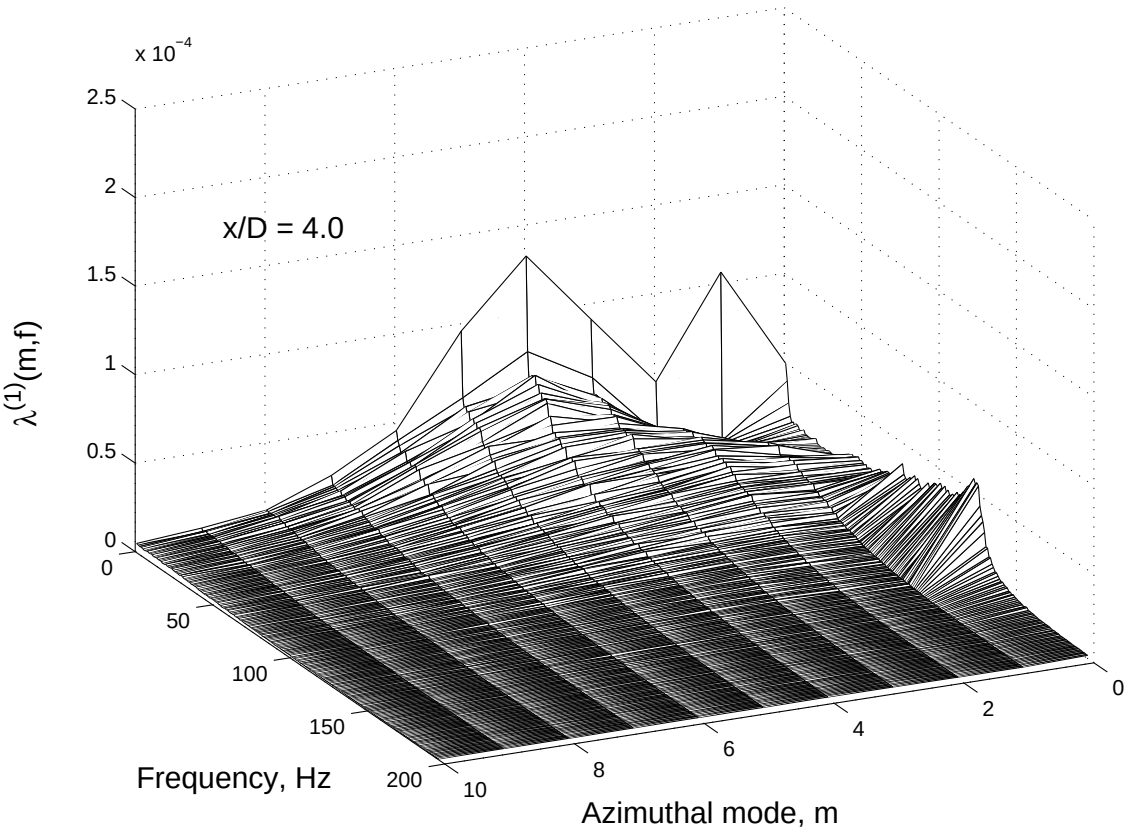

Figure 5.14: The first POD-mode energy, $\lambda^{(1)}(m, f)$, distribution with azimuthal mode number, m, and frequency, f, at $x/D = 4.0$ for $Re_D = 156\,800$.

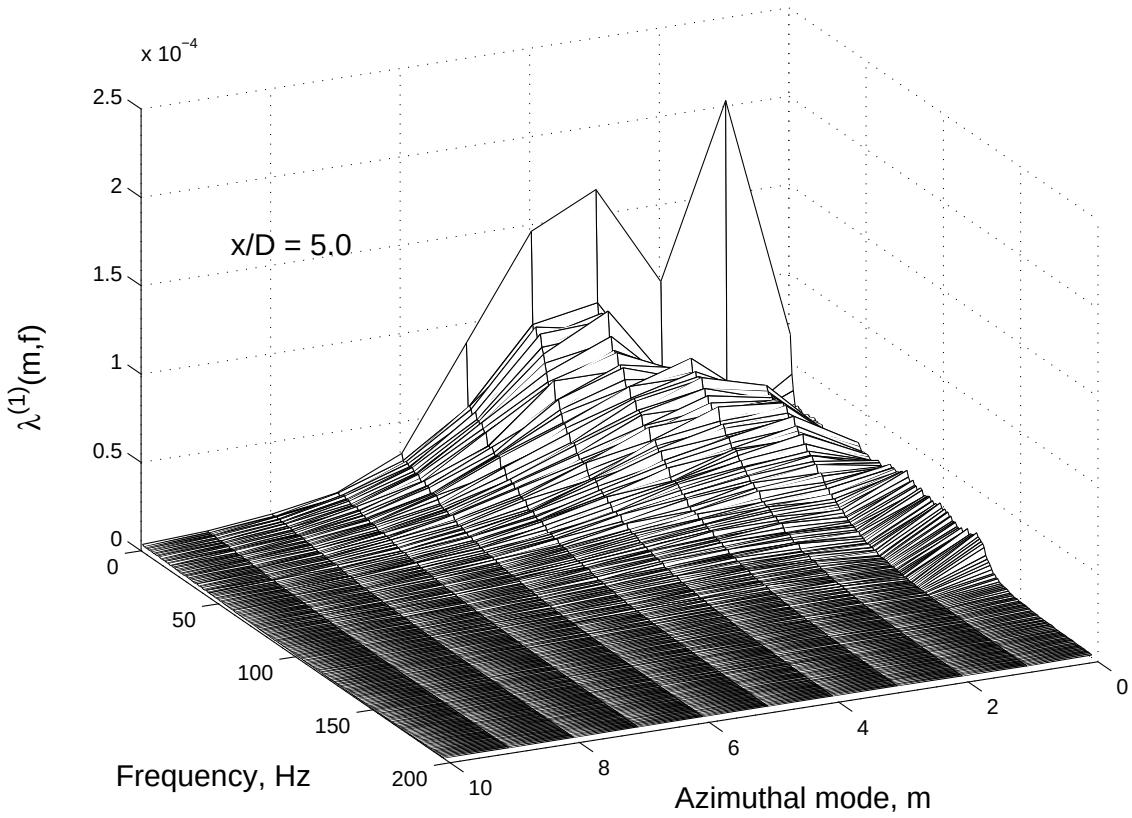

Figure 5.15: The first POD-mode energy, $\lambda^{(1)}(m, f)$, distribution with azimuthal mode number, m, and frequency, f, at $x/D = 5.0$ for $Re_D = 156\,800$.

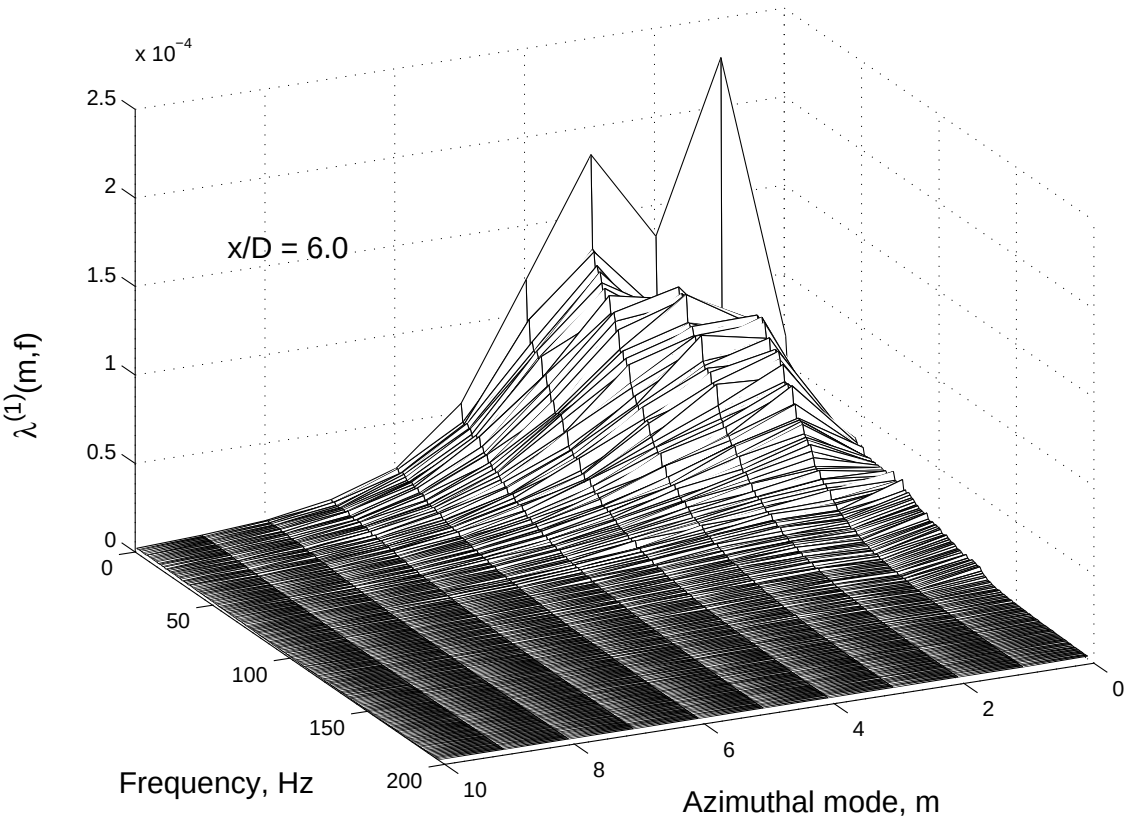

Figure 5.16: The first POD-mode energy, $\lambda^{(1)}(m, f)$, distribution with azimuthal mode number, m, and frequency, f, at $x/D = 6.0$ for $Re_D = 156\,800$.

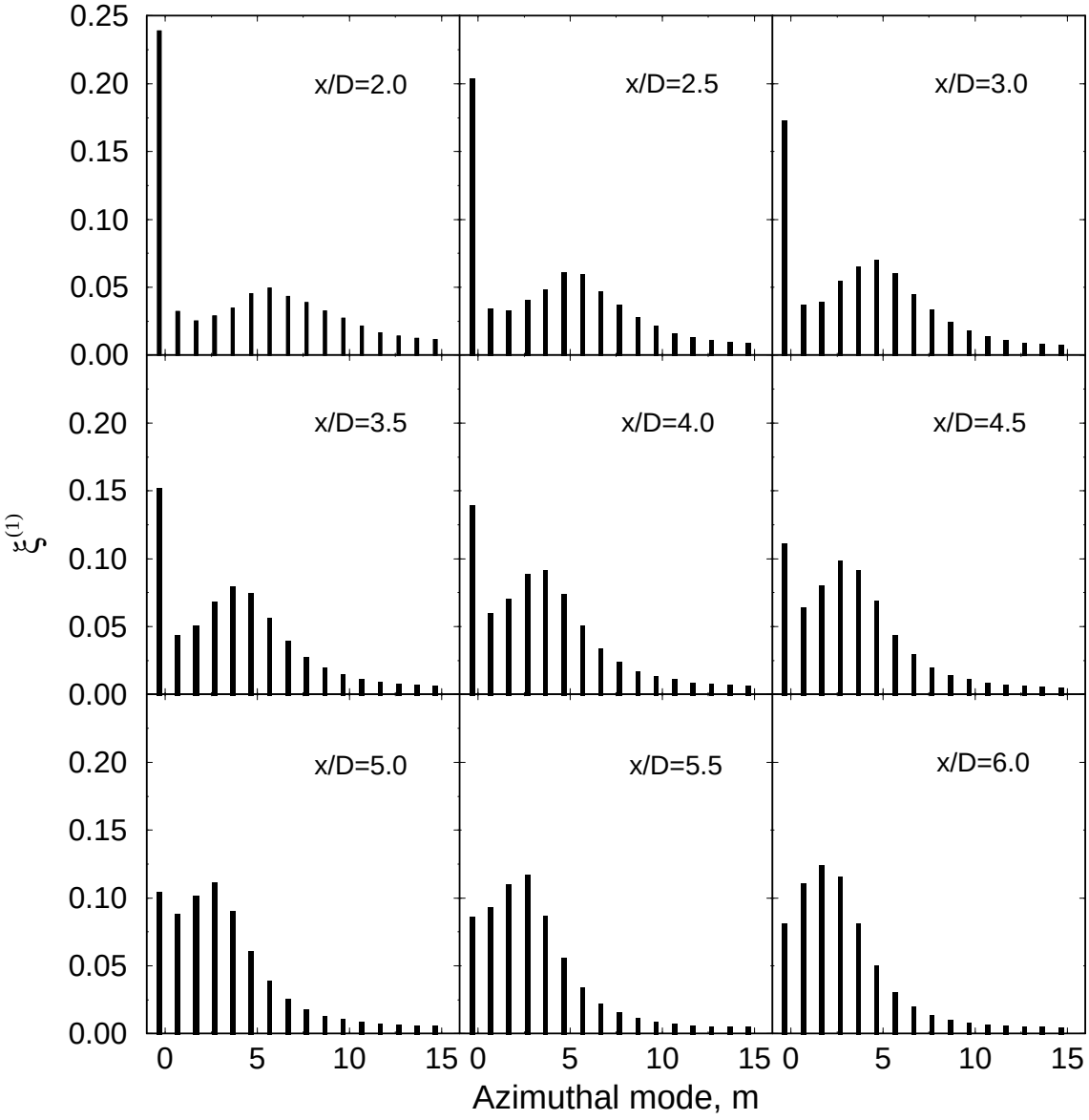

Figure 5.17: Normalized first POD-mode energy, $\xi^{(1)}(m)$, distribution along azimuthal mode number, m, at $Re_D = 78\,400$.

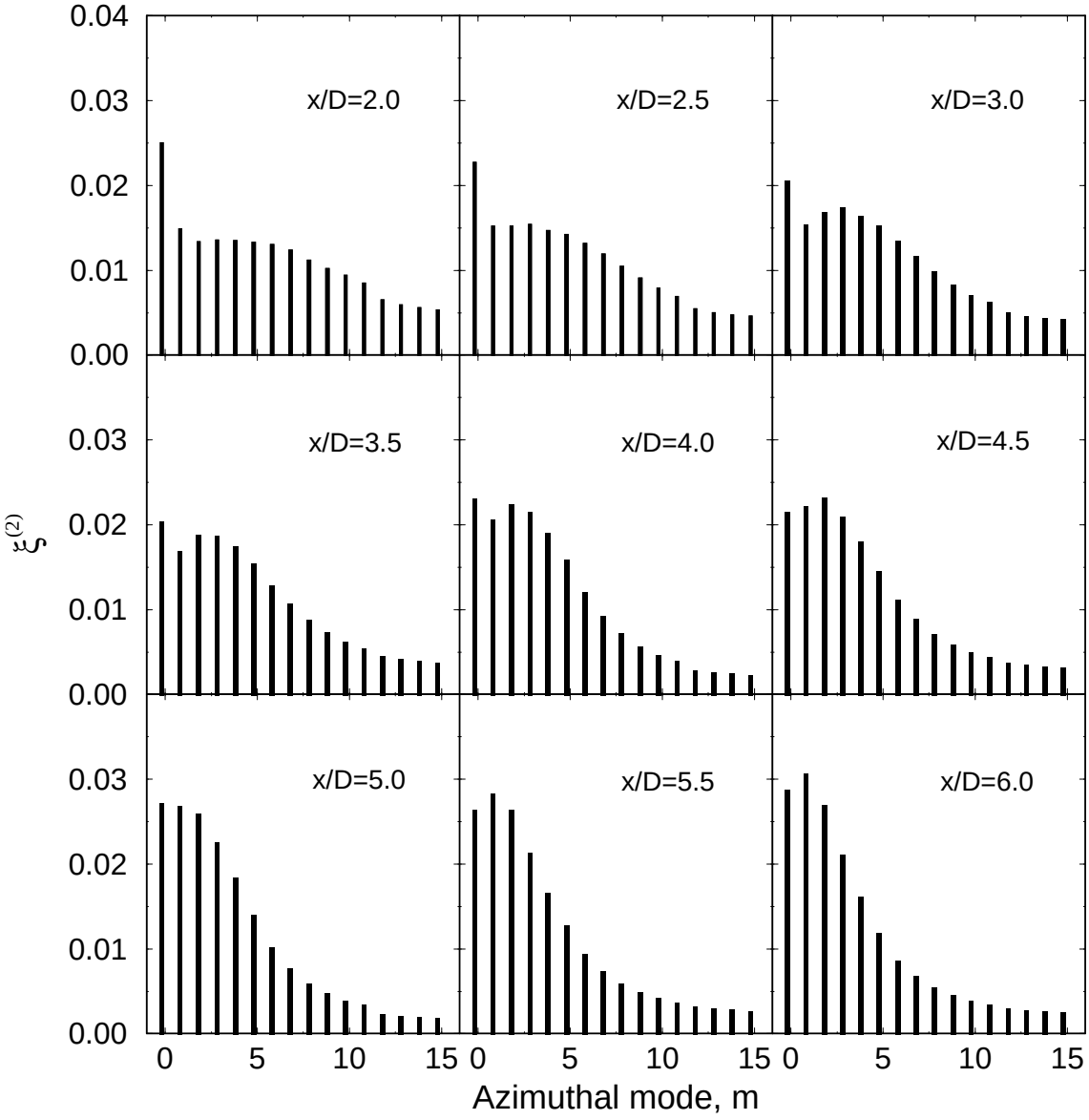

Figure 5.18: Normalized second POD-mode energy, $\xi^{(2)}(m)$, distribution along azimuthal mode number, m, at $Re_D = 78\,400$.

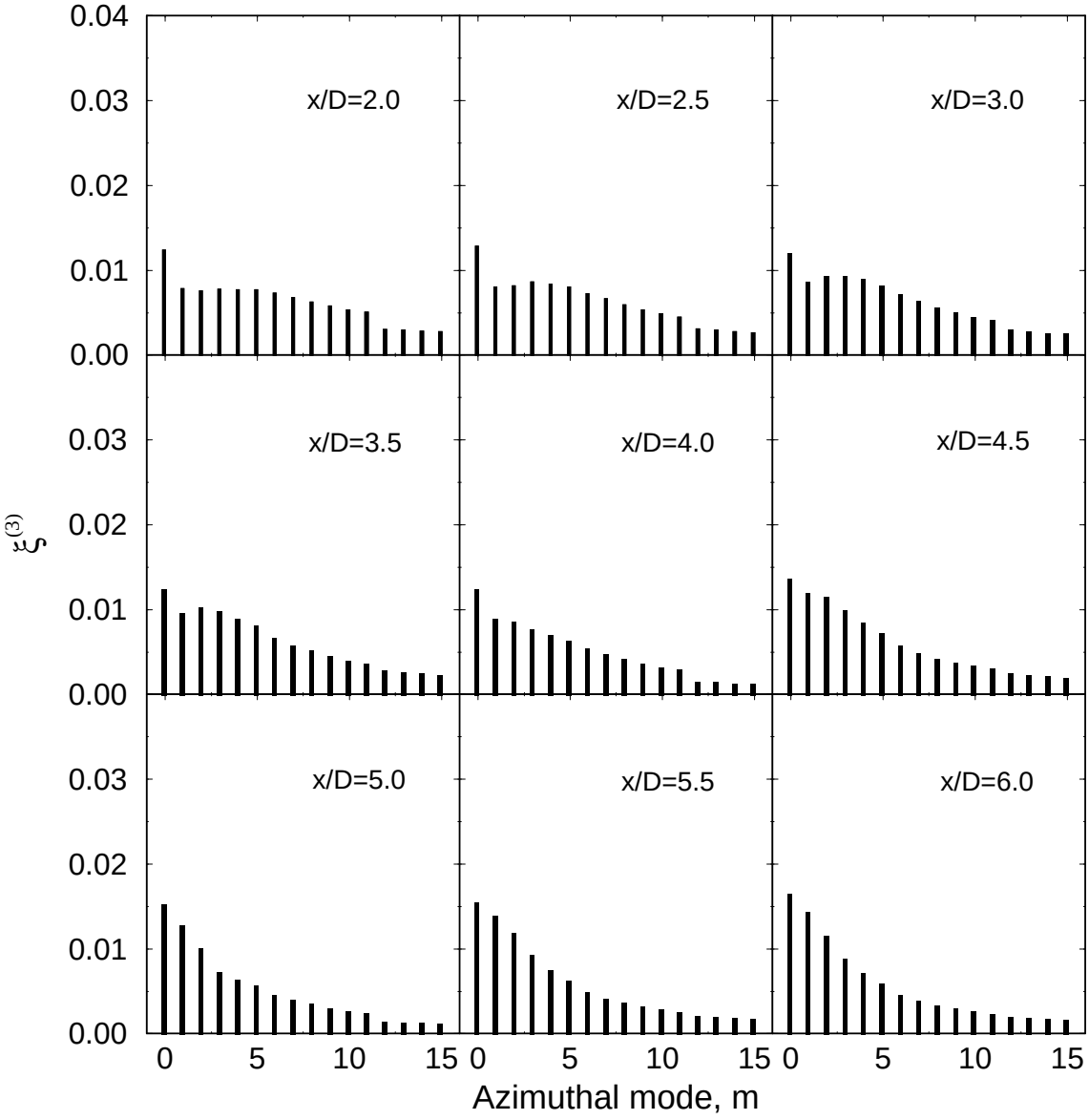

Figure 5.19: Normalized third POD-mode energy, $\xi^{(3)}(m)$, distribution along azimuthal mode number, m, at $Re_D = 78\,400$.

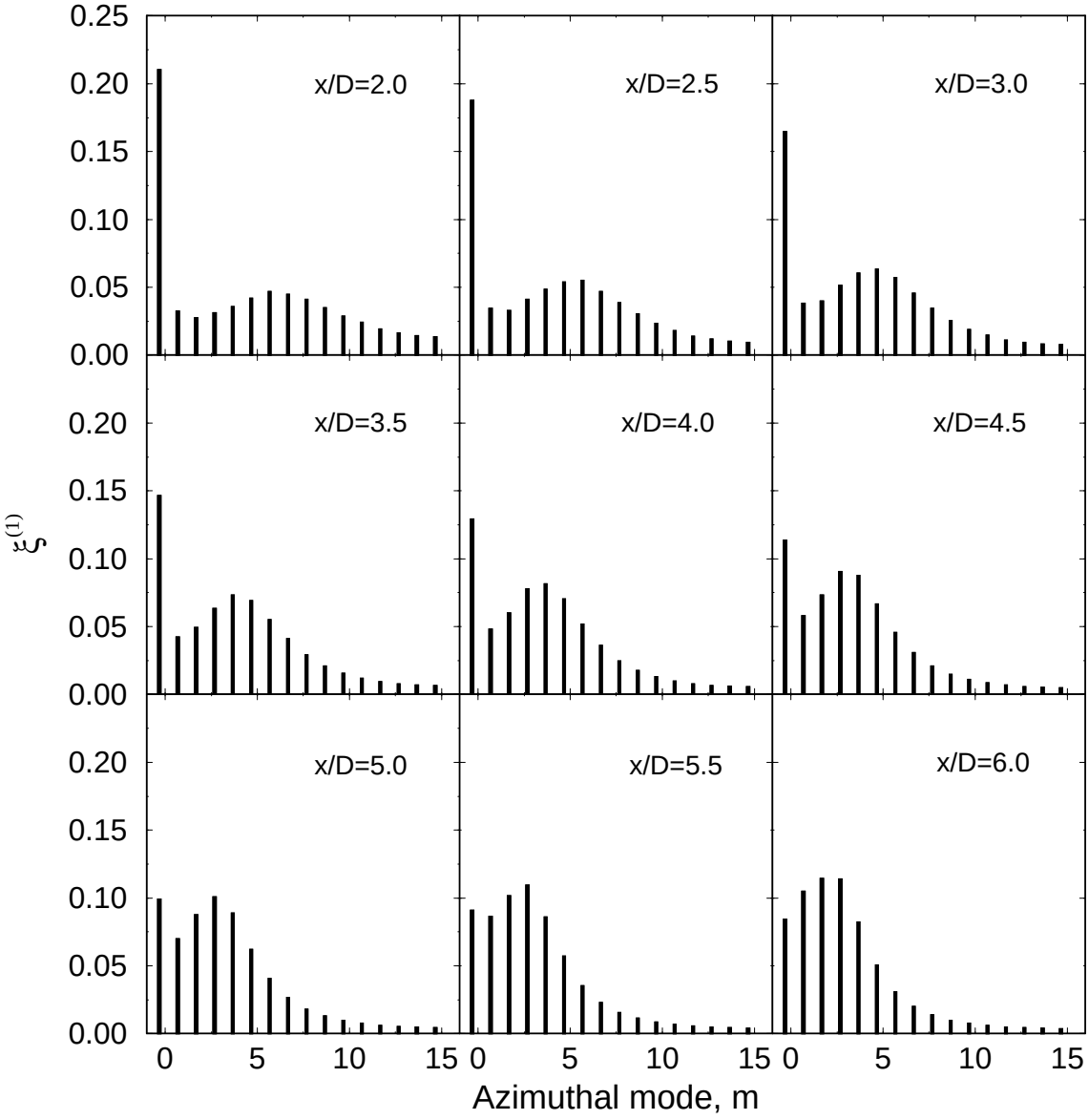

Figure 5.20: Normalized first POD-mode energy, $\xi^{(1)}(m)$, distribution along azimuthal mode number, m, at $Re_D = 117\,600$.

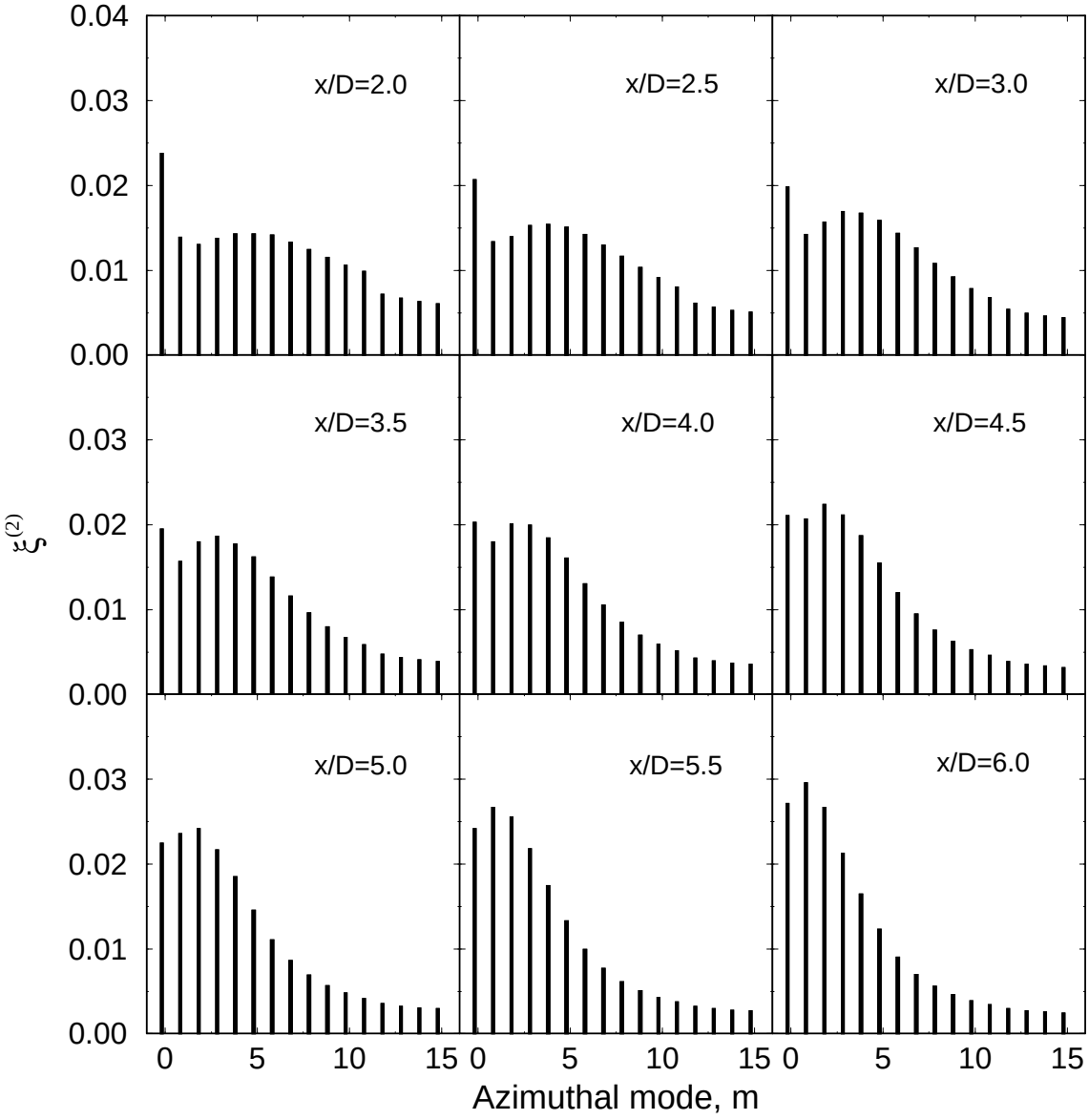

Figure 5.21: Normalized second POD-mode energy, $\xi^{(2)}(m)$, distribution along azimuthal mode number, m, at $Re_D = 117\,600$.

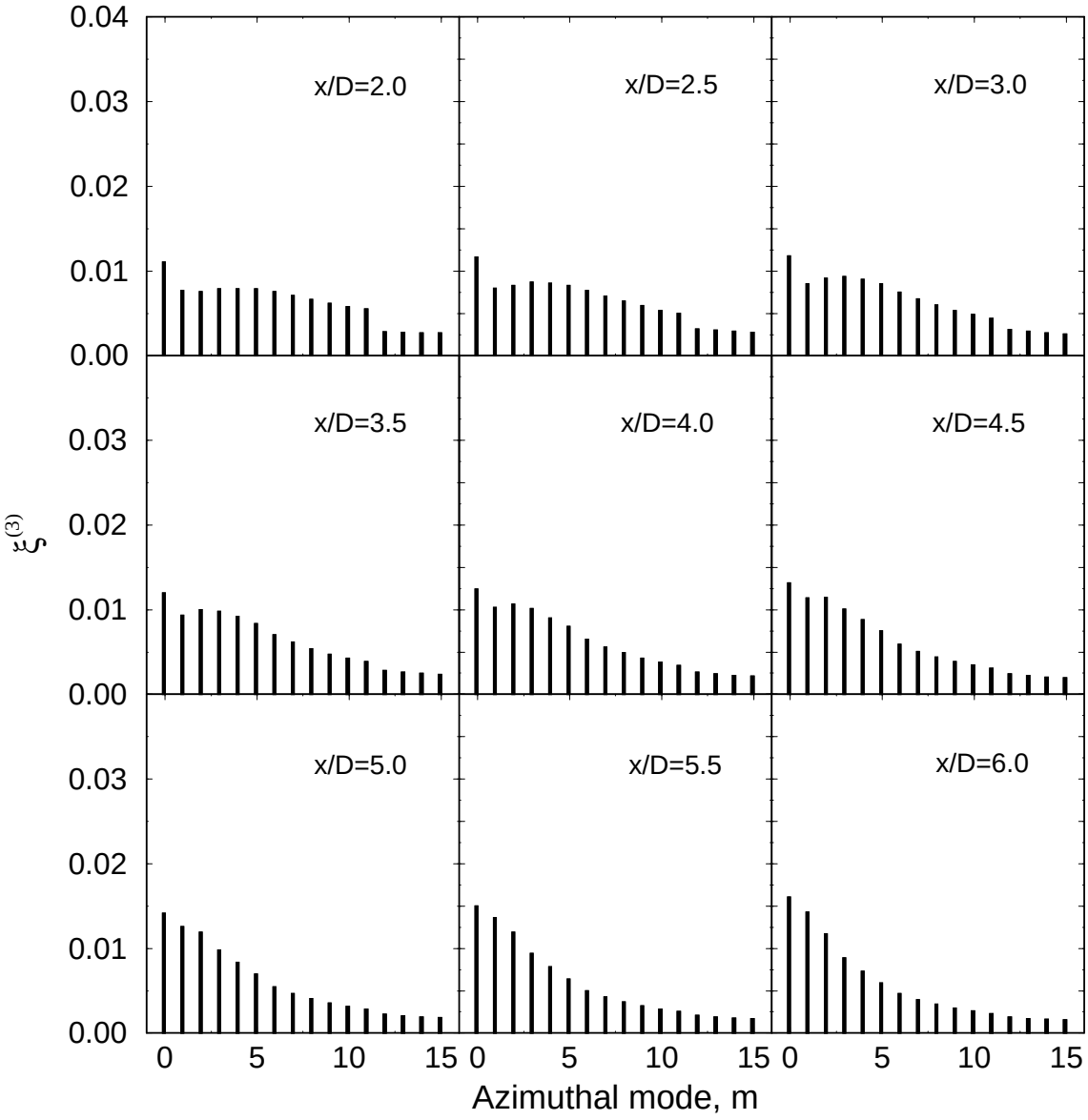

Figure 5.22: Normalized third POD-mode energy, $\xi^{(3)}(m)$, distribution along azimuthal mode number, m, at $Re_D = 117\,600$.

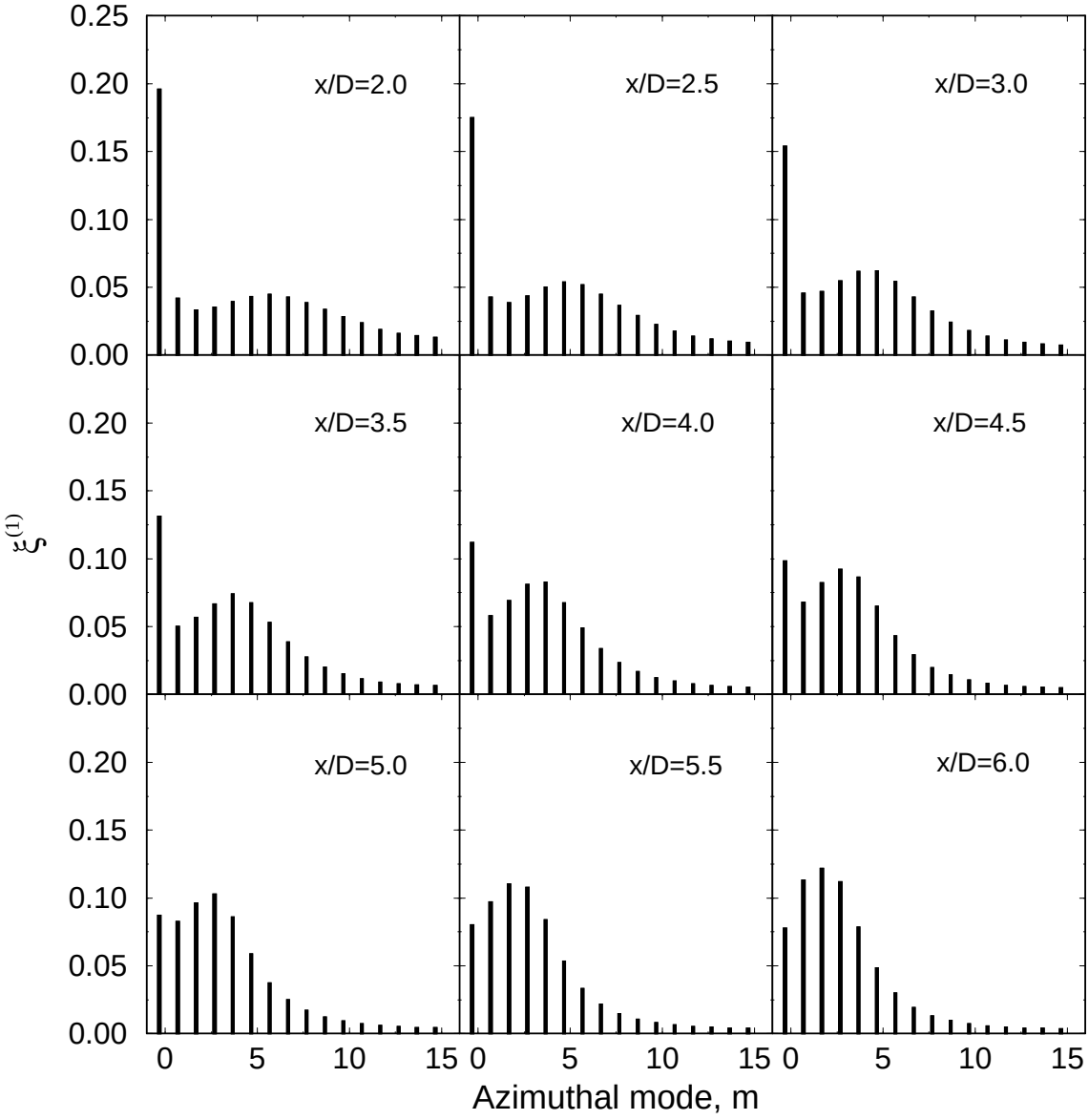

Figure 5.23: Normalized first POD-mode energy, $\xi^{(1)}(m)$, distribution along azimuthal mode number, m, at $Re_D = 156\,800$.

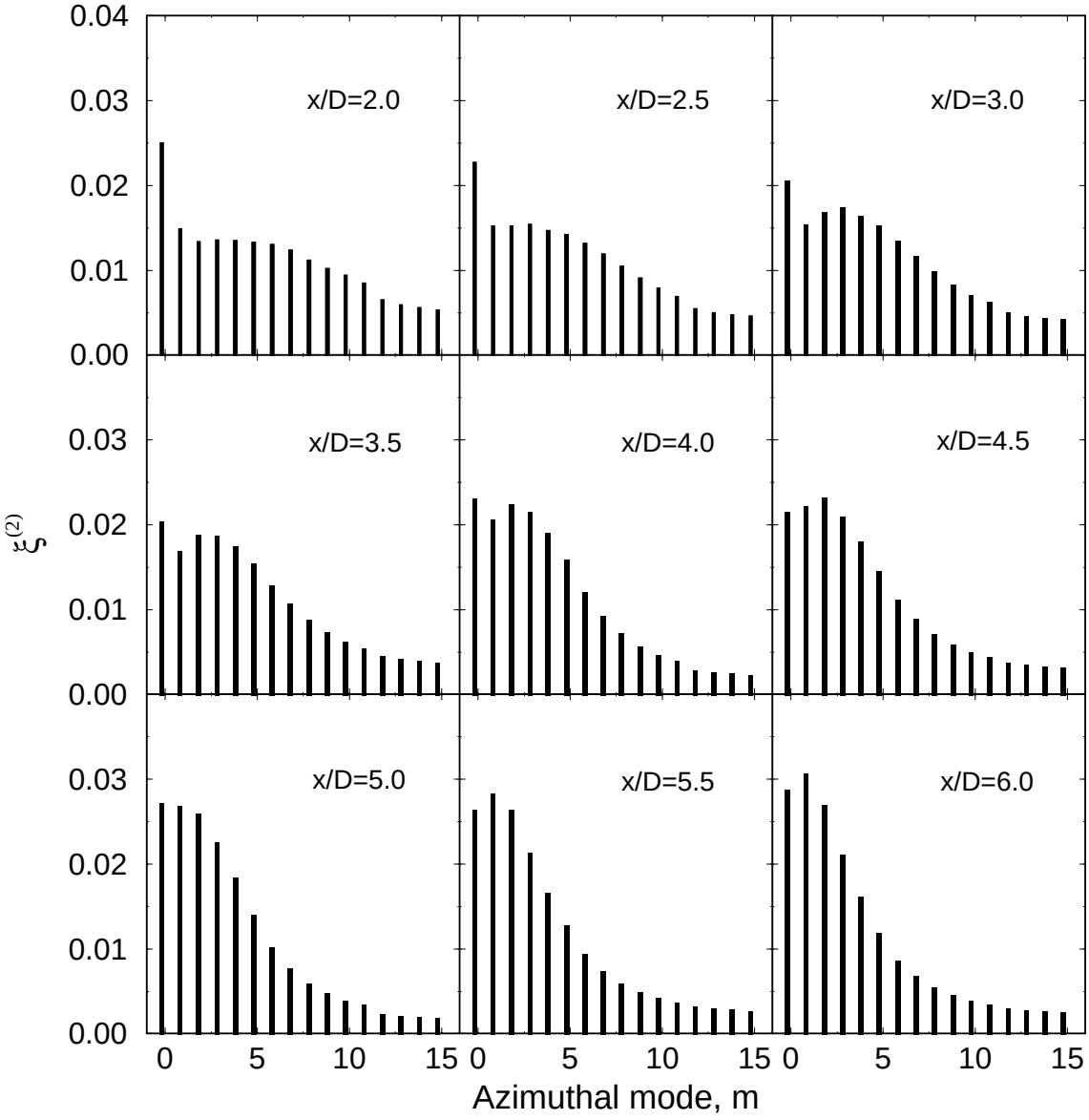

Figure 5.24: Normalized second POD-mode energy, $\xi^{(2)}(m)$, distribution along azimuthal mode number, m, at $Re_D = 156\,800$.

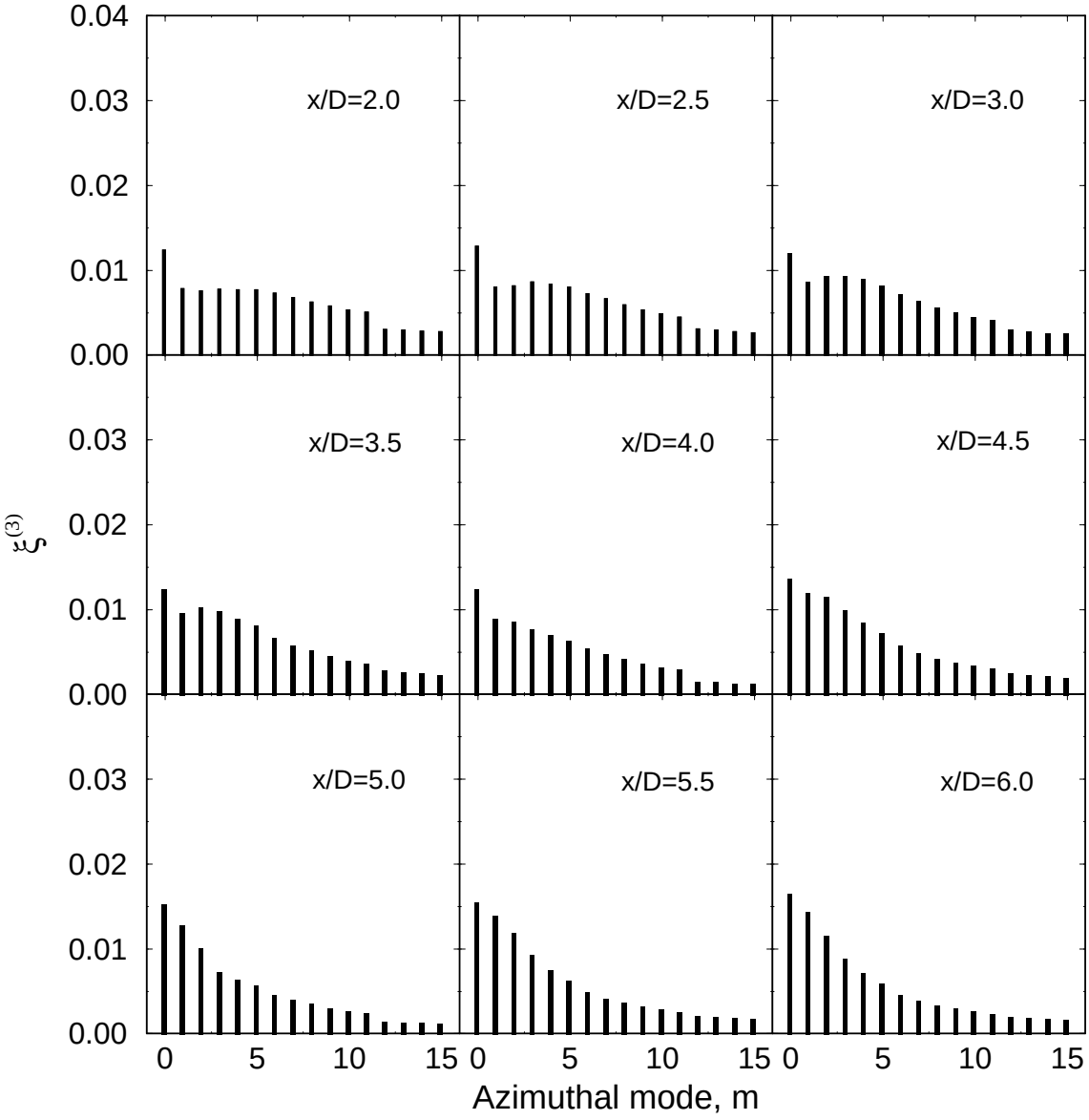

Figure 5.25: Normalized third POD-mode energy, $\xi^{(3)}(m)$, distribution along azimuthal mode number, m, at $Re_D = 156\,800$.

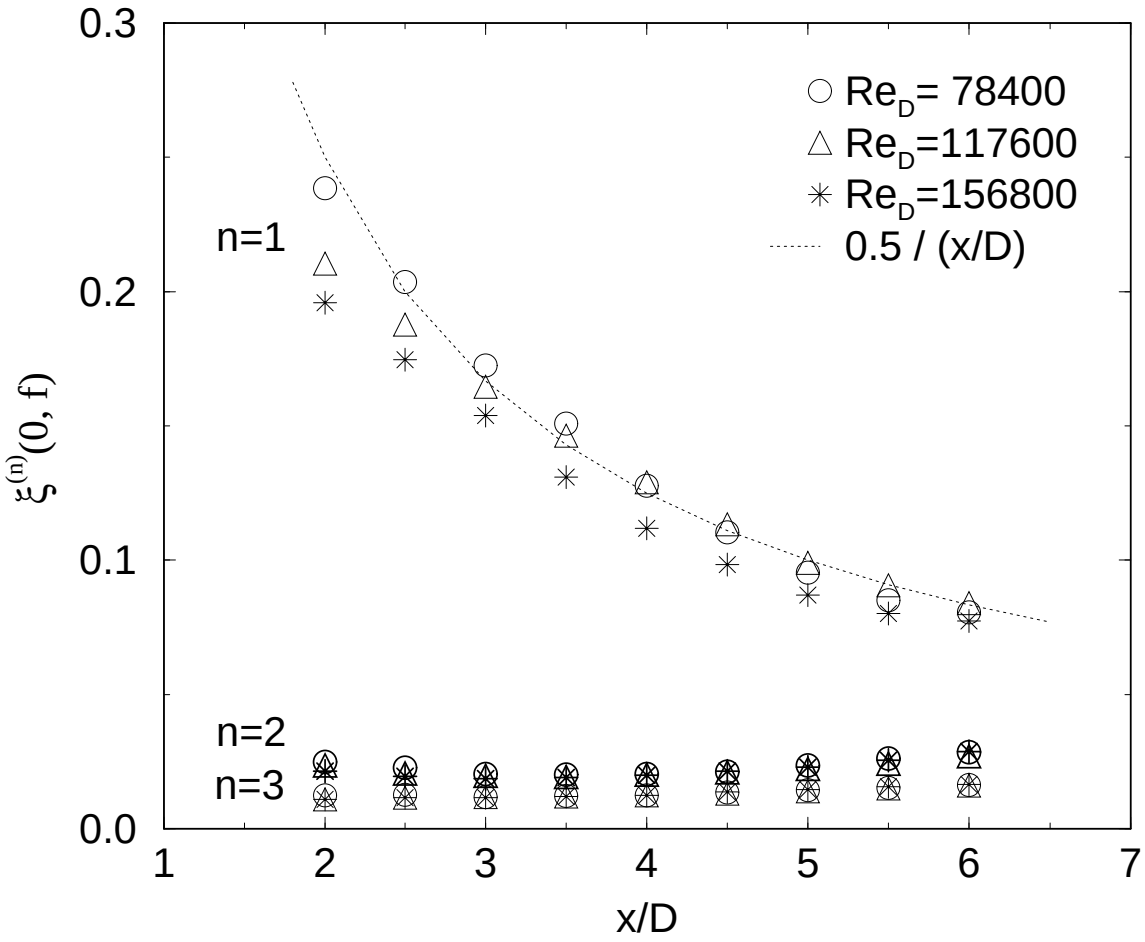

Figure 5.26: The variation with downstream positions of the 0th azimuthal mode energy distribution at POD mode $n = 1$, 2, and 3 at $Re_D = 78\,400$, $117\,600$, and $156\,800$.

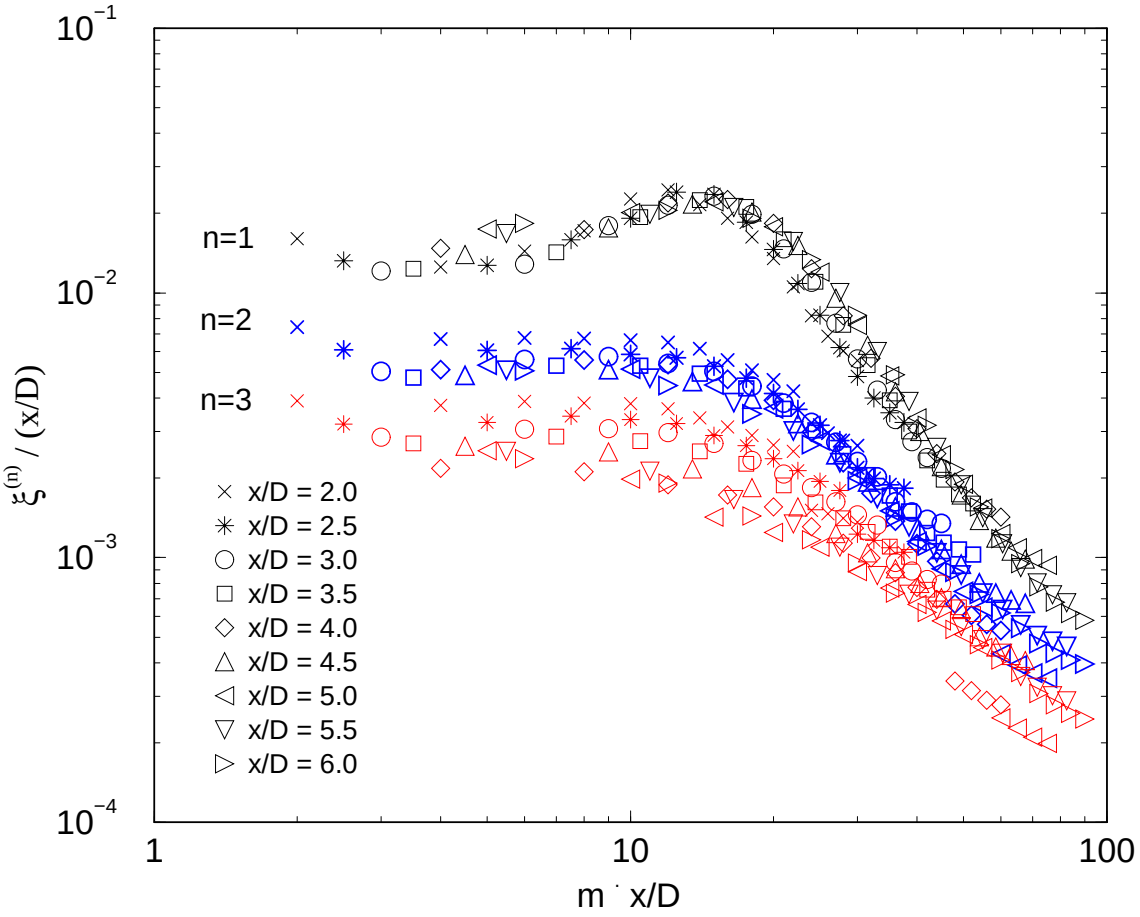

Figure 5.27: The first 3 POD-mode energy distribution normalized in shear layer variables, $(m \cdot x/D)$, at $Re_D = 78\,400$.

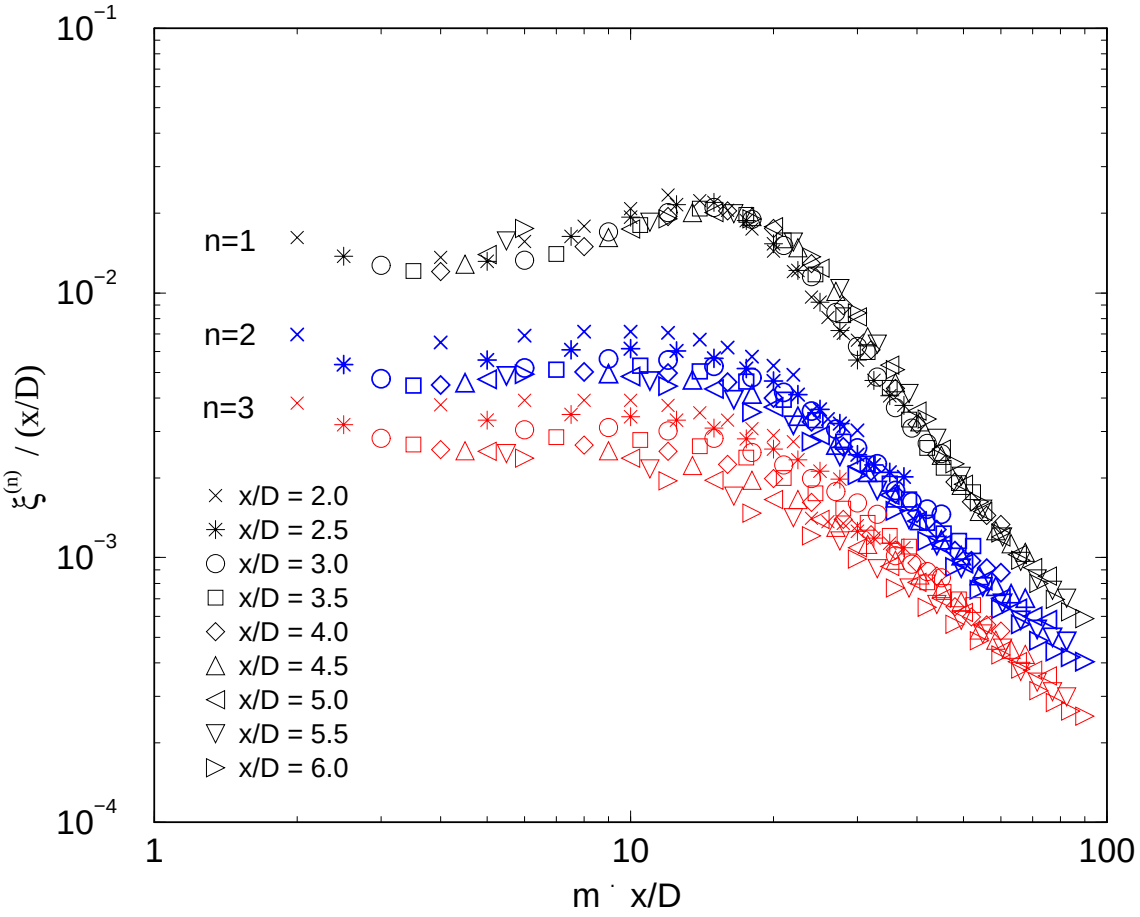

Figure 5.28: The first 3 POD-mode energy distribution normalized in shear layer variables, $(m \cdot x/D)$, at $Re_D = 117\,600$.

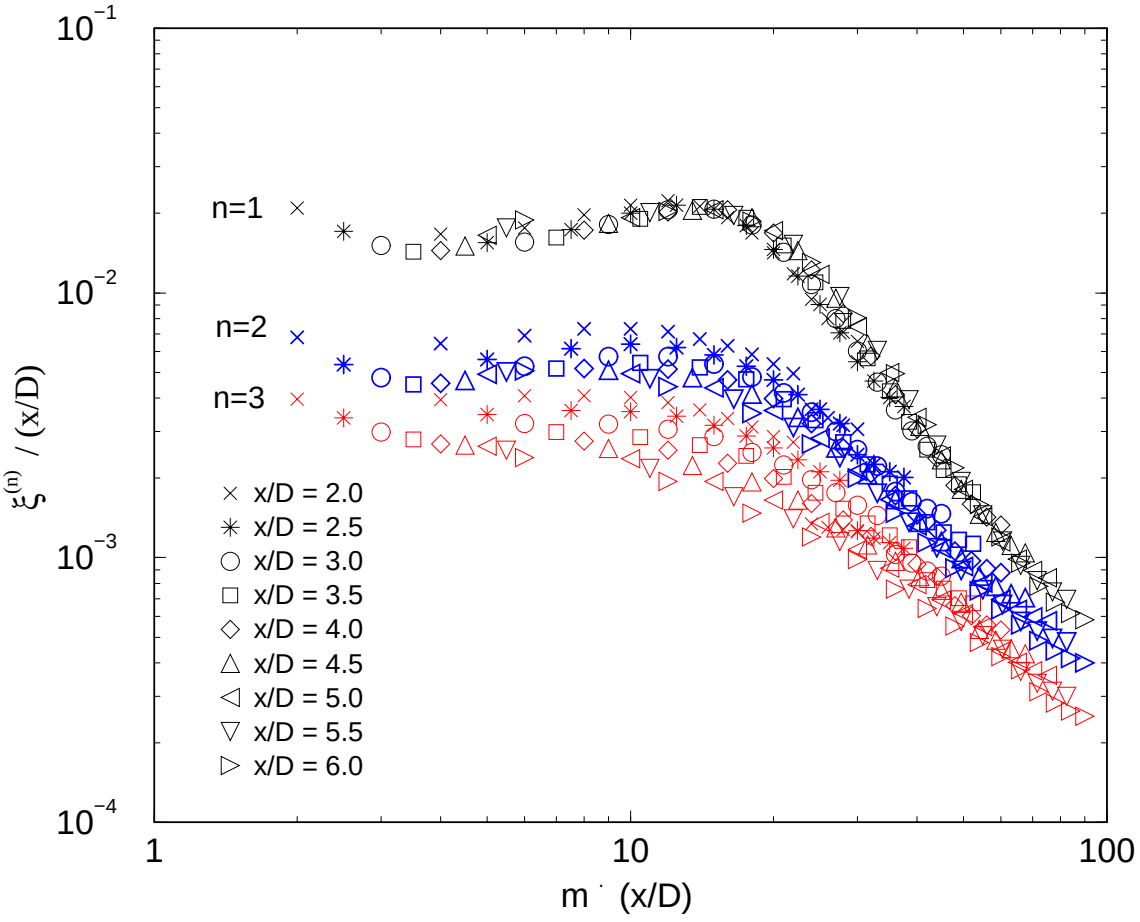

Figure 5.29: The first 3 POD-mode energy distribution normalized in shear layer variables, $(m \cdot x/D)$, at $Re_D = 156\,800$.

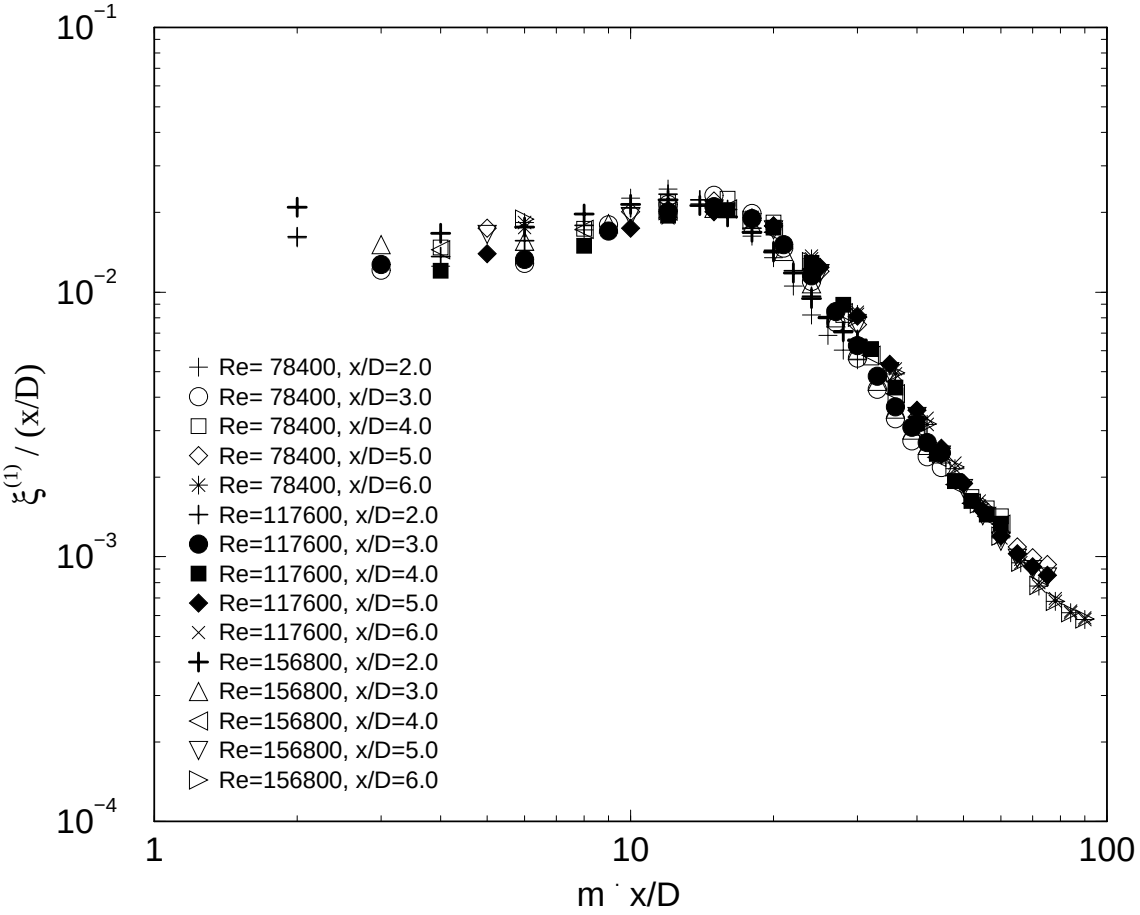

Figure 5.30: The first POD-mode energy distribution normalized in shear layer variables, $(m \cdot x/D)$, at $Re_D = 78\,400$, $117\,600$, and $156\,800$.

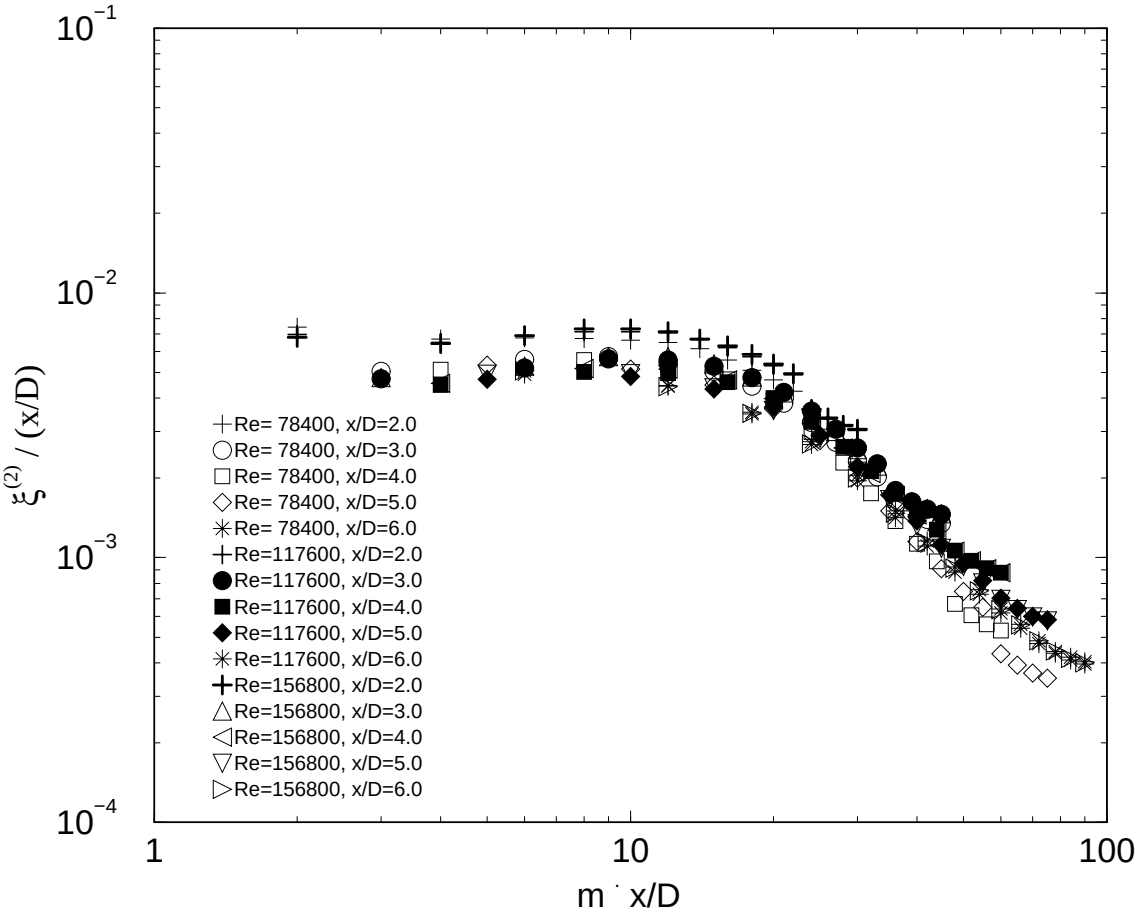

Figure 5.31: The second POD-mode energy normalized in shear layer variables, $(m \cdot x/D)$, at $Re_D = 78\,400$, $117\,600$, and $156\,800$.

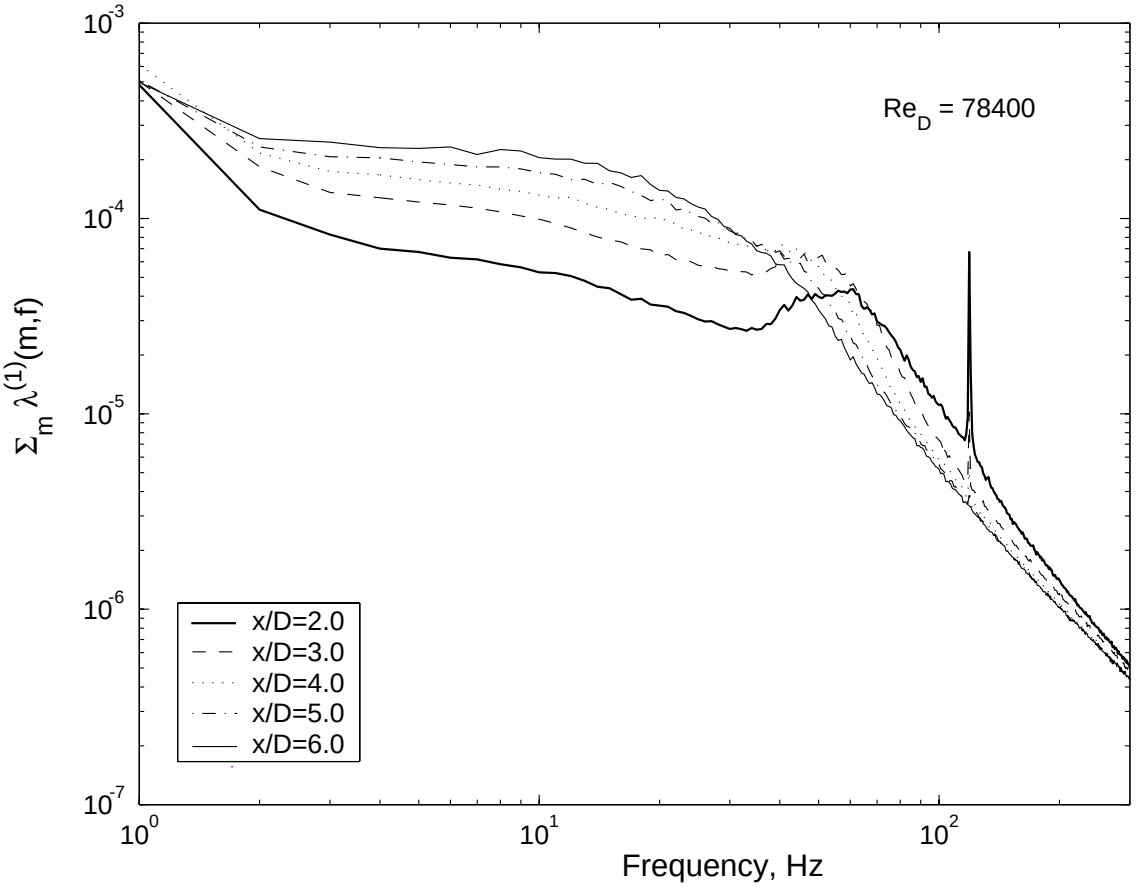

Figure 5.32: Eigenspectra of the first POD-mode energy, $\sum_m \lambda^{(1)}(f)$, with downstream positions at $Re_D = 78\,400$.

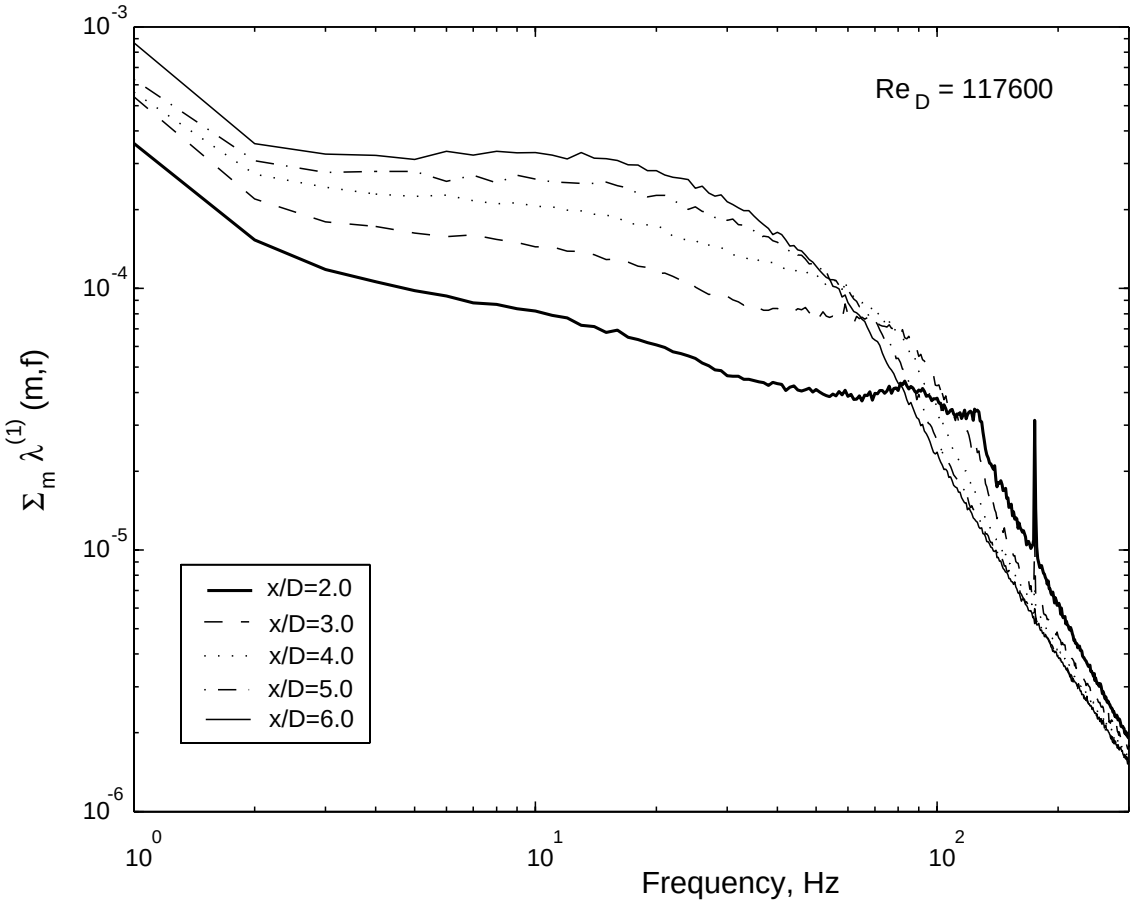

Figure 5.33: Eigenspectra of the first POD-mode energy, $\sum_m \lambda^{(1)}(f)$, with downstream positions at $Re_D = 117\,600$.

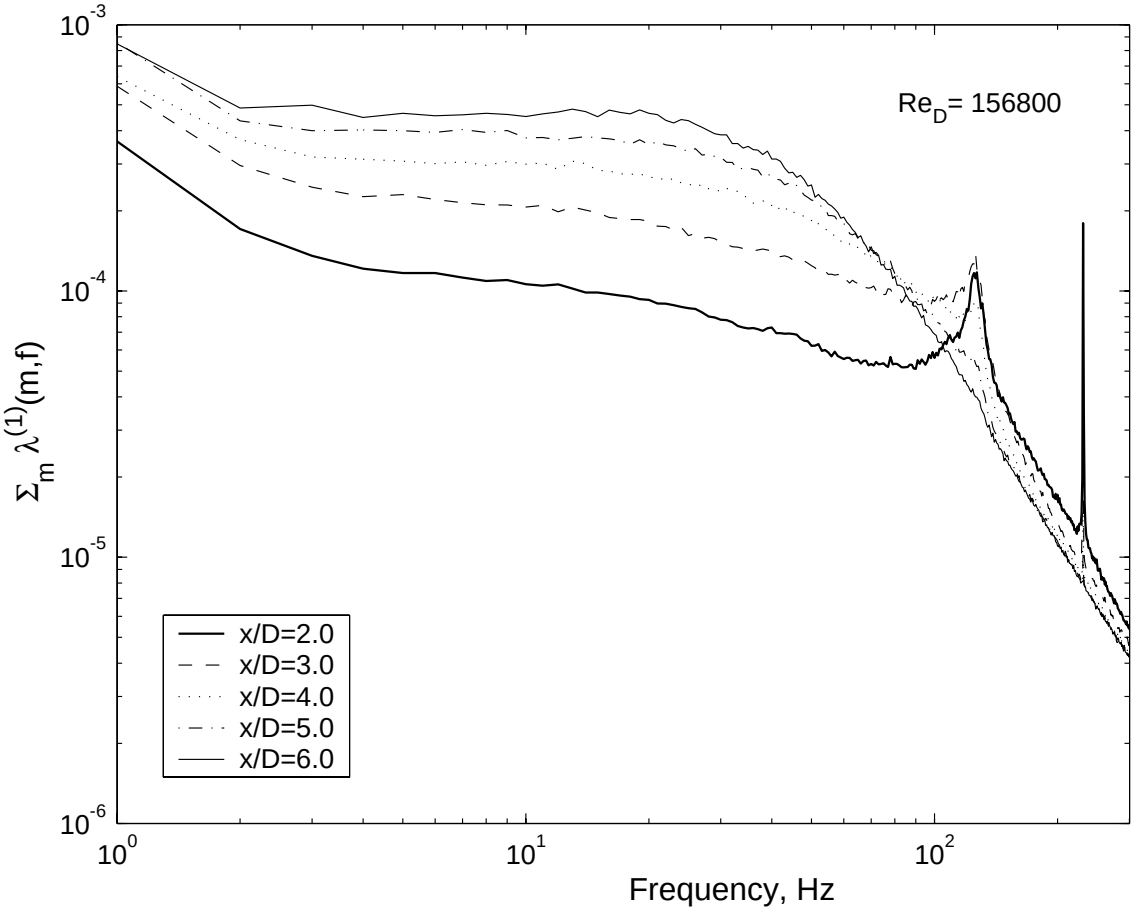

Figure 5.34: Eigenspectra of the first POD-mode energy, $\sum_m \lambda^{(1)}(f)$, with downstream positions at $Re_D = 156\,800$.

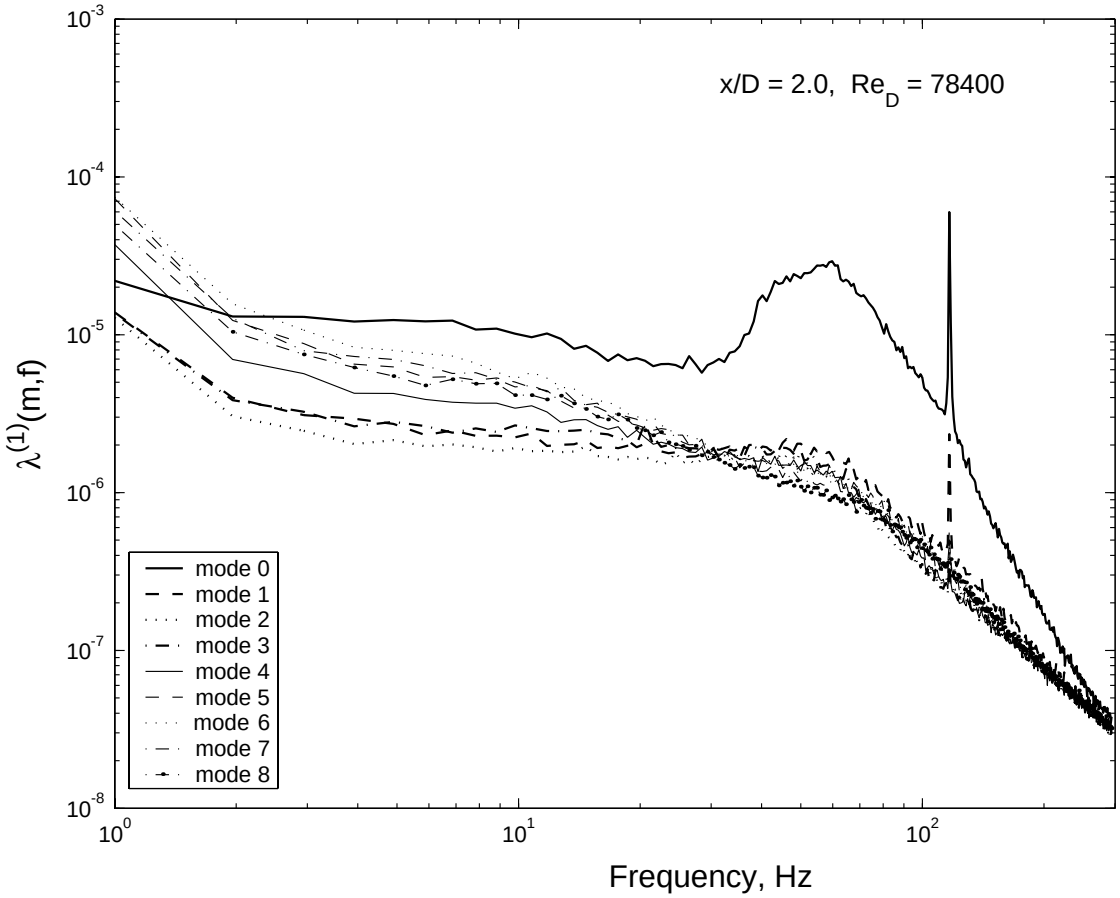

Figure 5.35: Eigenspectra of the first POD mode for the azimuthal mode at $x/D = 2.0$, and $Re_D = 78\,400$.

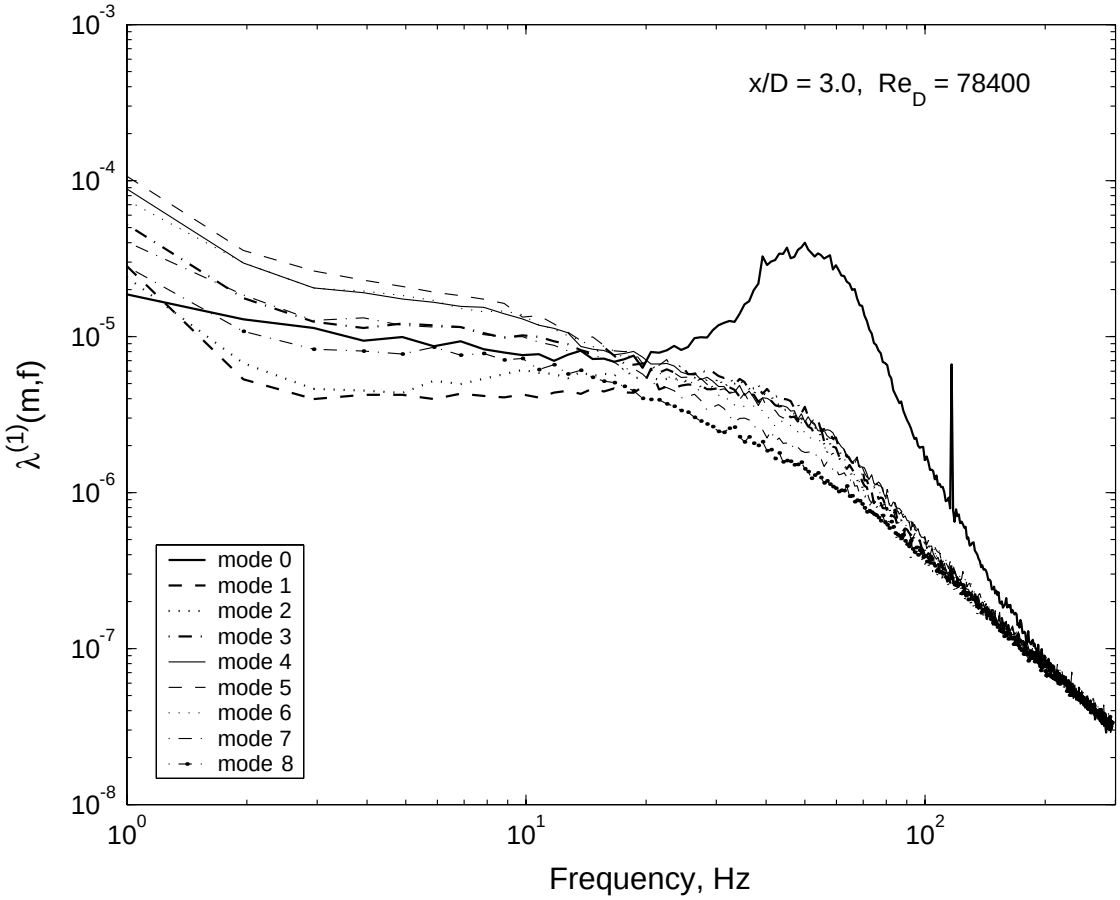

Figure 5.36: Eigenspectra of the first POD mode for the azimuthal mode at $x/D = 3.0$, and $Re_D = 78\,400$.

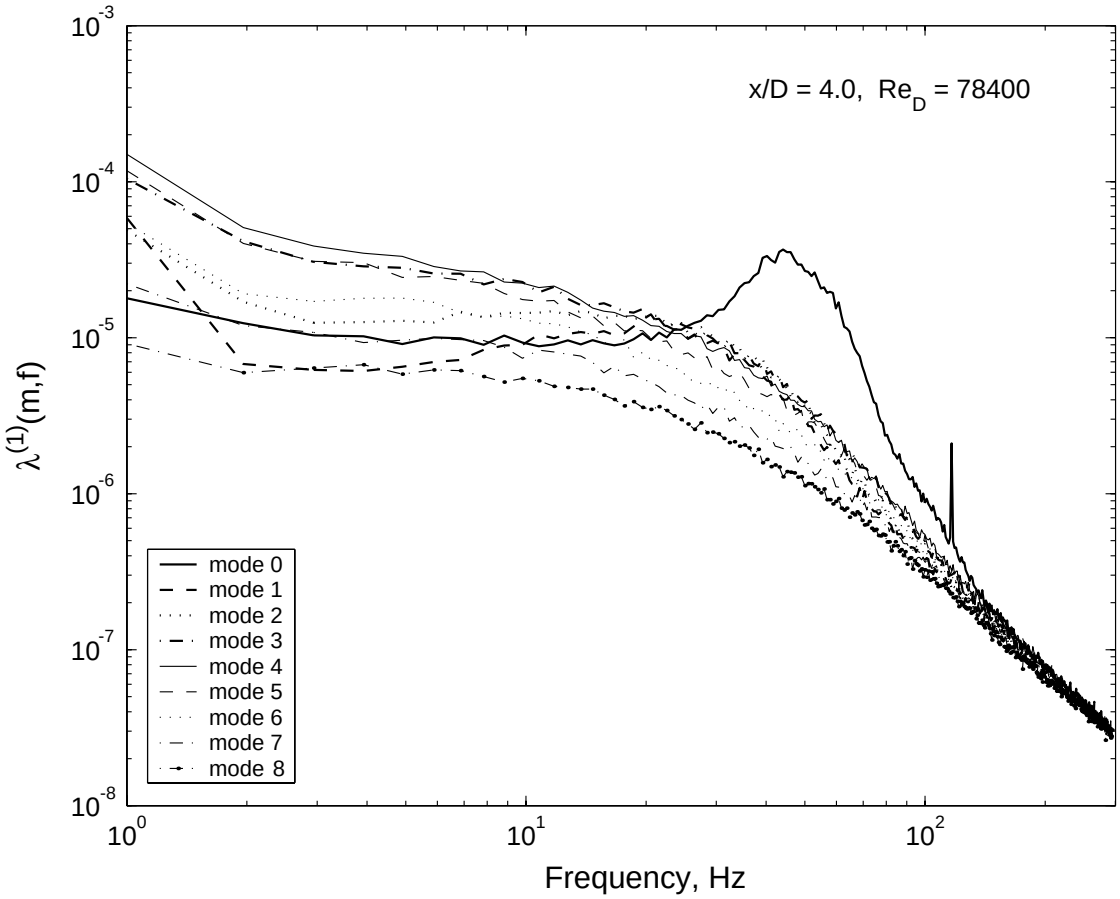

Figure 5.37: Eigenspectra of the first POD mode for the azimuthal mode at $x/D = 4.0$, and $Re_D = 78\,400$.

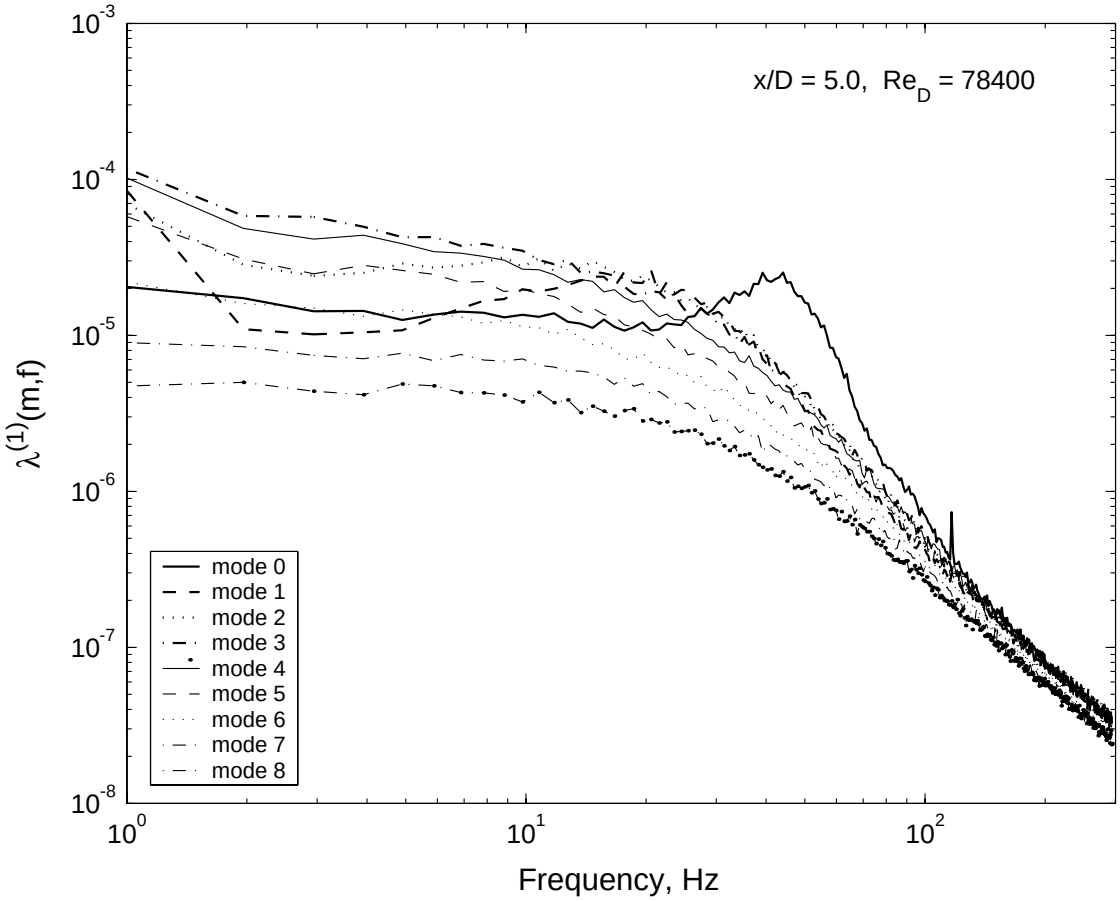

Figure 5.38: Eigenspectra of the first POD mode for the azimuthal mode at $x/D = 5.0$, and $Re_D = 78\,400$.

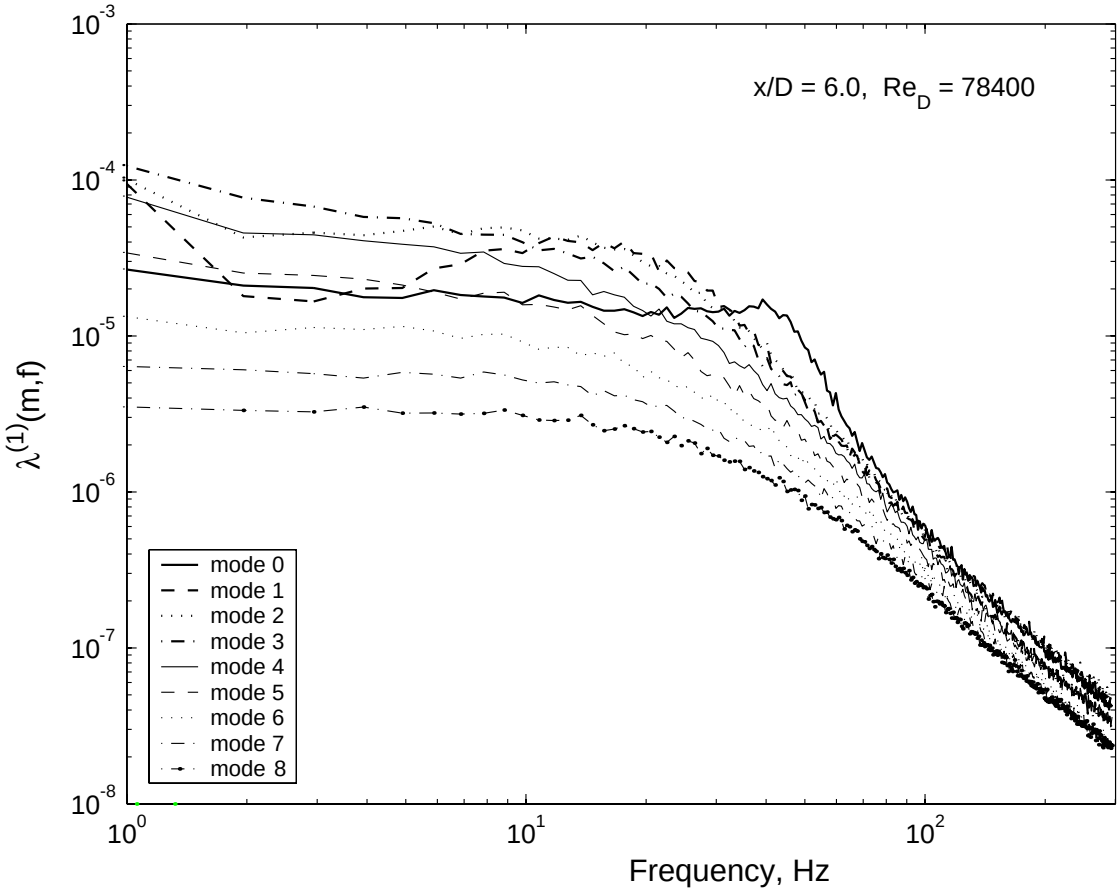

Figure 5.39: Eigenspectra of the first POD mode for the azimuthal mode at $x/D = 6.0$, and $Re_D = 78\,400$.

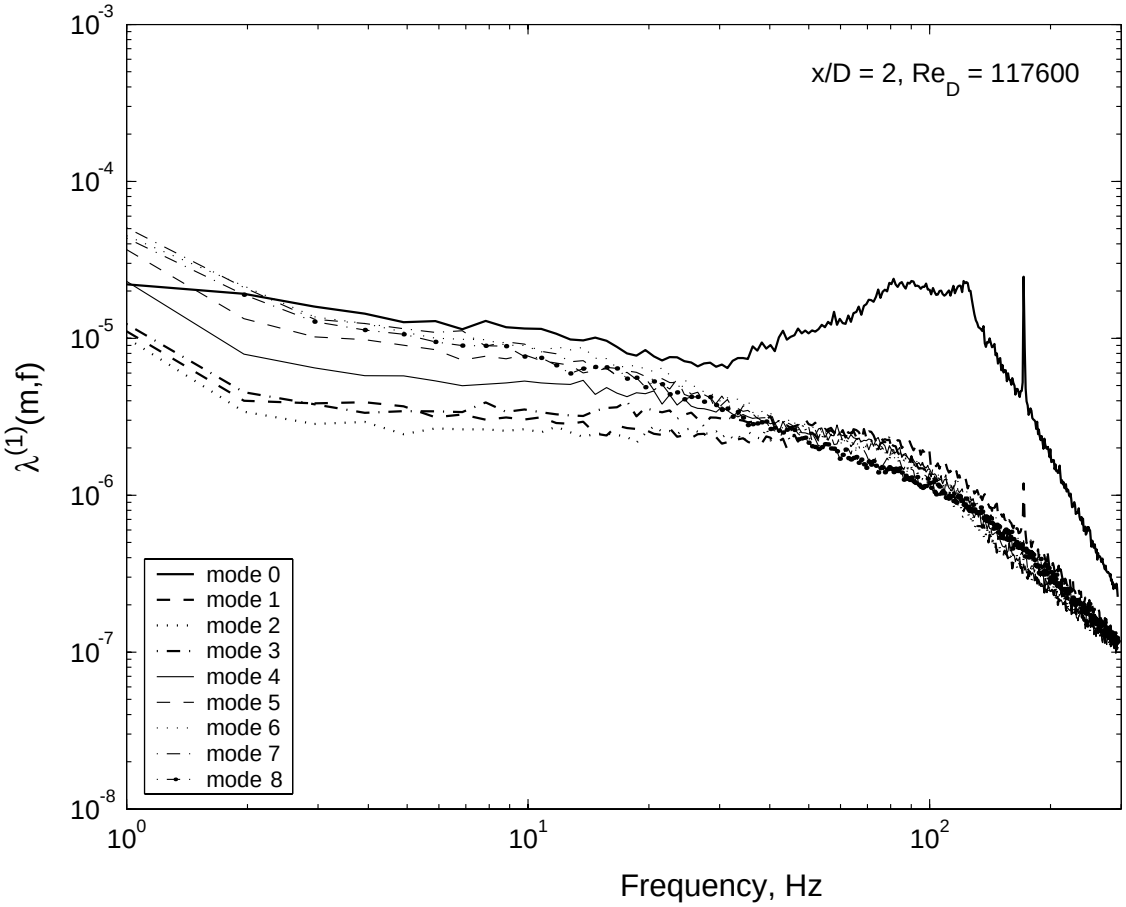

Figure 5.40: Eigenspectra of the first POD mode for the azimuthal mode at $x/D = 2.0$, and $Re_D = 117\,600$.

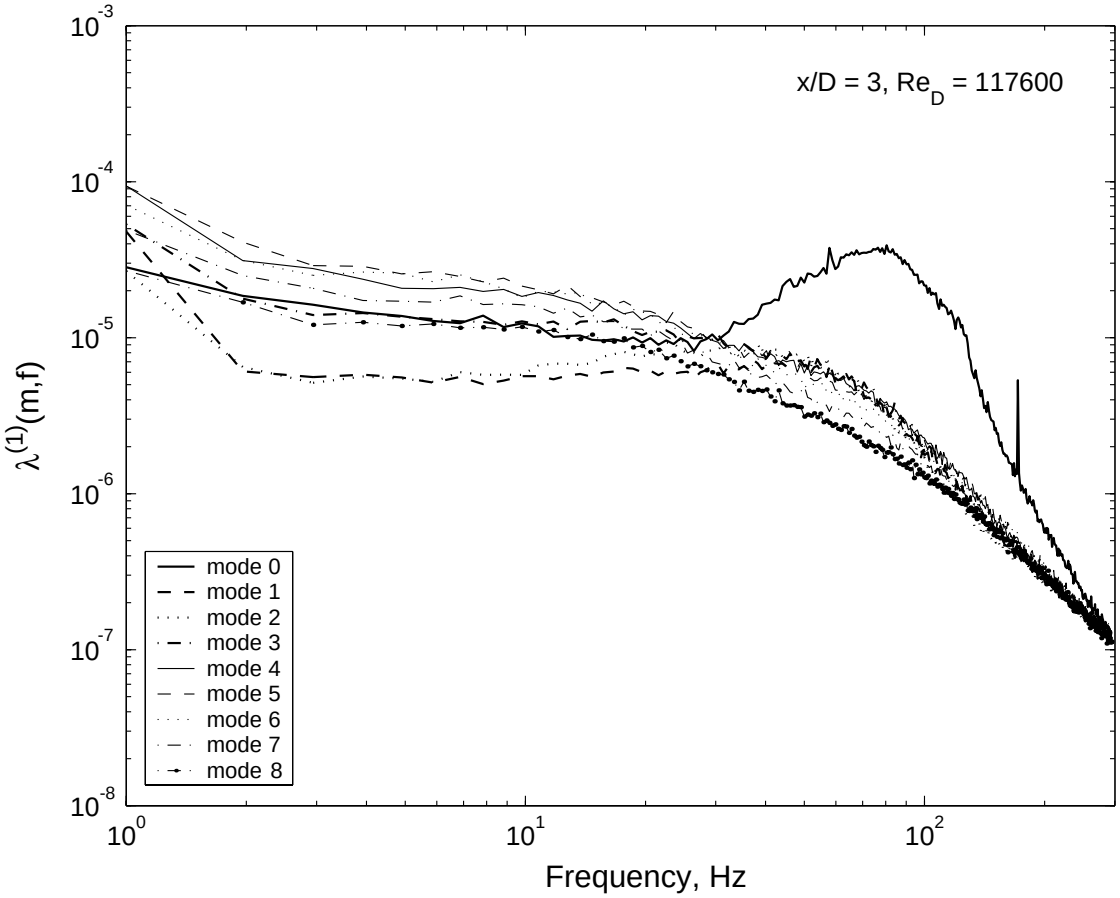

Figure 5.41: Eigenspectra of the first POD mode for the azimuthal mode at $x/D = 3.0$, and $Re_D = 117\,600$.

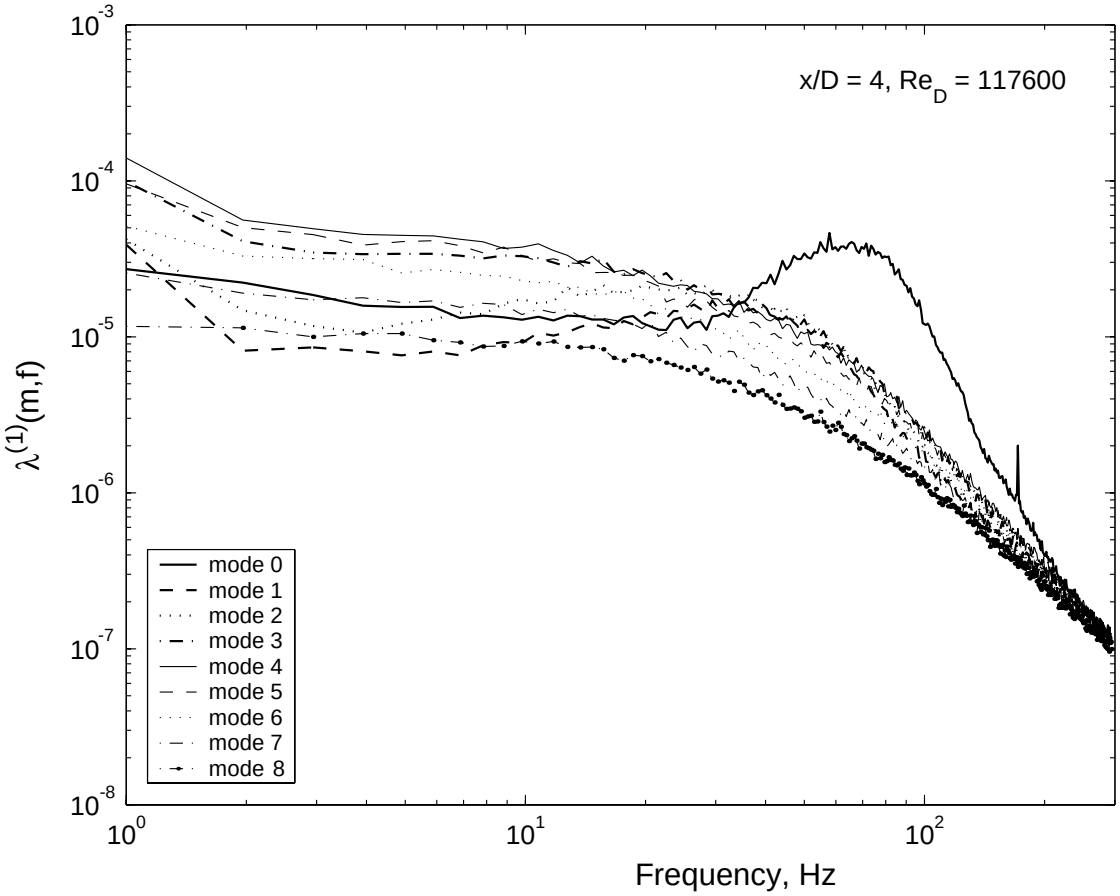

Figure 5.42: Eigenspectra of the first POD mode for the azimuthal mode at $x/D = 4.0$, and $Re_D = 117\,600$.

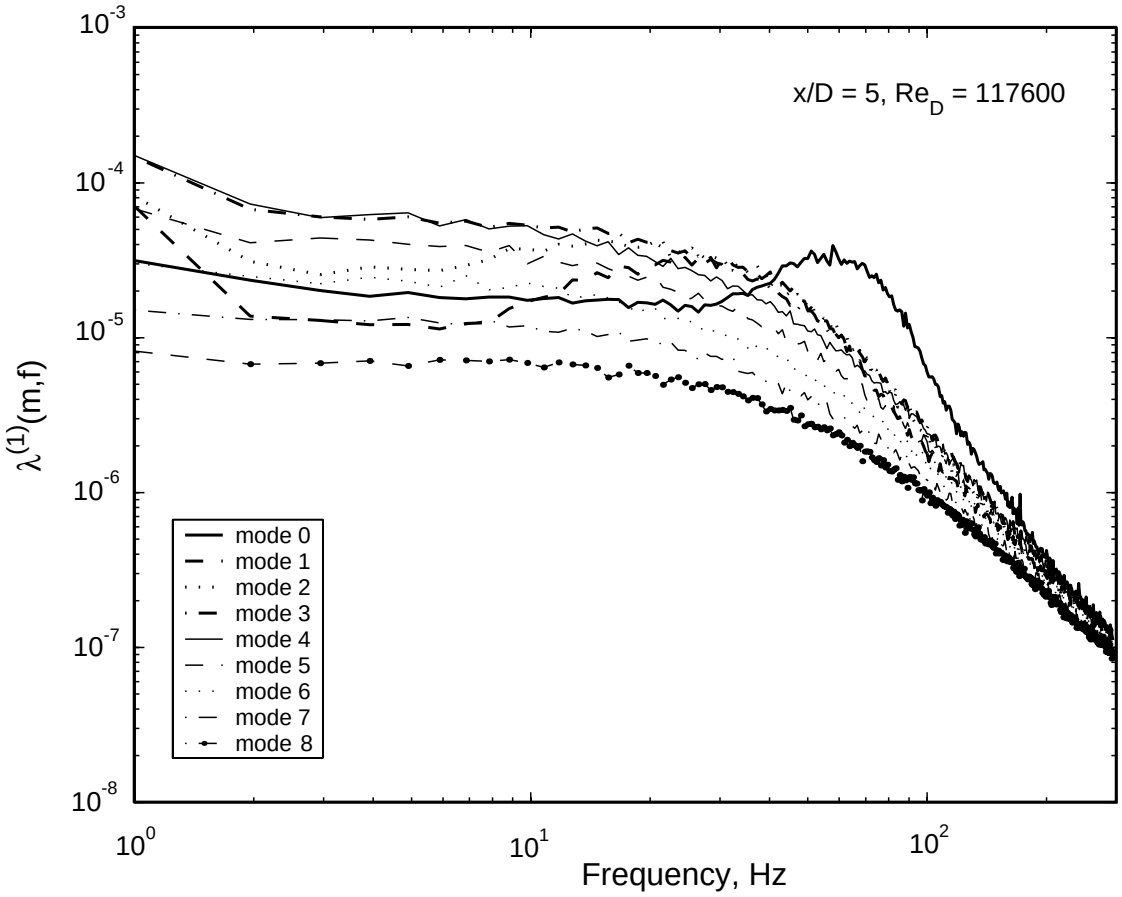

Figure 5.43: Eigenspectra of the first POD mode for the azimuthal mode at $x/D = 5.0$, and $Re_D = 117\,600$.

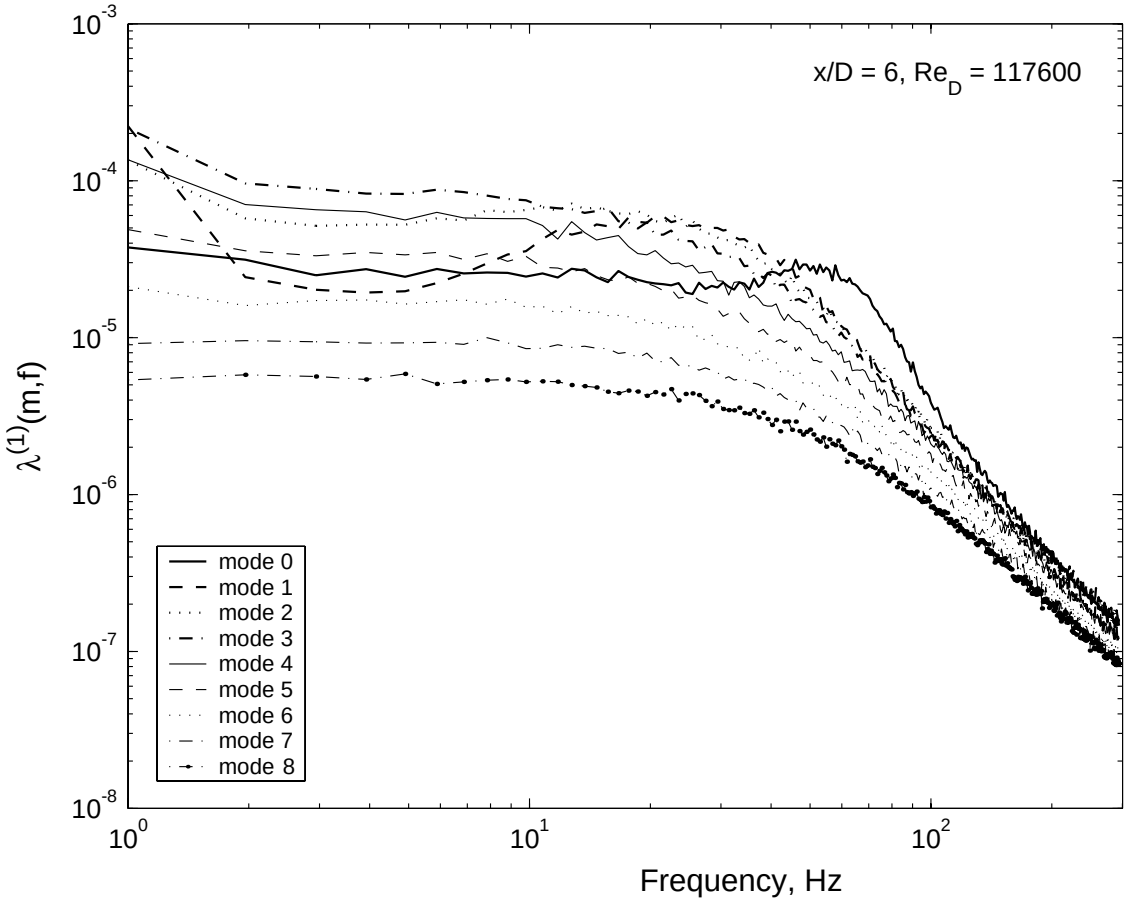

Figure 5.44: Eigenspectra of the first POD mode for the azimuthal mode at $x/D = 6.0$, and $Re_D = 117\,600$.

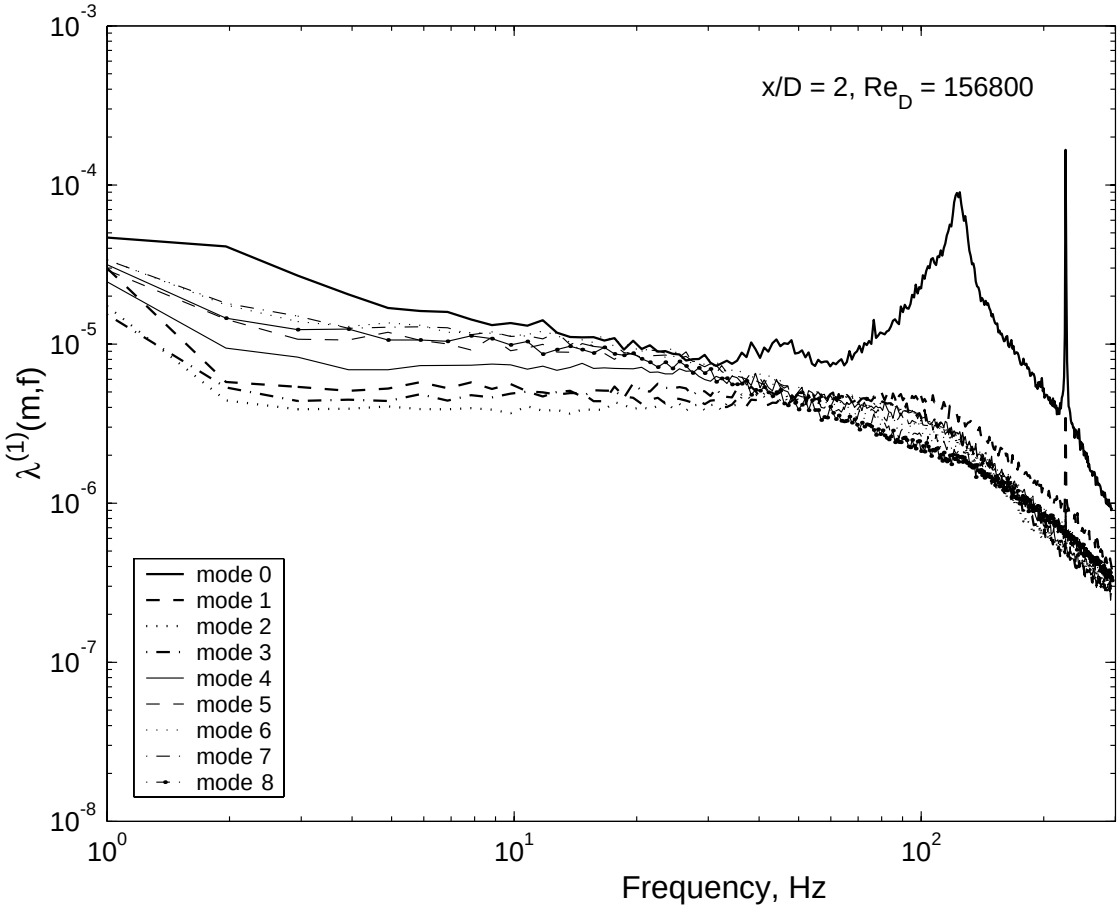

Figure 5.45: Eigenspectra of the first POD mode for the azimuthal mode at $x/D = 2.0$, and $Re_D = 156\,800$.

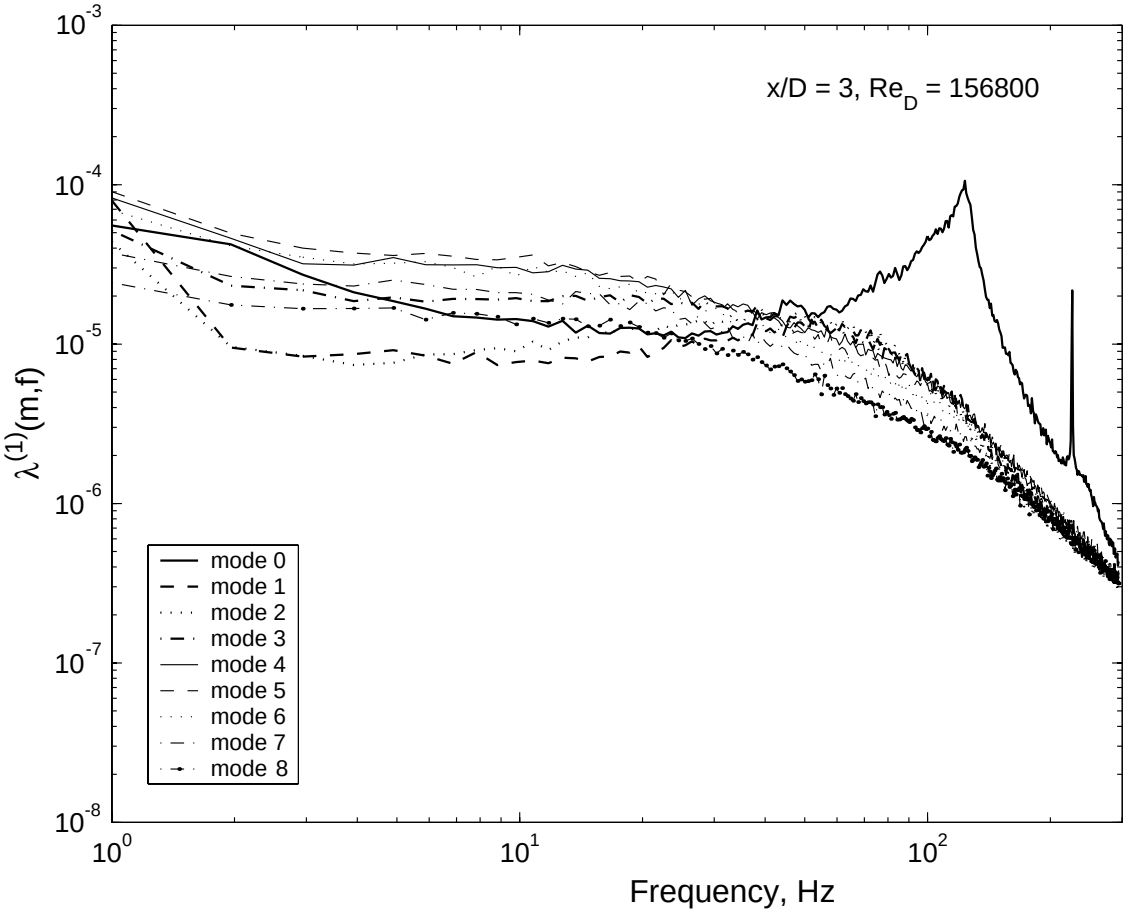

Figure 5.46: Eigenspectra of the first POD mode for the azimuthal mode at $x/D = 3.0$, and $Re_D = 156\,800$.

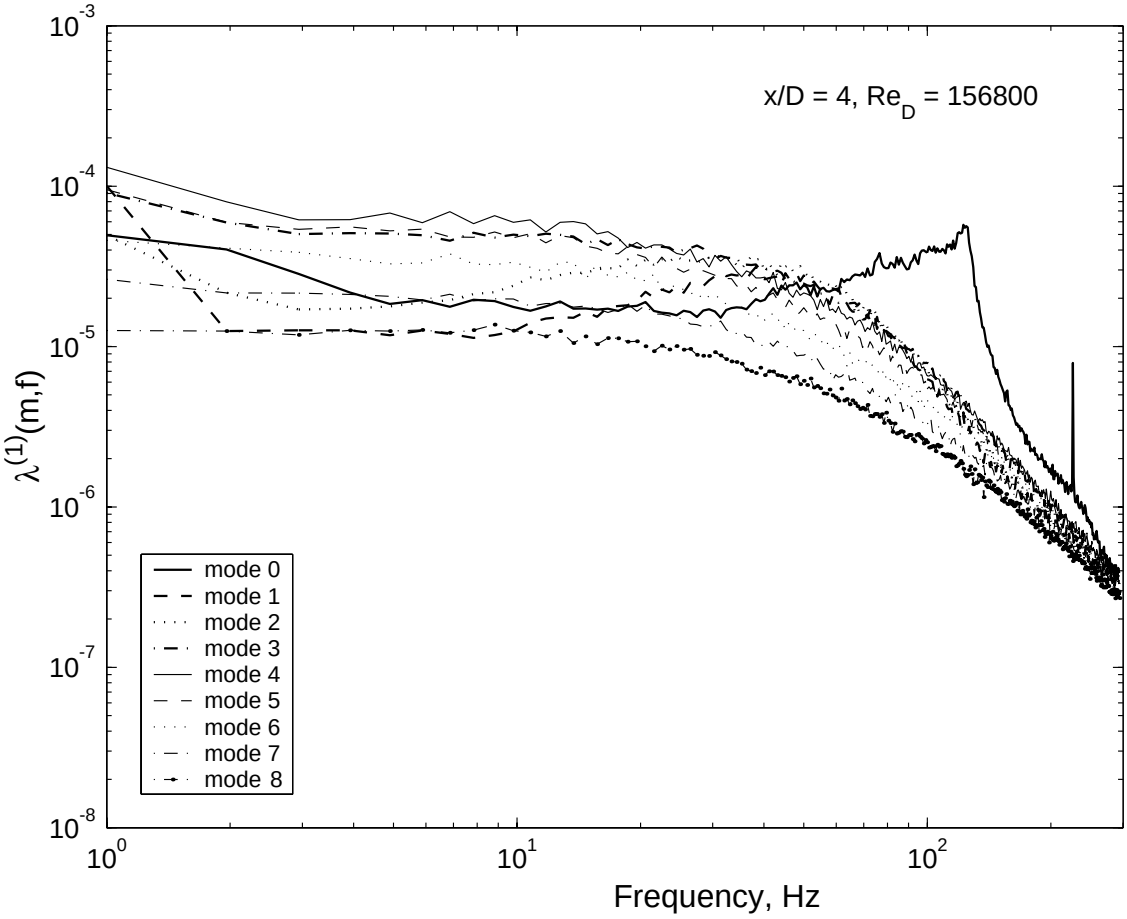

Figure 5.47: Eigenspectra of the first POD mode for the azimuthal mode at $x/D = 4.0$, and $Re_D = 156\,800$.

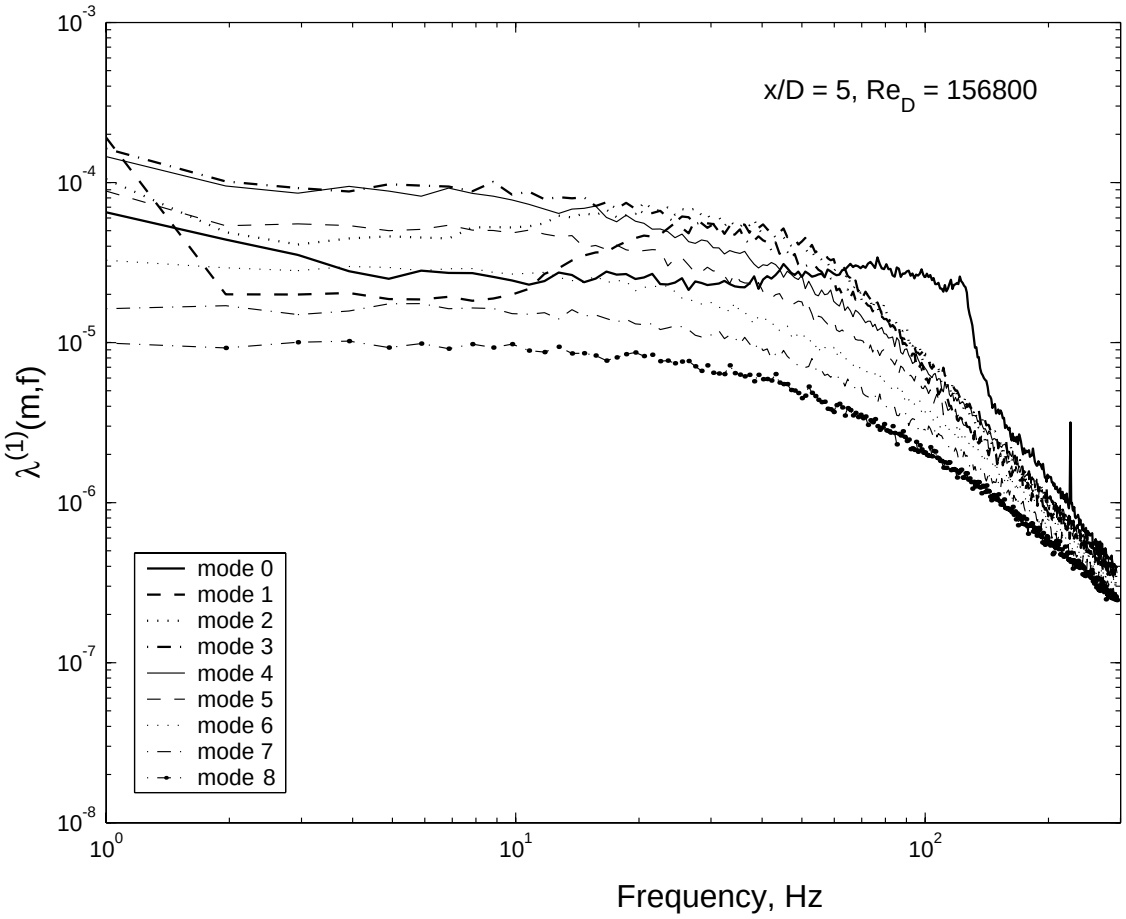

Figure 5.48: Eigenspectra of the first POD mode for the azimuthal mode at $x/D = 5.0$, and $Re_D = 156\,800$.

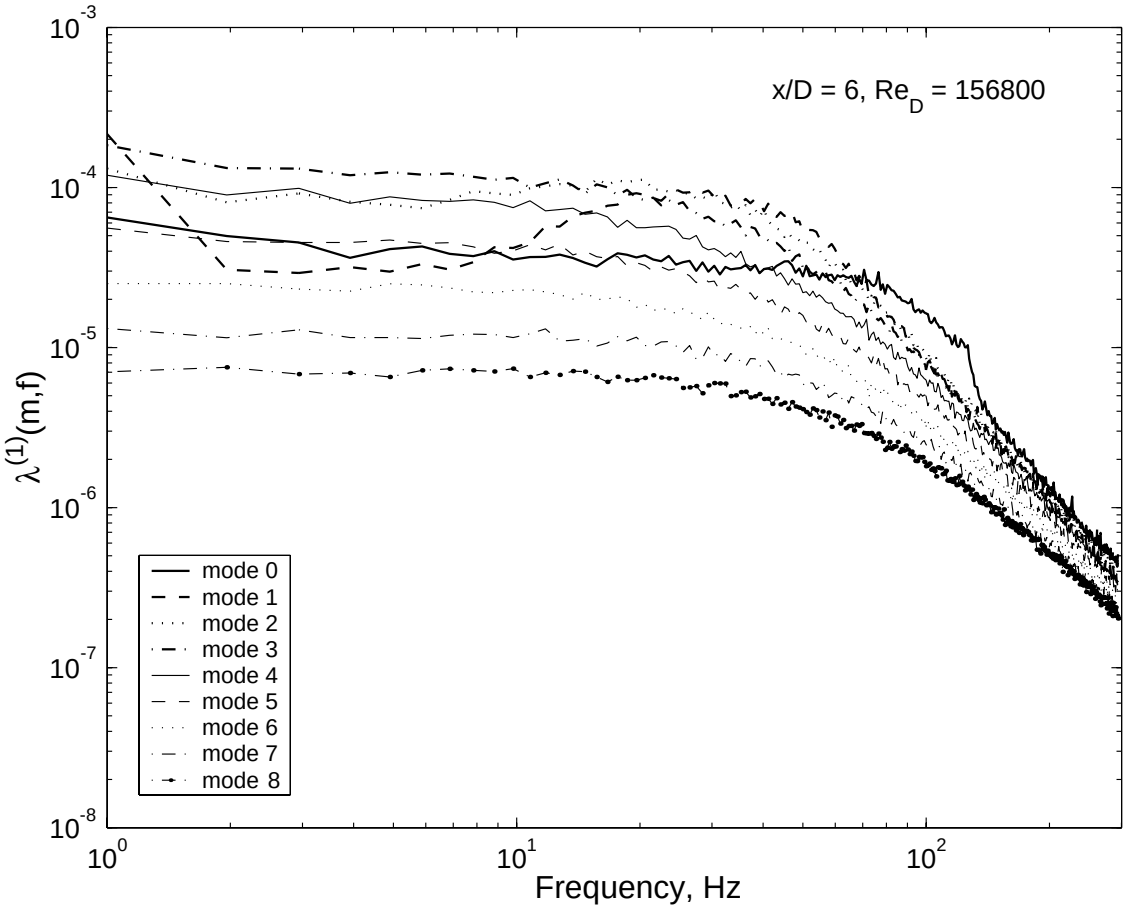

Figure 5.49: Eigenspectra of the first POD mode for the azimuthal mode at $x/D = 6.0$, and $Re_D = 156\,800$.

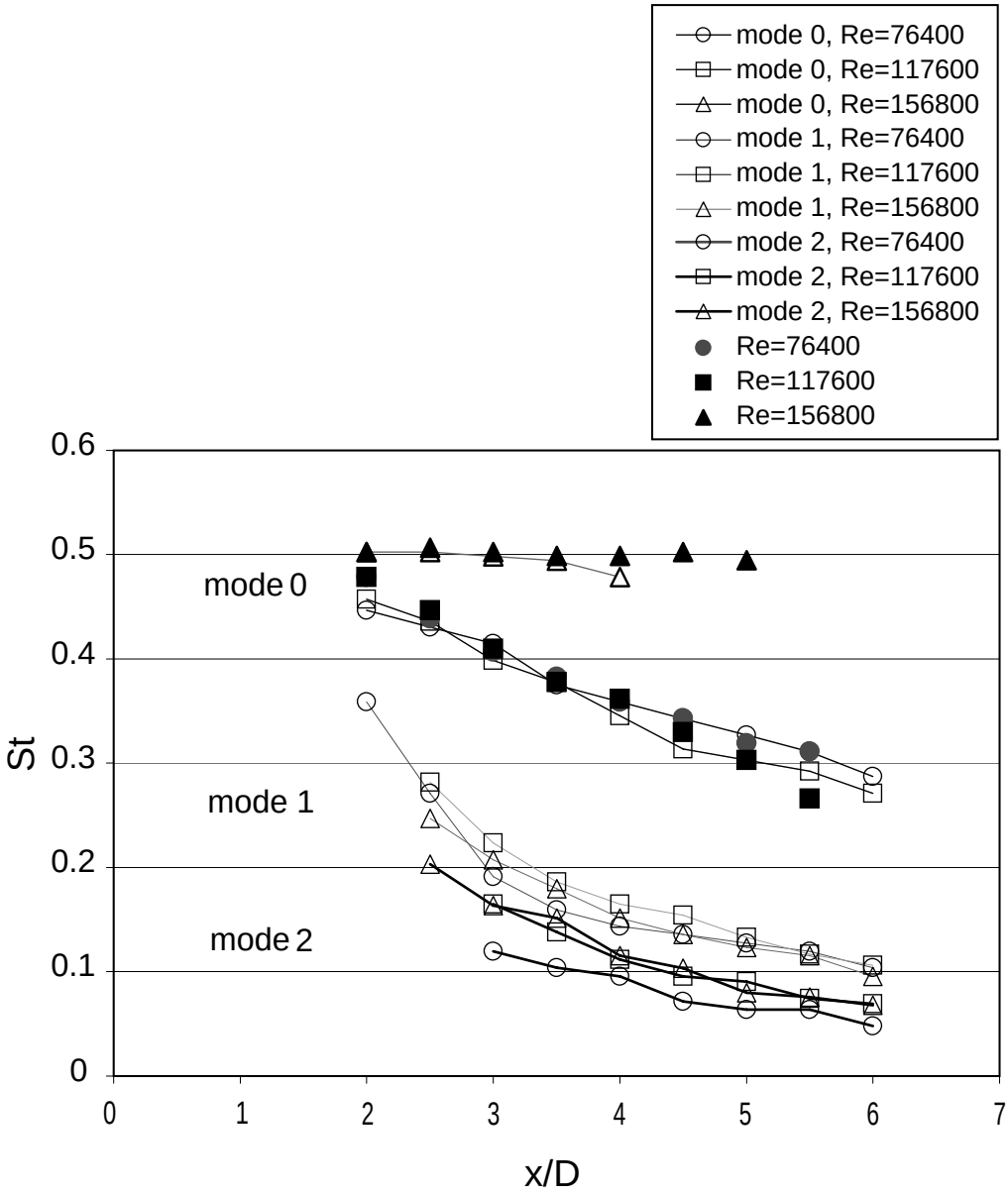

Figure 5.50: St_D numbers along downstream locations based on velocity spectra and eigenspectra.

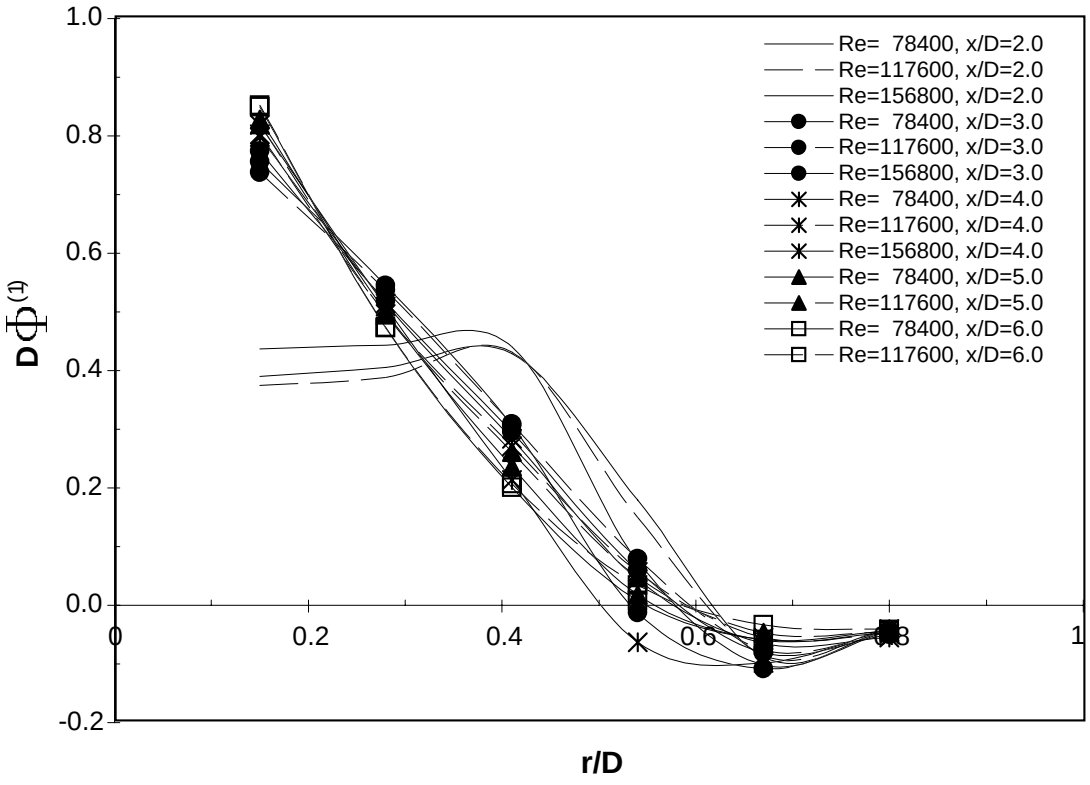

Figure 5.51: Eigenfunctions(real) from the peak of azimuthal mode-0 for 3 Reynolds numbers and 5 downstream positions.

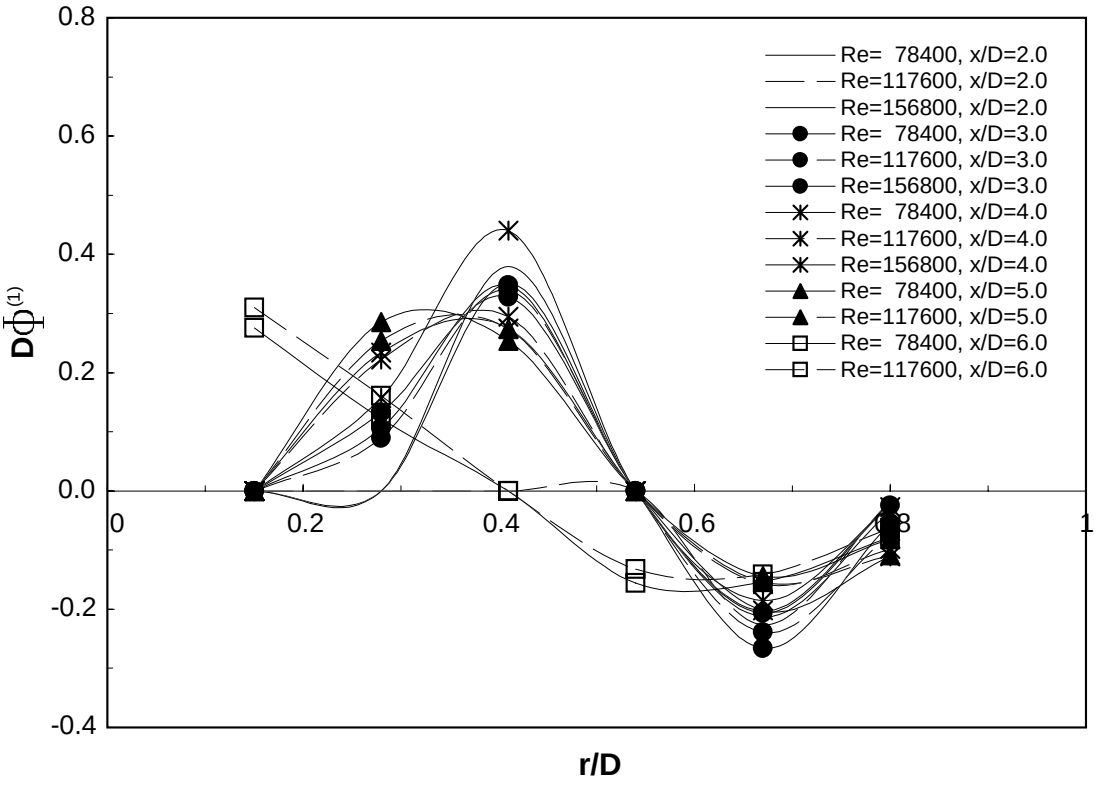

Figure 5.52: Eigenfunctions(imaginary) from the peak of azimuthal mode-0 for 3 Reynolds numbers and 5 downstream positions.

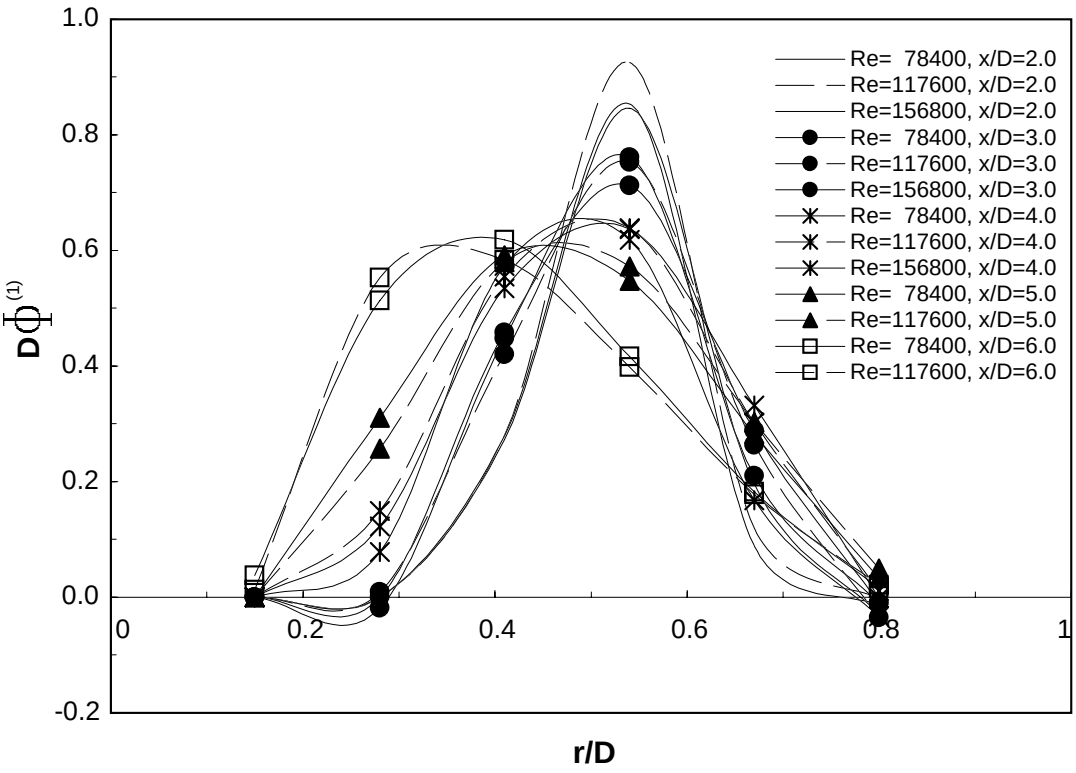

Figure 5.53: Eigenfunctions(real) from the peak of the most dominant azimuthal mode ($m > 0$) for 3 Reynolds numbers and 5 downstream positions

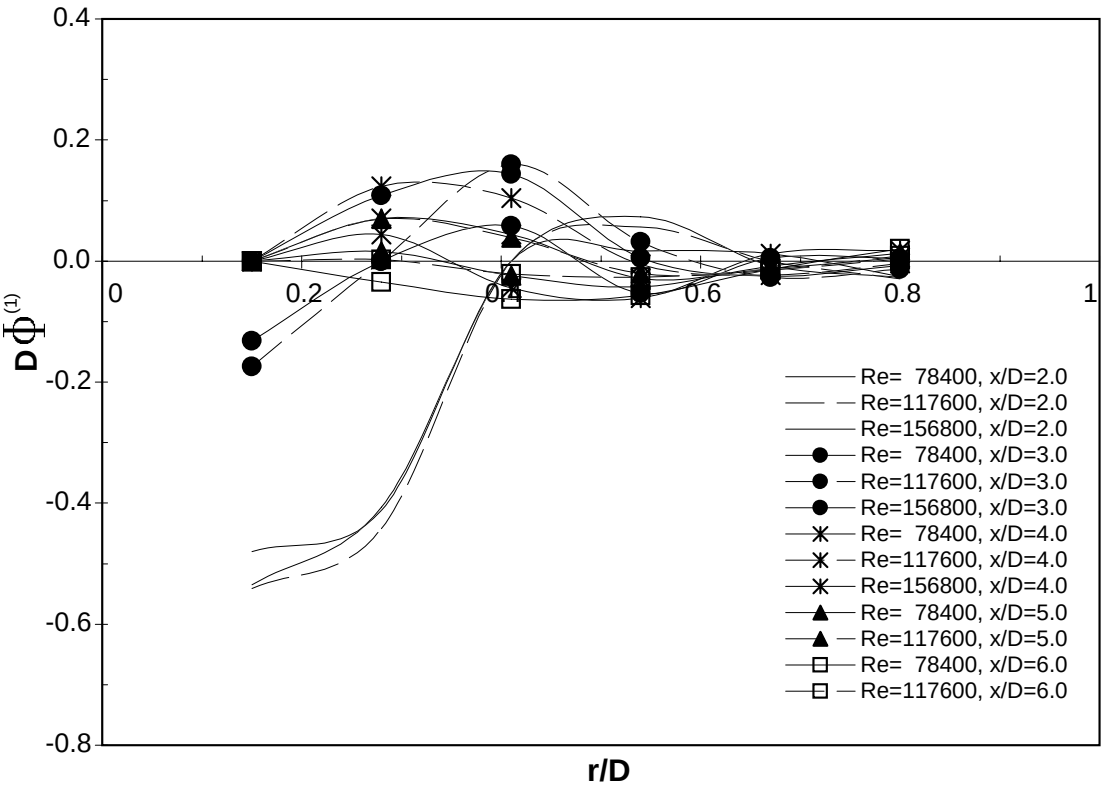

Figure 5.54: Eigenfunctions(imaginary) from the peak of the most dominant azimuthal mode ($m > 0$) for 3 Reynolds numbers and 5 downstream positions

Chapter 6

Reconstruction of the large-scale structures

6.1 Introduction

The POD generates an appropriate basis for dynamical models of turbulence by decomposing the field into an optimal set of functions. Its effectiveness has been shown by many researchers (v. Herzog 1986, Moin & Moser 1989, Ukeiley *et al.* 1991, Citriniti & George 2000 among others).

To understand how POD represents the original velocity signal, the instantaneous velocity field was reconstructed with time sequence. These reconstructed fluctuating velocities are presented to illustrate the dynamics and interactions of the large-scale structure at different downstream positions for various Reynolds numbers.

6.2 Reconstruction of the instantaneous velocity

The streamwise fluctuating velocity at a position in the mixing layer can be reconstructed as a linear combination of the eigenfunctions. For this experiment, as noted earlier, it is more convenient to work with a reconstruction of its double-Fourier

transform; i.e.,

$$r^{\frac{1}{2}}\hat{\hat{u}}_1^N(r,m,f) = \sum_{n=1}^{N} \hat{\hat{a}}_n(m,f)\,\hat{\hat{\phi}}_1^{(n)}(r,m,f) \tag{6.1}$$

The random coefficients, $\hat{\hat{a}}_n(m,f)$, are obtained via a projection of the POD eigenfunction onto the instantaneous signal using the orthogonality of the eigenfunctions (Equation 2.42); i.e.,

$$\hat{\hat{a}}_n(m,f) = \int r^{\frac{1}{2}}\hat{\hat{u}}_1(r,m,f)\,\hat{\hat{\phi}}_1^{(n)*}(r,m,f)\,dr \tag{6.2}$$

where the kernel of Equation 6.2 is an instantaneous realization of the velocity which has been decomposed into azimuthal mode number and frequency. The numerical implementation of Equation 6.2 is made with the trapezoidal rule as described in section 2.

Then this reconstructed double-transformed velocity from Equation 6.1 can be inverse transformed in frequency to obtain:

$$\hat{u}_1^N(r,m,t) = \int e^{i2\pi ft}\,\hat{\hat{u}}_1^N(r,m,f)\,df \tag{6.3}$$

Finally this can be inverse transformed in θ to obtain the reconstructed velocity as:

$$u_1^N(r,\theta,t) = \sum_{n=1}^{N}\sum_{m=0}^{M} e^{-im\theta}\,\hat{u}_1^N(r,m,t) \tag{6.4}$$

where the N in $u_1^N(r,\theta,t)$ denotes that the velocity is a numerically reconstructed one.

The fluctuating velocity can also be reconstructed using a partial sum of POD modes, N, and azimuthal modes, M. These are of primary interest here. None of these reconstructions are possible, of course, unless the original velocity field was measured simultaneously at all positions. Obtaining such measurements was the whole point of the 138-wire probe.

6.2.1 A velocity reconstruction at a point

To see how the POD modes contribute to the instantaneous velocity events, traces of reconstructed velocities are presented along with the original velocity signal in Figure 6.1. The absolute time is from the 1024th sample of the 234th block of data, sampled at the probe #17 for $Re_D = 156\,800$, and $x/D = 2.0$. The instantaneous velocity is the streamwise fluctuation velocity. There is nothing special about this choice; it was selected at random and any other interval could have been used.

In the top plots of Figure 6.1 the reconstructed velocities using only the first and the first two POD modes are compared to the original velocity trace. In the middle figure, the first 3 and first 4 POD modes are used. And in the bottom figure, the first 5 and all 6 POD modes are used for the reconstruction. All reconstructed traces follow the original velocity. After adding up first 3 POD modes, all major characteristics including peaks are recovered. It is clear that even the reconstructed velocity using only the first POD mode follows the main characteristics of the original velocity, although without the small fluctuation peaks. This is consistent with observations of Glauser & George (1987*b*) and Citriniti & George (2000). The difference between the different curves is relatively very small, since the higher POD modes contribute only a small portion of the total kinetic energy.

6.2.2 A full field simulation of the fluctuating velocity

The original streamwise velocity field measured by a 138 hot wire probe array can be compared to the reconstructed POD velocity field to see how POD truly recovers the original velocity field. Using the eigenvalue distribution the dominant modes were chosen as follows: For the POD (radial) mode shown in Figure 5.1, the first POD mode ($n = 1$) was used for reconstruction due to its dominance of the turbulent kinetic energy. For the azimuthal modes, modes of $m = 0, 3, 4, 5, 6, 7$ were chosen for the range of $x/D = 2.0$ to 3.0. In the range of $x/D = 3.5$ to 6.0 azimuthal mode $m = 0, 1, 2, 3, 4, 5$ were selected for the reconstruction. These are consistent with

Figures 5.17, 5.20, and 5.23.

Figure 6.2 presents a three-dimensional and a two-dimensional surface contour plot of the fluctuating streamwise velocity as a function of r, θ for a sequence of time steps. The fields selected is from the 1346th data set at a 234th block at downstream position, $x/D = 2.0$, for $Re_D = 76400$.

The original fluctuating velocity field has many peaks, and it is difficult to differentiate the large-scale structure from the seemingly random field. But when the first POD mode and all azimuthal modes (in b) are used for reconstruction, the reconstructed field shows large structures. But it has many peaks which makes the picture unclear in the surface plot. When the first POD mode and only the selected azimuthal modes 0,3,4,5,6, and 7 are chosen, the large-scale structures are clearly shown, and also the azimuthal mode character is clear. From the Figure (c), these modal interactions are quite clear, but it is not at all clear in Figure (a) and (b).

6.3 Large-scale structure dynamics

6.3.1 Animation of the structures

To illustrate the interaction and the evolution of the large-scale structures in the mixing layer, a sequence of 3-D animations is presented. This animation is reconstructed for a single downstream location, in the manner of Citriniti & George (2000). As noted in the preceding section, only a few modes are necessary to reconstruct the large-scale structures of the mixing layer. Therefore only the first POD mode ($n = 1$) and the dominant azimuthal modes are used here. Which azimuthal modes are dominant depends on the downstream direction. Therefore mode 0, and modes 3 to 7 are used in the range of $x/D = 2$ to 3.5, while modes 0 to 5 are used in the range of $x/D = 4$ to 6, according to their kinetic energy contributions (Figures 5.17, 5.20, and 5.23).

A data set for animation was chosen arbitrarily as the 234th block out of 388

blocks, starting at the 1024th data sample in the block. Each time step or index has a real time span of $249.9\mu s$ since data was sampled at frequency of $4001.6\,Hz$. To give a better understanding of the evolution and the interactions of the structures, a time series animated movie was made. Each movie has 12 frames per second with a range of data set of 1024 to 1624 out of the 4096 samples/block. The total real time span is $150\,\mu s$ ($600 \times 250\,\mu s$). These animated movies can be seen on the web site of "http://www.tfd.chalmers.se/trl/". All frames has a time index which tells the real time span.

The temporal integral scale can be estimated as:

$$\tau = \frac{l}{U_C}$$

where l is a longitudinal integral scale, and U_C is a convection velocity. The longitudinal scale in the shear layer is given as $0.07x$, and the convection velocity is assumed to be 60 % of the centerline velocity (Khwaja 1981; George *et al.* 1984). Thus, the temporal integral scales are in the range of 953 to $5700\,\mu s$, which means that there are at least 3 frames per integral scale.

In the following section, only a few frames are presented. These have been selected from the animated movies to describe the main characteristics of the coherent structures. Only the movies themselves can convey the entire picture.

6.3.2 Interactions of the large-scale structure

Sampled frames are presented at different downstream locations for three different Reynolds numbers in Figures 6.3 to 6.21. These have been chosen as representative of the main characteristics or dominant structures.

In Figures 6.3 to 6.6, the main characteristics of the azimuthally coherent structure are presented at $x/D = 2.0$ for three Reynolds numbers. The azimuthally coherent

volcano-like eruption described by Citriniti & George (2000) is clearly present in the uppermost figure, and it evolves in the same way they described. It assumed that this is one of the azimuthally coherent vortex rings observed in flow visualization (e.g. the pictures by Wille and Michalke in Van Dyke 1982) and conditional sampling experiments (e.g. Zaman & Hussain 1984). The eruption (top, Figure 6.3) forces high-velocity fluid through its center along with what we believe to be remnants of mode-6 in the potential core, while a new azimuthal mode-6 structure appears outside. The "volcano" passes quickly leaving an azimuthally coherent structure (mode-6) in the potential core. Note that the higher modes (e.g. 4 to 6) dominate the temporal pictures since they are mostly outside the core of the flow and are therefore being swept past the probes more slowly. But it is the eruption that has most of the energy. The same animation at higher Reynolds number clearly shows the same evolution, but with more velocity fluctuation.

Figures 6.7 to 6.10 are for the downstream location $x/D = 3.0$. These are similar to $x/D = 2.0$, where the large-scale structures are well-organized, and higher modes appear around the volcano-like structure. Mode-5 is dominant, however, and appears in both the potential core and the outside region as well.

The flow visualizations of Liepmann & Gharib (1992) show coherent structures with similar characteristics in the potential core and outside region while the potential core exists. They showed streamwise vortex ribs around the volcano and azimuthal coherent structures in the braid region. These together with observations here are consistent with the idea of the higher mode structure outside being entrained into a passing vortex ring.

Unlike the reconstruction at $x/D = 2$ and 3, those at $x/D = 4.0$ are quite different, as shown in Figures 6.11 to 6.13. The volcano-like eruption still exists, but it is very weak. Figures 6.12 and 6.13 show mode changing from mode-4 to mode-3, and

mode-2 to mode-3. This is consistent with the eigenspectra shown in Figures 5.17, 5.20, and 5.23, since the dominant azimuthal mode is around 4.

At downstream location $x/D = 5.0$ for all Reynolds numbers, the coherent features show disorganized evolution, and are not periodic. Mode-0 is very small and has almost disappeared. Unlike the volcano-like eruptions, a 'propeller-like' motion is observed here, which rotates slowly from frame to frame.

At $x/D = 6.0$, the coherent structure is more simple. Mode-0 is almost gone, and only lower mode numbers are observed for all Reynolds numbers, consistent with Figures 5.17, 5.20, and 5.23. Azimuthal mode-2 and mode-3 appear in Figures 6.17 to 6.21, showing quite large-scale structure. Energy shifting from one peak to another is quite obvious. Various mode numbers are observed, but the lower mode numbers dominate the evolution.

In summary, it is clear that the coherent feature changes structure from the volcano-like eruptions to the 'propeller-like' motion as the downstream distance is increased. This is explained easily by the disappearance of azimuthal mode-0, as expected from Figures 5.17, 5.20, and 5.23, and the shift of the higher mode peak to lower mode numbers (i.e., from mode-6 at $x/D = 2.0$ to mode 2 at $x/D = 6.0$). Of course, over this same span the mean velocity profile has evolved from a near top-hat with a well-defined potential core to an almost fully-developed profile.

6.4 Life-cycle of large-scale structure

6.4.1 Periodicity of coherent structures

While the mode-0 coherent structure exists, the volcano-like events show a quasi-periodic behavior in time. By counting the numbers of frames of the reconstructed

velocity field, the passage frequency of a life-cycle of the 0th mode coherent structure can be calculated using the sampling frequency, $4001.6\,Hz$ (in a manner Citriniti & George 2000). Passage frequencies are shown only for the range of $x/D = 2$ to 4, since the life-cycle of the evolution is clearly evident in that range only.

In Figure 6.22, the Strouhal frequencies from the velocity spectra (Figures 4.16 to 4.24), the 0th mode from eigenspectra (Figures 5.35 to 5.49), and the passage frequencies determined above are plotted altogether. They collapse reasonably for all Reynolds numbers ranging $x/D = 2.0$ to 4.0. Thus, it seems reasonable to conclude that all have a close relation to the volcano-like eruptions which appear to dominate the dynamics at these upstream locations.

6.4.2 The Glauser-George life-cycle

Glauser & George (1987*b*), and Grinstein *et al.* (1995) suggested a two-ring model for the axisymmetric jet which consists of 4 stages of turbulence evolution for the coherent structures in the mixing layer, summarized as;

1. **Formation from base flow**: Vortex ring-like concentrations arise from an instability of the base flow.

2. **Attempted Leap-frogging**: While multiple ring interactions may occur, the interaction between pairs of rings dominates. In particular, a rearward vortex ring overtakes the vortex ring ahead of it, the rearward vortex being reduced in radius and the forward being expanded by their mutual interaction.

3. **Instability**: The rearward ring is stabilized by the reduction in its vorticity and radius, and the increase in its core area, which explains the predominance of the 0th mode on the high speed side. The forward ring has its vorticity increased by stretching as it expands in radius. This narrowing if its core while the radius is expanding caused the vortex to become unstable, which explains the predominance of modes 4-6 from the center of the shear layer outwards.

The growing wavy deformation of the leading vortex ring causes it to acquire a streamwise component of vorticity which accelerates the instability.

4. **Breakdown and entrainment**: The continued effect of the rearward vortex on the forward and now highly distorted ring accelerates the instability, until its vorticity is entirely in small scale motion. This process is in effect an energy cascade from modes 4-6 all the way to dissipative scales.

From the full field simulations for three Reynolds numbers (Figures 6.3 to 6.21), it is very clear that the coherent structure associated with azimuthal mode-0 behaves as suggested by Glauser & George (1987*b*), and Citriniti & George (2000). Also from the reconstructed fluctuation velocity fields, stage 2 to stage 3 can be clearly seen in Figures 6.3 - 6.5, and 6.7 - 6.9.

There is no support from the reconstructions for this model beyond $x/D = 4$. In fact, the reconstruction (and eigenspectra) make it clear that a very different process takes over downstream. Perhaps the disappearance of mode-0 and the dominance of the higher modes is related to a different kind of stability. A more consistent picture might involve the growth and breakdown of mode-1 and/or mode-2. The mean profile has changed, especially in the core region of the flow. The possible implications of this will be discussed more in Chapter 7.

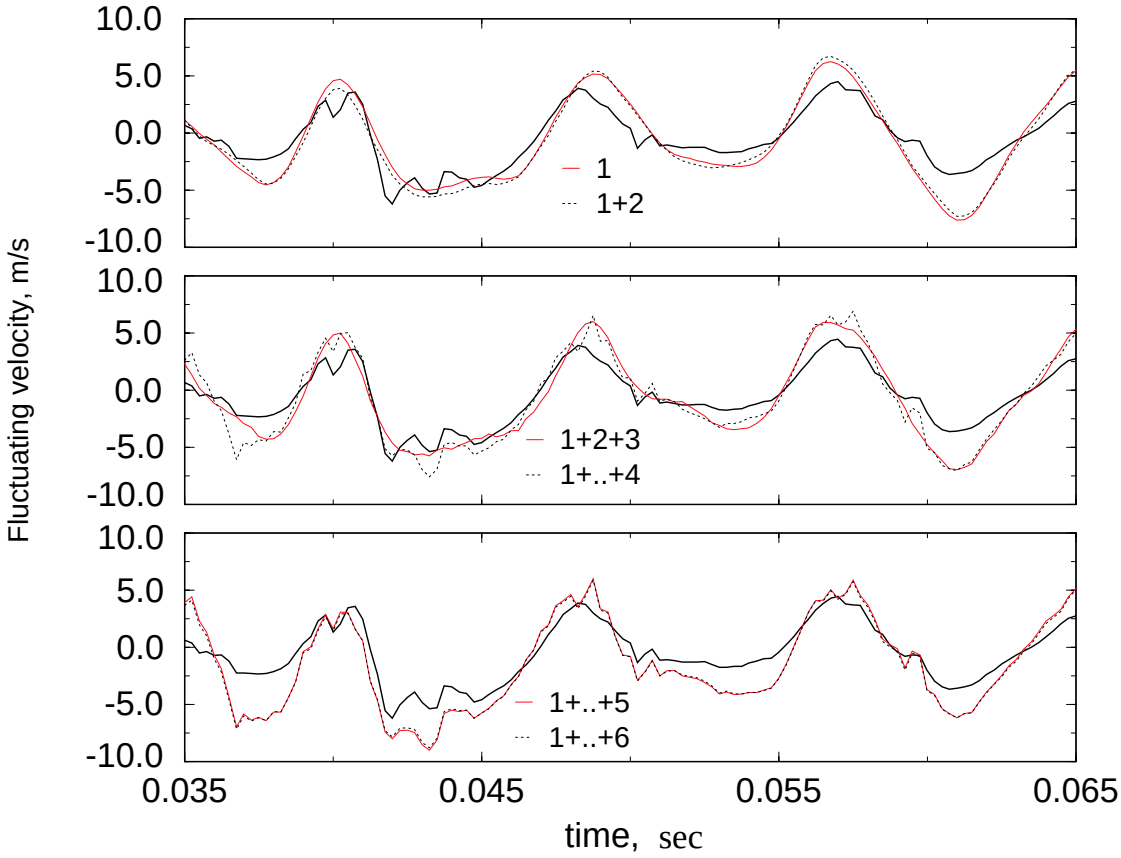

Figure 6.1: POD reconstruction of instantaneous velocity at $x/D = 2.0$ and $Re_D = 156,4800$ for randomly selected time at the probe #17 for Top: first 1 & 2 POD modes, Middle: first 3 & 4 POD modes, and Bottom: first 5 & 6 POD modes; dark solid: original velocity.

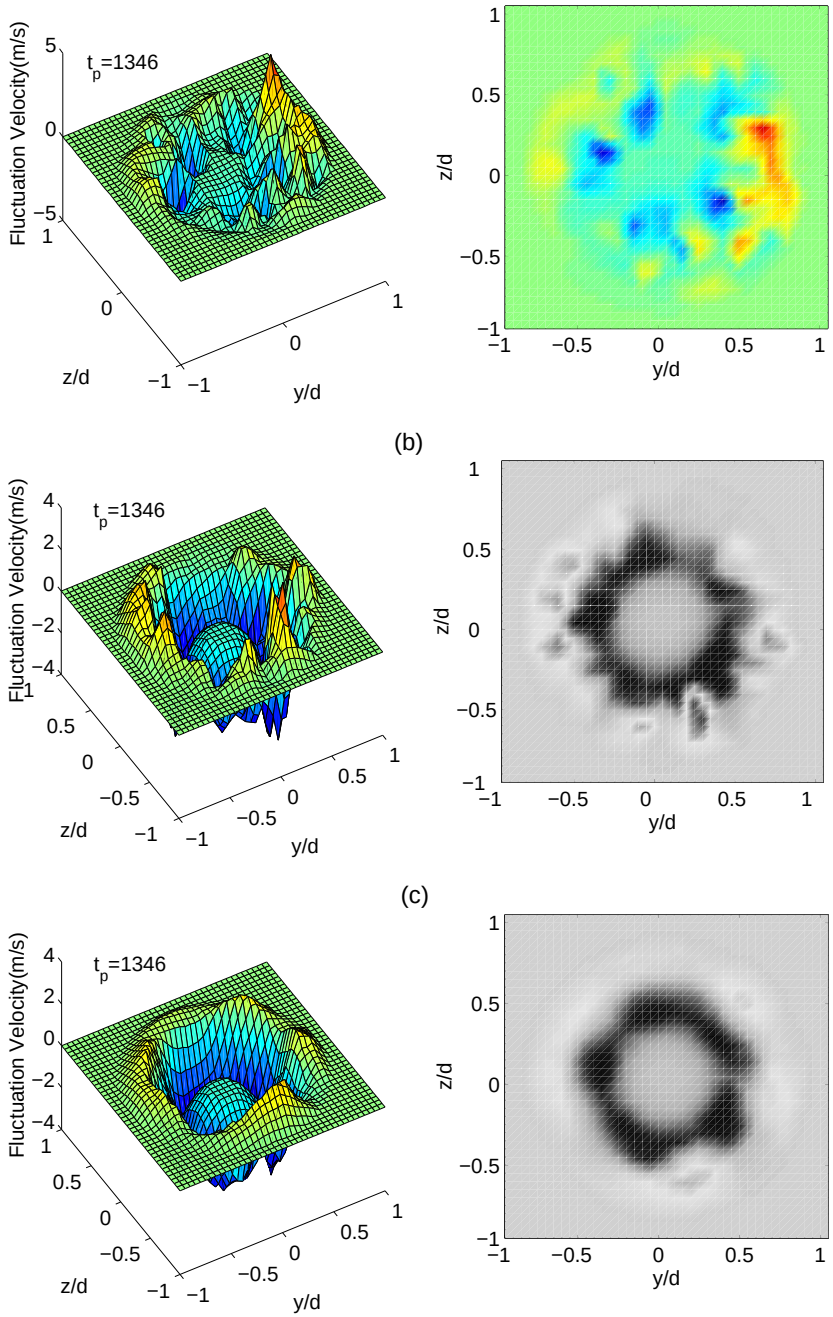

Figure 6.2: Reconstructed streamwise velocity at $x/D = 2.0$, $Re_D = 76400$, and $t_p = 1346$; (a) the original velocity field, and the reconstructed velocity field with the first POD mode and (b) all azimuthal mode, (c) mode=0, 3-7.

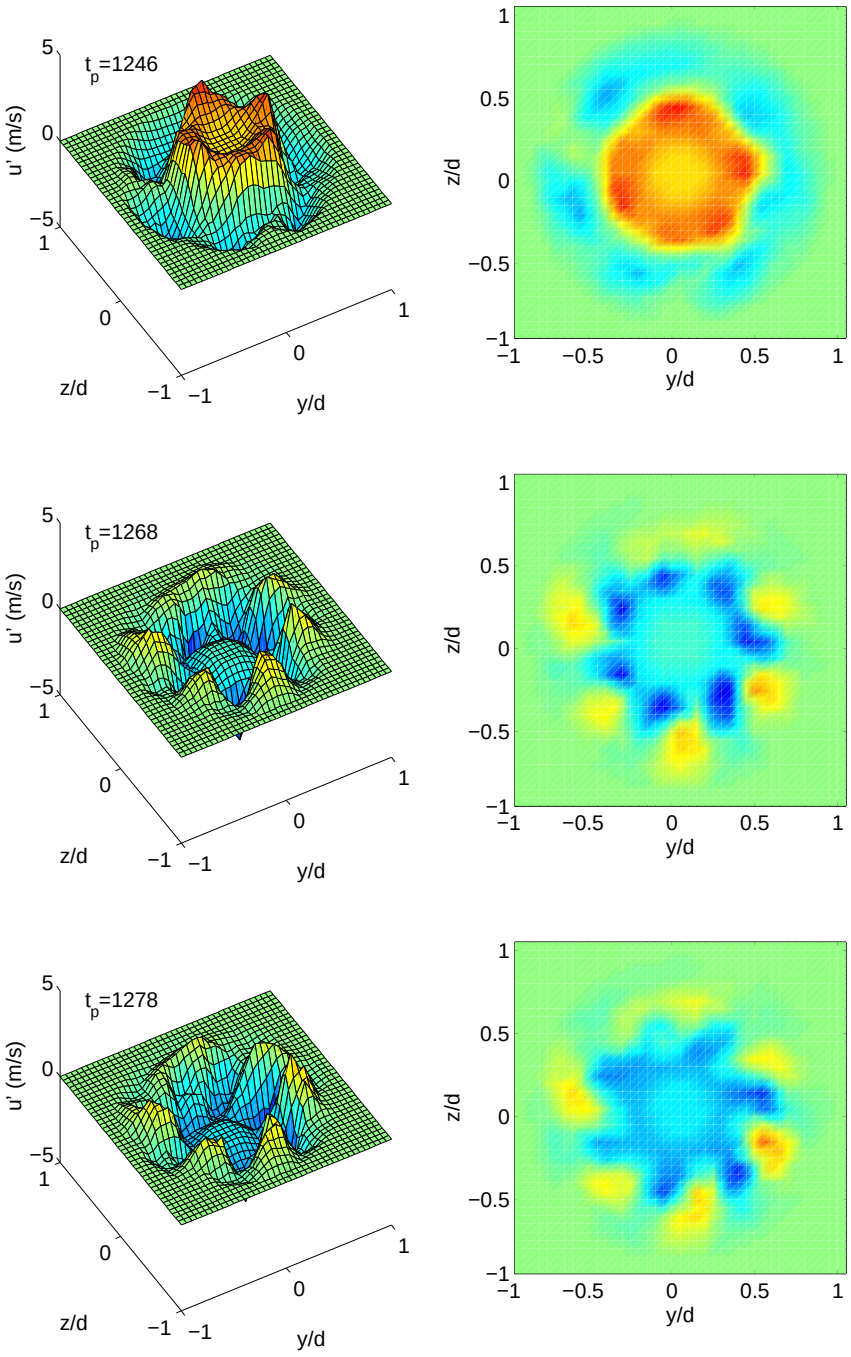

Figure 6.3: Main characteristics of the streamwise velocity field at $x/D = 2.0$, $Re_D = 76400$.

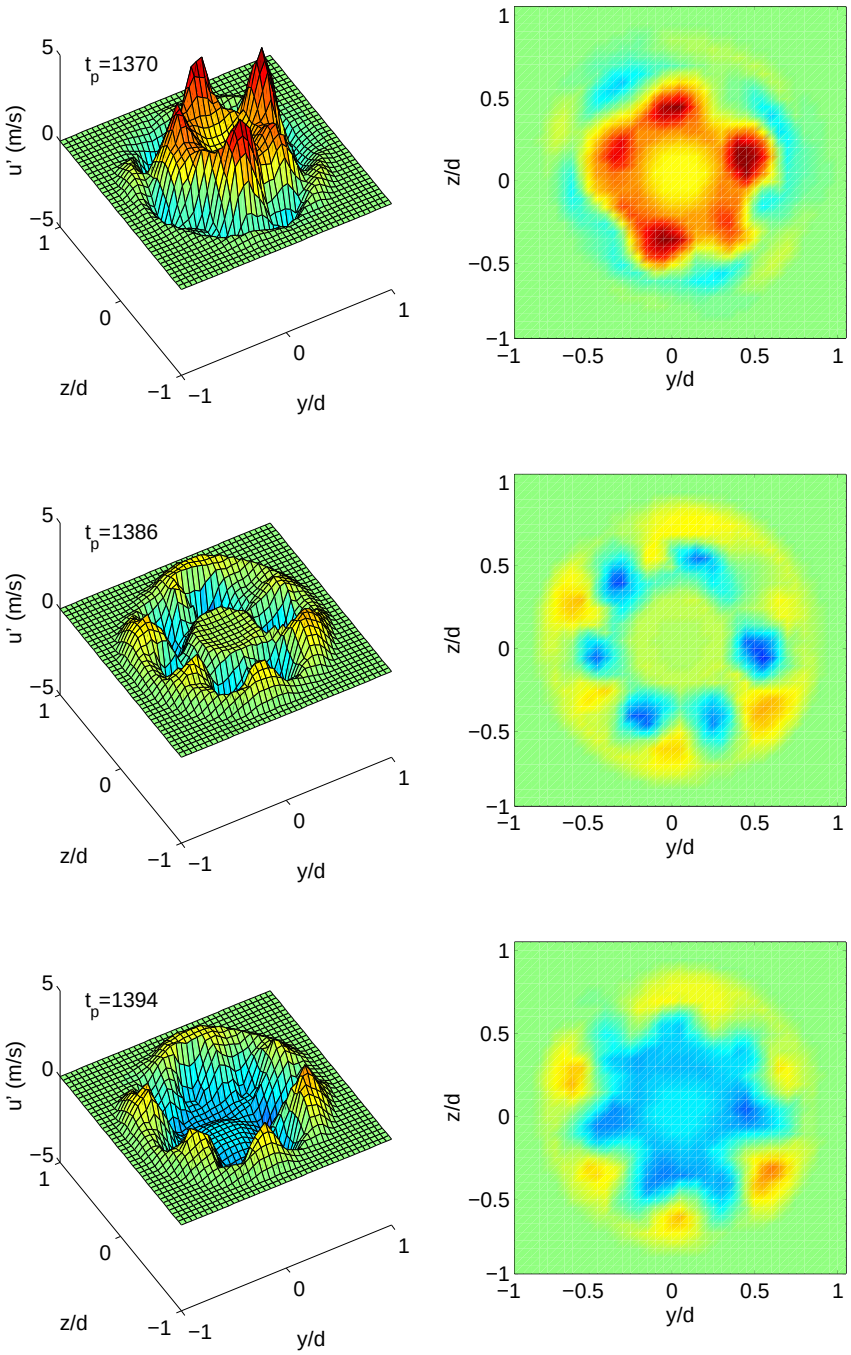

Figure 6.4: Main characteristics of the streamwise velocity field at $x/D = 2.0$, $Re_D = 117600$.

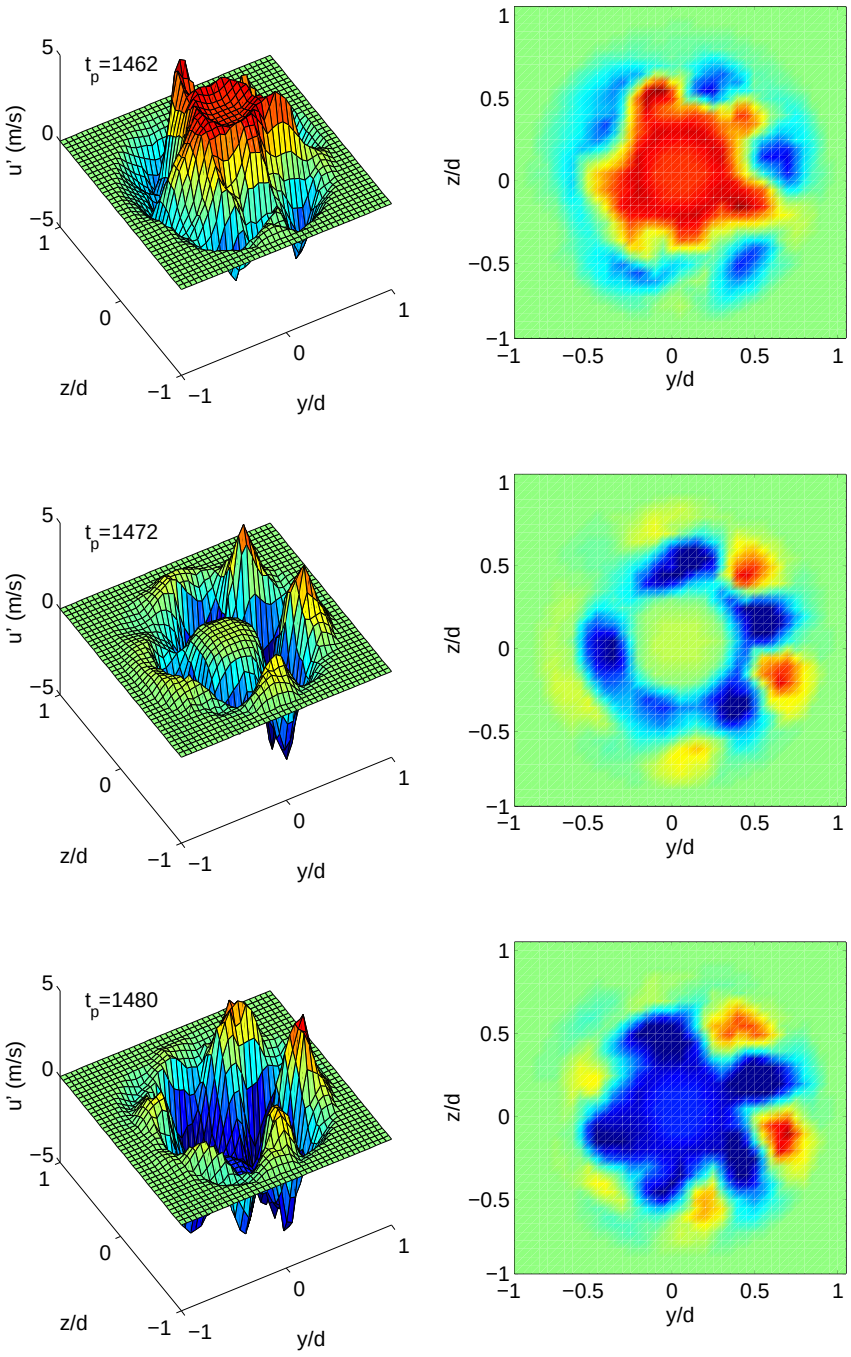

Figure 6.5: Main characteristics of the streamwise velocity field at $x/D = 2.0$, $Re_D = 156800$.

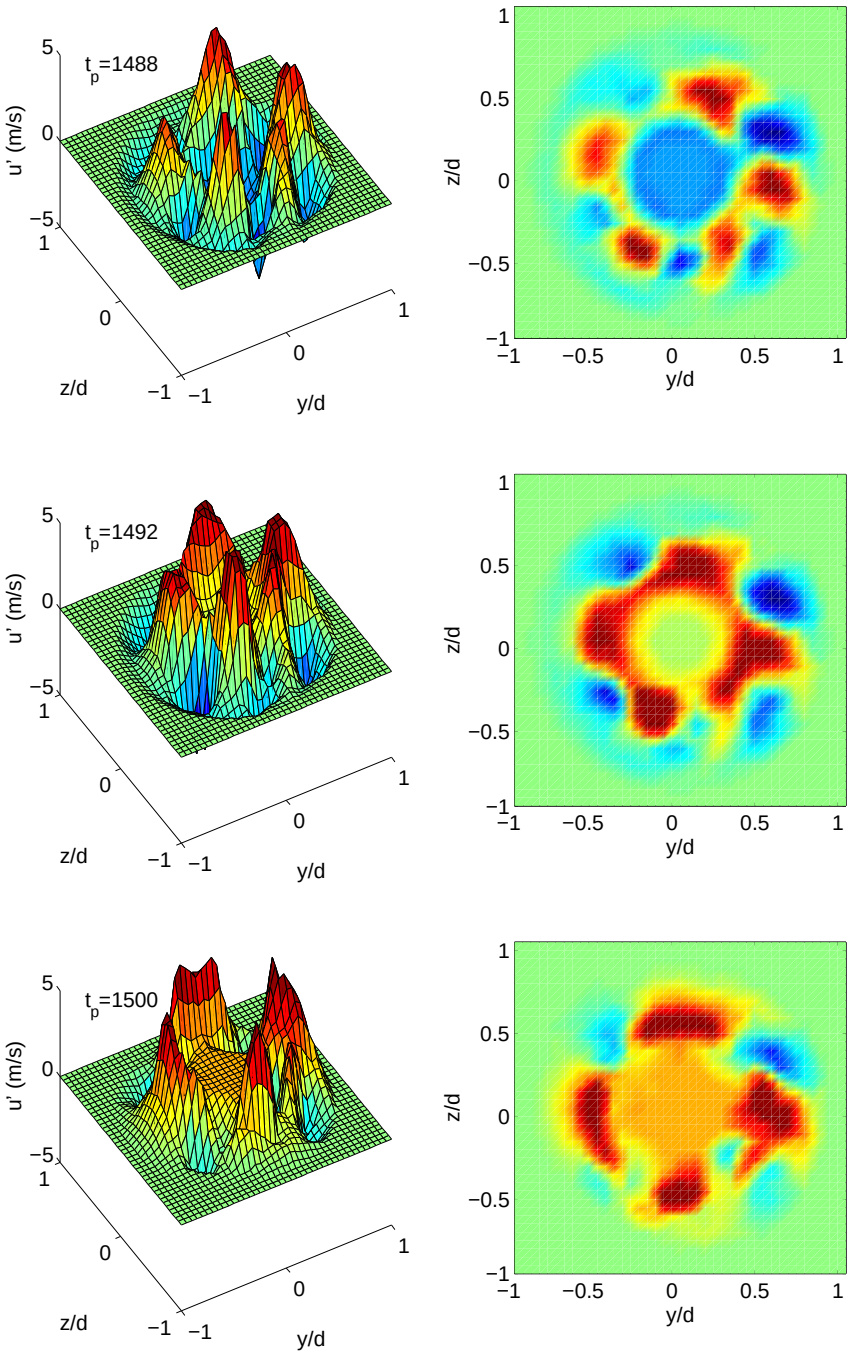

Figure 6.6: Main characteristics of the streamwise velocity field at $x/D = 2.0$, $Re_D = 156800$.

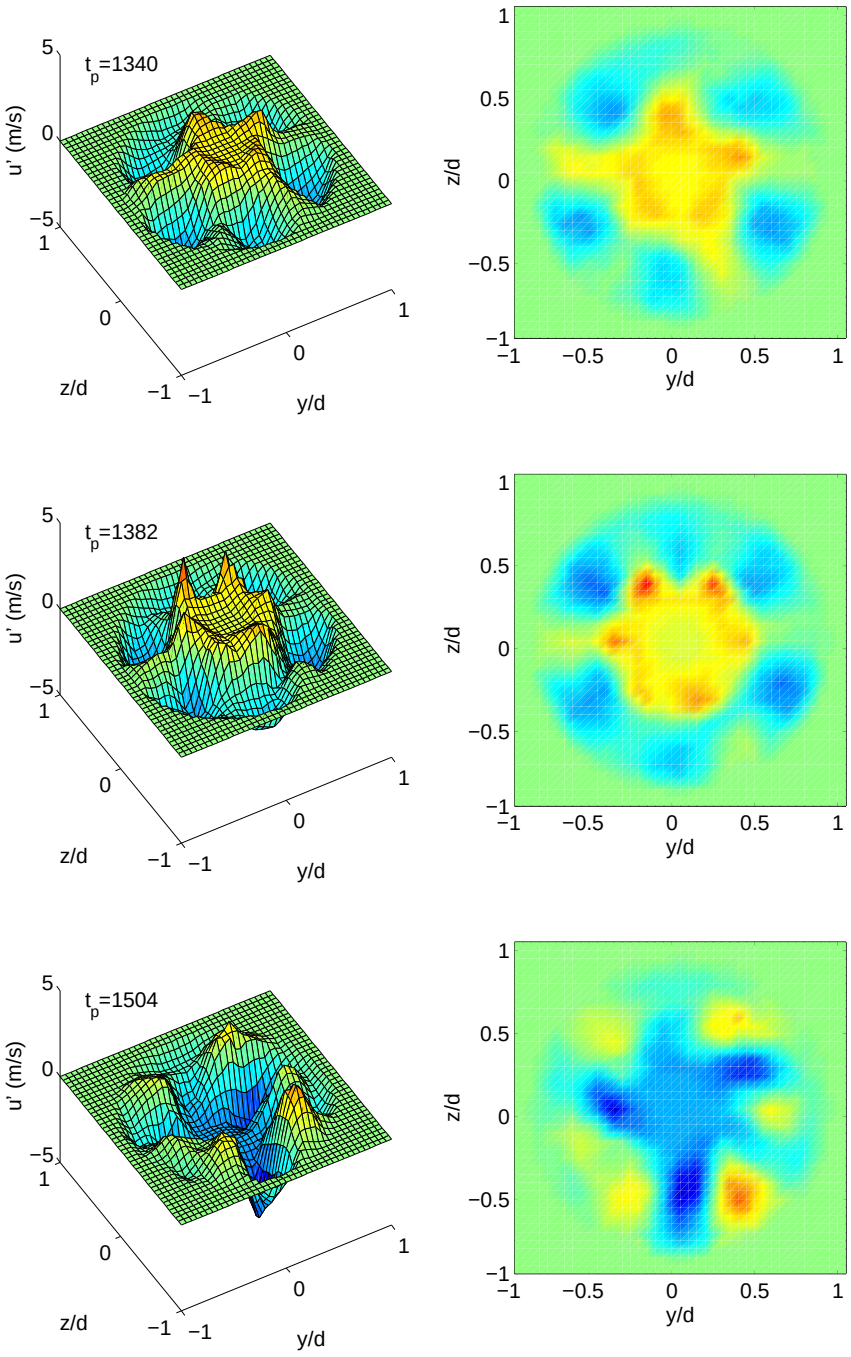

Figure 6.7: Main characteristics of the streamwise velocity field at $x/D = 3.0$, $Re_D = 76400$.

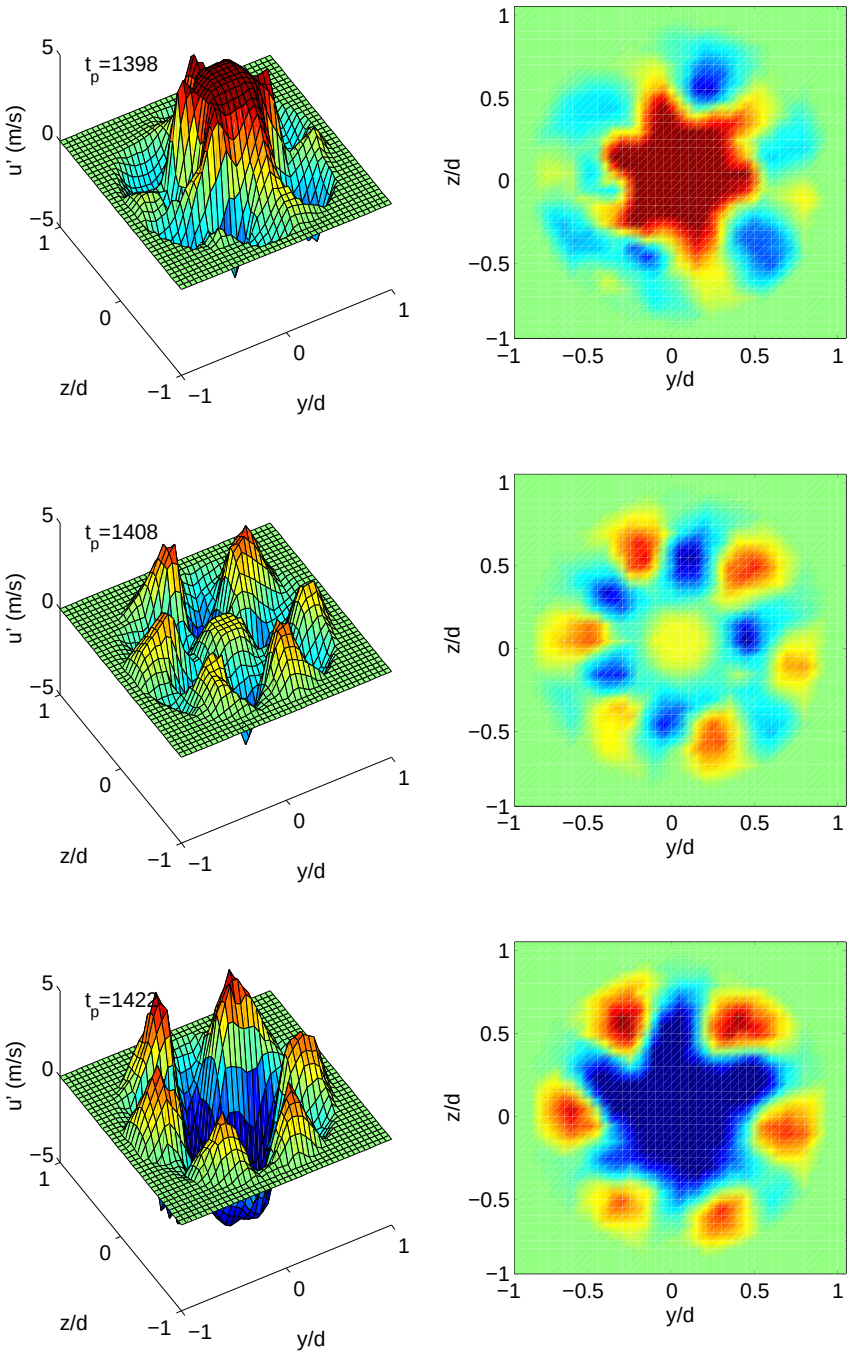

Figure 6.8: Main characteristics of the streamwise velocity field at $x/D = 3.0$, $Re_D = 117600$.

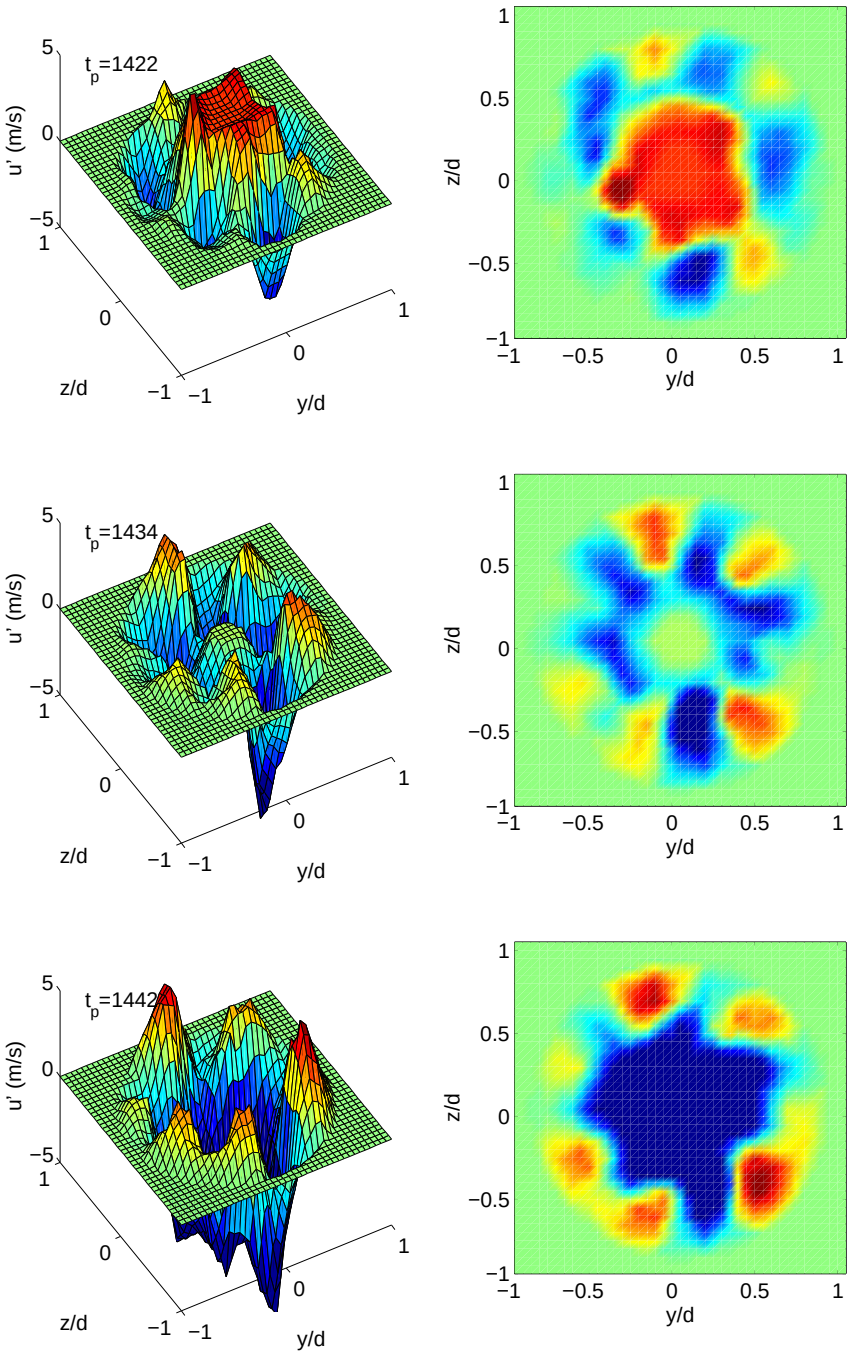

Figure 6.9: Main characteristics of the streamwise velocity field at $x/D = 3.0$, $Re_D = 156800$.

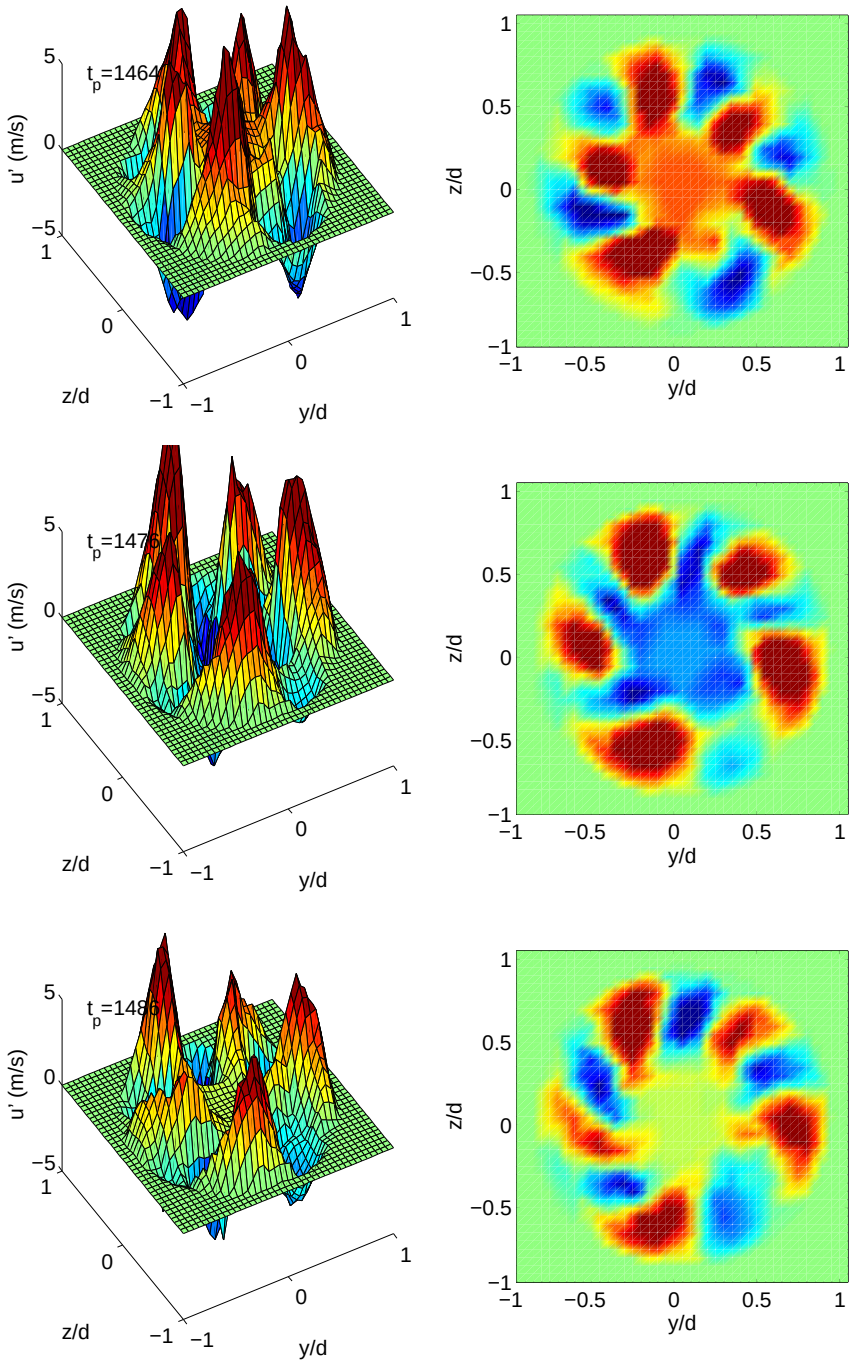

Figure 6.10: Main characteristics of the streamwise velocity field at $x/D = 3.0$, $Re_D = 156800$.

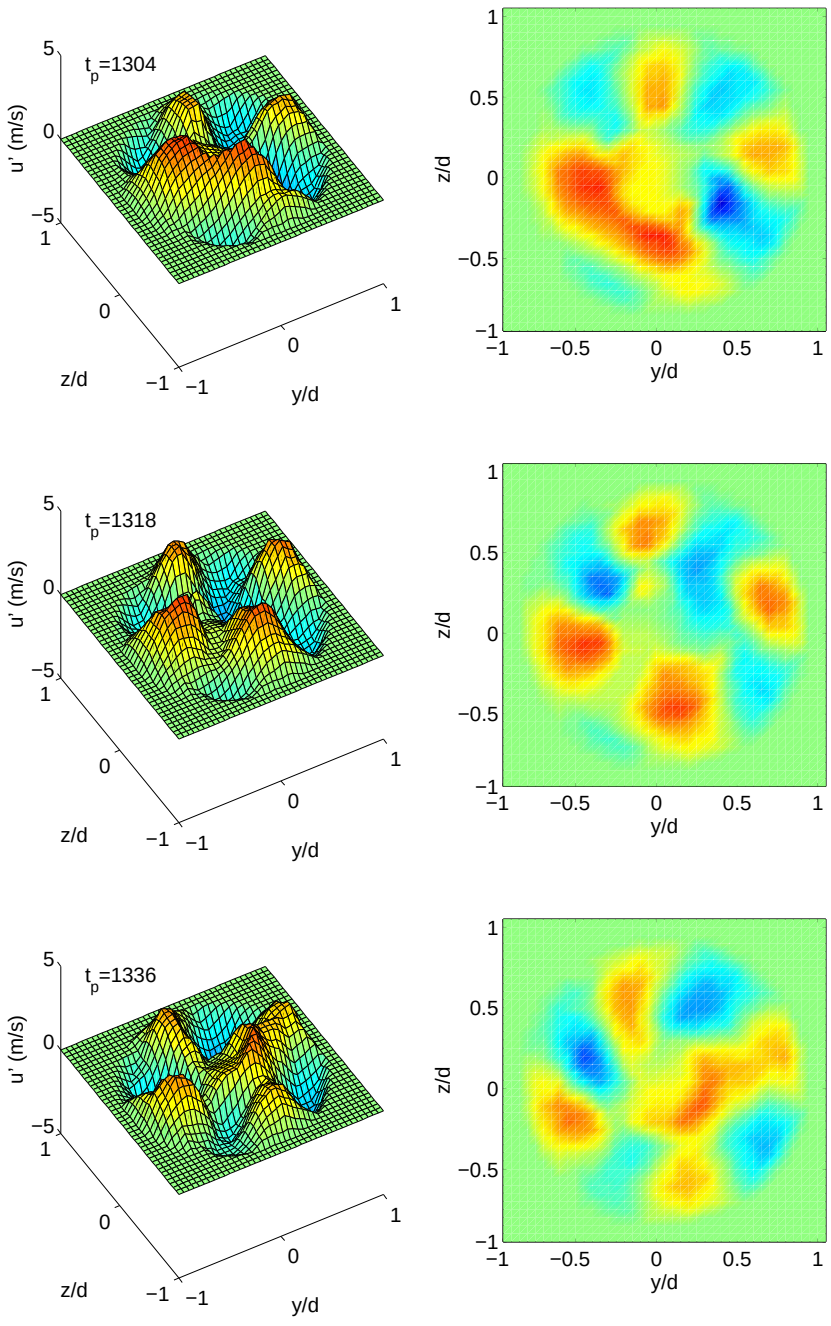

Figure 6.11: Main characteristics of the streamwise velocity field at $x/D = 4.0$, $Re_D = 76400$.

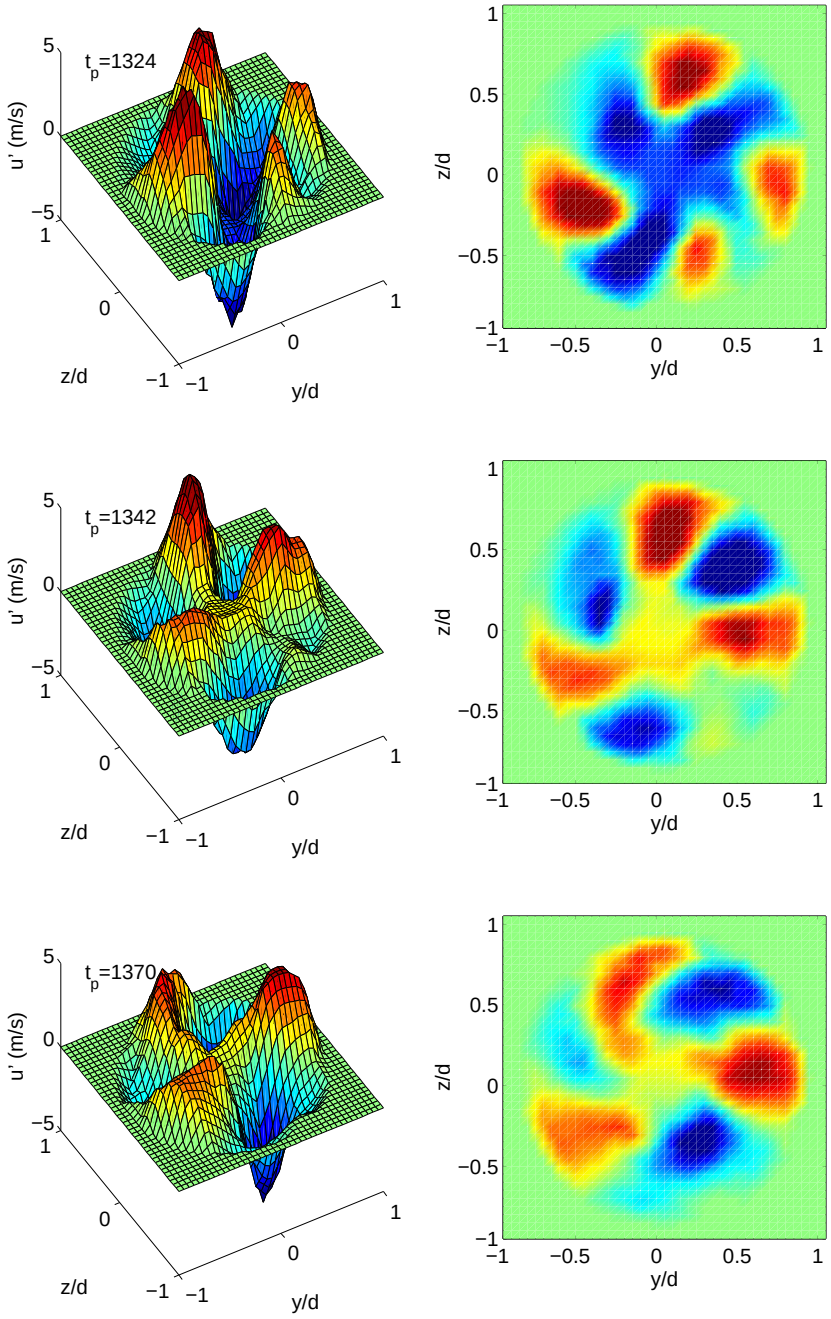

Figure 6.12: Main characteristics of the streamwise velocity field at $x/D = 4.0$, $Re_D = 117600$.

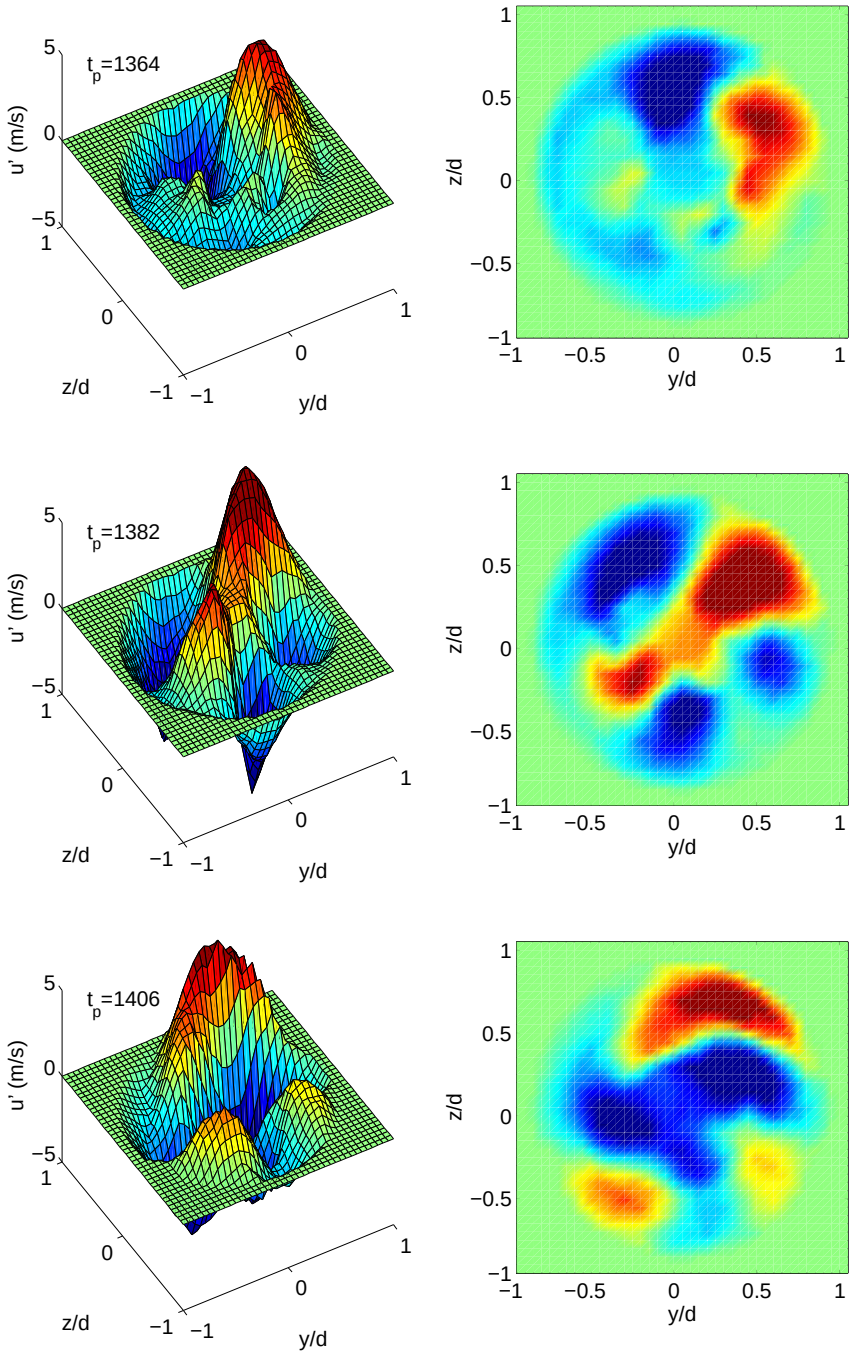

Figure 6.13: Main characteristics of the streamwise velocity field at $x/D = 4.0$, $Re_D = 156800$.

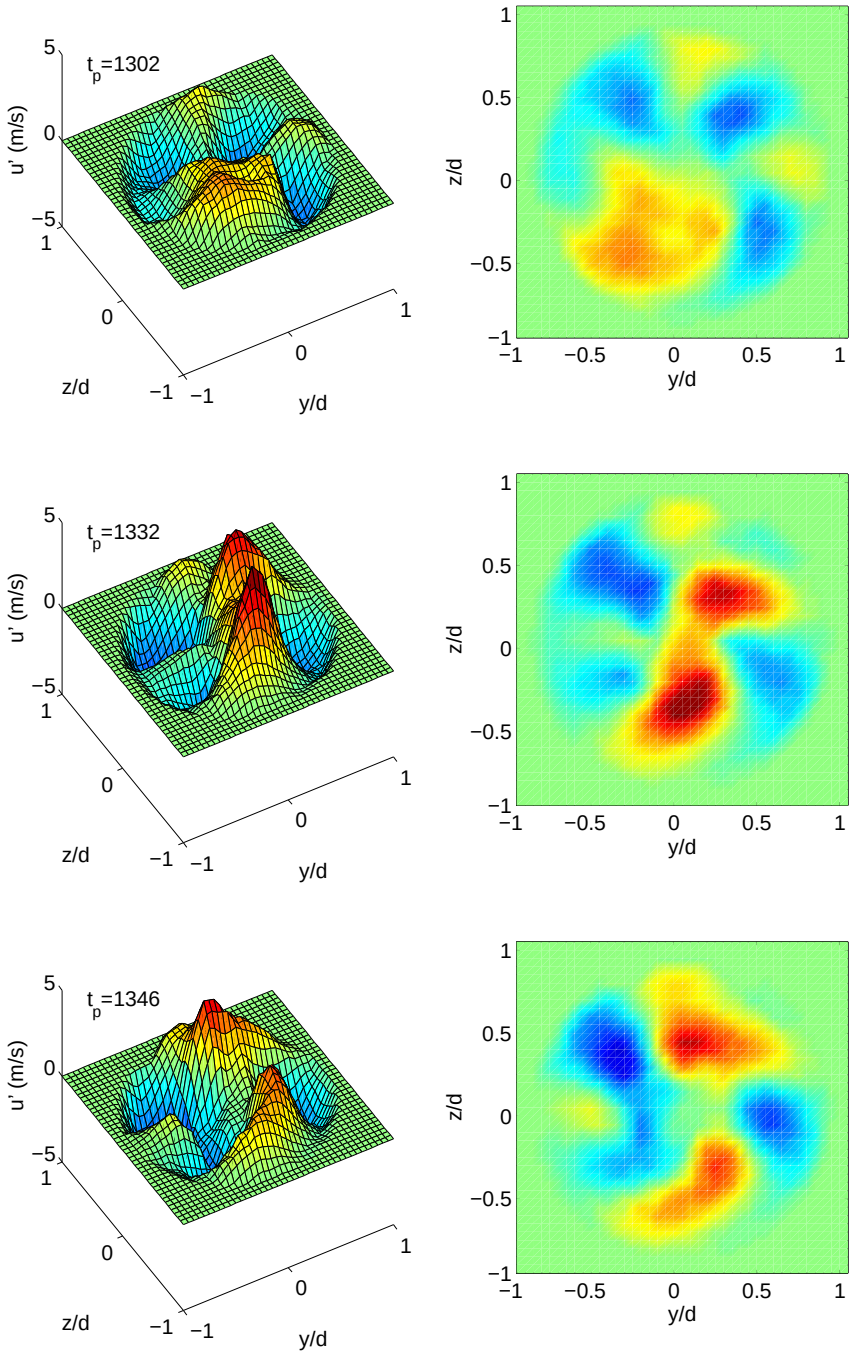

Figure 6.14: Main characteristics of the streamwise velocity field at $x/D = 5.0$, $Re_D = 76400$.

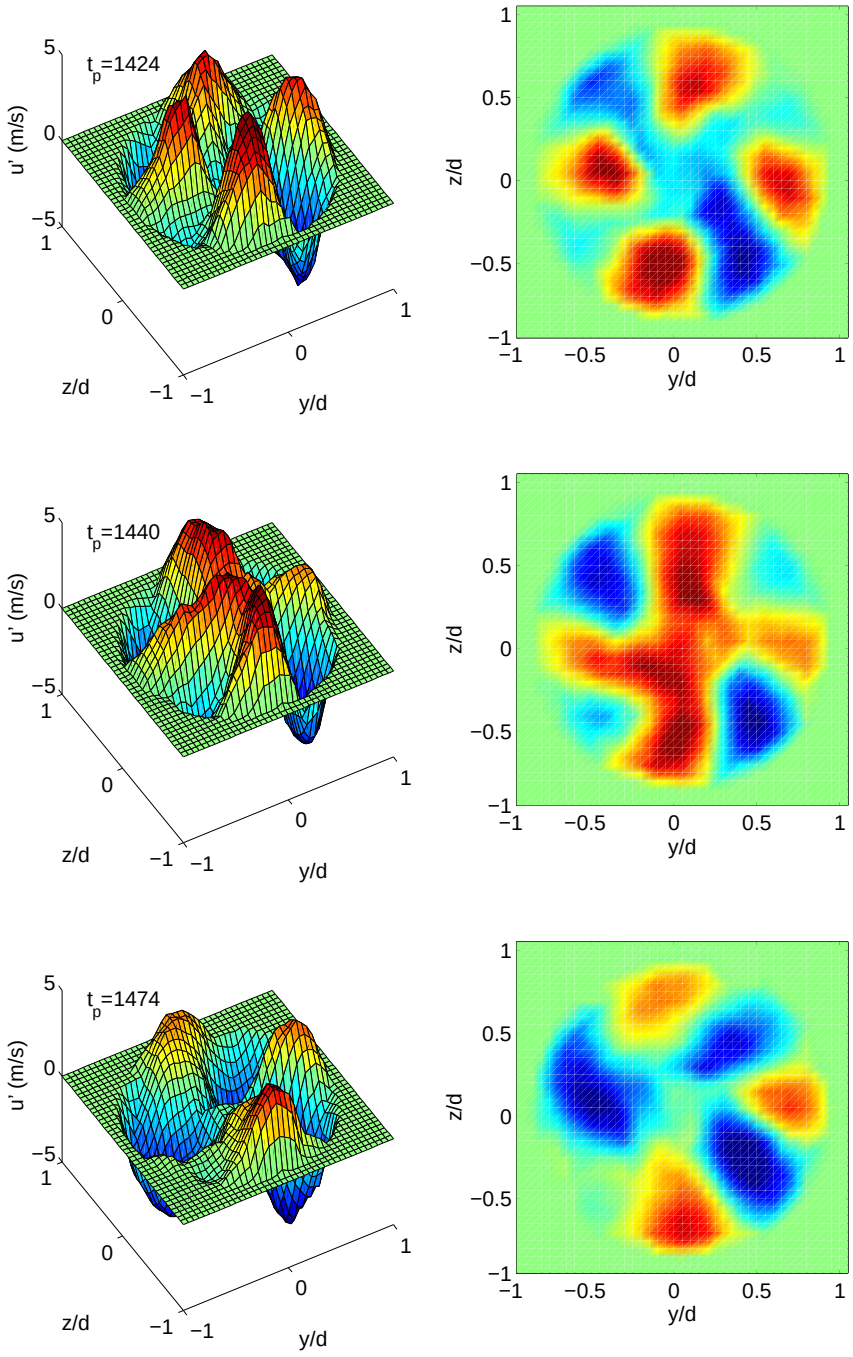

Figure 6.15: Main characteristics of the streamwise velocity field at $x/D = 5.0$, $Re_D = 117600$.

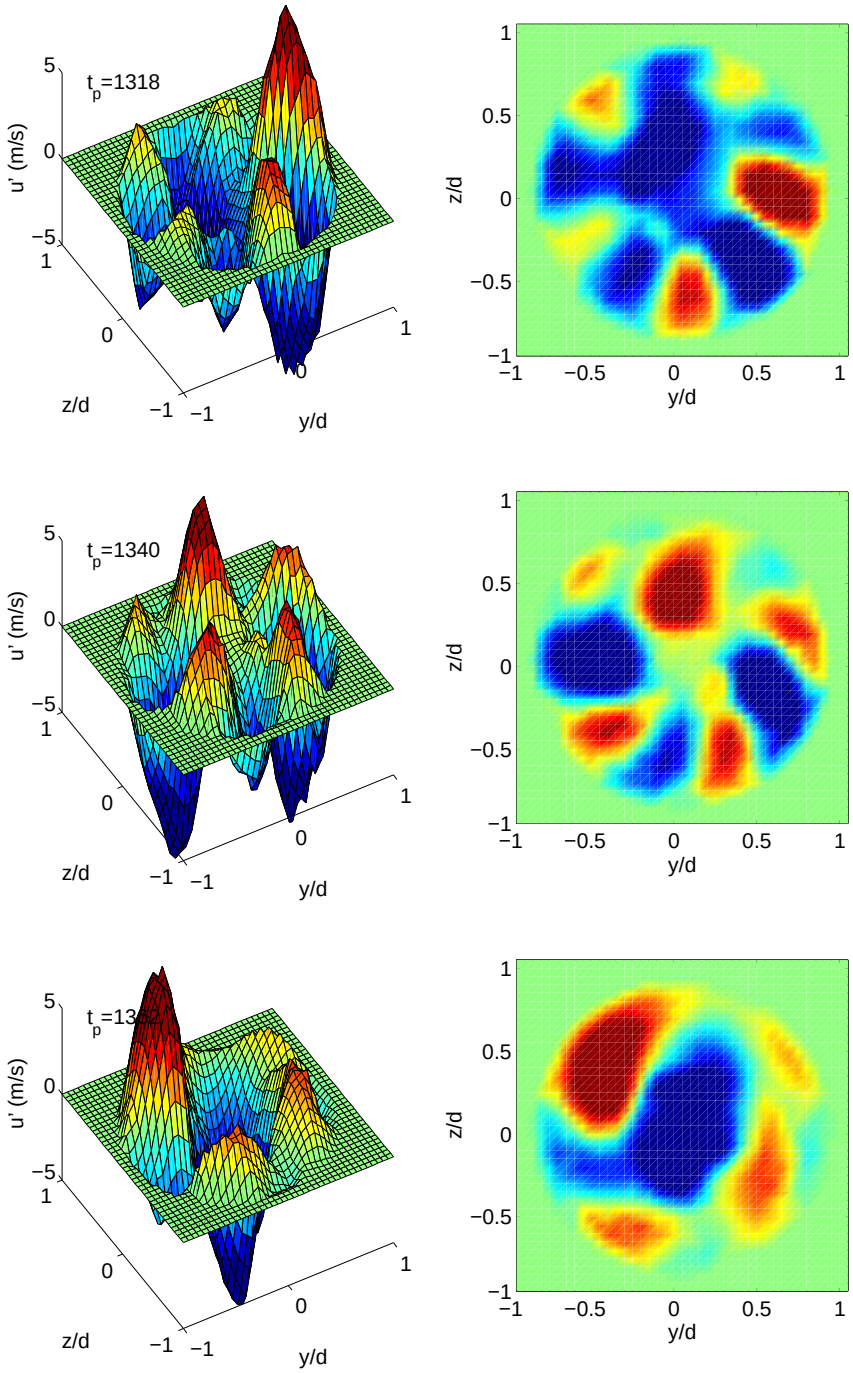

Figure 6.16: Main characteristics of the streamwise velocity field at $x/D = 5.0$, $Re_D = 156800$.

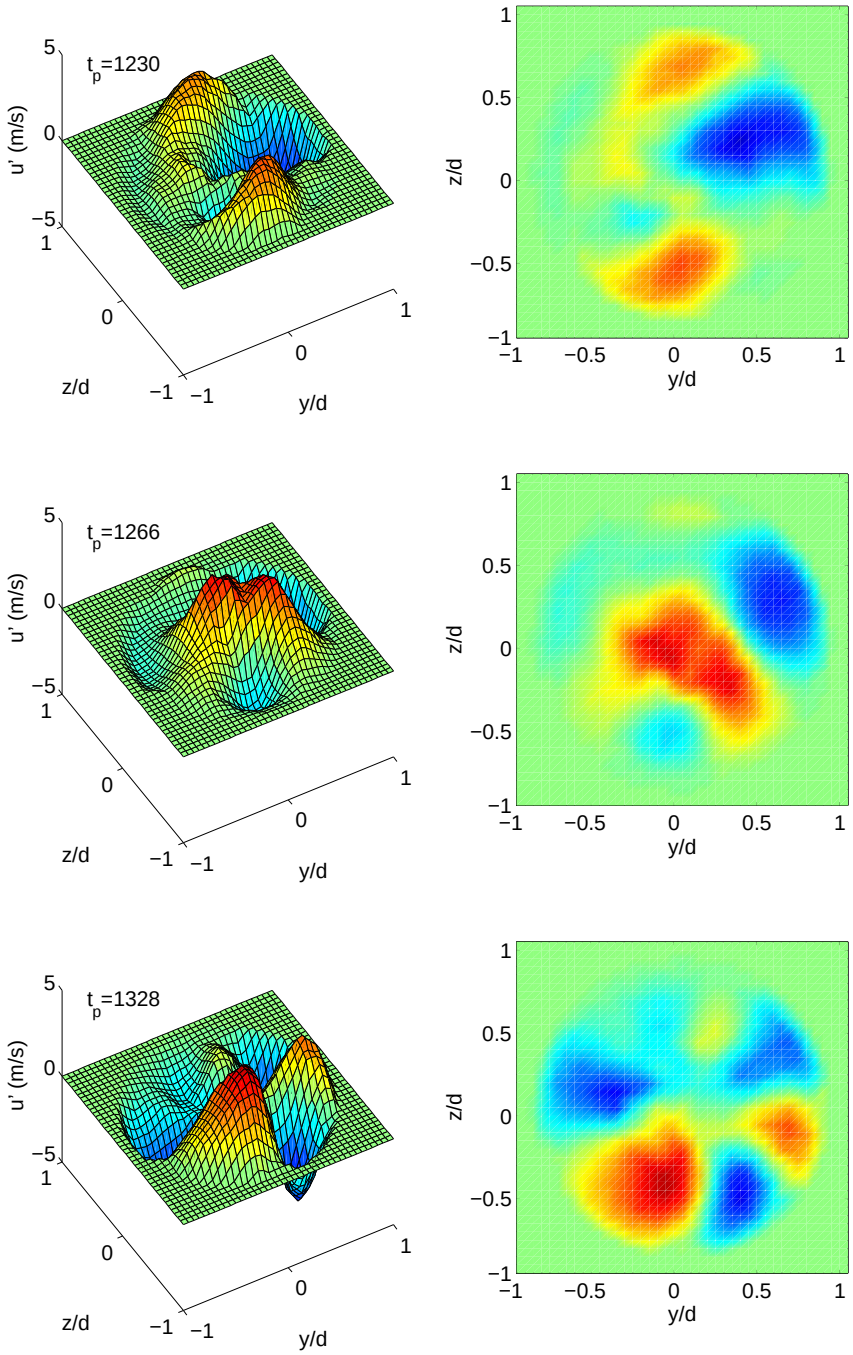

Figure 6.17: Main characteristics of the streamwise velocity field at $x/D = 6.0$, $Re_D = 76400$.

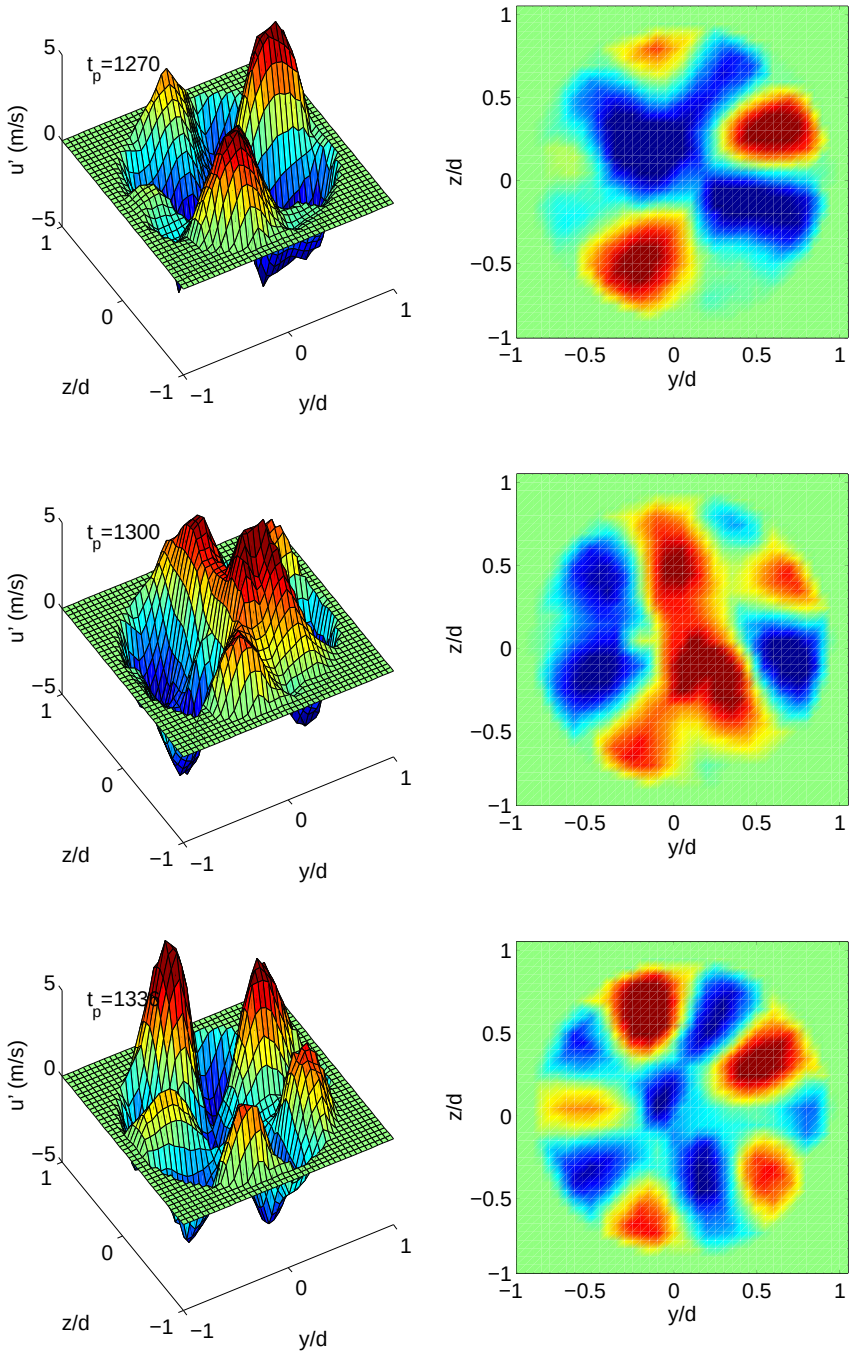

Figure 6.18: Main characteristics of the streamwise velocity field at $x/D = 6.0$, $Re_D = 117600$.

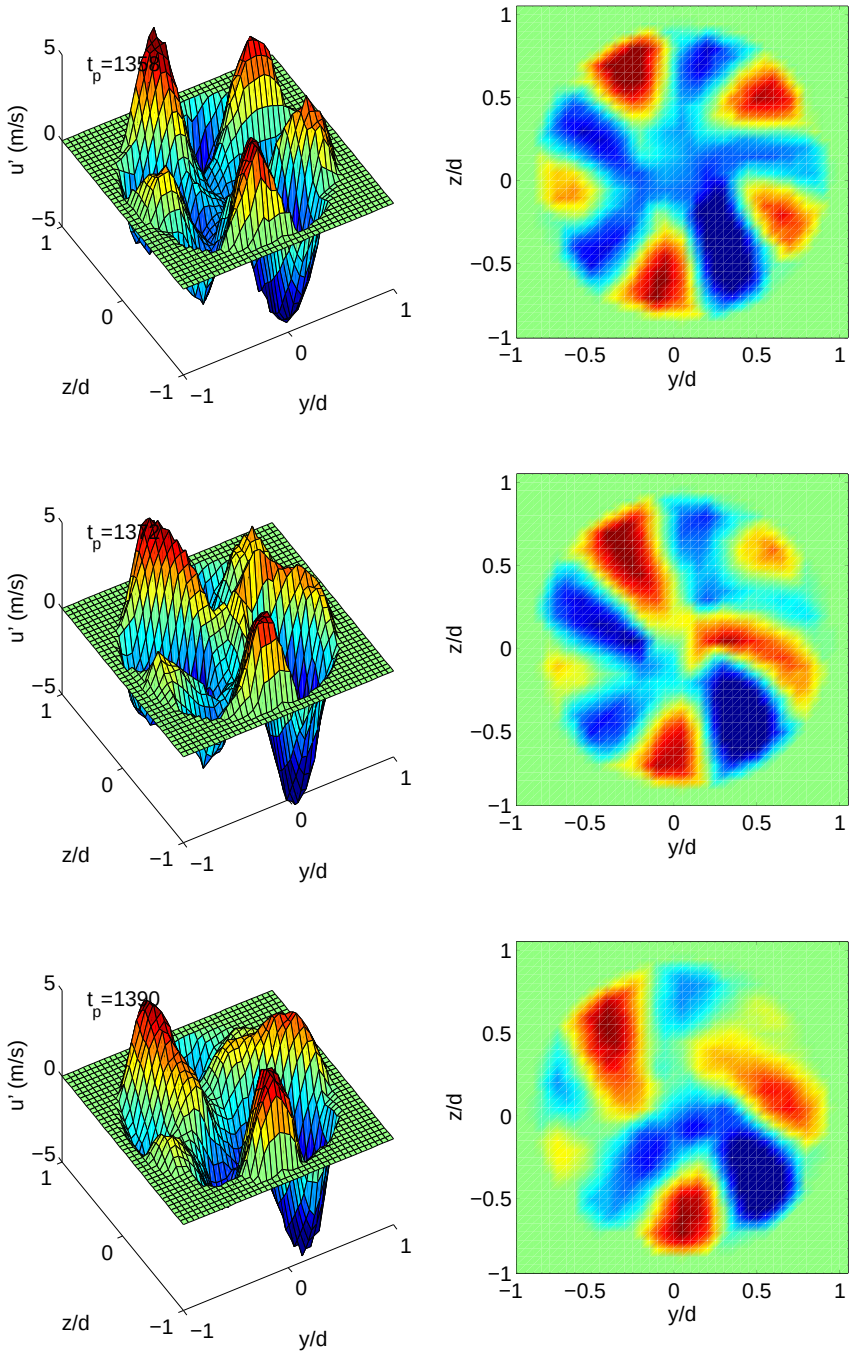

Figure 6.19: Main characteristics of the streamwise velocity field at $x/D = 6.0$, $Re_D = 117600$.

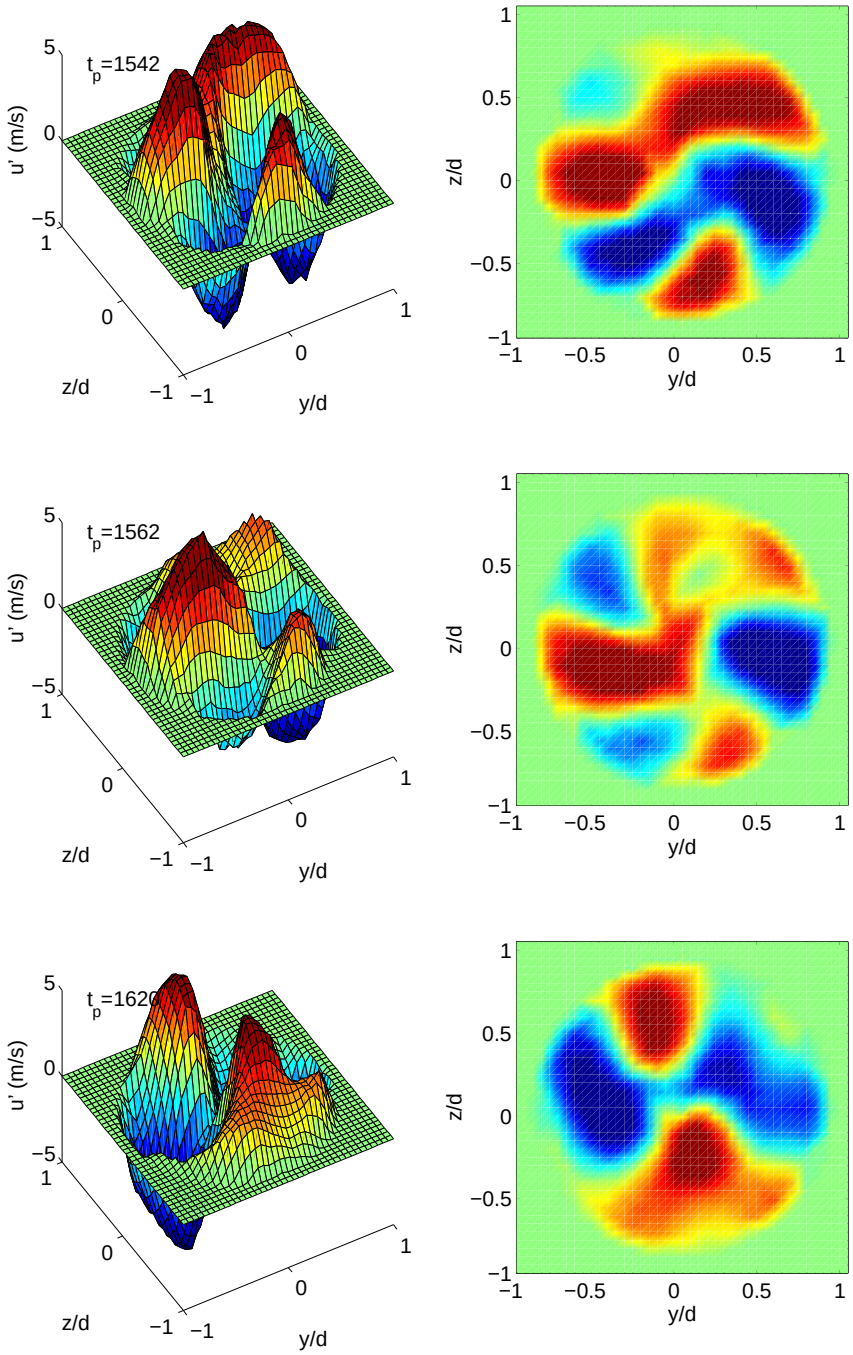

Figure 6.20: Main characteristics of the streamwise velocity field at $x/D = 6.0$, $Re_D = 117600$.

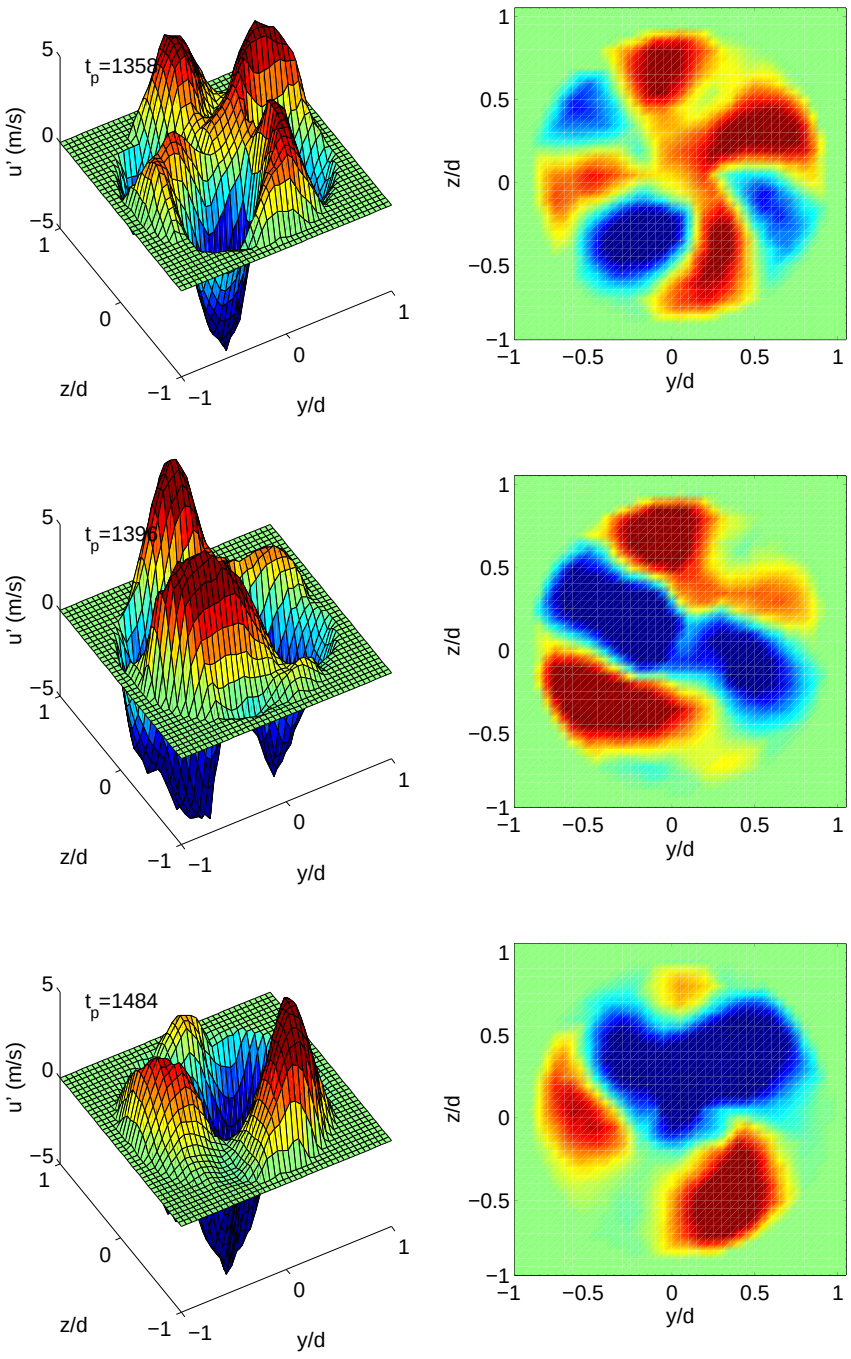

Figure 6.21: Main characteristics of the streamwise velocity field at $x/D = 6.0$, $Re_D = 156800$.

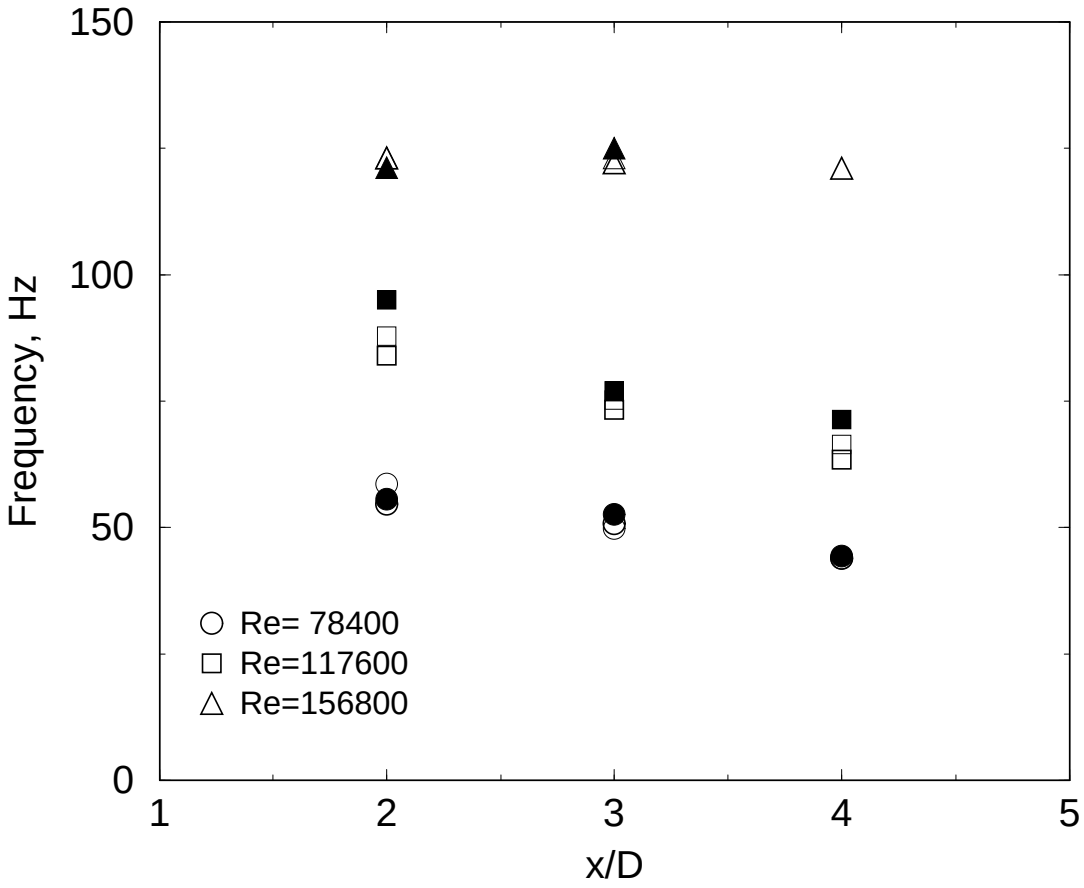

Figure 6.22: Strouhal frequency from velocity spectra (light, unfilled symbol), 0th azimuthal mode frequency from eigenspectra (dark, unfilled symbol), and passage frequency from a life-cycle of the volcano-like eruption (filled symbol).

Chapter 7

Summary, discussion, and conclusions

7.1 The experiment

The large-scale structure of an axisymmetric mixing layer was investigated using the POD for Reynolds numbers of 78 400, 117 600, and 156 800 at $x/D = 2.0$ to 6. Data were sampled simultaneously at all measuring positions at 4 001.6 Hz for 400 sec using 138 hot-wire probes of length of 1 cm. The sampling frequency was sufficient to satisfy the temporal Nyquist criterion. The record length of each block of data was 4 096 samples giving a bandwidth of 0.98 Hz and a length of 1.02 sec. In all, 388 blocks were used in the statistical analysis, which reduced the variance of the cross-spectra to less than 5 %. The Strouhal number of the spectral peak was in the range of 0.25 to 0.5 for all downstream locations.

In addition to applying the POD in the radial direction, the streamwise velocity at each cross-section was decomposed into Fourier modes by both azimuthal mode and temporal frequency. The variations due to downstream positions and Reynolds numbers were discussed in detail. The original velocity field was also reconstructed using only the first POD mode and selected azimuthal modes using a linear combina-

tion of the coefficients and eigenfunctions. From animations of the reconstruction, the interaction between the azimuthal modes and the dynamics of the coherent structure could be visualized.

7.2 Similarity of the energy distribution

From application of the POD in the radial direction, it was observed that the first POD mode contains more than 60 % of turbulent energy at all downstream positions and Reynolds numbers. The first 2 POD modes contain more than 80 %.

The eigenvalues have a strong dependence on the streamwise position, x/D. And mode-0 behaves in a manner entirely different than the higher modes. The main results are as follows:

1. The energy in mode-0 moves to lower frequencies as x/D increases, and the total energy in mode-0 decreases. (Note that because the flow is largely correlated by the probes, frequency is to more correctly representative of wavenumber, $k = 2\pi f/U_c$.) Corresponding to the diminution of mode-0 is the emergence of mode-1. This is consistent with an approach toward homogeneity in the downstream direction, and suggest that perhaps some residual value may control (or reflect) the growth rate of the far jet.

2. The behavior of mode-0 and mode-1 as x/D increases is similar to that predicted from inviscid instability theory. In particular, Batchelor & Gill (1962) show that for a top-hat profile all modes are unstable, but mode-0 grows the fastest. By contrast, once the profile is fully-developed, mode-0 is stable, and mode-1 grows the fastest, at least for a parallel flow. Similar conclusions were reached by Michalke (1965) and Michalke (1984) as well, but for spatially growing disturbances. These stability results are strikingly similar to the behavior of the POD modes which have the most energy and even the eigenfunctions appear to be similar.

3. The energy distribution (with azimuthal mode number and frequency) of the first, second, and third POD modes has a strong dependence on x/D.

4. For azimuthal mode greater than $m = 0$, the energy shifts from higher modes to lower modes ($m > 0$) as x/D increases. In fact, the eigenspectra collapse when scaled in shear layer similarity variables; i.e. λ/xU_0^2 versus fx/U_0 and mx/D.

5. The energy distribution of the first POD mode has no dependence on Reynolds numbers over the range of these experiments. This is contrary to the suggestion of Holmes *et al.* (1996) that more complicated modal structures might evolve with increasing Reynolds number. On the other hand, this observation is consistent with suggestion by Glauser (1987) and Citriniti & George (2000) that once the Reynolds number is sufficiently high, there should be no dependence.

6. The Strouhal number associated with the frequency of maximum energy of the eigenspectra of the first POD mode correlates well with Strouhal number of the velocity spectral peak.

7.3 The velocity reconstructions

The instantaneous fluctuating velocity field at each cross-section was reconstructed using the eigenfunctions and coefficients obtained from the projection onto the original instantaneous velocity measured by all of the probes (in the manner of Citriniti & George 2000). From the animations of the velocity field, these main characteristics were observed:

1. Near the jet exit, highly organized and near-periodic evolutions of the large-scale structures are observed.

2. Azimuthally coherent vortex rings, the volcano-like eruptions identified by Citriniti & George (2000), dominate the dynamics and the interactions of the structures until about $x/D \approx 4$.

3. The passage frequency for the volcanic eruption reasonably matches with the Strouhal frequency and 0th mode frequency in the range of $x/D = 2$ to 4.

4. Beyond $x/D \approx 4$, the volcano-like eruptions die off rapidly.

5. For $x/D \geq 4.0$, a "propeller-like" structure appears and dominates the pattern. For this experiment, at least, this "propeller-like" structure appears to rotate in a single direction. The direction of this rotation corresponds to the direction of a slight (1:1000) rotation at the exit plane of the jet, but the rate of rotation of the "propeller" is orders of magnitude faster.

Bibliography

Armstrong, R. R., Michalke, A. & Fuchs, H. V. 1977 Coherent structures in jet turbulence and noise. *AIAA* **15**, 1011–1017.

Arndt, R. R. A., Long, D. F. & Glauser, M. N. 1997 The proper orthigonal decomposition of pressure fluctuations surrounding a turbulent jet. *Journal of Fluid Mechanics* **340**, 1–33.

Baker, C. T. H. 1977 *The Numerical Treatment of Integral Equations*. Oxford: Clarendon Press.

Batchelor, G. & Gill, E. 1962 Analysis of the instability of axisymmetic jets. *Journal of Fluid Mechanics* **14**, 529–551.

Citriniti, J. 1996 Experimental investigation into the dynamics of the axisymmetric mixing layer utilizing the proper orthogonal decomposition. PhD thesis, State University of New York at Buffalo.

Citriniti, J., Ewing, D. & George, W. 1994*a* Long hot-wires and the measurement of large scale turbulent fluctuations. In *Fluid Measurement and Instrumentation 1994*, pp. 45–52. ASME FED-Vol. 183.

Citriniti, J. & George, W. 2000 Reconstruction of the global velocity field in the axisymmetric mixing layer utilizing the proper orthogonal decomposition. *Journal of Fluid Mechanics* **418**, 137–166.

Citriniti, J., Taulbee, K., Woodward, S. & George, W. 1994*b* Design of multiple channel hot-wire anemometers. In *Fluid Measurement and Instrumentation 1994*, pp. 67–73. ASME FED-Vol. 183.

Citriniti, J. H. & George, W. K. 1997 The reduction of spatial aliasing by long hot-wire anemometer probes. *Expts. in Fluids* **23,3**, 217–224.

Crow, S. C. & Champagne, F. H. 1971 Orderly structure in jet turbulence. *J. Fluid Mech.* **48**, 547–591.

Davies, P., Fischer, M. & Barrett, M. 1963 The characteristic of the turbulence in the mixing layer of a round jet. *Journal of Fluid Mechanics* **15**, 337–367.

Delville, J., Cordier, L. & Bonnet, J.-P. 1998 *Flow Control: fundamentals and practices*, chap. Large-Scale-Structure Identification and Control in Turbulent Shear Flows. New York, NY: Springer-Verlag.

Gad-el-Hak, M., Pollard, A. & Bonnet, J.-P. 1998 *Flow Control: fundamentals and practices*. New York, NY: Springer-Verlag.

George, W., Beuther, P. & Lumley, J. 1978 Processing of random signals pp. 757–800.

George, W., Beuther, P. D. & Arndt, R. 1984 Pressure spectra in turbulent free shear flows. *Journal of Fluid Mechanics* **148**, 155–191.

George, W., Beuther, P. D. & Shabbir, A. 1989*a* Polynomial calibrations for hot-wires in thermally varying flows. *J. of Exp. Thermal and Fluid Science* **2**, 230–235.

George, W., Hussein, H. & Woodward, S. 1989*b* An evaluation of the effect of fluctuating convection velocity on the validity of taylor's hypothesis. In *Proc. 10th Australasian Fluid Mechanics Conference V. II* (ed. P. *et al.*), pp. 11.5–11.8. University of Melbourne.

George, W. & Taulbee, D. 1992 Designing experiments to test closure hypothesis. *J. Experimental Thermal and Fluid Sciences* **5** (3), 249–60.

George, W. K. 1988 Another look at the log (or is it a power law?) velocity profile for a zero-pressure gradient boundary layer. In *Bulletin of the American Physical Society*, , vol. 33 no.10, p. 2301. APS-DFD meeting, Buffalo, NY.

George, W. K., Leib, S. J. & Glauser, M. N. 1983 An application of lumley's orthogonal decomposition to the axisymmetric jet mixing layer. In *American Physical Society, Division of Fluid Dynamics*. Houston, TX.

Glauser, M. & George, W. K. 1987*a* An orthogonal decomposition of the axisymmetric jet mixing layer utilizing cross-wire measurements. In *Proceedings of the Sixth Symposium on Turbulent Shear Flow*, pp. 10.11–10.1.6. Toulouse, France.

Glauser, M. N. 1987 Coherent structures in the axisymmetric turbulent jet mixing layer. PhD thesis, State University of New York at Buffalo.

Glauser, M. N. & George, W. K. 1987*b* An orthogonal decomposition of the axisymmetric jet mixing layer utilizing cross-wire velocity measurements. In *Proc. Sixth Symp. Turb. Shear Flows*, pp. 10.1.1–10.1.6. Springer Verlag.

Glauser, M. N. & George, W. K. 1992 Application of multipoint measurements for flow characterization. *Experimental Thermal and Fluid Science* **5**, 617–632.

Glauser, M. N., Leib, S. J. & George, W. K. 1987 Coherent structures in the axisymmetric mixing layer. In *Turbulent Shear Flows 5* (ed. F. D. et.al.), p. 134. Springer Verlag.

Grinstein, F. F., Glauser, M. N. & George, W. K. 1995 *Fluid Vortices*, chap. Vorticity in Jets. Kluwer.

Gutmark, E. & Ho, C. 1983 Preferred modes and the spreading rates of jets. *Phys. Fluids* **26**, 2932–2938.

Herzog, S. 1986 The large scale structure in the near-wall region of turbulent pipe flow. PhD thesis, Cornell University.

Ho, C. M. & Hsaio, F. B. 1982 In *Proceedings of the IUTAM Symposium on Structure of Comples Turbulence Shear Flows*, pp. 121–136. Marseille, France.

Holmes, P., Lumley, J. L. & Berkooz, G. 1996 *Turbulence, Coherent Structures, Symmetry and Dynamical Systems*. Cambridge.

Hussain, A. K. M. F. & Clark, A. R. 1981 On the coherent structure of the axisymmetric mixing layer: a flow-visualization study. *J. Fluid Mech.* **104**, 263–294.

Hussein, H. J., Capp, S. P., & George, W. K. 1994 Velocity measurements in a high-reynolds-number, momentum-conserving, axisymmetric, turbulent jet. *Journal of Fluid Mechanics* **258**, 31–75.

Khwaja, M. S. 1981 Investigation of the turbulent axisymmetric jet mixing layer. Master's thesis, State University of New York at Buffalo.

Lau, J. C. & Fisher, M. J. 1975 The vortex-street structure of 'turbulent' jets. *J. Fluid Mech.* **67** (2), 299–337.

Liepmann, D. 1991 Streamwise vorticity and entrainment in the near-field of a round jet. *Phys. Fluids A* **3**, 1179–1187.

Liepmann, D. & Gharib, M. 1992 The role of streamwise vorticity in the near-field entrainment of round jets. *J. Fluid Mech.* **245**, 643–668.

Lovitt, W. 1950 *Linear Intrgral Equations*. Dover, New York.

Lumley, J. L. 1967 The structure of inhomogeneous turbulent flows. In *Atmospheric Turbulence and Radio Wave Propagation* (ed. A. M. Yaglom & V. I. Tatarsky). Moscow, USSR: Nauka.

Lumley, J. L. 1970 *Stochastic Tools in Turbulence*. Academic Press, New York, NY.

Martin, J. & Meiburg, E. 1991 Numerical invesitgation of three-dimensionally evolving jets subject to axisymmetric and azimuthal perturbations. *J. Fluid Mech.* **230**, 271–318.

Michalke, A. 1965 On spatially growing disturbances in an in viscid shear layer. *J. Fluid Mech.* **23**, 521–544.

Michalke, A. 1984 Survey on jet instability theory. *Prog. Aerospace Sci.* **21**, 159–199.

Michalke, A. & Hermann, G. 1982 In the invisicid instability of a circular jet with external flow. *J. Fluid Mech.* **114**, 343–359.

Moin, P. & Moser, R. D. 1989 Characteristic-eddy decomposition of turbulence in a channel. *J. Fluid Mech.* **200**, 471–509.

Perry, A. 1982 *Hot Wire anemometry*. Oxford: Clardedon Press.

Petersen, R. & Samet, M. 1988 On the preferred mode of jet instability. *J. Fluid Mech.* **194**, 153–173.

Taylor, J. F., Ukeiley, L. S. & Glauser, M. N. 2001 A low-dimensional description of the compressible axisymmetric shear layer. *AIAA* **2001-0292**.

Ukeiley, L., Glauser, M. & Wick, D. 1993 Downstream evolution of proper orthogonal decomposition eigenfunctions in a lobed mixer. *AIAA Journal* **31** (8), 1392–1397.

Ukeiley, L., Varghese, M., Glauser, M. & Valentine, D. 1992 Multifractal analysis of a lobed mixer flowfield utilizing the proper orthogonal decomposition. *AIAA Journal* **30** (5), 1260–1267.

Ukeiley, L., Wick, D. & Glauser, M. 1991 Coherent structure identification in a lobed mixer. *ASME, Paper 91-GT-397* .

Van Dyke, M. 1982 *An album of fluid motion*. Stanford, California: Parabolic Press.

Woodward, S. H., Ewing, D. & Jernqvist, L. 2001 Anemometer system review. In *In Sixth Annual Symposium on Thermal Anemometry*. Melbourne, AU.

Wyngaard, J. C. 1968 Measurement of small-scale turbulence with hot wires. *J. Scientific Instruments* **1**, 1105–1108.

Yule, A. J. 1978 Large-scale structure in the mixing layer of a round jet. *J. Fluid Mech.* **89**, 413–432.

Zaman, K. B. M. Q. & Hussain, A. K. M. F. 1984 Natural large-scale structures in the axisymmetric mixing layer. *J. Fluid Mech.* **138**, 325–351.